

**Experimental (Spectroscopic) and Theoretical Studies of
Rhodanine (2-Thio-4-Oxothiazolidine) and its Derivatives**

By

Saima Jabeen

[BSc, MSc, MRes (Chemistry), AMRSC]

A thesis submitted in partial fulfillment of the requirements of the
University of Greenwich for the Degree of Doctor of Philosophy in
Chemistry

October, 2007

**School of Science,
University of Greenwich at Medway
Chatham Maritime,
Kent ME4 4TB, UK**



the
UNIVERSITY
of
GREENWICH

Abstract

Experimental (Spectroscopic) and Theoretical Studies of Rhodanine (2-Thio-4-Oxothiazolidine) and its Derivatives

There is paucity of data in the scientific literature pertaining to detailed assignments of the vibrational spectra of nitrogen containing thiocarbonyl compounds. Herein, three five membered heterocyclic compounds -*rhodanine*, *3-aminorhodanine*, and *3-methylrhodanine*-containing both amide and thioamide moieties have been investigated from both an experimental and theoretical perspective. Experimental Raman ($\lambda_0 = 632.8$ nm) and infrared spectra of the three compounds have been recorded in the solid state (protonated and deuteriated). Deuteriation studies revealed that not only are the protons attached to the nitrogen atom labile, but the protons of the active methylene group also undergo hydrogen-deuterium exchange. Comparisons of protonated and deuteriated spectra enable discrimination of the bands associated with N-H, NH₂, CH₂ and CH₃ vibrations. *Ab initio* calculations, using density functional theory (DFT; B3-LYP) employing the cc-pVTZ basis set, have been conducted in order to obtain the geometry optimized, energy minimized structures of the isolated molecules in the gas phase. The data generated was then used to (a) compare, where possible, the calculated structure with the experimentally determined X-ray crystallographic structure, and (b) carry out normal coordinate analysis in order to obtain the potential energy distributions (PEDs) of each *normal* vibrational mode thus allowing detailed vibrational band assignments for the three molecules. The assignment of the bands associated with the amide and thioamide groups have been made possible by comparing the spectra of the three molecules and DFT calculations. In the case of rhodanine, the *cis* amide I mode is attributed to the bands at ~ 1713 and 1779 cm⁻¹, whereas a band at ~ 1457 cm⁻¹ is assigned to the amide II mode (Raman and IR). The vibrational bands for the thioamide II and III modes of rhodanine, 3-aminorhodanine, and 3-methylrhodanine are observed at 1176 and 1066/1078; 1126 and 1044; 1107 and 984 cm⁻¹ in the Raman and 1187 and 1083; 1230 and 1074; 1116 and 983 cm⁻¹ in the IR spectra, respectively.

Surface enhanced Raman spectroscopy (SERS) studies of the three molecules have been conducted as a function of pH, concentration, and time in order to understand their interaction/adsorption behaviour with citrate-reduced Ag and Au colloidal

(substrate) nanoparticles, as well as for semi-quantitative trace analysis. The pH studies revealed that the optimum conditions for SERS analysis is in the presence of HCl and poly(L-lysine) at pH 2.3 ($\lambda_0 = 632.8$ nm). The SERS studies also revealed the presence of a strong band at 1566/1575/1572 cm^{-1} (for rhodanine, 3-aminorhodanine and 3-methylrhodanine, respectively), irrespective of experimental conditions used. The 1566 cm^{-1} band is only present in the solid state dispersive Raman spectrum of rhodanine (as a very weak band) and absent in the solution (methanol) state Raman spectra of all three molecules. It is hypothesized that upon interaction with Ag and Au SERS substrates all three molecules undergo photo-initiated condensation reactions, which result in the formation of dimers. *Ab initio* calculations have also been performed on the dimers of rhodanine (B3-LYP/cc-pVTZ basis set), and for its derivatives (B3-LYP/D95 basis sets), followed by normal coordinate analysis. Calculated PEDs of the dimers suggest that the bands at 1566/1575/1572 cm^{-1} can be assigned to C=C stretching modes. Data from concentration-dependent SER spectra have been used to hypothesize that changes in the SERS profiles are related to the adsorbate concentration which could be due to changes in either the orientation of the analyte molecule on the Ag surface, adsorption via different coordinating sites or different surface coverage effects. The bands associated with thioamide groups in solid state Raman spectra show a large shift upon adsorption to the substrates, which suggest that the analyte molecules are coordinating through the exo-sulfur atom. For semi-quantitative analysis by SERS, low limits of detection (LODs) and good linear (signal vs concentration) correlations have been achieved for all three molecules. SERS studies of rhodanine have been conducted using two laser exciting wavelengths (514.5 and 632.8 nm); the low LODs (*i.e.*, femtomolar, 10^{-14} mol/dm³) are achieved using 632.8 nm excitation. For the rhodanine derivatives, trace analysis has been carried out using 632.8 nm excitation only. The LOD values for the three molecules (632.8 nm excitation) are as follows: rhodanine (10^{-14} mol/dm³) > 3-methylrhodanine (10^{-13} mol/dm³) > 3-aminorhodanine (10^{-12} mol/dm³).

In order to investigate the aggregation behaviour of Ag and Au colloidal nanoparticles, photon correlation spectroscopic studies have been conducted using a number of colloidal aggregating agents [poly(L-lysine), KCl, Na₂SO₄, and Na₂S₂O₃]

as a function of concentration and time. The concentration of the three inorganic electrolytes required to achieve optimum SERS signals range from 17-26 mmol dm⁻³. Size (hydrodynamic diameter) measurements of the SERS substrate nanoparticles show that the aggregation process is dynamic, and depends on time and concentration of added aggregating agent. Zeta (ζ)-potential measurements highlighted the fact that the presence of both poly(L-lysine) and HCl in the colloidal system increases the stability of the system, and slows down the aggregation process. The hydrodynamic diameter and ζ -potential measurements for rhodanine and its derivatives adsorbed on Ag and Au surfaces, under different experimental conditions, have also been investigated. The results show that rhodanine, in contrast to its derivatives, causes aggregation of Ag and Au colloidal nanoparticles in the absence of aggregating agents. The aforementioned observations are supported by SERS studies of the three molecules (using both Ag and Au substrates) without any aggregating agents; SER spectra are only obtained for rhodanine.

Saima Jabeen [BSc, MSc, MRes, AMRSC]

Declaration

I declare that the work submitted in this thesis has not previously been submitted, and is not currently being submitted, for any Degree other than that of Doctor of Philosophy (in Chemistry) of the University of Greenwich. All work reported herein is that of the author, except where acknowledged in the text.

Saima Jabeen, (Saima Jabeen) (Candidate)

30/11/07
Date

B. Z. Chowdhry (Prof. B. Z. Chowdhry) (Supervisor)

30/11/2007
Date

S. A. Leharne (Prof. S. A. Leharne) (Supervisor)

30/11/2007
Date

Acknowledgements

Firstly, I would like to express my heart-felt gratitude to my supervisors at the University of Greenwich, Professor B. Z. Chowdhry and Professor S. Leharne, for their time, constructive advice, and willingness to share their insight and wisdom throughout my PhD studies. Especially, Professor B. Z. Chowdhry, who consistently offered a fresh perspective on the work; his efforts on my behalf have helped me to become a better scientist. It has been a privilege for me to have worked with and been co-supervised by Dr T. J. Dines (University of Dundee), who has helped me with the *ab initio* calculations presented in this thesis.

Secondly, thank you to my family for their invaluable support and encouragement; in particular to my mother; it would almost certainly have been impossible for me to undertake the work reported in this thesis without her sincere prayers.

I would also like to thank UK Universities for awarding me an Overseas Research Students Award for three years; equally I am grateful to Prof. John Mitchell for arranging the student bursary to pursue my academic study.

I am very grateful to Dr A. Mendham, Dr B. Alexander and Dr I. T. Shadi who; in spite of busy schedules, have been readily available for advice, reading, or simply a word of encouragement. Special thanks are also due to Ms Nighat Kausar for her help, support and friendship during my studies.

Finally, I would like to thank all of the Faculty and postgraduate students in Medway Sciences and the School of Science for their support and a convivial atmosphere in which to work.

Dedication

I would like to dedicate this thesis to my beloved mother.

Value your thinking.
You do it well.
If you don't value it, no one else will.

Contents

Abstract.....	i
Declaration.....	iv
Acknowledgments.....	v
Dedication.....	vi
Contents.....	vii
List of Figures.....	xii
List of Tables.....	xviii
Abbreviations.....	xix
Overview of thesis.....	xxii
Chapter One: Rhodanine and its Derivatives	
1.1. Introduction.....	1
1.2. Biological Applications	2
1.3. Application as a Nucleophile in Novel Organic Synthesis.....	3
1.4. Applications in Industry.....	3
1.5. Applications in Coordination/Analytical Chemistry.....	4
1.6. Tautomers of Rhodanine.....	4
1.7. References.....	6
Chapter Two: Theoretical Aspects of Experimental Techniques and Computational Methods	
2.1. Introduction.....	9
2.2. Vibrational Spectroscopy.....	10
2.3. Molecular Vibrations.....	11
2.4. Anharmonicity.....	12
2.5. Normal Modes of Vibration.....	13
2.6. Raman Spectroscopy.....	14
2.7. Selection Rules for Raman Spectroscopy.....	16
2.8. Raman Cross-Section.....	18
2.9. Limitations of Raman Spectroscopy.....	19
2.10. Fluorescence Quenching.....	20
2.11. Raman Techniques.....	20
2.12. Resonance Raman Spectroscopy.....	20
2.13. Surface Enhanced Raman Spectroscopy (SERS).....	21
2.13.1. Theory of the SERS Effect.....	22

2.13.2. The Electromagnetic Effect (EM).....	23
2.13.3. The Chemical (Electronic) Effect (CT).....	24
2.13.4. SERS Substrates.....	25
2.13.5. Aggregation of Colloidal NPs.....	27
2.14. Surface Enhanced Resonance Raman Spectroscopy (SERRS).....	28
2.15. Applications of Raman and SERS.....	28
2.16. Limitations of SERS.....	29
2.17. Infrared (IR) Spectroscopy.....	29
2.17.1. Selection Rules for IR Spectroscopy.....	30
2.18. Raman versus IR spectroscopy.....	31
2.19. Factor Group Splitting.....	33
2.20. Molecular Symmetry.....	33
2.21. Photon Correlation Spectroscopy (PCS).....	36
2.21.1. Hydrodynamic Diameter.....	36
2.21.2. Zeta Potential.....	37
2.22. Computational Chemistry.....	40
2.23. Electronic Structure Methods.....	41
2.24. The Born-Oppenheimer Approximation.....	41
2.25. The Hartree-Fock Method (HF).....	42
2.26. Density Functional Theory (DFT).....	42
2.27. DFT Approximations.....	44
2.28. Basis Sets.....	45
2.29. Geometry Optimization.....	45
2.30. Vibrational Spectra.....	46
2.31. Vibrational Coordinates.....	48
2.32. Potential Energy Distribution (PED).....	49
2.33. References.....	50
 Chapter Three: Experimental and Instrumentation	
3.1. Chemical Reagents.....	59
3.2. Deuteriation.....	59
3.3. Raman Spectroscopy.....	60
3.4. Raman Solid State Spectra.....	64
3.5. Solutions of Rd and its Derivatives for Raman Studies.....	64
3.6. Solutions of Rd and its Derivatives for SERS Studies.....	64
3.7. SERS Measurements.....	64

3.8. Ag and Au Nanoparticles (NPs) Synthesis.....	65
3.9. Aggregation of Colloidal NPs.....	66
3.10. Reproducibility/Time Dependence.....	67
3.11. Concentration Dependence.....	67
3.12. SERS pH Dependence.....	67
3.13. FT-Infrared Spectroscopy.....	68
3.14. Photo Correlation Spectroscopy (PCS).....	69
3.14.1. Hydrodynamic diameter of Ag and Au NPs.....	70
3.14.2. ζ -Potential Measurements of Ag and Au NPs.....	71
3.15. <i>Ab initio</i> Calculations (DFT).....	72
3.15.1. Normal Coordinate Analysis (NCA).....	72
3.16. <i>UV/vis</i> Absorption Spectroscopy.....	74
3.17. Transmission Electron Microscopy (TEM).....	74
3.18. References.....	75

Chapter Four: DFT Calculations and Vibrational Spectroscopic Investigations of Rhodanine and Structural Derivatives in the Solid State

4.1. Introduction.....	77
4.2. Experimental.....	77
4.2.1. Chemical Reagents.....	77
4.2.2. Vibrational Spectroscopy.....	77
4.2.3. <i>Ab initio</i> Calculations.....	77
4.3. Results and Discussion.....	77
4.3.1. Geometry Optimization.....	77
4.3.2. Vibrational Spectroscopic Assignments.....	82
4.3.2.1. NH and NH ₂ Vibrations.....	89
4.3.2.2. CH ₂ and CH ₃ Vibrations.....	91
4.3.2.3. C=O Vibrations (Amide group).....	93
4.3.2.4. N-C=S Vibrations (Thioamide group).....	95
4.3.2.5. C-N and N-N Vibrations.....	96
4.3.2.6. C-C and C-S Vibrations.....	98
4.3.2.7. Thiazolidine Ring Vibrations.....	99
4.3.2.8. Electronic Structure.....	108
4.4. Conclusions.....	109
4.5. References.....	110

Chapter Five: DFT Calculations and Surface Enhanced Raman Spectroscopic Studies of Rhodanine and its Derivatives

5.1. Introduction.....	111
5.2. Experimental.....	112
5.2.1. Chemical Reagents.....	112
5.2.2. Vibrational Spectroscopy.....	112
5.2.3. Synthesis and Aggregation of Au and Ag Colloids.....	112
5.2.4. SERS pH Dependence.....	112
5.2.5. <i>UV/vis</i> Absorption Spectroscopy.....	112
5.2.6. DFT Calculations.....	112
5.3. Results and Discussion.....	112
5.3.1. Solution State Spectra.....	112
5.3.2. SERS pH Dependent Studies.....	113
5.3.3. SER Spectra of Rd.....	117
5.3.4. Effect of 514.5 nm Excitation Wavelength.....	119
5.3.5. SER Spectra of H ₂ NRd.....	120
5.3.6. SER Spectra of MeRd.....	121
5.3.7. Electronic Absorption Spectra.....	123
5.3.8. Origin of the Vibrational Band at $\approx 1566/1575/1572\text{ cm}^{-1}$ in SER Spectra.....	124
5.3.9. DFT studies: Geometry Optimization.....	128
5.3.10. Vibrational Band Assignments.....	134
5.3.11. Rd Dimer (<i>E</i> -Isomer).....	134
5.3.12. H ₂ NRd Dimer (<i>Z</i> -Isomer).....	140
5.3.11. MeRd Dimer (<i>Z</i> -Isomer).....	144
5.4. Summary and Conclusion.....	148
5.5. References.....	149
Chapter Six: Semi-Quantitative Trace Analysis of Rd and its Derivatives Adsorbed on Citrate-Reduced Silver Colloids	
6.1. Introduction.....	152
6.2. Experimental.....	153
6.2.1. Synthesis and Aggregation of Ag Colloid.....	153
6.2.2. Solutions of Rd and its Derivatives.....	153
6.2.3. SERS Measurements.....	153
6.2.4. Reproducibility/Time Dependence.....	153
6.2.5. Concentration Dependence.....	153
6.3. Results and Discussion.....	153
6.3.1. Concentration-Dependent SER Spectra of Rd.....	153
6.3.2. Concentration-Dependent SER Spectra of H ₂ NRd.....	158

6.3.3. Concentration-Dependent SER Spectra of MeRd.....	160
6.3.4. Time-Dependence of SER Spectra.....	162
6.3.5. Linear Correlations.....	165
6.3.6. Multi-linear Regression Analysis.....	165
6.4. Summary and Conclusions.....	172
6.5. References.....	173
Chapter Seven: PCS Measurements: Influence of Aggregating Agents on Ag and Au nanoparticles (NPs) Aggregation	
7.1. Introduction.....	174
7.2. Experimental.....	174
7.2.1. Chemical Reagents.....	174
7.2.2. Synthesis and Aggregation of Ag and Au Colloids.....	174
7.2.3. Photon Correlation Spectroscopy (PCS).....	175
7.2.4. <i>UV/vis</i> Absorption Spectroscopy.....	175
7.3. Results and Discussion.....	175
7.3.1. Characterization of Ag and Au colloidal NPs.....	175
7.3.2. Size Measurements of Ag and Au Aggregates (Effect of Electrolyte Concentration).....	177
7.3.3. Size Measurements of Ag and Au Aggregates (Effect of PLL Concentration).....	181
7.3.4. ζ -potential of Ag and Au Aggregates (Effect of Electrolyte Concentration).....	182
7.3.5. ζ -potential of Ag and Au Aggregates (Effect of PLL Concentration).....	184
7.3.6. Size and ζ -Potential Measurements of SERS Optimized Experimental Protocols.....	188
7.4. Summary and Conclusions.....	189
7.5. References.....	192
Chapter Eight: Overall Summary and Future Studies	
8.1. Summary.....	194
8.2. Future Studies.....	197
8.3. References.....	199
Appendix	I
Addendum	XVI

List of Figures

Figure 1.1.	Schematic representation of the chemical structure of rhodanines; X = H, NH ₂ , and CH ₃ for Rd, H ₂ NRd, and MeRd, respectively.	1
Figure 1.2.	Schematic representation of the synthesis of Rd.	2
Figure 1.3.	Potential tautomeric forms of Rd.	5
Figure 2.1.	Plane-polarized electromagnetic radiation.	9
Figure 2.2.	Molecular potential energy curve for a simple harmonic oscillator. The Morse potential energy curve reproduces the general shape of a molecular potential energy curve. The dissociation energy of a molecule, D_o , differs from the depth of the potential well, D_e , on account of the zero potential energy of the vibrations of the bond.	13
Figure 2.3.	Schematic representation of energy transitions in: (a) IR, (b) Rayleigh scattering, (c) Stokes Raman scattering and (d) anti-Stokes Raman scattering.	16
Figure 2.4.	Comparison of energy levels for: (a) pre-resonance Raman, (b) resonance Raman, (c) and fluorescence spectra.	21
Figure 2.5.	Flow chart showing the key decisions in point group assignment.	35
Figure 2.6.	Character table representing C_{1v} , C_{1h} , or C_s point group.	35
Figure 2.7.	Schematic representation of ζ -potential.	38
Figure 2.8.	Typical plot representing ζ -potential versus pH showing the position of the isoelectric point (where ζ -potential is zero) and the pH values where the dispersion would be expected to be stable.	39
Figure 2.9.	Flow chart showing the different stages for quantum mechanical calculations of molecular structure and spectroscopic properties.	47
Figure 3.1.	Photograph of the ISA laser Raman spectrometer system.	60
Figure 3.2.	Optical arrangement of the internal components of the ISA laser Raman spectrometer employed in all experiments. The laser paths are highlighted in red ($\lambda_o = 632.8$ nm) and green ($\lambda_o = 514.5$ nm).	61
Figure 3.3.	Schematic diagram of the ISA laser Raman spectrometer (a) front view, (b) rear view.	62
Figure 3.4.	Colloidal nanoparticles: (a) Au and (b) Ag.	65
Figure 3.5.	Representative SER spectral profiles of: Ag NPs: (a) alone, (b) in the presence of methanol, (c) in the presence of 0.01 % PLL, (d) in the presence of HCl (1 mol dm ⁻³), (e) in the presence of PLL, and HCl, and (f) in the presence of PLL, methanol, and HCl ($\lambda_o = 632.8$ nm).	66
Figure 3.6.	Schematic of the internal components of a typical Perkin-Elmer FT infrared spectrometer.	69

Figure 3.7.	The optical arrangement of the Zetasizer Nano ZS. The main components of the instrument are illustrated; the numbered items are described in the text.	70
Figure 3.8.	Optical configuration of a Malvern Zetasizer Nano instrument for measurement of electrophoretic mobility.	71
Figure 4.1.	Schematic representation showing the chemical structure and atom number labeling used in normal coordinate analysis (NCA) for Rd (I), H ₂ NRd (II), and MeRd (III).	79
Figure 4.2.	The computed molecular geometries at cc-pVTZ/B3LYP level (in gas phase) of: Rd (I), H ₂ NR (II), and MeRd (III); together with the X-ray crystallographic structure of Rd (I').	79
Figure 4.3.	Experimental and calculated (a) Raman and (b) FT-IR spectra for Rd (protonated).	83
Figure 4.4.	Experimental and calculated (a) Raman and (b) FT-IR spectra for Rd (deuteriated).	84
Figure 4.5.	Experimental and calculated (a) Raman and (b) FT-IR spectra for H ₂ NRd (protonated).	85
Figure 4.6.	Experimental and calculated (a) Raman and (b) FT-IR spectra for H ₂ NRd (deuteriated).	86
Figure 4.7.	Experimental and calculated (a) Raman and (b) FT-IR spectra for MeRd (protonated).	87
Figure 4.8.	Experimental and calculated (a) Raman and (b) FT-IR spectra for MeRd (deuteriated).	88
Figure 5.1.	Solution state (in methanol) spectra of Rd and its derivatives ($\lambda_0 = 632.8$ nm).	113
Figure 5.2.	(a) SER spectra of Rd (1.0×10^{-3} mol dm ⁻³) adsorbed on the Ag colloid in the presence of 0.01 % (w/v) PLL and HCl in the pH range 2.3 to 11.3, (b) SERS pH profile for the band at 556 cm ⁻¹ (highlighted with red arrow); ($\lambda_0 = 632.8$ nm).	114
Figure 5.3.	SER spectra of H ₂ NRd (8.6×10^{-4} mol dm ⁻³) adsorbed on the Ag colloid in the presence of 0.01% PLL and HCl in the pH range from 2.3 to 11.3; ($\lambda_0 = 632.8$ nm).	115
Figure 5.4.	(a) SER spectra of MeRd (8.7×10^{-4} mol dm ⁻³) adsorbed on the Ag colloid in the presence of 0.01 % (w/v) PLL and HCl at pH values ranging from 2.3 to 11.3, (b) SERS pH profile for the band at 1255 cm ⁻¹ (highlighted with red arrow); ($\lambda_0 = 632.8$ nm).	117
Figure 5.5.	(a) Raman spectrum of Rd in the solid state ($\lambda_0 = 632.8$ nm), (b) SER spectrum of Rd adsorbed on Au colloid at pH 6.12 ($\lambda_0 = 632.8$ nm), SER spectra of Rd adsorbed on Ag colloids: (c) at pH 6.12, (d) in the presence of HCl at pH 2.3, (e) in the presence of PLL, and HCl at pH 2.3 ($\lambda_0 = 632.8$ nm) and (f) in the presence of PLL and HCl at pH 2.3 ($\lambda_0 = 514.5$ nm). The concentration of Rd for all the SER spectra was 1.0×10^{-3} mol dm ⁻³ .	118
Figure 5.6.	(a) Raman spectrum of H ₂ NRd (8.6×10^{-4} mol dm ⁻³) in the solid state	121

	($\lambda_o = 632.8$ nm). SER spectra of H ₂ NRd: (b) adsorbed on the Au colloid at pH 7.70, (c) adsorbed on the Ag colloid at pH 7.70, (d) in the presence of HCl at pH 2.3, and (e) in the presence of PLL and HCl at pH 2.3; ($\lambda_o = 632.8$ nm).	
Figure 5.7.	(a) Raman spectrum of MeRd (8.7×10^{-4} mol dm ⁻³) in the solid state ($\lambda_o = 632.8$ nm). SER spectra of MeRd: (b) adsorbed on the Au colloid at pH 7.62, (c) adsorbed on the Ag colloid at pH 7.62, (d) in the presence of HCl at pH 2.3, and (e) in the presence of both PLL and HCl at pH 2.3; ($\lambda_o = 632.8$ nm).	122
Figure 5.8.	Electronic absorption spectra of (a) non-aggregated and aggregated Ag colloid, (b) Rd (1×10^{-3} mol dm ⁻³), and (c) MeRd (8.7×10^{-4} mol dm ⁻³) under different experimental conditions.	124
Figure 5.9.	Possible tautomeric forms of Rd derivatives, R = Me or H ₂ N.	125
Figure 5.10.	Chemical structure representing Ag complex formation with Rd.	126
Figure 5.11.	Chemical structure of dimer, R = Me or H ₂ N	127
Figure 5.12.	Calculated (B3LYP/ cc-pVTZ) molecular geometries (in the gas phase) of Rd dimers, and atom number labeling of <i>E</i> -isomer.	129
Figure 5.13.	Calculated (B3LYP/ D95) molecular geometries (in the gas phase) of H ₂ NRd dimers and atom number labeling of <i>Z</i> -isomer.	129
Figure 5.14.	Calculated (B3LYP/ D95) molecular geometries (in the gas phase) of MeRd dimer, and atom number labeling of <i>Z</i> -isomer.	129
Figure 5.15.	Experimental and calculated SER spectra of the Rd dimer (<i>E</i> -isomer) under optimized experimental conditions using (a) $\lambda_o = 514.5$ and (b) $\lambda_o = 632.8$ nm.	137
Figure 5.16.	Experimental and calculated SER spectra of H ₂ NRd dimer (<i>Z</i> -isomer) under optimized experimental conditions ($\lambda_o = 632.8$ nm).	141
Figure 5.17.	Experimental and calculated SER spectra of MeRd dimer (<i>Z</i> -isomer) under optimized experimental conditions ($\lambda_o = 632.8$ nm).	145
Figure 6.1.	SER spectra of Rd adsorbed on the Ag colloid as a function of concentration, ($\lambda_o = 632.8$ nm excitation). The concentrations of Rd are: (a) 1×10^{-3} , (b) 4.8×10^{-4} , (c) 2.4×10^{-4} , (d) 1.2×10^{-4} , (e) 6×10^{-5} , (f) 3×10^{-5} , (g) 1.5×10^{-5} , (h) 7.5×10^{-6} , and (i) 3.7×10^{-6} mol dm ⁻³ .	155
Figure 6.2.	SER spectra of Rd adsorbed on the Ag colloid as a function of concentration ($\lambda_o = 632.8$ nm). The concentrations of Rd, from top to bottom, are: (a) 1×10^{-3} , 7.4×10^{-4} , 4.9×10^{-4} , 2.4×10^{-4} , 1×10^{-4} , 1×10^{-5} , and 1×10^{-6} mol dm ⁻³ . (b) Concentration of Rd vs. signal intensity (peak area for non-log data) for SERS bands at 556 (▲) and 1566 cm ⁻¹ (▲).	156
Figure 6.3.	Plausible adsorption orientations of Rd dimer on the Ag surface: (a) in the absence, and (b) presence of PLL and HCl.	157

- Figure 6.4.** SER spectra of H₂NRd adsorbed on the Ag colloid as a function of concentration ($\lambda_0 = 632.8$ nm). The concentrations of Rd from top to bottom are: 8.6×10^{-4} , 8.6×10^{-5} , 8.6×10^{-6} , 8.6×10^{-7} , and 8.6×10^{-8} mol dm⁻³. 159
- Figure 6.5.** Plausible adsorption orientations of H₂NRd dimer (*Z-isomer*) on the Ag surface: (a) at higher and (b) low concentrations in the presence of PLL and HCl. 159
- Figure 6.6.** SER spectra of MeRd adsorbed on the Ag colloid as a function of concentration ($\lambda_0 = 632.8$ nm). The concentrations of MeRd from top to bottom are: 8.7×10^{-4} , 8.7×10^{-5} , 8.7×10^{-6} , and 8.7×10^{-7} mol dm⁻³. 160
- Figure 6.7.** Plausible adsorption orientations of MeRd dimer (*Z-isomer*) on the Ag surface: (a) at higher and (b) low concentrations in the presence of PLL and HCl. 161
- Figure 6.8.** Time dependent SER spectra of: (a) Rd (1×10^{-3} mol dm⁻³) in the absence of PLL and HCl, (b) Rd (1×10^{-4} mol dm⁻³), (c) ln [signal intensity (peak area)] vs. time for SERS band at 1566 cm⁻¹, (d) H₂NRd (8.6×10^{-5} mol dm⁻³), and (e) MeRd (8.7×10^{-5} mol dm⁻³) in the presence of PLL and HCl; ($\lambda_0 = 632.8$ nm). 164
- Figure 6.9.** (a). Representative 514.5 nm excited SER spectra for Rd (at pH 2.3) in the linear signal vs. concentration region. Concentrations, from top to bottom, are 1×10^{-8} , 1×10^{-9} , 2.5×10^{-10} , 1×10^{-10} and 1×10^{-11} mol dm⁻³. The bands used for analysis are indicated with arrows. (b). Log (concentration) vs. log (signal intensity) (peak area) over the concentration range examined for 632.8 nm excited SERS bands at 452 (▲) and 1566 cm⁻¹ (◆). (c). Linear region of intensities of SERS bands of Rd at 452 (▲) and 1566 cm⁻¹ (◆) used for multi-linear regression analysis. 167
- Figure 6.10.** (a). Representative 632.8 nm excited SER spectra of Rd (at pH 2.3) in the linear signal vs. concentration region. Concentrations from top to bottom are 1×10^{-7} , 1×10^{-8} , 1×10^{-9} , 1×10^{-10} , 1×10^{-11} , 1×10^{-12} , and 1×10^{-13} mol dm⁻³. The bands used for analysis are indicated by arrows. (b). Log concentration Rd vs. log signal intensity (peak area) over the concentration range examined for 632.8 nm excited SERS bands at 556 (◁) and 1566 cm⁻¹ (○). (c). Linear region of intensities of SERS bands of Rd at 556 (◁) and 1566 cm⁻¹ (○) used for multi-linear regression analysis. 168
- Figure 6.11.** (a). Representative 632.8 nm excited SER spectra of H₂NRd (at pH 2.3) in the linear signal vs. concentration region. Concentrations from top to bottom are 8.6×10^{-7} , 8.6×10^{-8} , 8.6×10^{-9} , 8.6×10^{-10} , 8.6×10^{-11} , and 8.6×10^{-12} mol dm⁻³. The bands used for analysis are indicated with arrows. (b). Log concentration Rd vs. log signal intensity (peak area) over the concentration range examined for 632.8 nm excited SERS bands at 524 (▼) and 1166 (●) cm⁻¹. (c). Linear region of intensities of SERS bands of Rd at 524 (▼) and 1166 cm⁻¹ (●) used for multi-linear regression analysis. 169
- Figure 6.12.** (a). Representative 632.8 nm excited SER spectra of MeRd (at pH 2.3) in the linear signal vs. concentration region. Concentrations from top to bottom are 8.7×10^{-9} , 8.7×10^{-10} , 8.7×10^{-11} , 8.7×10^{-12} , and 8.7×10^{-13} mol dm⁻³. The bands used for analysis are indicated with arrows. (b). Log concentration vs. log signal intensity (peak area) over the concentration range examined for 170

632.8 nm excited SERS bands at 433 (■) and 1255 cm^{-1} (◄). (c). Linear region of intensities of SERS bands of Rd at 433 (■) and 1255 cm^{-1} (◄) used for multi-linear regression analysis.

- Figure 7.1.** UV/Vis spectra of: (a) Ag and (b) Au NPs prepared by chemical Reduction method with tri-sodium citrate. 175
- Figure 7.2.** Size distribution analysis by intensity: (a) Ag and (b) Au NPs. 176
- Figure 7.3.** Transmission electron micrograph of citrate reduced colloidal Ag Particles at a magnification of $\times 50,000$. 176
- Figure 7.4.** Hydrodynamic diameters (D_H) of: (a) Ag and (b) Au aggregates as a function of concentration of Na_2SO_4 (■), KCl (●), and $\text{Na}_2\text{S}_2\text{O}_3$ (▲). 178
- Figure 7.5.** Size distribution analysis by intensity of the Ag NPs in the presence of: (a) 100 mmoldm^{-3} KCl and (b) 100 mmoldm^{-3} Na_2SO_4 after 4.5 (■), 7.5 (●), 10.5 (▲), 13.5 (▼), 16.5 (◆), and 19.5 (◄) mins. 179
- Figure 7.6.** Hydrodynamic diameter (D_H) of: (a) Ag and (b) Au aggregates as a function of time in the presence of KCl over the concentration range of 7 (●), 17 (►), 26 (◄), 35 (◆), 53 (▼), 70 (▲), 84 (●), and 100 (■) mmoldm^{-3} . 179
- Figure 7.7.** Hydrodynamic diameter (D_H) of: (a) Ag and (b) Au aggregates as a function of time in the presence of Na_2SO_4 over the concentration range of 7 (►), 17 (◄), 26 (◆), 35 (▼), 56 (▲), 70 (●), and 100 (■) mmoldm^{-3} . 180
- Figure 7.8.** Hydrodynamic diameter (D_H) of Ag aggregates as a function of time in the presence of $\text{Na}_2\text{S}_2\text{O}_3$ over the concentration range of 7 (●), 17 (►), 21 (◄), 26 (◆), 35 (▼), 56 (▲), 70 (●), and 100 (■) mmoldm^{-3} . 181
- Figure 7.9.** Hydrodynamic diameters (D_H) of: (a) Ag and (b) Au aggregates as a function of concentration of PLL. 182
- Figure 7.10.** Hydrodynamic diameter (D_H) of: (a) Ag and (b) Au aggregates as a function of time in the presence of PLL over the concentration range of 1×10^{-4} (■), 2.5×10^{-4} (►), 5×10^{-4} (●), 1.2×10^{-3} (◆), 2.5×10^{-3} (▼), 5×10^{-3} (▲), and 0.01 (●) % (w/v). 183
- Figure 7.11.** Size distribution analysis by intensity of Ag NPs in the presence of: (a) 1.2×10^{-3} and (b) 0.01% (w/v) after 4.5 (■), 7.5 (●), 10.5 (▼), 13.5 (▲), 16.5 (◆), and 19.5 (◄) mins. 183
- Figure 7.12.** ζ -potential and electrophoretic mobility measurements of (a) Ag and (b) Au aggregates as a function of concentration of KCl. 185
- Figure 7.13.** ζ -potential and electrophoretic mobility measurements of (a) Ag and (b) Au aggregates as a function of concentration of Na_2SO_4 . 186
- Figure 7.14.** ζ -potential and electrophoretic mobility measurements of Ag aggregates as a function of concentration of $\text{Na}_2\text{S}_2\text{O}_3$. 187
- Figure 7.15.** ζ -potential and electrophoretic mobility measurements of (a) Ag and (b) Au aggregates as a function of concentration of PLL. 188

List of Appendix Figures

Figure 1.1.	^{13}C -NMR spectra of MeRd, H ₂ NRd, and Rd in the solid state.	III
Figure 1.2.	^{13}C -NMR spectra of Rd, H ₂ NRd and MeRd in the solution state (CD ₃ OD).	VI
Figure 1.3.	^1H -NMR spectra of Rd in the solution state.	VII
Figure 1.4.	^1H -NMR spectra of Rd in the solution state, in the presence of DCl.	VIII
Figure 1.5.	^1H -NMR spectra of H ₂ NRd in the solution state.	IX
Figure 1.6.	^1H -NMR spectra of MeRd in the solution state (CD ₃ OD).	X
Figure 1.9.	Mass spectra of Rd alone and Rd in HCl.	XI
Figure 1.10.	Mass spectra of H ₂ NRd alone and H ₂ NRd in HCl.	XII
Figure 1.11.	Mass spectra of MeRd alone and MeRd in HCl.	XIII
Figure 1.12.	Schematic representation of the possible resonance structures of rhodanine.	XIV
Figure 1.13.	X-ray crystallographic structure of Rd showing (a) an isolated molecule and (b) crystal packing.	XIV

List of Tables

Table 2.1.	Techniques used to characterize different properties of colloidal nanostructures.	26
Table 3.1.	Chemical reagents.	59
Table 4.1.	Comparison of calculated and experimental geometries for Rd together with the calculated geometries for H ₂ NRd and MeRd. Bond distances are quoted in Å, bond angles and torsion angles in degrees.	80
Table 4.2.	Experimental and theoretical calculations (NCA) for Rd in the solid state (protonated).	101
Table 4.3.	Experimental and theoretical calculations (NCA) for Rd- <i>d</i> ₃ in the solid state (deuteriated).	102
Table 4.4.	Experimental and theoretical calculations (NCA) for H ₂ NRd in the solid state (protonated).	103
Table 4.5.	Experimental and theoretical calculations (NCA) for H ₂ NRd- <i>d</i> ₄ in the solid state (deuteriated).	105
Table 4.6.	Experimental and theoretical calculations (NCA) for MeRd in the solid state (protonated).	106
Table 4.7.	Experimental and theoretical calculations (NCA) for MeRd- <i>d</i> ₂ in the solid state (deuteriated).	107

Table 4.8.	Partial charge on different atoms in Rd, H ₂ NRd, and MeRd calculated at the B3LYP level, using cc-pVTZ basis set.	109
Table 5.1.	Optimized geometry parameters of <i>Z</i> and <i>E</i> isomers of Rd. Bond distances are quoted in Å, bond angles and torsion angles in degrees.	130
Table 5.2.	Optimized geometry parameters of <i>Z</i> and <i>E</i> isomers of H ₂ NRd. Bond distances are quoted in Å, bond angles and torsion angles in degrees.	131
Table 5.3.	Optimized geometry parameters of <i>Z</i> and <i>E</i> isomers of MeRd. Bond distances are quoted in Å, bond angles and torsion angles in degrees.	132
Table 5.4.	Experimental and theoretical calculations (NCA) for Rd dimer.	138
Table 5.5.	Experimental and theoretical calculations (NCA) for H ₂ NRd dimer.	142
Table 5.6.	Experimental and theoretical calculations (NCA) for MeRd dimer.	146
Table 6.1.	Analytical parameters calculated from multi-linear regression analysis for Rd and its derivatives.	171
Table 7.1.	Hydrodynamic diameter (D_H), ζ -potential, and electrophoretic mobility (Mob) values for Ag and Au NPs in the presence and absence of different experimental reagents.	191

Abbreviations

Symbol	Description
H ₂ NRd	-3-aminorhodanine
ω	-angular frequency
A''	-anti-symmetric with respect to rotation about the main axis
AFM	-atomic force microscopy
k_B	-Boltzmann's constant
C=O	-carbonyl group (amide)
CT	-chemical transfer effect
χ^2	-chi squared
NPs	-colloidal nanoparticles
cc-pVTZ	-correlation consistent polarized triple zeta
EDL	-Debye layer or an electrical double layer
DFT	-density functional theory
ρ	-depolarization ratio
DLVO	-Derjaguin, Landau, Vervey and Overbeek
ε	-dielectric constant
D_f	-diffusion coefficient
σ_d	-dihedral plane
q	-displacement coordinate
DSP	-dual specificity phosphatases
DLS	-dynamic or static light scattering
μ_e	-electric dipole moment
T^{elec}	-electric kinetic energy
EM	-electromagnetic field enhancement
ρ	-electron density
EELS	-electron energy loss spectroscopy
\vec{r}	-electronic coordinate
V^{elec}	-electronic potential energy
U_e	-electrophoretic mobility,
r_e	-equilibrium bond distance
$E_{xc}[\rho]$	-exchange-correlation energy functional
$V_{xc}[\rho]$	-exchange-correlation potential
k	-force constant
FT-IR	-Fourier transform infrared
ν	-frequency
fwhm	-full-width at half maximum
GTOs	-Gaussian-type orbitals
GGA	-generalized gradient approximation
H	-Hamiltonian operator
HF	-Hartree-Fock

$f(ka)$	-Henry's function
D_h	-hydrodynamic diameter
ω_L	-incident light angular frequency
T_s	-kinetic energy functional
λ_o	-laser excitation wavelength
LOD	-limits of detection
LDA	-local density approximation
LSPR	-localization of the surface plasmon resonance
LSPRS	-localized surface plasmon Resonance spectroscopy
M	-magnetic field
MeRd	-3-methylrhodanine
MP	-Møller and Plesset
NSOM	-near field scanning probe techniques
NIR	-near-IR
NCA	-normal coordinate analysis
\bar{R}	-nuclear coordinate
T^{nucl}	-nuclear kinetic energy
NMR	-nuclear magnetic resonance
V^{nucl}	-nuclear potential energy
E_{ne}	-nuclear potential energy
E	-oscillating electric field
PRL	-phosphatase of regenerating liver
PCS	-photon correlation spectroscopy
h	-Planck's constant
PS-SERES	-plasmon-sampled surface-enhanced Raman excitation spectroscopy
PLL	-poly(L-lysine)
KBr	-potassium bromide
PEDs	-potential energy distributions
V_A	-potential energy due attractive forces
V_R	-potential energy due to repulsive forces
V_s	-potential energy due to the solvent
μ	-reduced mass
σ	-reflection
RAIRS	-reflection absorption infrared spectroscopy
RF	-resonance fluorescence
RRS	-resonance Raman Spectroscopy
Rd	-rhodanine
S_n	-rotation reflection axis
STM	-scanning tunneling microscopy
ω_s	-scattered light angular frequency
SCF	-self consistent field
SSRS	-shifted subtracted Raman spectroscopy
SMD	-single molecule detection
STOs	-slater orbitals

η	-solvent viscosity
c	-speed of light
SEIRA	-surface enhanced infrared absorption
SERS	-surface enhanced Raman spectroscopy
SERRS	-surface enhanced resonance Raman spectroscopy
SPs	-surface plasmons
A'	-symmetric with respect to rotation about main axis
C=S	-thiocarbonyl group (thioamide)
M	-transition dipole moment
TEM	-transmission electron microscopy
TNF- α	-tumor necrosis factor alpha
σ_v	-vertical plane
ψ	-wavefunction
Ψ_v	-wavefunction of final vibrational state
Ψ_v'	-wavefunction of initial vibrational state
λ	-wavelength
$\tilde{\nu}$	-wavenumber
ζ	-zeta potential

\sim = varies with

\approx = is approximately equal to

Blue shifted: moves to higher energy

Red shifted: moves to lower energy

Abbreviations for vibrational modes

ν = stretch, δ = deformation, ω = wag, τ = twist, ρ = rock, s = symmetric,

as = asymmetric, ip = in-plane, op = out-of-plane, b = bend

Overview

The investigations reported in this thesis relate to experimental and theoretical (chemical computation) studies of rhodanine and its two derivatives, namely 3-aminorhodanine and 3-methylrhodanine. Rhodanine belongs to the class of organic compounds referred to as thiazolidines, which consist of a saturated 5-membered heterocyclic ring with a sulfide and an amine group at positions 1 and 3, respectively (Fig.1).

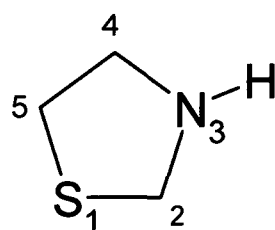


Figure 1. Schematic of the chemical structure of thiazolidine.

The thiazolidine ring of rhodanine is substituted with thiocarbonyl (C=S) and carbonyl (C=O) moieties at positions 2 and 4, respectively. Rhodanine is a mono-substituted cyclic *cis* thioamide/amide, whereas its derivatives are di-substituted thioamides/amides. Chapter one gives a -albeit brief- overview of the structure, synthesis, and uses of rhodanine and its derivatives.

Chapter two provides the theoretical background to experimental techniques and computational methods used to obtain the vibrational spectra and/or molecular structure of the molecules investigated. This chapter is divided into four parts. The first part focuses on dispersive Raman spectroscopy and related techniques, particularly surface enhanced Raman spectroscopy (SERS); the second part describes FT-IR, the third part photon correlation spectroscopy, and finally chemical computational methods (density functional theory (DFT) calculations) are discussed.

In chapter three general experiments, instrumentation, and methods used for Raman, FT-IR, SERS, photon correlation spectroscopy (PCS), *UV/vis*, and transmission electron microscopy are discussed. The methods employed for the synthesis/aggregation of colloidal nanoparticles, used as SERS substrates, are also described. In addition DFT

calculations and normal coordinate analysis used for structure determination and band assignments, respectively are discussed.

Chapter four examines experimental (solid state) vibrational (Raman/FT-IR) spectroscopic studies, supported by DFT calculations, for the three molecules (both protonated and deuteriated) under scrutiny. Dispersive, back-scattered Raman spectra have been recorded for rhodanine and its two derivatives using a confocal microscope. These experiments were conducted using a helium-neon laser ($\lambda_0 = 632.8$ nm), and a power of 8 mW at the sample. FT-IR spectra of rhodanine and its derivatives have also been recorded; solid state samples were examined as pressed KBr discs. The results from Raman and FT-IR studies are compared and contrasted. *Ab initio* calculations, employing density functional theory (DFT), have been carried out on the three molecules studied. Geometry optimisation was conducted using the hybrid SCF-DFT method B3-LYP, by employing the cc-pVTZ basis set. DFT calculations were based on a single, isolated molecule in the gas phase. Results have provided the minimum energy, geometry optimized structures for all the molecules examined, and subsequent normal coordinate calculations provided vibrational mode locations including relevant potential energy distributions (PEDs), thus allowing Raman and FT-IR vibrational band assignments to be made, in particular those associated with the N-C=S moiety. This group gives rise to bands in the lower frequency region and is susceptible to coupling effects. Hence, the identification and assignment of such bands is a difficult task if based on group frequency theory alone. Normal coordinate analysis (NCA) offers a solution to this problem by allowing calculations to be performed which provide the relative contribution of each vibrational mode, in terms of PEDs, to the overall band. The calculated optimized geometry of rhodanine has been compared and contrasted with the experimentally derived X-ray crystallographic structure. For the rhodanine derivatives, experimentally determined X-ray crystallographic structures have not been reported. Therefore, energy minimized/geometry optimized structures of rhodanine, 3-aminorhodanine and 3-methylrhodanine are compared and contrasted. Comparisons of protonated and deuteriated molecules have aided assignment of specific bands for CH₂ and N-H/NH₂

vibrations due to the fact that the protons in these chemical moieties are acidic in nature and subject to hydrogen-deuterium exchange, respectively.

Solution state Raman spectra were obtained in methanol due to the very low solubility, of the molecules examined, in water. Dispersive, visible Raman spectroscopy is rarely a sensitive technique for the analysis of samples in the solution state; it normally requires high concentrations of solutes. To overcome this limitation, surface enhanced (resonance) Raman spectroscopy [SER(R)S] is often used, where analyte samples are adsorbed onto a roughened metal surface (*e.g.* coinage metals such as Au and Ag) to give signal enhancements in the order of 10^6 - 10^8 (or more). Chapter five reports studies of rhodanine and its derivatives using colloidal Ag and Au nanoparticles (NPs) as SERS substrates. A number of experimental variables (pH, concentration, and excitation wavelength) have been investigated to optimize the SER spectra, in order to achieve reliable and reproducible data. This study reveals a pivotal feature of rhodanine and its derivatives adsorbed to Ag and Au nanoparticle surfaces *i.e.*, the presence of a strong band at $\approx 1566/1575/1572$ cm^{-1} for rhodanine, 3-aminorhodanine, and 3-methylrhodanine, respectively. It is hypothesized that, under the experimental conditions used, the rhodanines undergo a photo-catalyzed self-condensation reaction, which results in the formation of dimers. Quantum mechanical calculations have been carried out on dimers of the rhodanine molecules to assist in the interpretation of experimental SER spectra.

In chapter six, based on the results obtained in chapter five, the results of SERS concentration-dependent studies are reported in order to gain insight into the adsorption behaviour of the three rhodanine molecules to the Ag substrate. In the case of rhodanine and 3-aminorhodanine concentration dependent changes in SER spectral profiles are demonstrated. It is hypothesized that this phenomenon may reflect either changes in analyte orientation, interaction of the analyte with the substrate via different functional moieties (adsorption/coordination sites *e.g.* N-, S- or O-), or surface coverage effects. Furthermore, the sensitivity of SERS for semi-quantitative trace analysis of these molecules is also demonstrated.

Aggregation of colloidal NPs is an important factor in achieving enhanced signals in SERS experiments. Based on this premise, hydrodynamic diameter, zeta potential (ζ), and electrophoretic mobility measurements of Ag and Au NPs in the presence of different aggregating agents, using photon correlation spectroscopy (PCS) are reported in chapter seven. The values of the ζ -potential relate to the stability and surface charge of the colloidal system. Aggregation is a dynamic process; to shed light on the degree of aggregation PCS studies were conducted as a function of concentration of particular aggregating agents, and time. These investigations were further extended for different experimental protocols employed in chapter six to optimize SER spectra of rhodanine and its derivatives.

Chapter One

Rhodanine and its Derivatives

1.1. Introduction

Rhodanine [2-thio-4-oxothiazolidine (Rd)], 3-aminorhodanine [3-amino-2-thio-4-oxothiazolidine (H_2NRd)] and 3-methylrhodanine [3-methyl-2-thio-4-oxothiazolidine (MeRd)], are five-membered ring heterocyclic systems (Fig.1.1) with diverse applications particularly in biochemistry, medicinal chemistry, photochemistry, industry, and coordination chemistry.

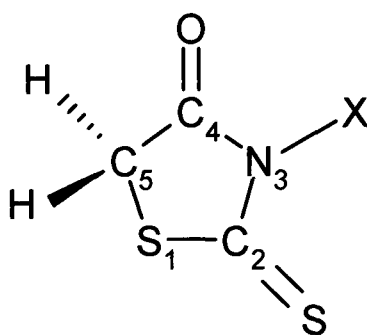


Figure 1.1. Schematic representation of the chemical structure of rhodanines; X = H, NH_2 , and CH_3 for Rd, H_2NRd and MeRd, respectively.

The Rd structure is not prevalent in natural molecules. The Rd moiety can be synthesized by various methods such as the addition of isothiocyanate to mercaptoacetic acid followed by acid cyclization, or the reaction of ammonia or primary amines with carbon disulfide and chloroacetic acid in the presence of bases¹⁻². One method of preparation adapted from that of Julian and Sturgis^{1b} is depicted in Fig.1.2. In this particular method Rd is synthesized by reacting ammonium dithiocarbamate with sodium chloroacetate followed by cyclization at high temperature, using hydrochloroacetic acid.

The starting materials for the synthesis of H_2NRd are the methyl and ethyl esters of S-(N-aminothiocarbonyl) thioglycolic acid; subsequent closure of the thiazolidine ring results in H_2NRd ³.

Treatment of chloro-acetylchloride with di-thiocarbamates in acetone/water in the presence of triethylamine yields MeRd⁴.

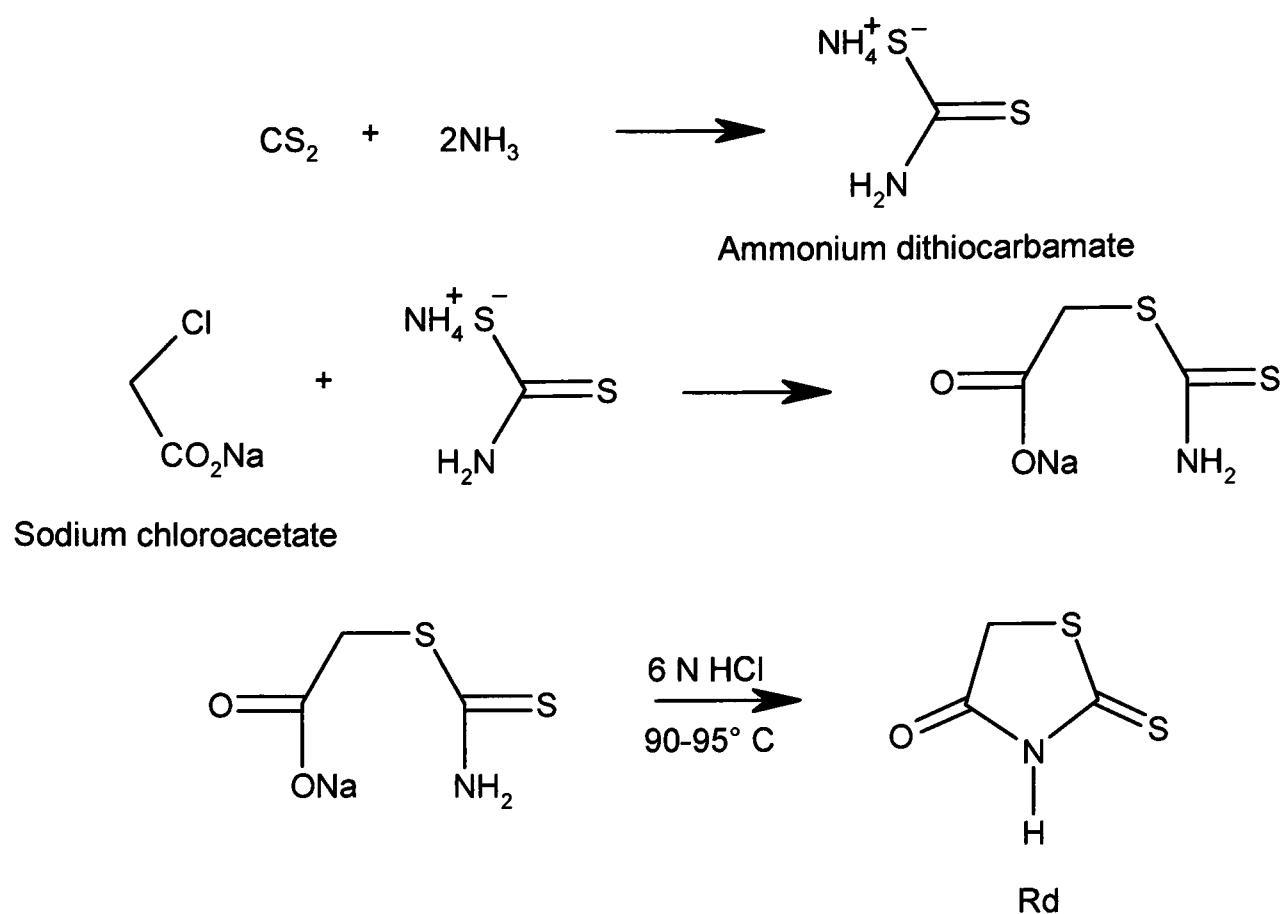


Figure 1.2. Schematic representation of the synthesis of Rd^{1b}.

The classification of Rd derivatives is based solely on whether the 2-thioxo-4-oxothiazolidine ring is linked to the rest of the molecule through an exocyclic double bond or via a single bond at the 5 position.

1.2. Biological Applications

Rd is widely used for the selective inhibition of the un-coating of echoviruses (the largest sub-group of enteroviruses which contribute to diseases such as aseptic meningitis, myocarditis, and encephalitis), but other processes of the viral infectious cycle are not affected⁵. During inhibition Rd binds to the virus capsid and prevents formation of non-infectious “A particles” thereby maintaining intact, infectious virions associated with the host cell. Rd derivatives are also known to be novel, potent and selective inhibitors against dual-specificity phosphatases (DSPs) including the family member JNK-stimulating phosphatase-1 (JSP-1)⁶ and mycobacterium tuberculosis⁷. The binding of tumor necrosis factor alpha (TNF- α) to the type-I TNF receptor (TNFRc1) plays an

important role in inflammation. The photochemically enhanced binding of Rd derivatives to the TNFRcI inhibits the binding of TNF- α . They bind reversibly to TNFRcI with weak affinity (*ca.* 40-100 mmol dm⁻³) and then covalently modify the receptor via a photochemical reaction⁸. The phosphatase of regenerating liver (PRL) is among the family of phosphatases, consisting of PRL-1, PRL-2, and PRL-3, and represents an intriguing group of proteins being validated as biomarkers and therapeutic targets in cancer⁹. A series of Rd derivatives have been synthesized and evaluated for their ability to inhibit PRL-3¹⁰⁻¹¹. The *N*-methyl and amino derivatives of Rd act as mimics of a common, naturally occurring cellular ligand: NAD⁺ (which is a common co-enzyme for many oxidoreductase enzymes)¹². Rd derivatives also exhibit anti-diabetic¹³⁻¹⁵, anti-fungal¹⁶, anti-microbial¹⁷, antimiotic¹⁸, hypoglycemic¹⁹, and anti-hyperlipaemic activity²⁰.

1.3. Application as a Nucleophile in Novel Organic Synthesis

Rd derivatives are used as precursors of cyclic cis amides of α -amino acids and can be easily condensed with aldehydes. The C-5 active methylene group acts as a nucleophile in aldol condensations²¹⁻²⁴. The use of microwave irradiation resulted in shortened reaction times, and increased yields in the aldol condensation of 3-formylchromones and 5-arylfuran-2-carboxaldehydes with the active methylene moiety of Rd derivatives in different reaction media²⁵⁻²⁶. Rd derivatives have also been used to facilitate the synthesis of 1, 3-oxathiolanes, where the thiocarbonyl moiety (C=S) acts as a nucleophile, and the reaction proceeds with high regio- and stereo-selectivity via an S_N2-type mechanism²⁷.

1.4. Applications in Industry

Rd effectively inhibits the corrosion of mild steel in hydrochloric acid solution²⁸. It has been used as an additive in order to understand the phenomenon of electro-less copper plating. The effect of additives on electro-less copper plating has been attributed to either complexation related to charge transfer resistance or adsorption related to double layer capacitance and charge transfer resistance. The effects of Rd are related to the strong adsorption of the molecule onto the substrate surface²⁹. Rd is used industrially as a

vulcanizing agent for natural or synthetic latex-base rubber³⁰ and is also used as a histological stain for copper³¹.

1.5. Applications in Coordination/Analytical Chemistry

It was reported in 1877 that Rd precipitated certain metal ions from aqueous solution³². However, analytical uses were not discovered until Feigl³³ reported the formation of the water insoluble complex of Rd and Ag⁺. Shortly afterwards, Feigl and Pollak³⁴ reported the use of Rd as a selective microgravimetric precipitant for Ag⁺. Since then, Rd and its derivatives have been used as important reagents in coordination chemistry. They form coordination complexes with, for example, Cu⁺, Ag⁺, Au³⁺ as well as other metal ions³⁵⁻³⁷. The carbonyl oxygen of the Rd moiety constitutes the chelating backbone in most complexes, and allows the formation of the enol form via the displacement of a proton. Gandhe and co-workers³⁸ have employed Rd as an amperometric reagent for the trace determination of metal ions such as Ni²⁺, Cd²⁺, Cu²⁺, and Zn²⁺. Proton-ligand dissociation constants of Rd and metal-ligand stability constants of its complexes with Mn²⁺, Co²⁺, Ni²⁺, Cu²⁺, Cd²⁺, La³⁺, Hf³⁺, and Zr⁴⁺ have also been reported³⁹. The formation of the metal complexes has been found to be spontaneous, endothermic, and entropically favourable. The photochemical reactions of Rd derivatives with metal complexes revealed that rhodanine ligands act as mono-dentate ligands coordinating via the sulfur (C=S) donor atom⁴⁰.

1.6. Tautomers of Rhodanine

An interesting property of Rd is its tautomerism. Previously, five potential tautomeric forms of Rd have been studied extensively by theoretical and experimental methods⁴¹⁻⁴⁸ (Fig.1.3). These studies revealed that tautomer **a** is the most stable form. Partial theoretical investigations of potential tautomeric forms of Rd, isorhodanine, thiazolidine-2-4-dione, and thioRd were performed by means of semi-empirical (AM1, PM3, MNDO) and low level *ab initio* (HF and MP2) methods⁴⁹. Quantum mechanical calculations were

exploited for the theoretical evaluation of experimental IR spectra in order to assign vibrational bands for the most stable tautomeric form **a**.

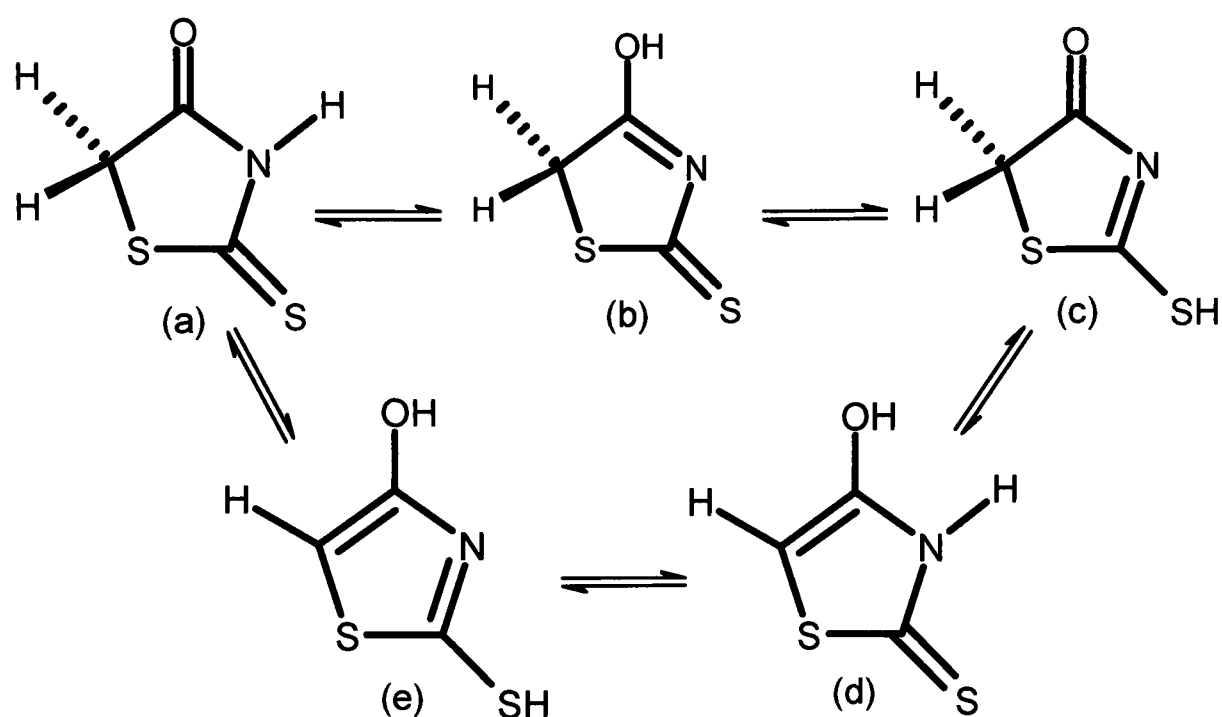


Figure 1.3. Potential tautomeric forms of Rd⁴⁶.

In another quantum mechanical study, 2, 4-substituted imidazoles have been compared with thiazoles in terms of their hyperpolarizabilities⁵⁰. It was suggested that the exocyclic heteroatoms have much more influence on the calculated hyperpolarizabilities than the ring heteroatoms.

1.7. References

- [1] a. F. C. Brown, *Chem. Rev.*, **61**, (1961), 463-521; b. Julian and Sturgis, *J. Am. Chem. Soc.*, **57**, (1935), 1126.
- [2] S. P. Singh, S. S. Parmer, K. Raman and V. I. Stenberg, *Chem. Rev.*, **81**, (1981), 175.
- [3] S. B. Savvin and R. F. Gureva, *Talanta*, **34**, (1987), 87.
- [4] K. Krus, A. Masias and I. P. Beletskaya, *J. Org. Chem. USSR (Engl. Transl.)*; Translated from *Zh. Org. Khim.*, **24**, (1988), 1576.
- [5] W. Kraus, H. Zimmermann, H. J. Eggers and B. Nelsen-Salz, *J. Virol.*, **71**, (1997) 1697.
- [6] N. S. Cutshall, C. Oday and M. Prezhdo, *Bioorg. Med. Chem. Lett.*, **15**, (2005), 3374.
- [7] C. F. Brown, C. K. Bradsher, B. F. Moser and S. Forrester, *J. Org. Chem.*, **24**, (1959), 1056.
- [8] P. H. Carter, P. A. Scherle, J. A. Muckelbauer, M. E. Voss, L. Rui-Qin, L. A. Thompson, A. J. Tebben, K. A. Solomon, Y. C. Lo, Z. Li, P. Strzemienski, G. Yang, N. Falahatpisheh, M. Xu, Z. Wu, N. A. Farrow, K. Ramnarayan, J. Wang, D. Rideout, V. Yalamoori, P. Domaille, D. J. Underwood, J. M. Trzaskos, S. M. Friedman, R. C. Newton and C. P. Decicco, *PNAS*, **98**, (2001), 11879.
- [9] B. J. Stephens, H. Han, V. Gokhale and D. Von Hoff, *Mol. Cancer Ther.*, **4**, (2005), 1653.
- [10] J. H. Ahn, S. J. Kim, W. S. Park, S. Y. Cho, D. J. Ha, S. S. Kim, S. K. Kang, D. G. Jeong, S. K. Jung, S. H. Lee, H. M. Kim, S. K. Park, K. H. Lee, C. W. Lee, S. E. Ryu and J. K. Choi, *Bioorg. Med. Chem. Lett.*, **16**, (2006), 2996.
- [11] H. T. Y. Fahmy and A. A. Bekhit, *Pharmazie*, **57**, (2002), 800.
- [12] Yu. Lin, US Pat. 0009526 AI; *Chem. Abstr.*, (2003).
- [13] Y. Ohishi, T. Mukai and M. Nagahara, *Chem. Pharm. Bull.*, **38**, (1990), 1911.
- [14] Y. Momose, K. Meguro, H. Ikeda, C. Hatanaka, S. Oi and T. Sohda, *Chem. Pharm. Bull.*, **39**, (1991), 1440.
- [15] P. N. Peet, *IDrugs*, **3**, (2000), 131.
- [16] Y. Sakagami, Y. Kumeda and M. Shibata, *Biosci. Biotech. Biochem.*, **62**, (1998), 1025.

-
- [17] V. Y. Gorishniy and R. B. Lesyk, *Farm. ZH. (Kiev)*, **2**, (1994), 52.
- [18] N. Khang, L. V. Minh, N. N. Vinh, T. M. Binh, P. G. Kohi, B. N. Dong, N. K. Lien and B. K. Lien, *Rev. Pharm.*, **110**, (1986); *Chem. Abstr.*, **109**, (1988), 73374.
- [19] D. A. Clark, S. W. Goldstein and B. Hulin, US Pat. 5 036079; *Chem. Abstr.*, **116**, (1992), 83663.
- [20] R. M. Hindley, D. Haigh and G. P. Cottam, PCT Int. Appl. WO 92 07 839; *Chem. Abstr.*, **117**, (1992), 212490.
- [21] C. L. Lee and M. M. Sim, *Tetrahedron Lett.*, **41**, (2000), 5729.
- [22] S. P. Singh, S. S. Parmer, K. Raman and V. I. Stenberg, *Chem. Rev.*, **81**, (1981), 175.
- [23] B. B. Lohray and V. Bhushan, *Bioorg. Med. Chem. Lett.*, **7**, (1997), 785.
- [24] G. Ravindran, S. Muthusubramanian, S. Selvaraj and S. Perumal, *Phosphorous, Sulfur Silicon Relat. Elem.*, **182**, (2007), 321.
- [25] R. Gasparova and M. Lacova, *Mol.*, **10**, (2005), 937.
- [26] E. Rabarova, P. Kois, M. Lacova and A. Krutosikova, *Arkivoc USA Inc.*, (2004), 110.
- [27] C. Fu, M. V. Thrane, A. Linden and H. Heimgartner, *Tetrahedron*, **60**, (2004), 5407.
- [28] R. Solmaz, G. Kardas, B. Yazici, and M. Erbil, *Prot. Met.*, **41**, (2005), 581.
- [29] J. S. Chang, S. C. Kou and A. Hung, *Plat. Surf. Finish.*, **92**, (2005), 52.
- [30] S. Borgman, *Ger. Dem. Rep.*, DD 251765 A1, (1987), 5.
- [31] L. Jonas, G. Fulda, T. Salameh, W. Schmidt, G. Kroning, U. T. Hopt and H. Nizze, *Ultrastruct. Pathol.*, **25**, (2001), 118.
- [32] M. Nencki, *J. Prakt. Chem.*, **16**, (1877), 1.
- [33] F. Z. Feigl, *Angew. Chem.*, **39**, (1926), 393.
- [34] F. Feigl and I. Pollak, *Mikrochemie*, **4**, (1926), 185.
- [35] A. C. Fabretti, G. Franchini, G. Peyronel and M. Ferrari, *Polyhedron*, **1**, (1982), 633.
- [36] A. C. Fabretti and P. Giorgio, *Transition Met. Chem.*, **2**, (1977), 224.
- [37] G. H. Ayres, *Anal. Chim. Acta*, **24**, (1962), 241.
- [38] S. Gandhe, A. Pradhan and M. Gautam, *J. Indian. Chem. Soc.*, **80**, (2003), 143.
- [39] M. F. El-Sherbiny, *Chem. Pap. Chem. Zvesti*, **59**, (2005), 332.
- [40] E. Subasi, A. Ercag, S. Sert and O. S. Senturk, *Synth. React. Inorg. Met. Org. Chem.*, **36**, (2006), 705.
- [41] V. Enchev, I. Petkov and S. Chorbadjiev, *Struct. Chem.*, **5**, (1994), 225.
-

- [42] R. Hilal, H. Ead and A. Osman, *Appl. Spectrosc.*, **32**, (1978), 557.
- [43] J. Elguero, A. R. Katritzky, P. Linda and C. Marzin, *The Tautomerism of Heterocycles*, Academic Press, New York, (1976).
- [44] J. S. Kwiatkowski, T. J. Zielinski and R. Rein, *Adv. Quantum Chem.*, **18**, (1986), 85.
- [45] M. Brent and J. S. Kwiatkowski, *Theoretical Chemistry of Biological Systems*, Elsevier, Amsterdam, (1986).
- [46] D. Tahmassebi, *J. Mol. Struct. (Theochem)*, **638**, (2003), 11.
- [47] A. Guven and N. Kaniskam, *J. Mol. Struct. (Theochem)*, **488**, (1999), 125.
- [48] M. V. Andreocci, C. Cauletti and L. Sestili, *Spectrochim. Acta. A* **40**, (1984), 1087.
- [49] V. Enchev, S. Chorbadjiev and B. Jordanov, *Chem. Heterocycl. Compd.*, **38**, (2002), 1110.
- [50] M. Spassova and V. Enchev, *Chem. Phys.*, **298**, (2004), 29.

Chapter Two

Theoretical Aspects of Experimental Techniques and Computational Methods

2.1. Introduction

The classical theory of light proposed by Maxwell, Young, and others in the nineteenth century demonstrated that light could be considered as a form of electromagnetic radiation (EM). EM is a transverse energy wave that is composed of an oscillating electric field component, E , and an oscillating magnetic field component, M . The electric and magnetic fields are orthogonal to each other, and they are orthogonal to the direction of propagation of the wave. A wave is described by the wavelength, λ , which is the physical length of one complete oscillation, and the frequency, ν , which is the number of oscillations per second (Fig.2.1). Conversely, Einstein proposed that light could be regarded as a continuous electromagnetic field, consisting of discrete packets of energy known as photons, which formed the basis of quantum mechanical theory. Each photon has an energy, $E = h\nu$, where h is Planck's constant (*i.e.*, 6.626076×10^{-34} J s)¹⁻².

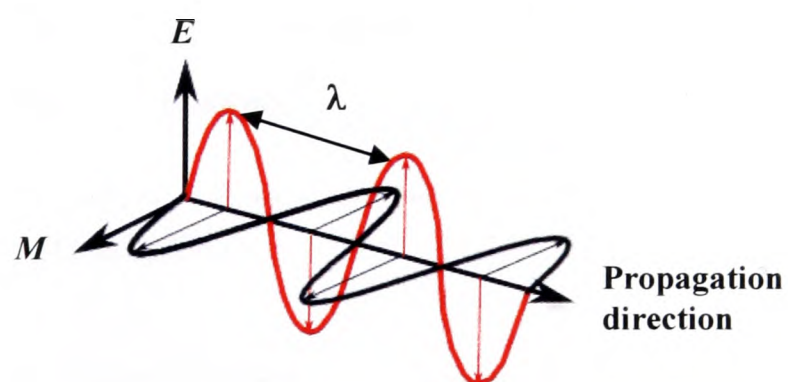


Figure 2.1. Plane-polarized electromagnetic radiation.

EM waves are one of the best known and most commonly encountered forms of radiation that undergo scattering. A scattering process is an interaction of a primary light quantum with atoms, molecules, or their aggregates as crystals, by which a secondary light quantum is produced, with a different phase and polarization and possibly a different energy from that of the primary light quantum. The scattering process occurs with an extremely short time delay (typically less than 1 ps), and can be classified as elastic or

inelastic scattering. An elastic scattering process produces radiation with the same photon energy as that of the primary light. Depending on the size of the sample from which scattering is observed, and also its refractive index relative to that of the surrounding medium, the process is referred to as *e.g.* Rayleigh, Mie or Tyndall scattering³⁻⁵. Specular reflection can also occur from large particles. Further, for collections of particles, processes of multiple reflection, refraction, and diffraction of powders may cause diffuse reflection or diffuse scattering.

An inelastic scattering process produces secondary light quanta with different energy; such processes include Brillouin scattering⁶, Raman scattering⁷, inelastic X-ray scattering and Compton scattering⁸. There are also other processes that produce secondary light quanta with different energies, but they occur with a much larger time delay (typically greater than 1 ns), and are not classified as scattering processes. An example is photoluminescence, by which a primary light quantum is absorbed and the excited state of the molecule or aggregate of molecules emits, after some delay, a secondary light quantum. Photoluminescence processes include fluorescence, delayed fluorescence, and phosphorescence⁹. This chapter is mainly focused on two important light scattering techniques Raman spectroscopy and photon correlation spectroscopy (PCS), and also infrared (IR) absorption spectroscopy.

2.2. Vibrational Spectroscopy

From its derivation the word spectroscopy appears to mean the watching of images, but the modern subject is concerned with the absorption, transmittance, emission, or scattering of electromagnetic radiation by atoms or molecules (interaction of EM radiation with matter). Vibrational spectroscopy was one of the first spectroscopic techniques to be widely used, in particular IR spectroscopy, so called because of the region of the electromagnetic spectrum used. There is a second form of vibrational spectroscopy, Raman spectroscopy, which provides similar information to IR but has a different physical basis. As the nomenclature suggests these forms of spectroscopy are intimately related to changes in the vibrational state of molecules.

2.3. Molecular Vibrations

In a simple diatomic molecule, the two atoms are held together by the overlap of a number of electronic orbitals, which are balanced by the attractive and repulsive forces between the electrons of the two atoms. The equilibrium bond distance (r_e) between two atoms can be changed by applying energy and the system can be treated as consisting of two balls (spheres) held together by a spring of certain strength (k). Classical physics holds that for small displacements the stretching and compression of the bond, obeys Hooke's law:

$$f = -kq \quad (2.1)$$

where f is the restoring force, k the force constant (the magnitude of which reflects the strength of the bond) and the displacement, q [$q = r - r_e$; where r is the internuclear distance]. A typical potential energy curve of a diatomic molecule behaving as a simple harmonic oscillator is shown in Fig.2.2. In regions close to r_e (at the minimum of the curve) the potential energy (V) can be approximated by a parabola, and can be expressed as follows:

$$V = \frac{1}{2}kq^2 \quad (2.2)$$

The classical vibrational frequency, for any diatomic molecule can be calculated via the following expression:

$$\nu_0 = \frac{1}{2\pi} \sqrt{\frac{k}{\mu}} \quad (2.3)$$

where μ is the reduced mass, and

$$\mu = \frac{m_1 m_2}{m_1 + m_2},$$

where m_1 and m_2 are the masses of atoms 1 and 2, respectively.

According to quantum mechanics, the vibration of a diatomic molecule can be treated as the motion of a single particle having a mass m , whose potential energy is expressed by equation 2.2. The Schrödinger wave equation for the relative motion of two atoms of masses m_1 and m_2 with a parabolic potential energy can be formulated as:

$$-\frac{\hbar^2}{2\mu} \frac{d^2\psi}{dq^2} + \frac{1}{2}kq^2\psi = E\psi \quad (2.4)$$

where \hbar is the Dirac constant or reduced Planck's constant (*i.e.*, 1.054571×10^{-34} J s) and ψ is the wavefunction. The vibrational terms of a molecule, the energies of its vibrational states, expressed in wavenumber or frequency, are as follows:

$$\tilde{\nu} = \frac{1}{2\pi c} \sqrt{\frac{k}{\mu}} \quad \text{or} \quad \nu = \frac{1}{2\pi} \sqrt{\frac{k}{\mu}} \quad (2.5)$$

where $\tilde{\nu}$ is the wavenumber, ν the frequency, and c speed of light (*i.e.*, 3×10^8 m s⁻¹).

The classical frequency equation is the same as the quantum mechanical frequency equation, but there are important differences between the two theories:

- classical theory states that E is zero when q is zero. Conversely, in quantum mechanics a harmonic oscillator has zero-point energy *i.e.*, $E_0 = \frac{1}{2}\hbar\omega$. This is a consequence of the Heisenberg uncertainty principle.
- classical mechanics would allow the particle to be perfectly still. However, in quantum mechanics, the particle fluctuates incessantly around its equilibrium position¹⁰⁻¹⁴.

2.4. Anharmonicity

The harmonic oscillator approximation cannot be correct for large atomic displacements because it does not allow for bond dissociation. At high vibrational excitation the oscillation of the atoms (more precisely, the spread of the vibrational wavefunction) allows the molecule to explore regions of the potential energy curve where the parabolic approximation is poor (the true potential is less confining). The motion then becomes anharmonic, in the sense that the restoring force is no longer proportional to the nuclear displacement coordinate (mechanical anharmonicity). One approach to the calculation of the energy levels in the presence of anharmonicity is to use a function that resembles the true potential energy more closely. One such function is the Morse potential function, as

illustrated in Fig.2.2. As the molecular potential is anharmonic, the higher-order terms of the potential energy, *i.e.*, those involving q^3 and q^4 , of the molecules are not negligible. This mechanical anharmonicity gives rise to combination frequencies, which may also be produced by the higher terms of the polarizability, *i.e.*, the electrical anharmonicity (*vide infra*). Thus, combinations of two or more normal vibrations *i.e.*, overtones, sum or difference frequencies are produced. These appear as bands in the spectra, but usually only of low intensity. Interactions of the combination frequencies with fundamentals also occur; the interaction of an overtone or combination with a fundamental of the same symmetry and nearly the same frequency is called Fermi resonance, which enhances the intensity of the overtone or combination at the expense of the fundamental, leading in the extreme case to two vibrational bands of nearly equal intensity¹⁴⁻¹⁵.

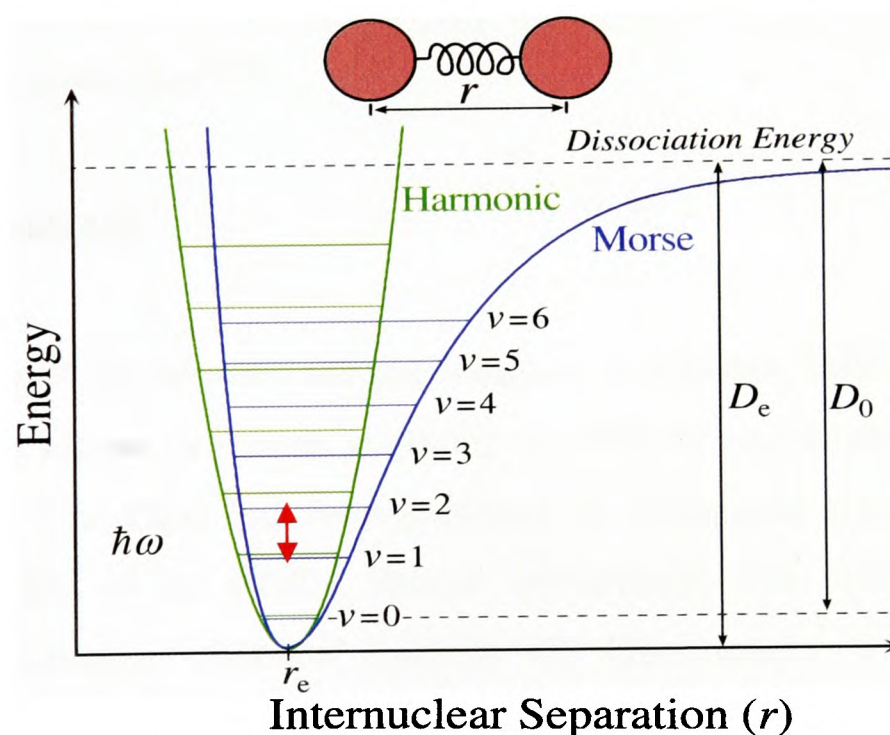


Figure 2.2. Molecular potential energy curve for a simple harmonic oscillator. The Morse potential energy curve reproduces the general shape of a molecular potential energy curve. The dissociation energy of a molecule, D_0 , differs from the depth of the potential well, D_e , on account of the zero potential energy of the vibrations of the bond.

2.5. Normal Modes of Vibration

The total number of Cartesian coordinates needed to specify the locations of N atoms is $3N$. Each atom may change its location by varying one of its three coordinates

(x , y , and z), so the total number of displacements available is $3N$. These displacements can be grouped together in a physically sensible way. For example, three coordinates are needed to specify the location of the centre of mass of the molecule; so three of the $3N$ displacements correspond to the translational motion of the molecule as a whole. The remaining $3N-3$ displacements are non-translation “internal” modes of the molecule. Two angles are needed to specify the orientation of a linear molecule in space; in effect, there is a need to give only the latitude and longitude of the direction in which the molecular axis is pointing. However, three angles are needed for a nonlinear molecule around the direction defined by the latitude and longitude. Therefore, two (linear) or three (non-linear) of the $3N-3$ internal displacements are rotational. This leaves $3N-5$ (linear) or $3N-6$ (non-linear) displacements of the atoms relative to one another, which are the vibrational modes. It follows that the number of modes of vibrations is $3N-5$ for linear molecules and $3N-6$ for non-linear molecules^{14, 16}.

2.6. Raman Spectroscopy

In 1928, C.V. Raman documented the phenomenon of inelastic light scattering, which bears his name and known as Raman scattering. In 1930 he was awarded a Nobel Prize for this discovery. The effect had been predicted on theoretical grounds, in 1923, by Smekal¹⁷. By the end of the 1930's, Raman spectroscopy had become the principal method of non-destructive chemical analysis. IR spectroscopy, the complementary technique to Raman spectroscopy, became the preferred method after World War II primarily because it became much easier to use due to the development of sensitive IR detectors and advances in electronics. IR spectroscopy measurements became routine, while Raman spectroscopy still required skilled operators and darkroom facilities. With the advent of lasers in the 1960's¹⁸, interest in Raman spectroscopy was renewed. Since then, Raman spectroscopy has progressed quite significantly and entered the present state of art as a powerful analytical technique. Nowadays, Raman spectrometers are equipped with sensitive detectors¹⁹, holographic notch filters²⁰, and intense laser sources in the UV, visible, as well as near-IR regions and used to examine either solid, liquid, or gaseous samples²¹.

During the interaction of the primary light quantum (of frequency ν_o) with a molecule or crystal, the energy of a vibrational state may be exchanged and a secondary light quantum (of lower or higher frequency (ν_{vib})) of lower or higher energy is created. The energy difference is equal to the vibrational energy (E_{vib}) of a molecule or crystal. This process is known as Raman scattering. The inelastic interaction of a primary light quantum with a molecule or crystal in its vibrational ground state produces the Stokes Raman spectrum, a red-shifted spectrum. Due to thermal excitation, according to the Boltzmann equation, some molecules may be in their vibrational excited states. The interaction of the primary light with these molecular states produces a blue-shifted Raman spectrum, the anti-Stokes Raman spectrum¹⁵ (Fig.2.3). The relative intensity of the Raman lines in the Stokes and anti-Stokes Raman spectra may be employed, by using the Boltzmann equation, for the determination of the vibrational temperature. The Boltzmann distribution function used to calculate the relative populations of the various energy levels is as follows:

$$\frac{n_i}{n_o} = e^{-(E_i - E_o)/kT} \quad (2.6)$$

where n_i and n_o are the numbers of molecules in the i th and zero energy levels, respectively; $(E_i - E_o)$ is the energy difference between the energy levels, k is the Boltzmann constant ($1.38054 \times 10^{-23} \text{ J K}^{-1}$), and T is the absolute temperature. The relative intensities of the Stokes and anti-Stokes lines in the Raman spectrum can then be calculated using the relationship:

$$\frac{I_{Stokes}}{I_{anti-Stokes}} = \frac{(\nu_o - \nu_{vib})^4}{(\nu_o + \nu_{vib})^4} e^{\frac{-h\nu_{vib}}{kT}} \quad (2.7)$$

The intensity of the anti-Stokes lines will always be much lower than the intensity of the Stokes lines, in agreement with experimental observations²².

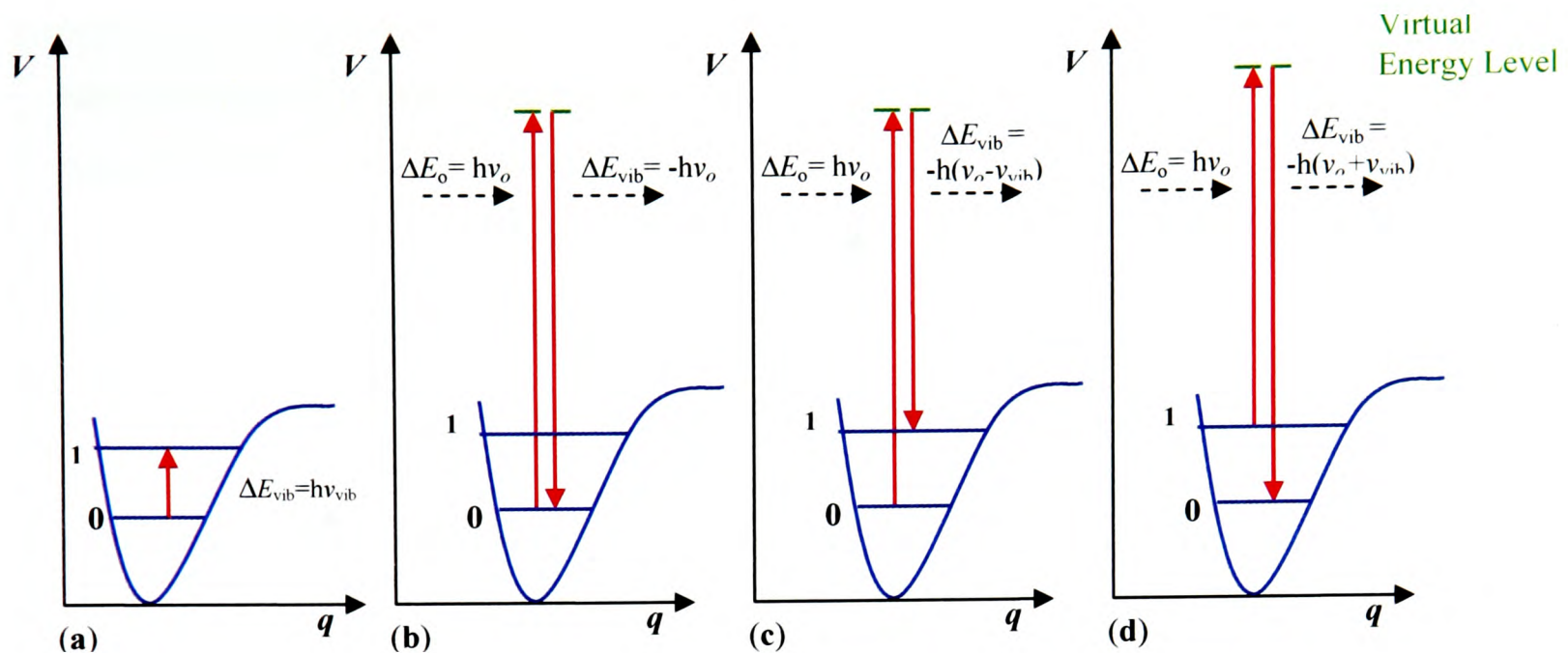


Figure 2.3. Schematic representation of energy transitions in: (a) IR, (b) Rayleigh scattering, (c) Stokes Raman scattering, and (d) anti-Stokes Raman scattering.

2.7. Selection Rules for Raman Spectroscopy

Raman scattering occurs only if the polarizability of a molecule changes with vibrational motion. The polarizability is a measure of the ease with which the electrons in a molecule can be distorted by an electric field, creating an induced dipole moment. In general, as an electron cloud is expanded (*i.e.*, when a bond is lengthened) it is easier to induce a dipole moment in the electron cloud with respect to a compressed cloud (*i.e.*, when the bond is shortened). The polarizability is a tensor quantity that acts as a proportionality constant between the induced dipole moment, μ , and the strength of the electric field of the incident light, E , such that:

$$\mu = \alpha \cdot E \quad (2.8)$$

where α is the polarizability. For a diatomic molecule, the polarizability can be expressed as:

$$\alpha = \alpha_o + \left(\frac{\partial \alpha}{\partial q} \right)_o q + \dots \quad (2.9)$$

where α_0 is the polarizability of the molecule at its equilibrium position and $\left(\frac{\partial\alpha}{\partial q}\right)_0$ the rate of change of α with respect to the rate of change of q . If the molecule is vibrating with frequency ν_0 (simple harmonic motion) then:

$$q = A \cos(2\pi\nu_{vib}t) \quad (2.10)$$

where A is the maximum amplitude of vibration and,

$$\alpha = \alpha_0 + \left(\frac{\partial\alpha}{\partial q}\right)_0 A \cos(2\pi\nu_{vib}t) + \dots \quad (2.11)$$

Since the oscillating electric field is of the form:

$$E = E_0 \cos(2\pi\nu_0 t) \quad (2.12)$$

where ν_0 is the frequency of the incident light, the induced dipole moment is:

$$\mu = E_0 \alpha_0 \cos(2\pi\nu_0 t) + E_0 \left(\frac{\partial\alpha}{\partial q}\right)_0 A \cos(2\pi\nu_0 t) \cos(2\pi\nu_{vib}t) \quad (2.13)$$

or

$$\mu = E_0 \alpha_0 \cos(2\pi\nu_0 t) + \frac{1}{2} E_0 A \left(\frac{\partial\alpha}{\partial q}\right)_0 [\cos 2\pi(\nu_0 - \nu_{vib})t + \cos 2\pi(\nu_0 + \nu_{vib})t] \quad (2.14)$$

The induced dipole oscillates at three frequencies and therefore it can emit light at these three frequencies, which correspond to the so-called Rayleigh scattering at the frequency of the incoming field and to Stokes and anti-Stokes Raman scattering, respectively which is shifted from the excitation frequency by the frequency of the molecular vibration. The emitted electric field from an oscillating dipole is given by the expression:

$$E = \frac{\partial^2 \mu}{\partial t^2} \quad (2.15)$$

where the intensity I of the emitted light is proportional to E^2 . This results in expressions for the Stokes and anti-Stokes scattering²³:

$$I_{stokes} = (\nu_0 - \nu_{vib})^4 \left(\frac{\partial\alpha}{\partial q}\right)_0^2 I_0(\nu_0) \quad (2.16)$$

$$I_{anti-stokes} = (\nu_0 + \nu_{vib})^4 \left(\frac{\partial\alpha}{\partial q}\right)_0^2 I_0(\nu_0) e^{\frac{-h\nu_{vib}}{kT}} \quad (2.17)$$

The scattering power is proportional to ν^4 , to the change of the polarizability vs. q , and to the intensity of the laser excitation. If there is no change in polarizability *i.e.*, if the rate of change of polarizability with respect to the vibrational coordinate $\left(\frac{\partial\alpha}{\partial q}\right) = 0$, then the vibration is Raman inactive. The Boltzmann factor in the anti-Stokes formula accounts for the smaller (less intense) anti-Stokes signal compared to the Stokes signal, since anti-Stokes scattering results from molecules in the excited vibrational level which is less populated according to the Boltzmann distribution. Experimentally, the intensity of the Raman (Stokes) scattering is given by the expression²⁴:

$$I = KCI_0(\nu_0 - \nu_{vib})^4 \quad (2.18)$$

where K is a constant of the instrument, C is the concentration of the species responsible for the scattering, I_0 is the intensity of the incident beam. To summarize, in the "classical view" of the Raman effect light is considered an electromagnetic wave which induces a dipole moment in the molecule. The generation of this dipole moment by the incoming electric field is modulated by the molecular vibrations since α is a function of the vibrational coordinate, q . Therefore, the induced dipole oscillates not only at the frequency of the incoming field, but also at "side bands", at the sum and difference frequencies between the incoming light, and the molecular vibrations. This results in the appearance of Stokes and anti-Stokes "side bands" in the scattered light.

2.8. Raman Cross-Section

The Raman scattering cross-section for a molecular vibrational mode is defined as the number of scattered photons per unit time per unit solid angle divided by the incident laser flux (number of photons per unit time per unit area). For a totally symmetric mode, the expression for the cross-section for parallel incident and scattered light polarization is given by the following expression:

$$\frac{d\sigma}{d\Omega} = \frac{\omega_L \omega_s^3}{c^4} \frac{\hbar}{2\omega_f} (\langle n_f \rangle + 1) |\alpha_f|^2 L \quad (2.19)$$

where ω_L is the incident light angular frequency, ω_s the scattered light angular frequency, c the speed of light, ω_f the angular vibrational frequency of the Raman mode, and $\langle n_f \rangle$ its mean occupation number. The factor L is a local field correction. The key molecular parameter which determines the Raman cross-section of a totally symmetric mode is the average α_f of the Raman tensor, which in the off-resonance limit can be written in terms of polarizability derivatives:

$$\alpha_f = \frac{1}{3}(\alpha_{xx,f} + \alpha_{yy,f} + \alpha_{zz,f}) \quad (2.20)$$

The differential Raman scattering cross-section calculated from equation (2.19) is as follows:

$$\frac{d\sigma}{d\Omega} \approx 10^{-29} - 10^{-31} \text{ cm}^2 \quad (2.21)$$

Raman scattering is typically 14 orders of magnitude weaker than fluorescence; therefore, Raman signals are, in most cases, several orders of magnitude weaker than fluorescence emission²⁵.

2.9. Limitations of Raman Spectroscopy

Like all analytical techniques Raman spectroscopy has its disadvantages and limitations. These include the fact that:

- Raman scattering is a weak effect and only a very small quantity (*ca.* 1 in 10^5 - 10^7) of photons with shifted frequency are observed. A powerful (intense) laser source is needed to observe this weak phenomenon. This may cause local heating and/or photodecomposition, especially in resonance Raman studies where the laser frequency is deliberately tuned to the absorption band of the molecule.
- some compounds fluoresce when irradiated by the laser beam. Intense fluorescence swamps the weak Raman signal. This is a major disadvantage of Raman spectroscopy.
- Raman scattering is not very sensitive for solutions (high concentrations of solute required).

2.10. Fluorescence Quenching

The usual approach to avoid fluorescence is to change the laser wavelength to avoid electronic excitation, but it is not always possible to find an effective wavelength, especially as the fluorescence may arise from impurities which are not easily removed. Sometimes this necessitates using a near-IR (NIR) laser and an interferometer detector [Fourier transform Raman spectroscopy (FT-IR)]. Alternative methods for avoiding fluorescence include *e.g.* use of the anti-Stokes region of a Raman spectrum by employing laser excitation wavelengths outside the fluorescence band for the analyte under investigation²⁶, the Kerr-gate technique in time-resolved Raman spectroscopy²⁷, and surface-enhanced (resonance) Raman spectroscopy (SER(R)S). In the SE(R)RS technique an analyte is adsorbed on *e.g.*, a metallic substrate, which provides non-radiative pathways for the decay of excited states. Another technique which has been recently developed is subtracted shifted Raman spectroscopy (SSRS), which involves obtaining two spectrophotometer-shifted spectra which are then subtracted and shown as a separate spectrum²⁸⁻²⁹.

2.11. Raman Techniques

Among different Raman techniques the most important ones, discussed below, are:

- resonance Raman spectroscopy (RRS),
- surface enhanced Raman spectroscopy (SERS), and
- surface enhanced resonance Raman spectroscopy (SERRS).

2.12. Resonance Raman Spectroscopy (RRS)

RR scattering occurs when the excitation wavelength is chosen such that it is within the manifold of an electronic state. In the liquid and solid states, vibronic levels are broadened to produce a continuum. In the gaseous state, a continuum exists above a series of discrete levels. Excitation of these continua produces RR spectra that show extremely strong enhancement of Raman bands (of the order of 10^3 to 10^5) originating in

this particular electronic transition (Fig.2.4.b). It is the chromophoric moiety of the molecule that gives rise to the enhancement²¹. This particular technique has been used to probe the chromophoric sites of metalloporphyrins³⁰, carotenoids³¹ and several other classes of biologically important molecules³². The term “pre-resonance” is used when the exciting laser line is close in energy to the electronic excited state, but not in exact resonance. Resonance fluorescence (RF) occurs when the molecule is excited to a discrete level of the electronic excited state, and is normally only observed from gas phase species. Fluorescence spectra are observed when the excited state molecule decays to the lowest vibrational level via radiationless transitions and then emits radiation (Fig.2.4.c). The lifetime of the excited state in RR is very short (10^{-14} s), whilst that of RF and fluorescence are much longer (10^{-8} to 10^{-5} s).

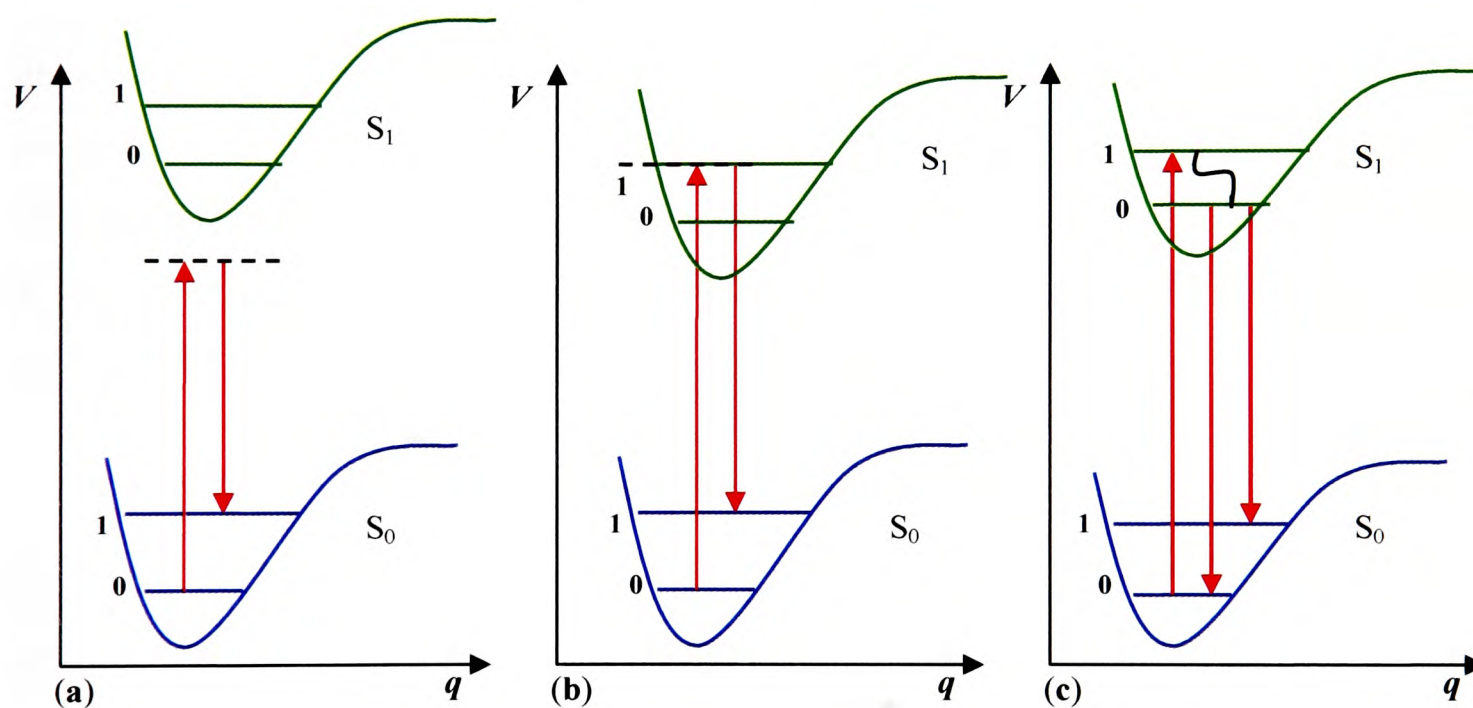


Figure 2.4. Comparison of energy levels for: (a) pre-resonance Raman, (b) resonance Raman, and (c) fluorescence spectra⁷.

2.13. Surface Enhanced Raman Spectroscopy (SERS)

This technique involves molecules adsorbed on certain rough metallic substrates. As a result of large optical fields and resonance related effects, the Raman cross-section for a molecule on a substrate surface may be enhanced by factors of up to 10^6 - 10^8 (or more). A combination of the SERS effect with an optical resonance in the molecule results in even

larger enhancement factors. The explosion of activity in the field of SERS started in the mid-1970's. Fleischmann *et al.*, in 1974 studied Raman scattering from pyridine molecules adsorbed on silver electrode surfaces that had been roughened electrochemically by oxidation-reduction cycles³³. Their observation of enhanced Raman intensities was later confirmed by Jeanmaire and Van Duyne³⁴⁻³⁵ as well as Albrecht and Creighton³⁶ and termed surface-enhanced Raman scattering (SERS). The early literature published on the SERS phenomenon has been reviewed by Otto³⁷ and Moskovitz³⁸; it is clear that noble metal nanostructures or nanoparticles (NPs) are responsible for the large signal enhancements.

2.13.1. Theory of the SERS Effect

Since the discovery of SERS the exact cause of the enhancement mechanism is still under debate due to the fact that there is undoubtedly more than one effect responsible for signal enhancement. However, the main factors involved in the enhancement of SER spectra [local electromagnetic field enhancement (EM) and the chemical effect (also known as the electronic effect)], are given by the expression:

$$s_R(\nu_S) = N' \sigma_{ads}^R |A(\nu_L)|^2 |A(\nu_S)|^2 I(\nu_L) \quad (2.22)$$

where $A(\nu_L)$ and $A(\nu_S)$ represent the enhancement factors for an excitation source of intensity $I(\nu_L)$ and Raman scattered fields, respectively; σ_{ads}^R is the increased Raman cross-section of the molecule in contact with the nanostructure, and N' is the number of molecules involved in the SERS process. A molecule at distance d from a metal sphere of radius r (where $r < \lambda_0$, the excitation wavelength) and complex dielectric constant $\varepsilon(\nu)$ is exposed to a field E_M , which is the superposition of the incident field E_0 and the field of a dipole E_{sp} induced in the metal sphere. The field enhancement factor $|A(\nu_L)|$ is the ratio of the field at the position of the molecule and the incident field,

$$A(\nu_L) = \frac{E_M(\nu_L)}{E_0(\nu_L)} \approx \frac{\varepsilon(\nu_L) - \varepsilon_r}{\varepsilon(\nu_L) + 2\varepsilon_r} \left[\frac{r}{r+d} \right]^3 \quad (2.23)$$

where $\varepsilon(\nu_L)$ is the complex dielectric function of the metal, at the frequency of the laser radiation and ε_r is the relative permittivity of the medium. Thus resonance occurs when $\text{Re}[\varepsilon(\nu_L)] = \varepsilon_r$, *i.e.*, when the laser radiation is in resonance with a surface plasmon excitation of the metal. A surface plasmon is a collective excitation of the free electrons in a metal and the frequency at which this occurs is usually much lower at the surface than in the bulk.

The Raman scattered field is enhanced in the same manner, but with ν_s instead of ν_L . Referring back to equation (2.22), the EM enhancement contribution can then be written as:

$$|A(\nu_L)|^2 |A(\nu_s)|^2 \approx \left| \frac{\varepsilon(\nu_L) - \varepsilon_r}{\varepsilon(\nu_L) + 2\varepsilon_r} \right|^2 \left| \frac{\varepsilon(\nu_s) - \varepsilon_r}{\varepsilon(\nu_s) + 2\varepsilon_r} \right|^2 \left[\frac{r}{r+d} \right]^{12} \quad (2.24)$$

Equation (2.24) explains several of the important properties of the EM component of SERS enhancement. First, the enhancement scales as the fourth power of the local metallic nanostructure field. Second, the enhancement is maximized when both the incident laser and Raman scattered fields are in resonance with the surface plasmons. Third, although the enhancement does not require direct contact of the molecule and the metal the dependence on distance is extremely strong, *i.e.*, the inverse twelfth power³⁹.

2.13.2. The Electromagnetic Effect (EM)

The maximum values of the EM enhancement⁴⁰⁻⁴¹ for isolated single NPs are typically $\sim 10^6$ - 10^7 . Stronger enhancements arise from sharp features and areas of large curvature, such as those found in nanostructures *e.g.* colloidal aggregates⁴²⁻⁴³ or nano-crystal junctions or edges⁴⁴. This effect involves the local field acting on each molecule, the induced molecular dipole and its radiation. The interaction in the presence of a radiation field has been extensively studied⁴⁵⁻⁵⁶. The main source of local field enhancement is that arising from surface plasmons (SPs).

To date, the detailed physics of the SERS process is not entirely understood (as mentioned above) although it is generally accepted that the EM effect results from localization of the surface plasmon resonance (LSPR), effectively trapping photons and increasing the probability of a Raman interaction with vibrational excitations of neighbouring molecules. Incident light excites localized plasmons, which in turn excite molecular dipoles that then lose packets of energy to particular phonon vibrations. These molecular dipoles subsequently re-emit red-shifted plasmons, which are re-emitted back as photons⁵⁷. The LSPR for noble metal NPs (of size in the range 20 to a few hundred nanometers) occurs in the visible and IR regions of the spectrum and can be measured by UV-visible-IR extinction spectroscopy. Because the material, size, shape, and dielectric environment dictate the characteristics of the LSPR⁵⁸, these properties also control the surface-enhancing capability of the SERS substrates. The most effective SERS substrates have been found to be copper (Cu), silver (Ag) and gold (Au) (*i.e.*, coinage metals/noble metals), which all exhibit surface plasmon resonance in the visible region.

2.13.3. The Chemical (Electronic) Effect (CT)

The contribution of this effect toward SERS enhancement is roughly $\sim 10^2$. The first theory of adsorbate-induced resonant Raman scattering was proposed by Otto and co-workers⁵⁹⁻⁶¹. In this additional chemical or electronic mechanism, the enhancement is due to the formation of a charge transfer (CT) complex between atomic scale roughness features on the metal surface (adatoms) and the adsorbed molecule. The energies of the frontier molecular orbitals of the adsorbed molecule are close to the Fermi level of the metal because of complex formation. The difference in energy between the Fermi level and the frontier orbital of the adsorbed species is close in frequency to the incident light, and an enhancement mechanism occurs, which is analogous to the resonance Raman process⁶²⁻⁶³. The theories which have been evolved to explain CT effect are developing slowly in contrast to the EM effect; recently Otto has published a theoretical model supported with experimental examples to shed some light on the electronic mechanism⁶⁴.

2.13.4. SERS Substrates

The design and fabrication of a variety of NPs and nanostructures as new substrates has been a hot topic in SERS since the mid-1990s. Because the SERS intensity depends on the excitation of the LSPR, it is important to control all of the factors influencing the LSPR to maximize signal strength, and ensure reproducibility⁶⁵. The following factors: size, shape, and inter-particle spacing of the material as well as the dielectric environment must be chosen carefully to ensure that the incident laser light excites the LSPR. A necessary, but insufficient, requirement for generating measurable SERS signals from existing metallic films or electrodes is some surface roughness at the sub-micron scale⁶⁶⁻⁶⁷. SERS substrates, which provide the desired optical properties, include electrodes roughened by a series of oxidation-reduction cycles (ORCs)⁶⁸⁻⁷¹, island films⁷²⁻⁷⁴, surface-confined nanostructures⁷⁵⁻⁸³ and colloidal NPs⁸⁴⁻⁸⁷.

Metal colloids are frequently used in SERS analysis, because their dispersions are easily prepared by simple chemical, thermal, or photo-induced reduction of a dilute solution of any of a number of readily available metal salts. By far the most universally used method for the preparation of metal NPs, in suspension, for SERS is by chemical reduction. Generally, the size regime relevant to SERS experiment is between 10 and 80 nm. The colloidal particles will thus exhibit different plasmon resonances depending on the size, shape and the dielectric constant of the metal. The first two parameters can be partially controlled by appropriate choice of the method of preparation. The most important parameters in this regard are the nature of the metal/reducing reagent, the temperature, and the metal ion concentration. A number of transition metals (*e.g.* Pt, Ru, Rh, Pd, Fe, Co, Ni, and their alloys) have also been tested for SERS activity⁸⁸⁻⁹². However, the best results continue to be achieved with the coinage metals/noble metals.

Colloidal NPs lead to very strong SERS enhancement and have several advantages such as ease of handling and manipulation, variable composition, and a more tractable morphology for theoretical study. Another important consideration is that the frequency of the plasmon band gives an indication of the average particle size and the full-width at

half maximum (FWHM) provides a measure of polydispersity. As a result, it is possible to characterize metal colloids, to some degree, by simply using UV-vis spectroscopy. There are several reviews of SERS with emphasis on metal colloids; in particular, ultra high enhancement SERS and single molecule detection (SMD) using colloids is discussed by Kneipp *et al.*⁹³⁻⁹⁴, while the applications of metal colloids to provide average SERS enhancement for the detection of biological molecules has been reviewed by Dou and Ozaki⁹⁵. Specific aspects of SERS using colloids can be found in the review by Pettinger⁹⁶ and Aroca *et al.*⁹⁷, while the review of optical properties of metal particles of differing size and shape as those found in metal sols can be found in the reports by Kelly *et al.*⁹⁸, Mulvaney⁹⁹ and El-Sayed¹⁰⁰. The techniques employed to characterize colloidal nanostructures/NPs are tabulated in Table 2.1.

Table 2.1. Techniques used to characterize different properties of colloidal nanostructures.

Techniques	Properties	References
Transmission electron microscopy (TEM) Atomic force microscopy (AFM) Scanning tunneling microscopy (STM) Dynamic or static light scattering (DLS/SLS)	Morphology, particle size and shape	101-102 103-104
Electron energy loss spectroscopy (EELS), X-rays (XAS,XAFS, XPS), Reflection absorption infrared spectroscopy (RAIRS), Surface enhanced Raman spectroscopy (SERS), Surface enhanced infrared absorption (SEIRA) Plasmon-sampled surface-enhanced Raman excitation spectroscopy (PS SERES)	Chemical species adsorption	105-106 107-108
Near field scanning probe techniques (NSOM) UV-visible spectroscopy (UV) Localized surface plasmon resonance spectroscopy (LSPRS) Plasmon-sampled surface-enhanced Raman excitation spectroscopy (PS SERES)	Optical properties of surface plasmons	109 110-111 112 113-114
Photon correlation spectroscopy (PCS)	Surface potential, surface charge	115

2.13.5. Aggregation of Colloidal NPs

In many instances the experimental data indicate the partial aggregation of metal NPs, and that aggregation leads to an increase in SERS activity¹¹⁶⁻¹¹⁷. This enhancement is due to the analyte residing at the junction of two or more Ag NPs¹¹⁸ which results in an enhanced EM field. As two metal NPs are brought together to form aggregates, their transition dipoles couple to each other. The enhanced fields of each particle begin to coherently interfere at the junction site between the particles. Calculations by Xu *et al.*¹¹⁹ have shown that electromagnetic enhancements of $\sim 10^{10}$ are present between two nanospheres separated by 1 nm. These results suggest that aggregates are better substrates for SERS applications than individual NPs because large enhancements can be achieved at particle junctions¹²⁰.

Several other experimental studies have shown that intentional aggregation of Au and Ag NPs significantly increases the observed SERS enhancement¹²¹⁻¹²². A number of aggregating agents can be employed for this purpose *e.g.* perchlorate, nitrate, and chloride are among the most frequently used¹²³⁻¹²⁴. Organic polymers such as poly(L-lysine) can also be employed for such purposes¹²⁵. Inorganic aggregation agents which do not include chloride ions are preferred because of the complex effects that chloride ions can have on these systems¹²⁶, as well to avoid the interference effects of organic molecules. Clearly, there is involvement of partial aggregation of the colloidal particles which can be induced by controlling the final concentration of the added adsorbate and/or aggregating agent. The addition of halides to Ag colloid has drastic consequences on the morphology of the particles and the chemical properties of the corresponding surfaces. For example, the addition of chloride ions induces a significant change in the surface properties by induction of atomic roughness, with the creation of atomic clusters that passivate surface reaction centers¹²⁷.

2.14. Surface Enhance Resonance Raman Spectroscopy (SERRS)

Stacy and Van Duyne¹²⁸ originally reported the SERRS technique in 1983. SERRS occurs when a molecule containing a chromophore is adsorbed onto a suitably roughened surface, which is SERS active (normally Ag or Au is used), and the surface is excited using a laser beam of an appropriate frequency. The overall enhancement is a combination of resonance enhancement from the chromophore and SERS from the surface, and these two effects operate in synergy¹²⁹. The key to maximising the effect is to promote strong interaction of the analyte to the SERRS-active substrate. The laser excitation frequency of the absorption band can be chosen either to coincide with the frequency of the absorption band for the chromophore or to coincide with the maximum of the plasmon resonance.

2.15. Applications of Raman and SERS

Raman spectroscopy has applications in every field of science; it is beyond the scope of this chapter to discuss them all. Examples of applications include:

- as a diagnostic tool to detect cervical cancer¹³⁰, single cancer cells living or fixed¹³¹, and HIV¹³².
- as a fast and non-invasive optical method for the determination of the influence of IR radiation on the degradation of carotenoid antioxidant substances beta-carotene and lycopene in the human skin¹³³.
- *in situ* qualitative and quantitative analyses¹³⁴⁻¹³⁵.
- non-destructive analysis of biofilms¹³⁶.
- as a characterization tool to study advanced and ancient ceramics, semiconductors and polymers¹³⁷⁻¹³⁸.
- *in situ* reaction monitoring *e.g.* the Knoevenagel condensation¹³⁹, esterification¹⁴⁰, and polymerization of methymethacrylate¹⁴¹.
- forensic science: drug abuse, explosives¹⁴².
- in pharmaceutical science: mapping¹⁴³ and polymorphism¹⁴⁴⁻¹⁴⁵.

- “single” molecule detection¹⁴⁶⁻¹⁴⁷.

2.16. Limitations of SERS

The inherent limitations of the technique must also be considered:

- the most apparent constraint lies in the limited substrate choices that exhibit LSPR behavior. The most commonly used substrates are coinage metals.
- in addition, the need for a roughened surface still poses some experimental challenges. For experimental and theoretical SERS investigations to be correlated, the substrates roughness features must be well characterized by atomic force microscopy (AFM), scanning electron microscopy (SEM), or transmission electron microscopy (TEM). This step is often tedious to perform on randomly roughened surfaces. Furthermore, many roughened surfaces have limited stability and reproducibility. For example, with time, colloids tend to aggregate, and changes in molecular surface coverage occur. Variation in the fabrication processes used to produce SERS-active substrates leads to inconsistent optical properties and, accordingly, discrepant enhancement factors.
- because most of the current nanofabrication techniques used to create SERS active substrates exhibit some degree of irreproducibility, enhancement factors can fluctuate by up to an order of magnitude for substrates fabricated with seemingly identical methodology.
- although SERS is very effective as a surface-science technique, it has limited applicability when the molecule of interest is not adsorbed directly onto the substrate.

2.17. Infrared (IR) Spectroscopy

In IR, the frequency of the incident radiation is varied continuously and the transmittance/absorbance of the radiation through the sample is plotted against the incident frequency (more usually wavenumber, cm^{-1}). The vibrations detected by IR

spectroscopy are those that produce a change in the dipole moment of the molecule. IR spectroscopy can be divided into three areas based on spectral region: far-IR (500-10 cm^{-1}), mid-IR (4000-400 cm^{-1}), and near-IR (13,300-4000 cm^{-1}). Far IR is used for the detection of very low frequency vibrations, such as the stretching of metal-metal bonds, and also for metal-ligand interactions. Mid-IR is the most commonly used form of vibrational spectroscopy, for both on line processing, and in the research laboratory. This information-rich (fingerprint) region contains all of the common vibrational energies of organic and non-metallic inorganic species¹⁴⁸.

2.17.1. Selection Rules for IR Spectroscopy

A diatomic molecule will absorb IR radiation only if its dipole moment changes upon a change in the inter-nuclear distance. The transition probability is a product of the population difference between two quantum states (ΔN), and the square of the transition dipole moment (M):

$$\text{transition probability} \sim \Delta N \times M^2 \quad (2.25)$$

For a molecule in a given electronic state, the transition dipole moment for a vibrational transition is given by:

$$M = \int \Psi_{v'}^* \mu_o^{(e)} \Psi_{v'} d\tau \quad (2.26)$$

The wave functions $\Psi_{v'}$ and $\Psi_{v''}$ represent the final and initial vibrational states, respectively, and $\mu_o^{(e)}$ is the permanent electric dipole moment in this electronic state. For the vibrational motion of a diatomic molecule, the permanent electric dipole moment can be expanded in a Taylor series about the equilibrium inter-nuclear separation, r_e :

$$\mu_o^{(e)} = \mu_e + \left(\frac{\partial \mu}{\partial r} \right)_{r_e} q + \frac{1}{2} \left(\frac{\partial^2 \mu}{\partial r^2} \right)_{r_e} q^2 + \dots \quad (2.27)$$

where μ_e is the dipole moment, when the bond is in the equilibrium position. The probability for a vibrational transition occurring in a diatomic molecule can be derived by substituting the expanded form of the permanent electric dipole moment into the equation of the dipole moment for the vibrational transition:

$$\int \Psi_v^* \mu^{(e)} \Psi_v d\tau = \mu_e \int \Psi_v^* \Psi_v d\tau + \left(\frac{\partial \mu}{\partial r} \right)_{r_e} \int \Psi_v^* q \Psi_v d\tau + \frac{1}{2} \left(\frac{\partial^2 \mu}{\partial r^2} \right)_{r_e} \int \Psi_v^* q^2 \Psi_v d\tau + \dots \quad (2.28)$$

The first term in equation 2.28 is equal to zero since the vibrational wavefunctions (Ψ_v and Ψ_v) are orthogonal. The second term is non-zero if the dipole moment depends on the inter-nuclear distance (r):

$$\left(\frac{\partial \mu}{\partial r} \right) \neq 0 \quad (2.29)$$

Therefore, diatomic molecules will only exhibit a vibrational absorption spectrum if there is a change in dipole moment during the vibrational motion. Homonuclear diatomic molecules, such as H_2 and N_2 , have zero dipole moments and do not show vibrational absorption spectra. In general heteronuclear diatomic molecules have dipole moments that change with internuclear distance, and so they exhibit vibrational absorption spectra. Quantum mechanical theory specifies that absorption of IR light will only occur if a vibrational mode involves a change in dipole moment and that vibrational energy levels in molecules are quantized. The theory also dictates that transitions can take place between adjacent energy levels only when the integral in the second term for the Hermite polynomials, that describe the wavefunction of the harmonic oscillator, is non-zero i.e., $\Delta v = \pm 1$ ¹⁴⁹.

2.18. Raman versus IR Spectroscopy

Raman and IR spectroscopy are complementary techniques and provide the same/complementary information regarding vibrational spectra of molecules. There are, however, certain advantages and disadvantages to each type of vibrational spectroscopy.

- the selection rules for two techniques are markedly different. Only those vibrations are Raman active which cause changes in the oscillating polarizability of the molecule. Conversely, IR active modes are due to change in oscillating dipole moment. Molecules possessing a centre of symmetry follow the mutual

exclusion rule, for which no vibration is active in both IR and Raman and totally symmetric vibrations are always Raman active but IR inactive.

- some vibrations are inherently weak in IR and strong in Raman spectroscopy. Examples are the stretching vibrations of the C=C, P=S, S-S, and C-S bonds. Bending vibrations are generally weaker than stretching vibrations in Raman spectra.
- measurement of the depolarization ratio provides a mean of distinguishing totally symmetrical vibration from the asymmetrical vibrations in Raman spectroscopy. The depolarization ratio (ρ) is defined as the ratio of the intensity of scattered light polarized perpendicular to the polarization of the incident radiation to that which is polarized parallel to the polarization of the incident radiation. Vibrational modes which are totally symmetric can have depolarization ratio values between 0 and 0.75, whereas for non-totally symmetric vibrational modes $\rho = 0.75$. Such information cannot be obtained from IR spectra of solutions where molecules are randomly oriented, $\rho = \frac{I_{\perp}}{I_{\parallel}}$ (where I_{\perp} and I_{\parallel} represent perpendicular and parallel vibrational intensities, respectively).
- using the resonance Raman effect, it is possible to selectively enhance vibrations of a particular chromophore in the molecule. This is particularly advantageous in vibrational studies of large (high molecular weight) biological molecules containing different chromophores.
- Raman spectroscopy requires very little sample preparation and the sample size can be very small, although care must be taken not to thermally degrade the sample due to the intense laser radiation. IR sample preparation is more tedious, *e.g.* preparation of KBr discs.
- since water is a weak Raman scatterer, Raman spectra of samples in aqueous solution can be obtained without major interference from water vibrations. Thus, Raman spectroscopy is ideal for the studies of biological compounds in aqueous solution. In contrast, IR spectroscopy suffers from the strong absorption of water.

2.19. Factor Group Splitting

Factor group splitting is also referred to as Davydov splitting¹⁵⁰. This phenomenon involves the splitting of fundamental vibrational modes, in the solid state, due to the presence of more than one molecule in the crystalline unit cell. Instead of the expected $3N-6$ normal modes of vibration, additional bands are observed due to intermolecular effects. Factor group splitting can easily be assigned as, of course, this phenomenon would not be observed in the solution state. This splitting phenomenon has been successfully employed to assess *e.g.* the crystalline content and morphology, polymorphism, and crystal density in a range of aliphatic polyketones and polyethylenes. The potential of this spectroscopic phenomenon to yield information about the crystalline phase present in these polymers can therefore be regarded as analogous to that gained by wide-angle X-ray scattering¹⁵¹. The defining parameter responsible for this phenomenon is the presence of more than one molecule per crystallographic unit cell.

2.20. Molecular Symmetry

The symmetry of a molecule is a valuable tool to gain insight into molecular vibrations. For example, symmetric vibrations give rise to the intense Raman bands, whereas asymmetric modes are usually weak and sometimes unobservable. According to the rule of mutual exclusion, if a molecule has a centre of symmetry then Raman active vibrations are IR inactive, and *vice versa*. If there is no centre of symmetry then some (but not necessarily all) vibrations may be both Raman and IR active. Molecular symmetry can be classified in terms of symmetry operations, which are movements of the atoms which leave the molecule indistinguishable from the original. There are five symmetry operations.

1. The identity (E) is possessed by every molecule no matter how unsymmetrical it is, the corresponding operation being to leave the molecule unchanged. This operation represents a rotation of 360° and is the equivalent of doing nothing to the object.

2. An n -fold rotation axis (C_n) generates n symmetry operations corresponding to rotations through multiples of $(360^\circ/n)$, each of which leaves the resulting molecule indistinguishable from the original.
3. The reflection operation takes place with respect to a mirror plane, both of which are given the symbol σ . There are three types of mirror plane that need to be distinguished. A horizontal mirror plane σ_h is one which is perpendicular to the principal rotation axis. If the mirror plane contains the principal rotation axis it is called a vertical plane and is given the symbol σ_v . Vertical planes which bisect bond angles are called dihedral planes, and labelled σ_d .
4. The operation of inversion is carried out with respect to a centre of inversion (also referred to as centre of symmetry) and involves moving every point (x , y , and z) to the corresponding inverted position ($-x$, $-y$, and $-z$). Both the symmetry element and the symmetry operation are given the symbol i . Molecules which contain an inversion centre are described as being centrosymmetric.
5. The rotation reflection axis (S_n), is a two step operation. The molecule is rotated $360^\circ/n$ and then reflected in a plane which is perpendicular to the axis, resulting in a configuration indistinguishable to that of the starting point.

A point group is a collection of symmetry elements. A simple method to classify point groups is illustrated in Fig.2.5. Group theory can be used to determine the number of vibrational modes of the molecule, and the symmetry group to which these vibrational modes belong. For example, Rd has a planar structure and exhibits C_s symmetry¹⁵². The character table for C_s symmetry is shown in Fig.2.6.

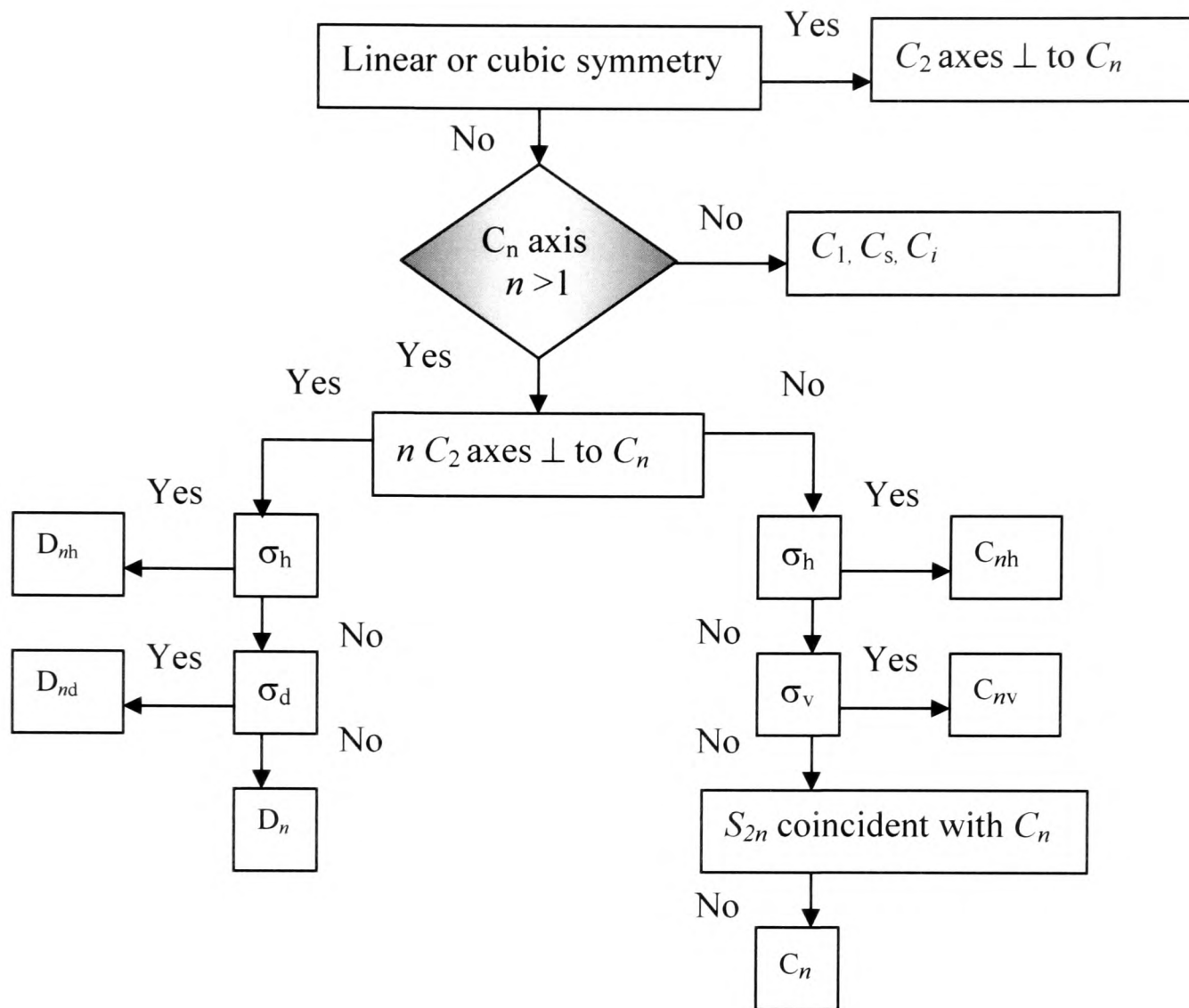


Figure 2.5. Flow chart showing the key decisions in point group assignment.

Symmetry elements $I, \sigma(xy)$				
Symmetry types and Characters				
$C_{1v}=C_{1h}=C_s$	I	$\sigma(xy)$		
A'	1	1	T_x, T_y, R_z	$\alpha_{xx}, \alpha_{yy}, \alpha_{zz}, \alpha_{xy},$
A''	1	-1	T_z, R_x, R_y	$\alpha_{yz}, \alpha_{xz},$

Figure 2.6. Character table representing C_{1v} , C_{1h} , or C_s point group.

2.21. Photon Correlation Spectroscopy (PCS)

PCS is a light scattering technique (also referred to as dynamic light scattering (DLS) and quasi-elastic light scattering (QELS)). PCS is a powerful and useful analytical tool successfully applied to interrogate a variety of systems in many technological and scientific disciplines such as colloid chemistry, biochemistry, biophysics, molecular biology, food technology, etc. Nowadays, PCS is a standard method for the determination of hydrodynamic diameter and size distribution of colloidal NPs. The rate of movement of particles in water is inversely proportional to particle size, and can be detected by analyzing the time dependence of the light intensity fluctuations scattered from particles when they are illuminated with a laser beam. In PCS the time dependence of the light scattered from a very small region of solution, over a time range from a tenth of a microsecond to milliseconds is measured.

2.21.1. Hydrodynamic Diameter

PCS uses the Brownian motion of the particles within a dispersion to measure their hydrodynamic diameter. Brownian motion is the random movement of particles as a result of bombardment by solvent molecules. As particles move, due to Brownian motion, any light that is scattered by the particle will experience a Doppler shift from a higher to lower frequency, depending on whether the particle is moving toward or away from the point of detection. For an assembly of these particles in random motion, a broadening of the Doppler frequency will be observed. The broadened frequency and that of the incident light combine to produce a pattern of frequencies, from which the particle diffusion can be calculated. For spherical particles, the diffusion coefficient can be used to obtain the particle diameter by using the Stokes-Einstein equation. This applies only to dilute suspensions where interactions between particles can be neglected.

Einstein's law of diffusion states that:

$$Df = k_B T \quad (2.30)$$

where, D is the diffusion coefficient and f is the frictional coefficient, k_B is Boltzmann's constant and T is the temperature. For spherical particles the frictional coefficient is given by Stokes law of diffusion:

$$f = 6\pi\eta D_h \quad (2.31)$$

where D_h is the hydrodynamic diameter of the particle, and η is the solvent viscosity. The amount of movement is defined by the translational diffusion coefficient (defines the velocity of the Brownian motion). A combination of the above equations allows the calculation of the hydrodynamic diameter from the particle diffusion coefficient:

$$D_h = \frac{k_B T}{3\pi\eta D} \quad (2.32)$$

The particle diameter is termed the hydrodynamic diameter when it is related to particle diffusion through a liquid. D_h is the diameter of a sphere possessing the same diffusion coefficient¹⁵³⁻¹⁵⁴.

2.21.2. Zeta Potential

The zeta potential (ζ) is the electric potential at the interface of a colloidal particle and dispersion medium. In a colloid, particles are electrically charged due to their ionic characteristics. The development of a net charge at the particle surface affects the distribution of ions in the surrounding interfacial region, drawing oppositely charged ions (counter-ions) towards it and driving like-charged ions (co-ions) away. This shielding layer around a particle is commonly known as the Debye layer or an electrical double layer (EDL). Most double layer models are variations of the Gouy-Chapman-Stern (GCS) model¹⁵⁵, wherein the EDL is comprised of a diffuse layer and a Stern layer. In the Stern layer or Helmholtz layer, ions are strongly bound to the surface. Contrary to this, the diffuse layer or Gouy-Chapman layer consists of mobile ions. Within the diffuse layer there is a notional boundary inside which the ions and particles form a stable entity. When a particle moves (*e.g.* due to gravity), ions within the boundary move with it, but any ions beyond the boundary do not travel with the particle. This boundary is called the

surface of hydrodynamic shear or slipping plane. When a voltage is applied to a solution, the potential at this sliding surface is called the ζ -potential (Fig.2.7).

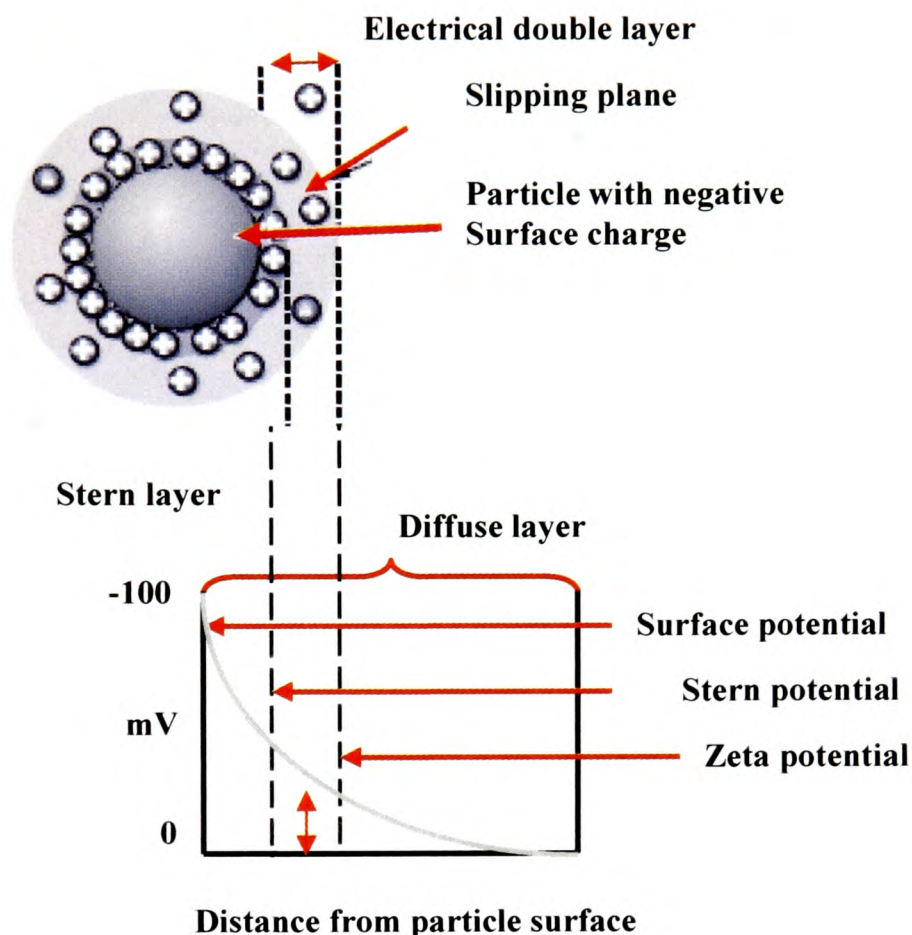


Figure 2.7. Schematic representation of ζ -potential.

The potential of a particle can be calculated by Henry's equation if the electrophoretic mobility of the sample is known:

$$U_E = \frac{2\varepsilon\zeta f(ka)}{3\eta} \quad (2.33)$$

where U_e is the electrophoretic mobility, ε is the dielectric constant of the sample, ζ is the zeta potential, $f(ka)$ is Henry's function [most often used are the Huckel (for non-aqueous media) and Smoluchowski (for aqueous media) approximations of 1 and 1.5, respectively], and η is the viscosity of the solvent. Electrophoretic mobility is the velocity of a particle under the influence of an applied electric field. One of many factors affecting ζ -potential is pH. A typical graph representing ζ -potential *versus* pH is depicted in Fig.2.8.

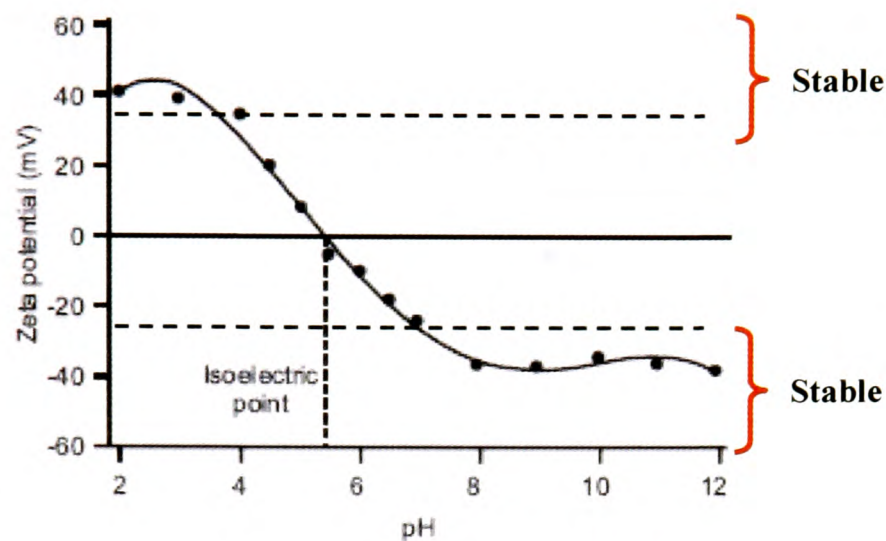


Figure 2.8. Typical plot representing ζ -potential versus pH showing the position of the isoelectric point (where ζ -potential is zero) and the pH values where the dispersion would be expected to be stable.

The primary relevance of the ζ -potential of a colloid is as a relative measure of the stability of a system. The dividing line between stable and unstable suspensions is generally taken at ζ -potential values of either +30 or -30 mV. Particles with zeta potentials more positive than +30 mV or more negative than -30 mV are normally considered stable. The Deryagin-Landau-Verwey-Overbeek (DLVO) theory for colloidal interactions dictates that a colloidal system will remain stable if and only if the Coulombic repulsion, arising from the net charge on the surface of the particles in a colloid, is greater than the van der Waals force between those same particles. When the reverse is true, the colloidal particles will cluster together and form flocculates and aggregates (depending on the strength of the van der Waals attraction and the presence/absence of steric effects). Since the higher the absolute ζ -potential, the stronger the Coulombic repulsion between the particles, and therefore the lesser the impact of the van der Waals force on the colloid. A general expression for DLVO theory is as follows:

$$V_T = V_A + V_R + V_S \quad (2.34)$$

where V_S is the potential energy due to the solvent, and V_A and V_R represent the contributions from attractive force and repulsive forces, respectively¹⁵⁶⁻¹⁶¹.

The aggregation process for colloidal NPs can be divided into two types, perikinetic aggregation and orthokinetic aggregation. Brownian motion is the driving mechanism in the former process, whereas the latter is driven by fluid shear. Two regimes exist for perikinetic aggregation: (a) diffusion limited aggregation (DLA), in which rate-limiting step is particle diffusion; and (b) reaction limited aggregation (RLA), in which the collision probability between the particles is small and becomes the controlling step. The main difference refer to the size, distribution and growth kinetics; RLA aggregates tend to be more compact, having a fractal dimension of ~ 2.1 as opposed to ~ 1.8 for DLA¹⁶²⁻¹⁶³.

2.22. Computational Chemistry

Computational chemistry attempts to simulate chemical structure and reactions numerically or analytically, based in full or in part on the fundamental laws of chemistry and physics. It allows chemists to study chemical phenomena by undertaking calculations using computers rather than by examining reactions and compounds experimentally, or by comparing calculated data with experimentally derived data. In recent years, the margin of interaction between computational chemistry and most branches of experimental chemistry has increased at a fast pace. The experimental characterization of new molecular systems relies more and more on computational approaches, *e.g.* for the evaluation and rationalization of structural, energetic, electronic and dynamical features. In particular, the ability to employ reliable quantum-mechanical methods to obtain accurate estimates for many kinds of spectroscopic parameters has given rise to many successful, synergic interactions between experimentalists and theoretically oriented chemists. There are two broad areas within computational chemistry devoted to the structure of molecules and their reactivity:

- molecular mechanics (MM); use the laws of classical physics to predict the structure and properties of molecules.
- electronic structure theory; use the laws of quantum mechanics instead of classical physics. The work in this thesis is mainly focused on applications of electronic structure methods.

2.23. Electronic Structure Methods

Electronic structure methods use the laws of quantum mechanics rather than classical physics as the basis for the computations. Quantum mechanics (QM) states that the energy and other related properties of a molecule maybe obtained by solving the Schrödinger equation:

$$H\Psi = E\Psi \quad (2.35)$$

In this equation, Ψ is the wave function, H is the Hamiltonian operator and E is the energy of the system. Electronic structure methods are characterized by their various mathematical approximations to its solutions. There are two major classes of electronic structure methods: semi-empirical methods and *ab-initio* methods.

2.24. The Born-Oppenheimer Approximation

The Born-Oppenheimer approximation is one of several approximations used to simplify the solution of the Schrödinger equation¹⁶⁴. It simplifies the general molecular problem by separating nuclear and electronic motions. This approximation is reasonable since the mass of a typical nucleus is thousands of times greater than that of an electron. Nuclei therefore move much more slowly than electrons, and the electrons react essentially instantaneously to changes in nuclear position. Thus, the electron distribution within a molecular system depends on the positions of the nuclei, and not on their velocities. The full Hamiltonian for a molecular system can then be written as:

$$H = T^{elec}(\vec{r}) + T^{nucl}(\vec{R}) + V^{nucl-elec}(\vec{R}, \vec{r}) + V^{elec}(\vec{r}) + V^{nucl}(\vec{R}) \quad (2.36)$$

where T^{elec} is the electronic kinetic energy, T^{nucl} nuclear kinetic energy, \vec{r} electronic coordinate, \vec{R} nuclear coordinate, V^{elec} electronic potential energy, and V^{nucl} nuclear potential energy.

2.25. The Hartree-Fock Method (HF)

The simplest of the the *ab-initio* methods is the self consistent field (SCF) method originally developed by Hartree and Fock¹⁶⁵. The HF method is used to determine the optimum wavefunction, *i.e.*, to give the lowest energy. SCF is an iterative process, which starts with initial guesses for the wavefunctions (usually estimated from a semi-empirical calculation), then the integrals are calculated and the minimum energy obtained. The wavefunctions are fractionally altered in order to assess if energy minimization decreases, and the process is repeated to find the minimum energy. Convergence of the energy may require repetition over many cycles. The wavefunctions are said to be “*self-consistent*”. The major deficiency of the HF-SCF method is that it treats each electron as moving under the influence of the average effect of all other electrons. However, this approach fails to account completely for Coulombic interactions between electrons, which cause them to repel each other. In other words motion of the electron is said to be correlated, and electron correlation causes electrons to be further apart than described by the HF-SCF approach. Electron correlation can be treated by a perturbation approach, since the problem that we are trying to solve is similar to the HF-SCF solution. Møller and Plesset used a perturbation theory method to determine the correlation energy correction, following an HF-SCF calculation¹⁶⁶. The perturbation can be truncated at second order (MP2), third order (MP3) or even higher orders (MP4 and MP5). However, this procedure is computationally intensive. Recently, a new class of electronic structure methods have come into wide use: density functional theory methods (DFT). DFT methods are, in many ways, similar to *ab-initio* methods. DFT calculations require only marginally greater computational resources than HF-SCF calculations.

2.26. Density Functional Theory (DFT)

DFT provides an alternative approach to electron correlation. The basis of this theory, developed by Hohenberg and Kohn in 1964¹⁶⁷, is the idea that the ground state electronic energy is determined completely by the electron density, ρ . All properties are therefore a functional of the density, because the density determines the potential, which determines

the Hamiltonian, which determines the energy and the wavefunction from which all physical properties can be determined. The ‘functional’ part of the name comes from the fact that the energy of the molecule is a function of the electron density, written $E_{DFT}[\rho]$, and electron density is itself a function of position $\rho(r)$, and in mathematics a function of a function is called a functional. The aim of DFT methods is to design functional connecting electron density with the energy. A general DFT energy expression is:

$$E_{DFT}[\rho] = T_S[\rho] + E_{ne}[\rho] + J[\rho] + E_{xc}[\rho] \quad (2.37)$$

where T_S is the kinetic energy functional (S denotes that the kinetic energy is obtained from a Slater determinant). E_{ne} is the nuclear potential energy and $E_{xc}[\rho]$ the exchange-correlation energy, which takes into account all the effects due to spin. The orbitals used to construct the electron density from:

$$\rho(r) = \sum_{i=1}^N |\psi_i(r)|^2 \quad (2.38)$$

are calculated from the Kohn-Sham equation, which are found by applying the variation principle to the electron energy. These are like the Hartree-Fock equations except for an additional term which is called the exchange-correlation potential:

$$\left\{ \begin{array}{l} \text{kinetic} \\ \text{energy} \\ \frac{\hbar^2}{2m_e} \nabla_i^2 \\ \text{Electron-nucleus} \\ \text{attraction} \\ - \sum_{j=1}^N \frac{Z_j e^2}{4\pi\epsilon_0 r_{j1}} \\ \text{Electron-electron} \\ \text{repulsion} \\ + \int \frac{\rho(r_2) e^2}{4\pi\epsilon_0 r_{12}} dr_2 \\ \text{Exchange-} \\ \text{correlation} \\ + V_{XC}(r)_1 \end{array} \right\} \psi_i(r_1) = \epsilon_i \psi_i(r_1) \quad (2.39)$$

The exchange-correlation potential is the ‘functional derivative’ of the exchange-correlation energy:

$$V_{XC}[\rho] = \frac{\delta E_{XC}[\rho]}{\delta \rho} \quad (2.40)$$

The Kohn-Sham equations are solved iteratively and self-consistently. The first step is to guess the electron density. For this step it is common to use a superposition of atomic electron densities. Then the exchange-correlation potential is calculated by assuming an approximate form of the dependence of the exchange-correlation energy on the electron density and evaluating the functional derivative in equation 2.40¹⁴.

2.27. DFT Approximations

Since the exchange-correlation energy functional is not known, one has to use approximations that are as accurate as possible, and the elaboration of new functionals is still an area of intense active work. The exchange-correlation energy functionals have been classified by Ziegler¹⁶⁸ into three generations.

1. The first generation of functionals is the local density approximation (LDA). This approximation involves the 1927 Dirac exchange functional¹⁶⁹. Central to this model is the assumption that we can write E_{xc} in the following, very simple form:

$$E_{xc}^{LDA}[\rho] = \int \rho(\vec{r}) \varepsilon_{xc}(\rho(\vec{r})) d\vec{r} \quad (2.41)$$

where, $\varepsilon_{xc}(\rho(\vec{r}))$ is the exchange-correlation energy per particle of a uniform electron gas of density $\rho(\vec{r})$. This energy per particle is weighted with the probability $\rho(\vec{r})$ that there is, in fact, an electron at this position in space.

2. The second generation of functionals makes use of both the density and its gradients. These are collectively known as the generalized gradient approximation (GGA). The first gradient-corrected energy functionals were proposed in 1986 by Becke¹⁷⁰ and Perdew and Wang¹⁷¹ for exchange and Perdew¹⁷² for correlation. The most popular functionals at the present time are those of Becke for exchange¹⁷³, Perdew for correlation¹⁷², Lee *et al.*¹⁷⁴ for correlation, as well as Perdew and Wang for exchange and correlation¹⁷⁵⁻¹⁷⁶.
3. The third generation of exchange-correlation energy functionals are those which go “beyond the GGA”. These comprise various options, some giving rise to more accuracy through increased sophistication and therefore computational cost. The most important ones are the hybrid functionals. Hybrid functionals are energy functionals which contain both a DFT exchange (*i.e.*, an LDA part and a GGA part) and a Hartree-Fock type exchange calculated from the orbitals. The most widely used hybrid is the so-called B3LYP functional, which incorporates Becke’s 3-parameter exchange functional (B3)¹⁷⁷ with the Lee, Yang and Parr correlation functional (LYP)¹⁷⁴. Hybrid DFT-SCF methods are, in general, particularly attractive because they are only marginally more computationally

intensive than HF-SCF, yet provide results that are comparable with those obtained using the much more demanding MP methods.

2.28. Basis Sets

The next approximation involves expressing the molecular orbital as a linear combination of a pre-defined set of one-electron functions known as basis functions. These basis functions are usually centered on atomic nuclei and so bear some resemblance to atomic orbitals. Initially, these atomic orbitals were typically Slater-type orbitals (STOs), which corresponded to a set of functions which decay exponentially with distance from the nuclei. Later, it was realized that these Slater-type orbitals could, in turn, be approximated as linear combinations of Gaussian orbitals instead. Because it is easier to calculate overlap and other integrals using Gaussian basis functions, this led to huge computational savings. Today, there are hundreds of basis sets composed of Gaussian-type orbitals (GTOs). The smallest of these are called *minimal basis sets*, and they are typically composed of the minimum number of basis functions required to represent all of the electrons in each atom. The largest of these can contain literally dozens to hundreds of basis functions for each atom. Recently it has been suggested that the double, triple or quadruple zeta (DZ, TZ or QZ) split basis sets are far superior to the commonly used 6-31IG basis sets¹⁷⁸.

2.29. Geometry Optimization

Geometry optimizations usually attempt to locate minima on the potential energy surface, thereby predicting equilibrium structures of molecular systems. At the minima the first derivative of the energy, known as the gradient, is zero. Since the gradient is the negative of the forces, the forces are also zero at such a point. A point on the potential energy surface where the forces are zero is called a stationary point. All successful optimizations locate a stationary point. Most optimization algorithms also estimate or compute the value of the second derivative of the energy with respect to the molecular coordinates, updating the matrix of force constants (known as the Hessian). A sensible starting point

for geometry optimization is to use experimental data whenever possible. For example the geometry of the molecule may be obtained from gas-phase microwave or Raman data, or in the solid state from X-ray crystallography, in which case it may be convenient to provide the input as Cartesian coordinates. Many of the known crystal structures are available from internet database; for example: CrystalWeb can be accessed from the Cambridge Database. In the absence of experimental data one can construct models using reasonable values for bond lengths, valence bond angles and dihedral/torsional angles. Model building may be done using molecular visualization software, such as the Gaussian graphical interface GaussView, or by the Z-matrix method. Fig.2.9 shows a flowchart for the steps involved in geometry optimization.

2.30. Vibrational Spectra

The Gaussian software package can also compute the vibrational spectra of molecules in their ground and excited states. In addition to predicting the frequencies and intensities of spectral lines, the program can also describe the displacements a system undergoes in its normal modes. Molecular frequencies depend on the second derivatives of the energy with respect to the nuclear positions. Because of the nature of the computations involved, frequency calculations are valid only at stationary points on the potential energy surface. For this reason, it is necessary to run a geometry optimization prior to doing a frequency calculation. Raw frequencies values computed at the Hartree-Fock level contain known systematic errors due to the neglect of electron correlation, resulting in overestimates of about 10-12% and it is therefore usual to scale frequencies predicted at the Hartree-Fock level by an empirical factor, 0.8929. Use of this factor has been demonstrated to produce very good agreement with experiment for a wide range of systems¹⁷⁹.

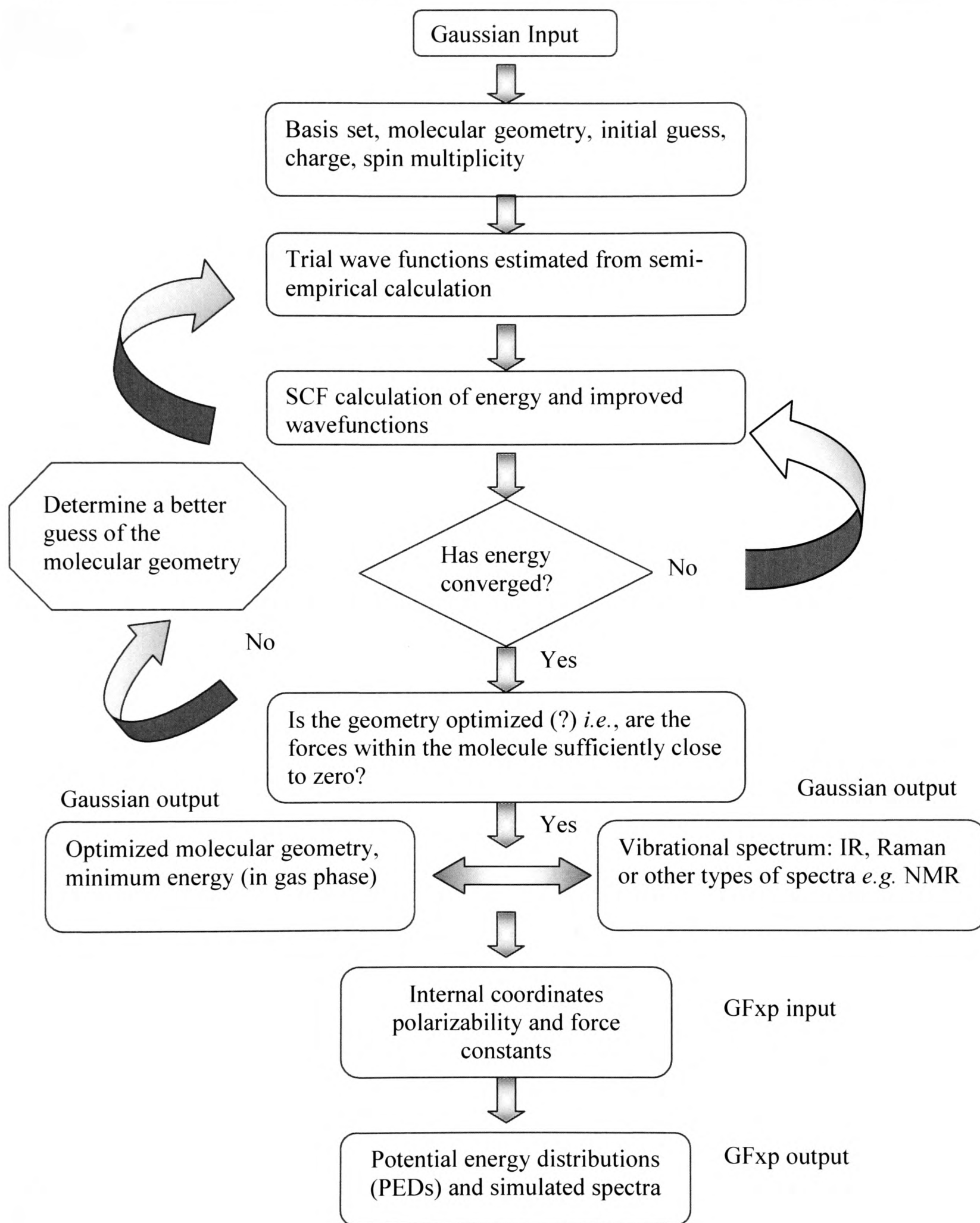


Figure 2.9. Flow chart showing the different stages of quantum mechanical calculations of molecular structure and spectroscopic properties.

2.31. Vibrational Coordinates

The positions of atoms within a vibrating molecule can be described by a variety of coordinate systems, for example Cartesian coordinates may be used. Each atom i is represented by a set of three Cartesian coordinates x_i , y_i and z_i . Thus there are a total of $3N$ Cartesian coordinates, where N is the number of atoms in the molecule. However, Cartesian coordinates are not very helpful when dealing with molecular vibrations. Since molecular vibrations are usually described in terms of the stretching of bonds and deformation of interbond angles etc. It is more meaningful to use internal coordinates. These are composed of all the bond stretches, bond angles and torsional angles within the molecule, and also out-of-plane angles. There are $3N-6$ independent internal coordinates. Symmetry coordinates are appropriate linear combinations of symmetry-related internal coordinates. The relationship between symmetry coordinates and internal coordinates is given by the matrix equation:

$$\mathbf{S} = \mathbf{UR} \quad (2.42)$$

where, \mathbf{S} is the column matrix of symmetry coordinates and \mathbf{R} is the column matrix of internal coordinates. There are $3N-6$ independent symmetry coordinates. If a larger number have been defined then some of them are described as redundant. For example, in the case of the trigonal planar XY_3 molecule, where θ_j defines the three X_iYX_j bond angles, the combination:

$$\frac{1}{\sqrt{3}}(\theta_1 + \theta_2 + \theta_3)$$

is a redundant coordinate, since it is impossible for all three bond angles to increase. It is obvious that if two angles increase then the third must decrease. Vibrational coordinates are described as normal coordinates, Q , and these may be expressed as linear combinations of either internal or symmetry coordinates. In matrix form the relationships are:

$$\mathbf{R} = \mathbf{LQ} \text{ and } \mathbf{S} = \mathbf{LQ}$$

Since $\mathbf{S} = \mathbf{UR}$ it follows that $\mathbf{L} = \mathbf{UL}$

The reverse transformations, *i.e.*, for expressing normal coordinates in terms of internal or symmetry coordinates are:

$$\mathbf{Q} = \mathbf{L}^{-1}\mathbf{R} \quad \mathbf{Q} = \mathbf{L}^{-1}\mathbf{S} \quad (2.43)$$

where \mathbf{L} is a matrix of normalization factors that relates the internal coordinates \mathbf{R} to the normal coordinates. \mathbf{L} is a matrix that relates the normal coordinates to the symmetry coordinates.

2.32. Potential Energy Distribution (PED)

Because the dimensions of \mathbf{L} are different for stretching and bending coordinates it is sometimes preferable to use the potential energy distribution to characterize the form of the normal coordinates. When only one normal coordinate is activated the potential energy can be represented as follows:

$$2v_k = Q_k^2 \sum_{ij} F_{ij} L_{ik} L_{jk} \quad (2.44)$$

The potential energy distribution is the fractional part of the potential energy of a normal mode of vibration contributed by each force constant, F_{ij} . If each $F_{ij} L_{ik} L_{jk}$ term is divided by the total sum of $F_{ij} L_{ik} L_{jk}$ terms for this vibration ($\lambda_k = \sum_{ij} F_{ij} L_{ik} L_{jk}$), then the potential energy distribution (PED) can be expressed as:

$$PED = \frac{F_{ij} L_{ik} L_{jk}}{\lambda_k} \quad (2.45)$$

Because the terms in equation first where $i=j$ are large (compared to terms where $i \neq j$) an approximate potential energy distribution for internal or symmetry coordinates in each normal coordinate Q_k can be defined percentage using only diagonal terms ($i=j$)¹⁶:

$$PED_{diag} = \left(\frac{100 F_{ii} L_{ik}^2}{\sum_i F_{ii} L_{ik}^2} \right) \% \quad (2.46)$$

2.33. References

- [1] A. S. Raymond and W. J. Jewett, *Physics for Scientists and Engineers*, 6th Ed., Thomson Brooks/Cole (2004).
- [2] P. Tipler, W. H. Freeman, *Physics for Scientists and Engineers: Electricity, Magnetism, Light, and Elementary Modern Physics*, 5th Ed., Thomson Brooks/Cole (2004).
- [3] C. F. Bohren, D. Huffman, *Absorption and scattering of light by small particles*, John Wiley, New York, (1983).
- [4] R. W. Ditchburn, *Light*, 2nd Ed., London: Blackie & Sons, (1963), 582.
- [5] G. Mie, *Ann. Phys.*, **25**, (1908), 377.
- [6] L. Brillouin, *Ann. Phys.*, **17**, (1922), 88.
- [7] C. V. Raman and K. S. Krishnan, *Indian. J. Phys.*, **2**, (1928), 387.
- [8] H. Compton, *Phys. Rev.*, **21**, (1923), 483.
- [9] A. Sharma and S. G. Schulman, *Introduction to Fluorescence Spectroscopy*, John Wiley & Sons, New York, (1999), 1.
- [10] M. J. Hollas, *Modern Spectroscopy*, 2nd Ed, Chichester, Wiley, (1992).
- [11] C. N. Banwell, E. M. McCash, *Fundamentals of Molecular Spectroscopy*, 4th Ed, London, McGraw-Hill, (1994).
- [12] E. Bright Wilson Jr., J. C. Decius and P. C. Cross, *Molecular Vibrations. The Theory of Infrared and Raman Vibrational Spectra*, New York, Dover, (1980).
- [13] J. B. Lambert, H. F. Shurvell, D. A. Lightner and R. G. Cooks, *Organic Structural Spectroscopy*, London, Prentice-Hall, (1998).
- [14] P. Atkins and Julio de Paula, *Atkins Physical Chemistry*, 8th Ed, Oxford Press New York, (2006).
- [15] B. Schrader and D. S. Moore, *Pure & Appl. Chem.*, **69**, (1997), 1451.
- [16] N. B. Colthup, L. H. Daly and S. E. Wiberley, *Introduction to Infrared and Raman Spectroscopy*, 3rd Ed, Academic Press, (1999).
- [17] A. Smekal, *Die Naturewiss.*, **11**, (1923) 873.
- [18] T. H. Maiman, *Nature*, **187**, (1960), 493.
- [19] C. A. Murray and S. B. Dieker, *J. Opt. Soc. Am. A* **3**, (1986), 2151.
- [20] B. Yang, M. D. Morris and H. Owen, *Appl. Spectrosc.*, **45**, (1991), 1533.

- [21] J. R. Ferraro and K. Nakamoto, *Introductory Raman Spectroscopy*, San Diego, Academic Press, (1997).
- [22] L. S. Ornstein, J. Rekveld and B. Utrecht, *Phys. Rev.*, **34**, (1929), 720.
- [23] H. W. Schrötter and H. W. Klöchner, *Raman Spectroscopy of Gases and Liquids*, Springer-Verlag, Berlin, (1979), 123.
- [24] E. Smith and G. Dent, *Modern Raman Spectroscopy*, John Wiley & Sons, Chicester , (2005).
- [25] J. R. Nestor and E. R. Lippincott, *J. Raman. Spectrosc.*, **1**, (1973), 305-318.
- [26] R. L. McCreery, *Raman Spectroscopy for Chemical Analysis*, Wiley-Interscience, New York, (2000).
- [27] N. Everall, T. Hahn, P. Matousek, M. Towrie and A. W. Parker, *Central Laser Facility Annual Report*, (2000/2001), 94.
- [28] I. Osticioli, A. Zoppi, E. C. Mario, *J. Raman. Spectrosc.*, **37**, (2006), 974.
- [29] S. E. J. Bell, A. E. S. O. O'Grady, J. Villaumie and A. C. Dennis, *Spectrosc. Eu.*, **14**, (2002), 17.
- [30] S. N. Terekhov and A. M. Shulga, *J. Mol. Struct.*, **484**, (1999), 63.
- [31] B. R. Hammond and B. R. Wooten, *J. Biomed. Opt.*, **10**, (2005), 054002.
- [32] C. Y. Huang, G. Balakrishnan, and T. G. Spiro, *J. Raman. Spectrosc.*, **37**, (2006), 1.
- [33] M. Fleischmann, P. J. Hendra and A. J. Mac Quillan, *Chem. Phys. Lett.*, **26**, (1974), 163.
- [34] D. J. Jeanmaire and R. P. Van Duyne, *J. Electroanal. Chem.*, **84**, (1977),1.
- [35] R. P. Van Duyne and J. P. Haushalter, *J. Phys. Chem.*, **87**, (1983), 2999.
- [36] M. G. Albrecht and J. A. Creighton , *J. Am. Chem. Soc.*, **99**, (1977), 5215.
- [37] A. Otto, *Top. Appl. Phys.*, **54**, (1984), 289.
- [38] M. Moskovits, *Acc. Chem. Res.*, **17**, (1985), 370.
- [39] G. A. Baker and D. S. Moore, *Anal. Bioanal. Chem.*, **382**, (2005), 1751.
- [40] G. C. Schatz, *Acc. Chem. Res.*, **17**, (1984), 370.
- [41] D. S. Wang, H. Chew and M. Kerker, *Appl. Opt.*, **19**, (1980), 2256.
- [42] H. X. Xu, J. Aizpurua, M. Käll and P. Apell, *Phys. Rev. E* **62**, (2000), 4318.
- [43] D. A. Weitz , M. Y. Lin and C. J. Sandroff, *Surf. Sci.*, **158**, (1985), 147.
- [44] A. M. Michaels, J. Jiang and L. Brus, *J. Phys. Chem. B* **104**, (2000), 11965.

- [45] P. Etchegoin and L. F. Cohen, *J. Chem. Phys.*, **119**, (2003), 5281.
- [46] G. C. Schatz and R. P. Duyne, *Handbook of Vibrational Spectroscopy*; J. M. Chalmers and P. R. Griffiths, Eds.; **1**, (2002); 759; John Wiley & Sons: New York.
- [47] G. C. Schatz, *Theochem.*, **573**, (2001), 73.
- [48] T. Jensen, *J. Cluster. Sci.*, **10**, (1999), 295.
- [49] R. Jin, *Science*, **294**, (2001), 1901.
- [50] G. C. Schatz, M. A. Young and R. P. Van Duyne, *Top. Appl. Phys.*, **103**, (2006), 19.
- [51] H. Xu, *Appl. Phys. Lett.*, **85**, (2004), 5980.
- [52] E. Hao and G. C. Schatz, *J. Chem. Phys.*, **120**, (2004), 357.
- [53] S. Zou and G. C. Schatz, *Chem. Phys. Lett.*, **403**, (2005), 62.
- [54] C. L. Haynes, A. D. McFarland, L. Zhao, R. P. Van Duyne, G. C. Schatz, L. Gunnarsson, J. Prikulis, B. Kasemo, and M. Käll, *J. Phys. Chem. B* **107**, (2003), 7337.
- [55] M. Käll, X. Hongxing and P. Johansson, *J. Raman. Spectrosc.*, **36**, (2005), 510.
- [56] M. Moskovits, *J. Raman. Spectrosc.*, **36**, (2005), 485.
- [57] C. L. Haynes, C. R. Yonzon, X. Zhang and R. P. Van Duyne, *J. Raman. Spectrosc.*, **36**, (2005), 471.
- [58] C. L. Haynes and R. P. Van Duyne, *J. Phys. Chem. B* **105**, (2001), 5599.
- [59] A. Otto, I. Pokrand and C. Pettenkofer, *Surface Enhance Raman Scattering*, R. K. Chang, and T. E. Furtak, Eds., Plenum, New York, (1982), 147.
- [60] A. Otto, *Appl. Surf. Sci.*, **6**, (1982), 309.
- [61] A. Otto, *J. Raman. Spectrosc.*, **22**, (1991), 743.
- [62] R. J. H. Clark and T. J. Dines, *Angew. Chem. Int. Ed. Engl.*, **25**, (1986), 131.
- [63] A. G. Brolo, D. E. Irish, and B. D. Smith, *J. Mol. Struct.*, **405**, (1997), 29.
- [64] A. Otto, *J. Raman. Spectrosc.*, **36**, (2005), 497.
- [65] C. L. Haynes and R. P. Van Duyne, *J. Phys. Chem. B* **105**, (2001), 5599.
- [66] D. J. Semin and K. L. Rowlen, *Anal. Chem.*, **66**, (1994), 4324.
- [67] S. E. Roark and K. L. Rowlen, *Anal. Chem.*, **66**, (1994), 261.
- [68] Z. Q. Tian, B. Ren and D. Y. Wu, *J. Phys. Chem. B* **106**, (2002), 9463.
- [69] S. H. Macomber, T. E. Furtak and T. M. Devine, *Chem. Phys. Lett.*, **90**, (1982), 439.
- [70] D. Thierry and C. Leygraf, *Surf. Sci.*, **149**, (1985), 592.

- [71] X. Gi and J. Dong, *Anal. Chem.*, **63**, (1991), 2393.
- [72] M. J. Weaver, *J. Raman Spectrosc.*, **33**, (2002), 309.
- [73] C. J. L. Constantino, T. Lemma, P. A. Antunes and R. Aroca, *Anal. Chem.*, **73**, (2001), 3674.
- [74] S. F. Wolf, L. Haines, J. Fisch, J. N. Kremsky, J. P. Dougherty and K. Jacobs, *Nucleic Acids Res.*, **15**, (1987), 2911.
- [75] L. Gunnarsson, E. J. Bjerneld, H. Xu, S. Petronis, B. Kasemo and M. Käll, *Appl. Phys. Lett.*, **78**, (2001), 802.
- [76] N. Felidj, S. L. Truong, J. Aubard, G. Lévi, J. R. Krenn, A. Hohenau, A. Leitner, and F. R. Aussenegg, *J. Chem. Phys.*, **120**, (2004), 7141.
- [77] L. He, M. J. Natan and C. D. Keating, *Anal. Chem.*, **72**, (2000), 5348.
- [78] L. A. Dick, A. D. McFarland, C. L. Haynes and R. P. Van Duyne, *J. Phys. Chem. B* **104**, (2000), 752.
- [79] L. A. Dick, A. D. McFarland, C. L. Haynes and R. P. Van Duyne, *J. Phys. Chem. B* **106**, (2002), 853.
- [80] M. Litorja, C. L. Haynes, A. J. Haes, T. R. Jensen, R. P. Van Duyne, *J. Phys. Chem. B* **105**, (2001), 6907.
- [81] C. L. Haynes and R. P. Van Duyne, *J. Phys. Chem. B* **107**, (2003), 7426.
- [82] X. Zhang, M. A. Young, O. Lyandres and R. P. Van Duyne, *J. Am. Chem. Soc.*, **127**, (2005), 4484.
- [83] O. Lyandres, N. C. Shah, C. R. Yonzon, J. T. Walsh, Jr, M. R. Glucksberg and R. P. Van Duyne, *Anal. Chem.*, **77**, (2005), 6134.
- [84] J. J. Laserna, E. L. Torres and J. D. Winefordner, *Anal. Chim. Acta.*, **200**, (1987), 469.
- [85] S. Sanchez-Cortes, J. V. Garcia-Ramos and G. Morcillo, *J. Coll. Interf. Sci.*, **175**, (1995), 358.
- [86] C. H. Munro, W. E. Smith, M. Garner, J. Clarkson and P. C. White, *Langmuir*, **11** (1995), 3712.
- [87] N. Shirtcliffe, U. Nickel and S. Schneider, *J. Coll. Interf. Sci.*, **211**, (1995), 122.
- [88] Z. Q. Tian and B. Ren, *Annu. Rev. Phys. Chem.*, **B 55**, (2004), 197.
- [89] M. A. Bryant, S. L. Joa and J. E. Pemberton, *Langmuir*, **8**, (1992), 753.

- [90] Z. Q. Tian, B. Ren and D. Y. Wu, *J. Phys. Chem. B* **106**, (2002), 9463.
- [91] B. Ren, X. F. Lin, J. W. Yan, B. W. Mao and Z. Q. Tian, *J. Phys. Chem. B* **107**, (2003), 899.
- [92] B. Ren, G. K. Liu, X. B. Lian, Z.L. Yang and Z. Q. Tian, *Anal. Bioanal. Chem.*, **1**, (2007), 29.
- [93] K. Kneipp , Y. Wang , H. Kneipp, L. T. Perelman, I. Itzkan and R. R. Dasari, *Phys. Rev. Lett.*, **78**, (1997), 1667.
- [94] K. Kneipp, H. Kneipp, I. Itzkan, R. R. Dasari and M. S. Feld, *Chem. Rev.*, **99**, (199), 2957.
- [95] X. M. Dou and Y. Ozaki, *Rev. Anal. Chem.*, **18**, (1999), 285.
- [96] B. Pettinger, G. Picardi, R. Schuster and G. Ertl, *Single. Mol.*, **3**, (2002), 285.
- [97] R. F. Aroca, R. A. Avarez-Puebla, N. Pieczonka, S. Sanchez-Cortez and J. V. Garcia, *Adv. Coll. Interf. Sci.*, **116**, (2005), 45.
- [98] K. L. Kelly, E. Coronado, L. L. Zhao and G. C. Schatz, *J. Phys. Chem. B* **107**, (2003), 667.
- [99] P. Mulvaney, *Langmuir*, **2**, (1996), 778.
- [100] M. A. El. Sayed, *Acc. Chem. Res.*, **37**, (2004), 326.
- [I01] Y. W. Chung, *Practical Guide to Surface Science and Spectroscopy*, San Diego Academic Press; (2001).
- [102] J. B. Hudson, *Surface science: an introduction*, Butterworth-Heinemann, Boston, (1992).
- [103] S. Lecomte, P. Matejka and M. H. Baron, *Langmuir*, **14**, (1998), 4373.
- [104] K. Faulds, R. E. Littleford, D. Graham, G. Dent and W. E. Smith, *Anal. Chem.*, **76**, (2004), 592.
- [105] R. J. Clark, R. E. Hester, *Spectroscopy of Inorganic-based Materials*, John Wiley & Sons, Chichester , (1987).
- [106] R. J. H. Clark, R. E. Hester, *Spectroscopy for Surface Science*, John Wiley & Sons, Chichester, (1998).
- [107] M. Moskovits, *Rev. Mod. Phys.*, **57**, (1985), 783.
- [108] R. F. Aroca, D. Ross and C. Domingo, *Appl. Spectrosc.*, **58**, (2004), 324.

- [109] T. Klar, M. Perner, S. Grosse, G. Plessen, W. Spirkl and J. Feldmann, *Phys. Rev. Lett.*, **80**, (1998), 4249.
- [110] C. F. Bohren, D. R. Huffman, *Absorption and scattering of light by small particles*, Wiley Interscience, New York, (1983).
- [111] D. L. Feldheim and C. A. Foss, *Metal nanoparticles: synthesis, characterization and applications*, Marcel Dekker, New York, Inc; (2002).
- [112] A. J. Haes and R. P. Van Duyne, *Proc. of SPIE*, **5221**, (2003), 47.
- [113] C. L. Haynes and R. P. Van Duyne, *J. Phys. Chem. B* **107**, (2003), 7426.
- [114] C. L. Haynes, C. R. Yonzon, X. Zhang and R. P. Van Duyne, *J. Raman. Spectrosc.*, **36**, (2005), 471.
- [115] R. A. Alvarez-Puebla, E. Arceo, P. J. G. Goulet, J. J. Garrido and R. F. Aroca, *J. Phys. Chem. B* **109**, (2005), 3787.
- [116] S. Sanchez-Cortes, J. V. Garcia-Ramos and G. Morcillo, *J. Coll. Interf. Sci.*, **167**, (1994), 428.
- [117] S. Sanchez-Cortes, J. V. Garcia-Ramos, G. Morcillo and A. Tinti, *J. Coll. Interf. Sci.*, **175**, (1995), 358.
- [118] A. M. Michaels, J. Jiang and L. Brus, *J. Phys. Chem. B* **104**, (2000), 11965.
- [119] H. X. Xu, E. J. Bjerneld, M. Käll and L. Borjesson, *Phys. Rev. Lett.*, **83**, (1999), 4357.
- [120] K. Kneipp and H. Kneipp, *Isr. J. Chem.*, **46**, (2006), 299.
- [121] C. G. Blatchford, J. R. Campbell and J. A. Creighton, *Surf. Sci.*, **120**, (1982), 435.
- [122] L. Brus, *J. Am. Chem. Soc.*, **221**, (2001), 112.
- [123] M. Kim, J. S. Kang, S. B. Park and M. S. Lee, *Bull. Korean Chem. Soc.*, **24**, (2003), 633.
- [124] C. H. Munro, W. E. Smith, D. R. Armstrong and P.C. White, *J. Phys. Chem.*, **99**, (1995), 879.
- [125] I. T. Shadi, B. Z. Chowdhry, M. J. Snowden and R. Withnall, *J. Raman. Spectrosc.*, **35**, (2004), 501.
- [126] D. L. Van Hying, W. G. Klemperer and C. F. Zukoski, *Langmuir*, **17**, (2001), 3120.
- [127] S. Sanchez-Cortes and R. J. Garcia-Ramos, *Surf. Sci.*, **473**, (2001), 133.

- [128] A. M. Stacy and R. P. Van Duyne, *Chem. Phys. Lett.*, **102**, (1983), 365.
- [129] I. R. Lewis and G. W. Edwards, *Handbook of Raman Spectroscopy*, (2002), 733.
- [130] F. M. Lyng, E. O. Faolain, J. Conroy, A.D. Meade, P. Knief, B. Duffy, M. B. Hunter, J. M. Byrne, P. Kelehan and H. J. Byrne, *Exp. Mol. Pathol.*, **82**, (2007), 121.
- [131] H. Tang, X. B. Yang, J. Kirkham and D. A. Smith, *Anal. Chem.*, **79**, (2007), 3646.
- [132] N. R. Isola, D. L. Stokes and T. Vo-Dinh, *Anal. Chem.*, **70**, (1998), 1352.
- [133] M. E. Darvin, I. Gersonde, H. Albrecht, L. Zastrow, W. Sterry, J. Lademann, *Laser Phys. Lett.*, **4**, (2007), 318.
- [134] K. Castro, M. Perez-Alonso, M. D. Rodriguez-Laso, N. Etxebarria and J. M. Madariaga, *Anal. Bio. Anal. Chem.*, **387**, (2007), 847.
- [135] G. Li and G. P. Zhang, *4th International Conference on Photonics and Imaging in Biology and Medicine*, Pts 1 and 2 6047: U472-U472, (2006).
- [136] R. Patzold, M. Keuntje and A. Anders-von Ahlften, *Anal. Bioanal. Chem.*, **386**, (2006), 286.
- [137] G. Gouadec and P. Colomban, *Prog. Cryst. Growth. Ch.*, **53**, (2007), 1.
- [138] L. Khriachtchev and S. Novikov, *Appl. Phys. A. Mater.*, **87**, (2007), 761.
- [139] M. P. Lopez, A. Dominguez-Vidal, M. J. Ayora-Canada, T. Laurell, M. Valcarcel and B. Lendl, *Lab on a Chip*, **7**, (2007), 126.
- [140] N. E. Leadbeater, R. J. Smith and T. M. Barnard, *Org. Biomol. Chem.*, **5**, (2007), 822.
- [I41] H. G. M. Edwards, K. S. Johal and A. F. Johnson, *Vib. Spectrosc.*, **41**, (2006), 160.
- [142] A. Burnett, W. H. Fan, P. Upadhyaya, J. Cunningham, H. Edwards, T. Munshi, M. Hargreaves, E. Linfield and G. Davies, *Optics and photonics for counterterrorism and crime II 6402: B4020-B4020*, (2006).
- [143] J. H. Kirk, S. E. Dann and C. G. Blatchford, *Int. J. Pharm.*, **334**, (2007), 103.
- [144] A. Bashkirava, P. C. Andrews, P. C. Junk, E. G. Robertson, L. Spiccia and N. Vanderhoek, *Chem. Asian J.*, **2**, (2007), 530.
- [145] P. Garidel and M. Boese, *Microsc. Res. Tech.*, **70**, (2007), 336.
- [146] Y. C. Liu, C.C. Yu and T.C. Hsu, *Electrochem. Commun.*, **4**, (2007), 639.
- [147] T. H. Reilly, S. H. Chang, J. D. Corbman, G.C. Schatz and K.L. Rowlen, *J. Phys.Chem.*, **111**, (2007), 1689.

- [148] P. R. Griffiths and J. A. Dehaseth, *Fourier Transform Infrared Spectrometry*, New York, Wiley, (1986).
- [149] B. Schrader, *Infrared and Raman Spectroscopy: Methods and Applications*, Wiley-VCH, (1998).
- [150] S. A. Davydov, *Theory of molecular excitons*. McGraw-Hill, New York,(1962).
- [151] J. M. Lagaron, *Macromol. Symp*, **184**, (2002), 19.
- [152] K. C. Molloy, *Group Theory for Chemists*, Harwood, (2004).
- [153] Particle Sizing by DLS for the Zetasizer Nano series and HPPS training course, presentation from Malvern website, www.malvern.co.uk.
- [154] A. Menniti, K. Rajagopalan, T. A. Kramer, M. M. Clarka, *J. Coll. Interf. Sci.*, **284**, (2005), 477.
- [155] R. J. Hunter, *Foundations of Colloid Science*, Oxford Univ. Press, New York, (2001).
- [156] B. J. Kirby and E. F. Hasselbrink Jr., *Electrophoresis*, **25**, (2004), 203.
- [157] J. H. Lyklema, *Fundamentals of Interface and Colloid Science*, Academic Press, London, (1991).
- [158] P. A. Kralchevsky, K. D. Danov and N. D. Denkov, *Handbook of Surface and Colloid Chemistry*, Birdi, K. S. (Ed.),CRC Press, Boca Raton, FL (2003), 137.
- [159] E. Gileadi, E. Kirowa-Eisner and J. Penciner, *Interfacial Electrochemistry: An Experimental Approach*, Addison-Wesley, Reading, MA, (1975).
- [160] J. T. G. Overbeek, *Colloid Science*, *1*, Elsevier, Amsterdam, (1952).
- [161] A. J. Bard and L. R. Faulkner, *Electrochemical Methods: Fundamentals and Applications*, Wiley, New York, (2001).
- [162] M. Y. Lin, H. M. Lindsay, A. D. Weitz, R. C. Ball, R. Klein, P. Meakin, *Proc. R. Soc. London A* **423**, (1989), 71.
- [163] H. Sonntag and K. Strenge, *Coagulation Kinetics and Structure formation*, Plenum Press, New York, (1987).
- [164] M. Born and J. R. Oppenheimer, *Ann. Physik*, **84**, (1927), 457.
- [165] D. R. Hartree, *The Calculation of Atomic Structures*, Wiley, New York, (1957) , V. Fock, *Z. Phys.*, **61**, (1930), 126; Z. Fock, *Z. Phys.*, **62**, (1930), 795.
- [166] C. Møller and M.S. Plesset, *Phys. Rev.* **46**, (1934), 618.

- [167] P. Hohenberg and W. Kohn, *Phys. Rev. B* **136**, (1964), 684.
- [168] T. Ziegler, *Can. J. Chem.*, **73**, (1995), 743.
- [169] P. A. Dirac, *Proc. Cambridge Philos. Soc.*, **26**, (1930), 376.
- [170] A. D. Becke, *J. Chem. Phys.*, **84**, (1986), 8524.
- [171] J. P. Perdew, Y. Wang, *Phys. Rev. B* **33**, (1986), 8800.
- [172] J. P. Perdew, *Phys. Rev. B* **33**, (1986), 8822.
- [173] A. D. Becke, *Phys. Rev. A* **38**, (1988), 3098.
- [174] C. Lee, W. Yang and R.G. Parr, *Phys. Rev. B* **37**, (1988), 785.
- [175] J. P. Perdew, *Electronic Structure of Solids*, P. Ziesche, H. Eschrig (Eds.), 91, Academic Press, Berlin, (1991).
- [176] J. P. Perdew, K. Burke and Y. Wang, *Phys. Rev. B* **54**, (1996), 16533.
- [177] A. D. Becke, *J. Chem. Phys.*, **98**, (1993), 5648.
- [178] Gaussian 03 official website: www.gaussian.com
- [179] S. Bell, B. Z. Chowdhry, T. J. Dines and R. Withnall, *J. Chem. Ed.*, **84**, (2007), 1364.

Chapter Three

Experimental and Instrumentation

3.1. Chemical Reagents

The chemical reagents used in the experimental studies are listed in Table 3.1. Unless otherwise stated all chemical reagents were purchased from Sigma-Aldrich (Dorset, UK) and used as received.

Table 3.1. Chemical reagents.

Chemical name	Chemical formula	Mol. Wt	Purity (%)
Rh ^a	C ₃ H ₃ NOS ₂	133.19	99
MeRd	C ₄ H ₅ NOS ₂	147.22	97
H ₂ NRd	C ₃ H ₄ N ₂ OS ₂	148.21	99
Poly(L-lysine) hydrobromide	[C ₆ H ₁₂ N ₂ O] _n . HBr	4,000- 15,000	-
Silver nitrate	AgNO ₃	169.8	99
Tri-sodium citrate dihydrate	C ₆ H ₅ O ₇ Na ₃ . 2H ₂ O	294.1	-
Potassium tetra-chloroaurate (III)	KAuCl ₄	377.8	99.9
Deuterium oxide	D ₂ O	20.03	99.9
Sodium chloride	NaCl	58.44	99.5
Magnesium sulphate	MgSO ₄	120.37	99.9
Potassium chloride	KCl	74.55	Analar
Sodium thiosulphate	Na ₂ S ₂ O ₃	158.11	Analar

^aPurchased from Fluka.

Where required, in-house produced double-deionized water was used.

3.2. Deuteriation

Deuteriated isotopomers of Rd and its derivatives were prepared by dissolving ~10 mg of sample in 10 mL of deuterium oxide (D₂O). Solid, dry material was recovered by placing

frozen samples (~ -20 °C) into an Edwards freeze drying apparatus, incorporating an Edwards 8, dual stage vacuum pump. Samples were left 'on the pump' for ~ 4 hours or until completely dry. This deuteration process was repeated at least an additional two times, in order to improve the percentage yield of the deuteriated product.

3.3. Raman Spectroscopy

The Raman and SER spectra of Rd and derivatives, including their *N*- and/or *C*-deuteriated derivatives, were investigated using a LabRam Raman spectrometer (Horiba Jobin Yvon Ltd, Figs.3.1, 3.2, and 3.3). The spectrometer is equipped with an 1800 groove/mm holographic grating, a holographic notch filter, a Spectrum One Peltier-cooled CCD (MPP1 chip) for detection and an Olympus BX40 microscope. A helium-neon laser provided exciting, monochromatic radiation of wavelength (λ_0) at 632.8 nm and an argon-ion laser at 514.5 nm. In both cases the power at the sample was 8 mW. Raman measurements largely consisted of acquiring multiple spectral windows in the range 50 - 4000 cm^{-1} (Stokes shifts). The Raman instrument was calibrated using the ν_1 line of silicon at 520.7 cm^{-1} . The centring of the silicon line was checked by using the frequencies of the principal lines of a neon lamp.



Figure 3.1. Photograph of the ISA laser Raman spectrometer system.

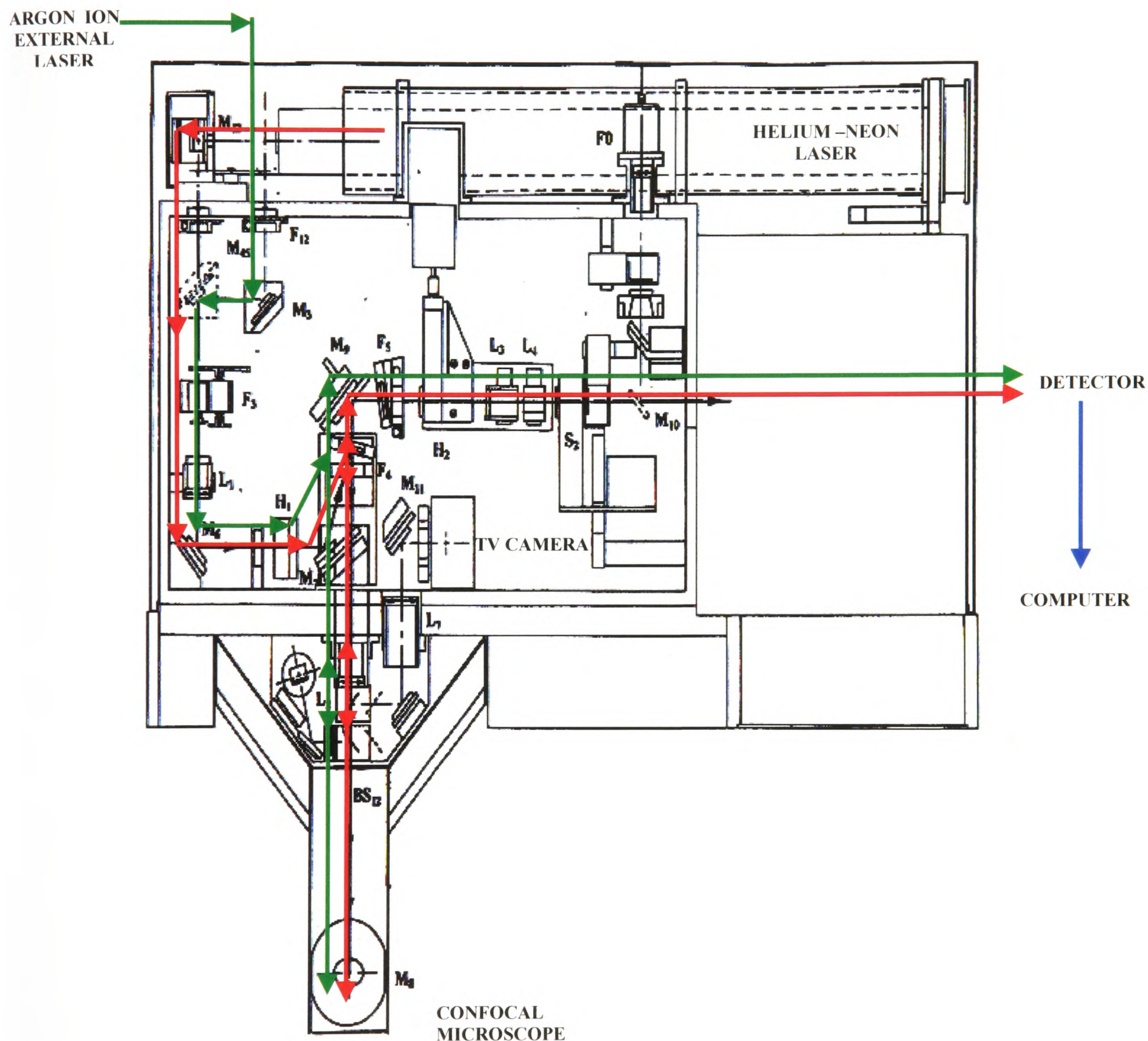


Figure 3.2. Optical arrangement of the internal components of the ISA laser Raman spectrometer employed in all experiments. The laser paths are highlighted in red ($\lambda_0 = 632.8 \text{ nm}$) and green ($\lambda_0 = 514.5 \text{ nm}$).

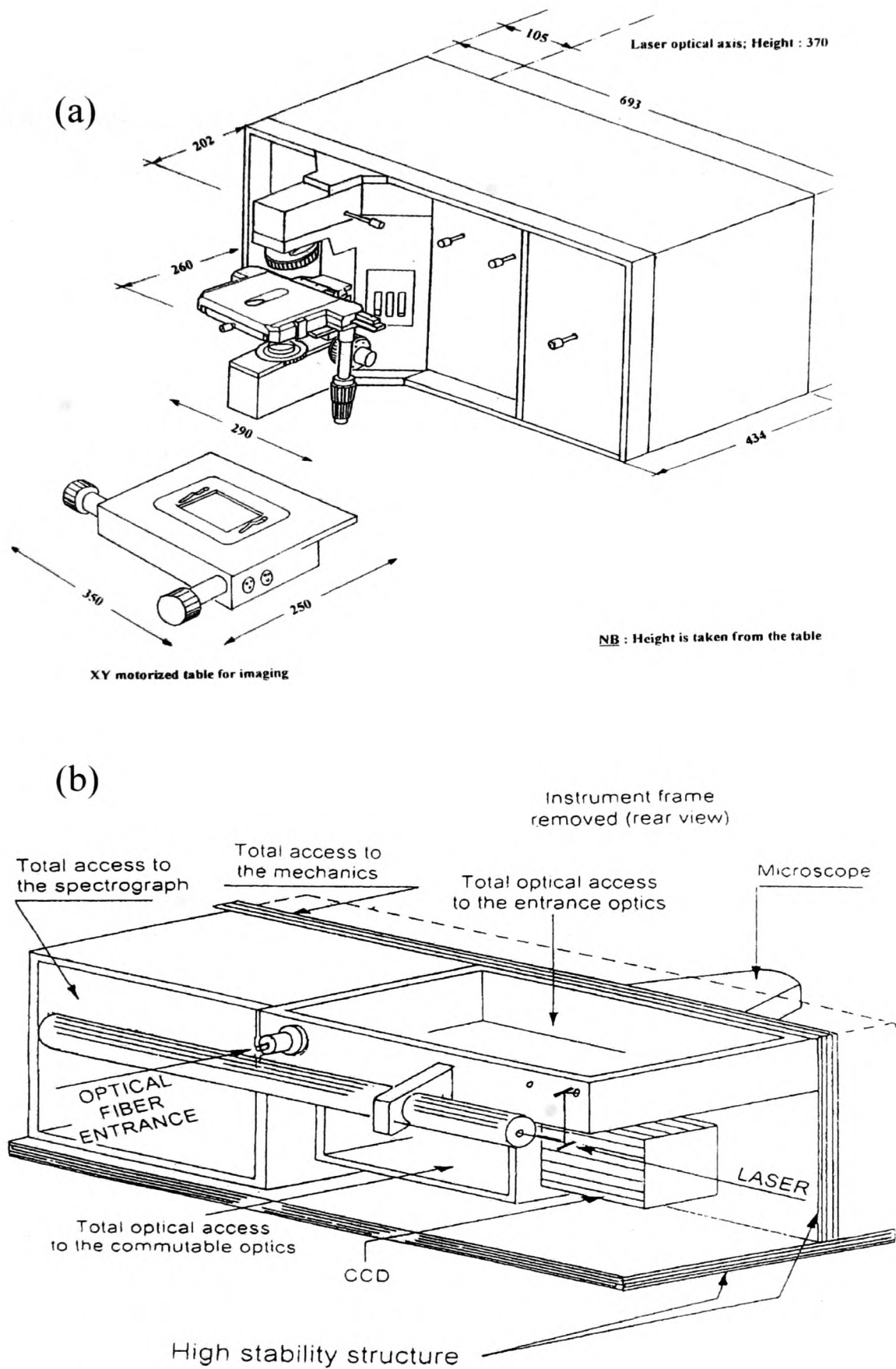


Figure 3.3. Schematic diagram of the ISA laser Raman spectrometer (a) front view, (b) rear view¹.

Fig.4.2 illustrates that the laser beam is directed by two mirrors, M_{12} in order to pass through two irises, located before the interference filter F_{12} (used to filter out laser plasma lines) and the laser lens L_1 (focuses the laser onto the pinhole H_1). The pinhole is used as a reference for alignment and is conjugated with the spot on the sample. F_3 represents the filter wheel comprises of six different filters with different optical densities to reduce the power of the incident laser beam, for instance when laser causes thermal degradation. The laser beam from H_1 is then reflected by the mirror M_7 , onto the angle-tuned holographic notch filter (F_4), which enables the laser beam to be reflected towards the sample. A confocal microscope objective is used to focus the laser onto the sample. A 180° back scattering configuration allows to the collection of Rayleigh and Raman scattered radiation, which follows the same path back to the notch filter. The notch filter filters the Rayleigh radiation and allows only Raman radiation to pass through. The lens L_2 directs the laser spot onto the confocal hole H_2 . The lenses L_3 and L_4 (polarisation analysers and scramblers may be placed between L_3 and L_4) image the confocal hole onto entrance slit S_2 . The image of the hole is reduced by a factor of five on the entrance slit. A shutter is installed after the slit, enabling the Raman scattered radiation to enter the spectrometer. A beam splitter BS_{12} can be placed in the optical beam from the sample, to allow observation on a TV camera, which can be used for instance, to facilitate the focusing of the sample using the confocal microscope. The spectrometer is equipped with a motorised holographic grating (1800 groove/mm), which disperses the Raman signal to the CCD detector. The spectral resolution depends on the number of grooves per millimetre, the larger the number of grooves/mm, the better the spectral resolution.

The spectrum One CCD detector is a solid state photodetector array made of silicon². The CCD area is divided into a two dimensional matrix of pixels. When illuminated with light, by opening the shutter, each pixel gains a charge from the photoelectric effect. The charges of the neighbouring pixels are kept separated by a grid of electrodes that confine the charges. After data acquisition when shutter is closed, the charges of the pixels are analysed row by row, to the edge of the chip into a read out register, after processing signal is converted into the digital data for software manipulation. The CCD is equipped

with a Peltier cooler to reduce the dark noise and hence improve the signal to noise ratio. The detector is cooled to -37 °C.

3.4. Raman Solid State Spectra

Raman spectra of solid state samples were collected, at room temperature, on a microscope slide (generally) using a microscope objective of $\times 50$ magnification to focus the laser beam. If there appeared to be a problem from polarisation effects of the solid state sample, the spectra were re-collected using a $\times 10$ microscope objective to focus the laser beam.

3.5. Solutions of Rd and its Derivatives for Raman Studies

Solution phase spectra (in methanol) were acquired using 1 cm path length glass cuvettes. The concentration range of the compounds used was, typically, between 20-25 mg/mL, depending on the solubility of the sample. The glass cuvettes were mounted in a thermostatically controlled cell holder at ambient temperature. A 40 mm focal length macro-lens was used to focus the laser beam, and collect the back-scattered light in these experiments. A back-scattering (180° excitation and collection) geometry was used in all experiments.

3.6. Solutions of Rd and its Derivatives for SERS Studies

In order to conduct quantitative analysis, methanolic solutions of Rd and its derivatives were used. For Rd, H₂NRd, and MeRd the range of concentrations investigated were: 10^{-3} - 10^{-15} , 10^{-4} - 10^{-13} , and 10^{-4} - 10^{-15} mol dm⁻³, respectively.

3.7. SERS measurements

All SER spectra were collected by using 180° back-scattering geometry. An Olympus microscope objective, having a magnification of $\times 50$ and numerical aperture of 0.45 was

used both to focus the incident laser light and to collect the back-scattered Raman light. The acquisition time for each SER spectrum is 90s. For kinetic studies of SER spectra the glass cuvettes were mounted into a thermostatically controlled cell holder with continuous stirring at ambient temperature. A 40 mm focal length macro lens was used to focus the laser beam, and collect the back-scattered light in these experiments. The acquisition time for SER spectra is 240s with 2s integration time.

3.8. Ag and Au Nanoparticle (NP) Synthesis

Ag colloid was prepared according to a modified Lee- Meisel procedure³⁻⁵. All glassware was washed with *aqua regia* [$\text{HNO}_3\text{-HCl}$ (1:3, v /v)] followed by gentle scrubbing with a soap solution. Silver nitrate (90 mg) was suspended in 500 mL of de-ionised water at 45 °C and rapidly heated to boiling before a 1 % solution of tri- sodium citrate (10 mL) was added under vigorous stirring. The solution was held at boiling for 90 min with continuous stirring. The resulting colloids show a turbid gray-green colour (Fig. 3.4.a). Similarly, gold colloid was synthesized by the chemical reduction method. Potassium tetra-chloroaurate (18 mg) was dissolved in triply deionised water (100 mL) and heated to boiling. Then 2.5 mL 1% solution of tri-sodium citrate was added under vigorous stirring. The solution was kept boiling for 20 minutes⁶. The resulting colloid has a deep wine red colour (Fig.3.4.b). Generally, the Au and Ag NPs prepared by the above mentioned method are covered with a layer of citrate with pendant negatively charged groups. The characterization of colloids is explained in detail in chapter seven.



(a) (b)

Figure 3.4. Colloidal nanoparticles: (a) Au and (b) Ag.

3.9. Aggregation of Colloidal NPs

For SERS studies, aggregation of Ag and Au NPs was induced by poly(L-lysine) [PLL]. 150 μL of a 0.01% (w/v) aqueous solution of PLL was added to 1 mL of Ag or Au colloid that had been diluted with 1 mL of de-ionized water, followed by 150 μL of the analyte solution and 35 μL of HCl (1 mol dm^{-3}). SER spectral profiles of Ag and Au colloids in the presence and absence of PLL, methanol, and HCl were collected to further clarify the optimum experimental protocols employed, to provide a baseline and determine the vibrational band positions from the Ag and Au sol (almost identical spectral profiles were obtained with both sols, therefore the results from Ag colloid only are included in the experimental chapter). Fig.3.5 displays the optimum experimental conditions for the Ag sol in the absence and presence of methanol, PLL, and HCl. All experiments were conducted at ambient temperature. It is worth mentioning that SERS signal enhancement also depends on the analyte being investigated.

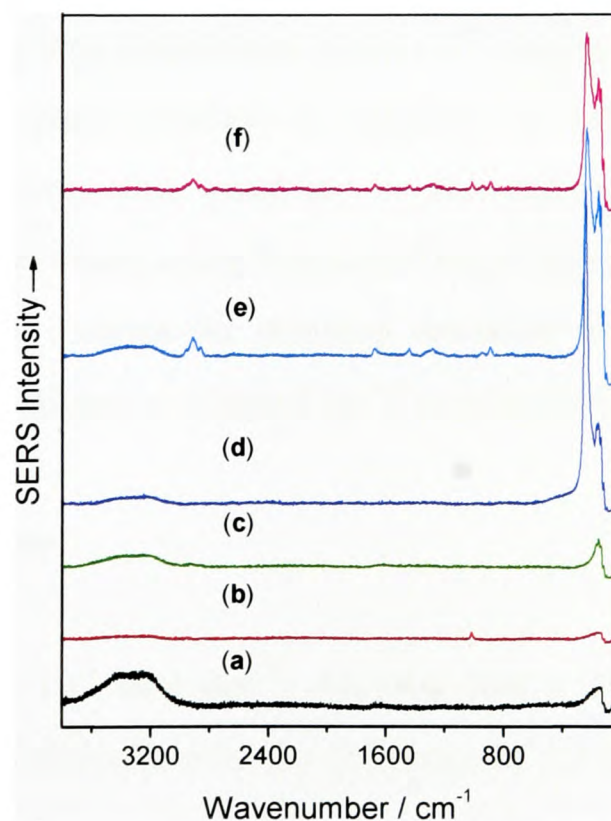


Figure 3.5. Representative SER spectral profiles of Ag NPs: (a) alone, (b) in the presence of methanol, (c) in the presence of 0.01 % PLL, (d) in the presence of HCl (1 mol dm^{-3}), (e) in the presence of PLL, and HCl, and (f) in the presence of PLL, methanol, and HCl ($\lambda_0 = 632.8 \text{ nm}$).

3.10. Reproducibility/time Dependence

Following the mixing of Rd, or its derivatives, with Ag colloid and aggregation of the NPs time dependent 2D SER spectra were obtained after 2 minutes. To ensure reproducibility, in some experiments 4 measurements were made at different spots of the same sample. This methodology showed that SERS signals were reproducible from spot to spot with a relative standard deviation of 2-3 %. For the time dependent 3D stack plots, following the mixing of Rd and its derivatives with Ag colloid and aggregation of NPs, SER spectra were undertaken immediately.

3.11. Concentration Dependence

The concentration dependence of the SERS signals for Rd and its derivatives were determined from logarithmic plots of band intensities *versus* concentration of analyte. The intensities of the bands used for analysis were obtained from base-line corrected peak heights. The baseline was determined from a 9th degree polynomial fit within the Labspec data analysis program (version 4) supplied by Jobin Yvon. The calculated baseline was subtracted from the spectrum in the region of interest. Multi-linear regression analysis was performed using Microcal Origin (version 7). Limits of detection were determined by taking 3 times the standard deviation of the intercept (of the non logged plots) divided by its slope, as adopted by Womack *et al*⁷.

3.12. SERS pH Dependence

pH profiles of Rd (1.0×10^{-3} mol dm⁻³), H₂NRd (8.6×10^{-4} mol dm⁻³), and MeRd (8.7×10^{-4} mol dm⁻³) were obtained over the pH range of 2.3 to 11.3 ($\lambda_0 = 632.8$ nm). A fresh, aggregated Ag colloid was prepared (as discussed above in section 3.9) and the pH adjusted using aqueous solutions of either hydrochloric acid or sodium hydroxide. The optimum condition for SERS studies was obtained by plotting, after base line correction, the logarithm of the peak intensity (area) of the vibrational bands at 556 and 1255 cm⁻¹ for Rd and MeRd, respectively *vs* pH.

3.13. FT-Infrared Spectroscopy

FT infrared spectra were recorded on a Perkin Elmer Paragon 1000 FT-IR spectrometer operating at a resolution of 1 cm^{-1} in the $450\text{-}4000\text{ cm}^{-1}$ range. A dry nitrogen gas purge was maintained in the sample compartment to facilitate a simpler background subtraction. Solid state samples were examined as pressed KBr discs, and spectra were recorded over the $450\text{-}4000\text{ cm}^{-1}$ region. Fig.3.6 displays the internal components of a typical Perkin-Elmer FT infrared spectrometer. The excitation source (1) splits the light into parallel beam, which is directed towards the interferometer. The interferometer comprises of a beam splitter (1) and two mirrors (one of them is fixed, while the second is moving mirror (2)). The former (1) is a plate of potassium bromide (KBr), which is angled and transparent enough to allow 50% of the radiation falling on it to be reflected and 50 % to pass straight through. This arrangement allows the half of the infrared beam to fall onto the fixed mirror and other half falls onto a moving mirror. The moving mirror is the integral part of the interferometer and is used to produce an interferogram for the infrared beam. The incident radiation reflected from the moving mirror passes through another KBr window (7), and focussed onto the sample (6). An interferogram is then collected and passed to the detector (8). The detector is a photoconductivity cell, which is made out of deuteriated triglycine sulphate (DTGS). The interferogram can be converted into the original frequencies emitted by the source by computing the Fourier transform. For the sample positioning, a pre-aligned laser (9) determines the path of the infrared beam. All the internal optics are encased in a hard plastic cover (10, 4) to protect from the ingress of moisture, dust, and other vapours. The optical chamber is kept dry by molecular desiccant (11). Owing to the single beam mode of the instrument, it is important to run a background spectrum with the sample compartment (5) empty to subtract from the infrared spectrum of the sample. To further limit errors in the background subtraction due to moisture and CO_2 in the atmospheric air, dry nitrogen can be purged in the sample compartment⁸⁻⁹.

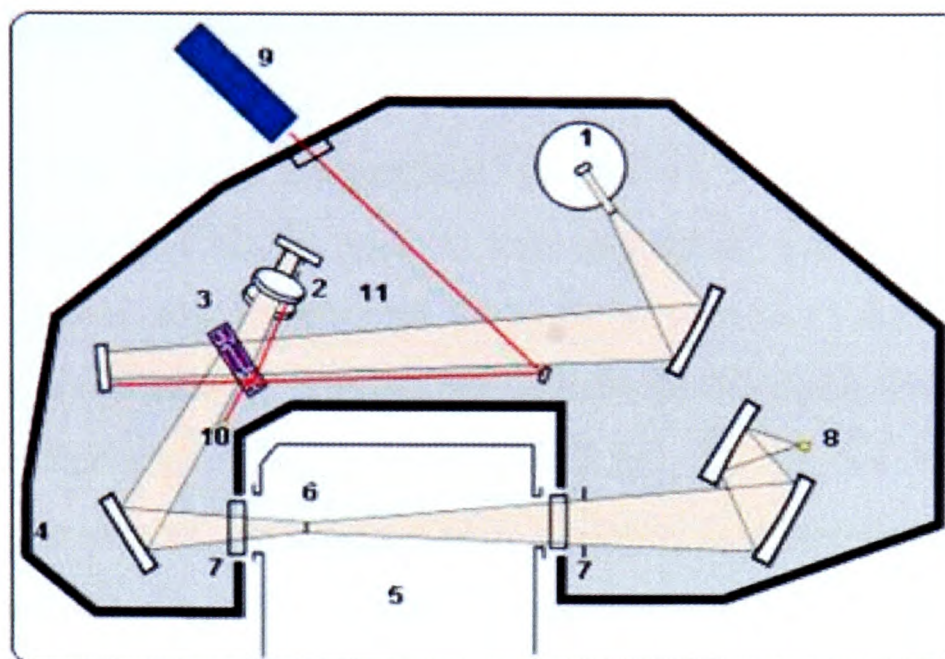


Figure 3.6. Schematic of the internal components of a typical Perkin-Elmer FT infrared spectrometer.

3.14. Photon correlation spectroscopy (PCS)

PCS measurements were performed using a Malvern Zetasizer Nano ZS in ζ -potential and size mode. For the hydrodynamic diameter and ζ -potential measurements folded capillary cells integrated with gold electrodes were used. The size of a particle is calculated from the translational diffusion coefficient by using the Stokes-Einstein equation. The ζ -potential was calculated from the measured electrophoretic mobility using the Smoluchowski approximation for Henry's function (see Chapter two). Aggregation of NPs was induced by the addition of 150 μL of an aqueous solution of appropriate concentration of aggregating agent to 1 mL of Ag and Au NPs which had been diluted with 1 mL of de-ionized water. At 60 s after addition of the aggregating agent, an aliquot of the sample (1 mL) was placed into a folded capillary cell and measurements were started after 30 s later. Six measurements were made for each sample to determine the hydrodynamic diameter and ζ -potential, with time intervals of 3 mins and 1 min, respectively.

3.14.1. Hydrodynamic diameters of Ag and Au NPs

Fig.3.7 displays the optical arrangement of the PCS instrument for measuring hydrodynamic diameter. A He-Ne laser (1) with an exciting wavelength of 633 nm and power of 4mW is used to illuminate the colloidal NPs. Most of the laser beam passes through the sample (2), however some is scattered by the particles. The scattered light is measured by the detector (3), which is positioned at 173° from the laser beam passing straight through the sample. An attenuator (4) is used to avoid the saturation of detector, reduce the intensity of the beam passing through a strong light scatter, or increase the intensity for a weakly scattering sample. The scattering signal from the detector is passed to a digital processing board known as the correlator (5), whose function is to compare the scattering intensity at successive time intervals to measure the rate at which the intensity is fluctuating. The data from the correlator is then passed onto the computer (6), where the Malvern software analyses the data and derives the hydrodynamic diameter¹⁰.

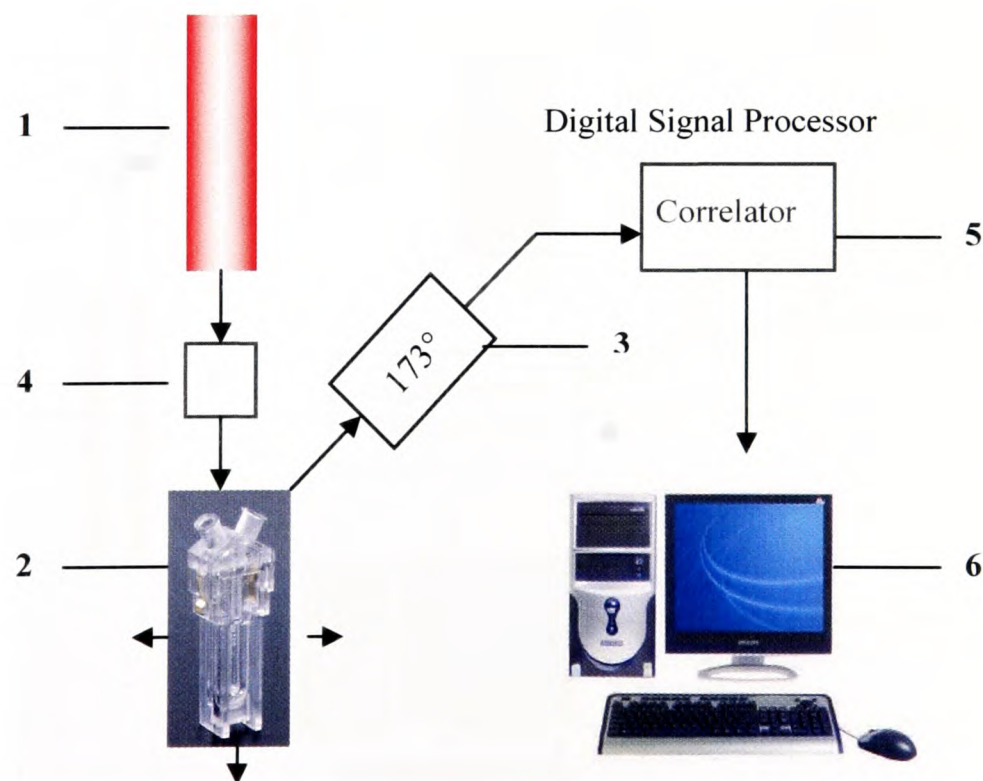


Figure 3.7. The optical arrangement of the Zetasizer Nano ZS. The main components of the instrument are illustrated; the numbered items are described in the text.

3.14.2. ζ -potential measurements of Ag and Au NPs

The optical configuration for the electrophoretic mobility measurements is depicted in Fig.3.8. A He-Ne laser (1) having an exciting wavelength of 633 nm and power of 4 mW was used to illuminate the colloidal NPs. This light source is split to provide an incident and reference beam. The intensity of the reference beam is fixed and is normally between 2000 and 3500 kcp. The incident laser beam passes through the centre of the sample cell (2). The scattering is detected at an angle of 173° (3). When an electric field is applied across the cell, any particles moving through the measurement volume will cause the intensity of light detected to fluctuate with a frequency dependent on the particle speed and this information is passed to a digital signal processor (4) and PC (5). The Zetasizer Nano software produces a frequency spectrum from which the electrophoretic mobility is calculated.

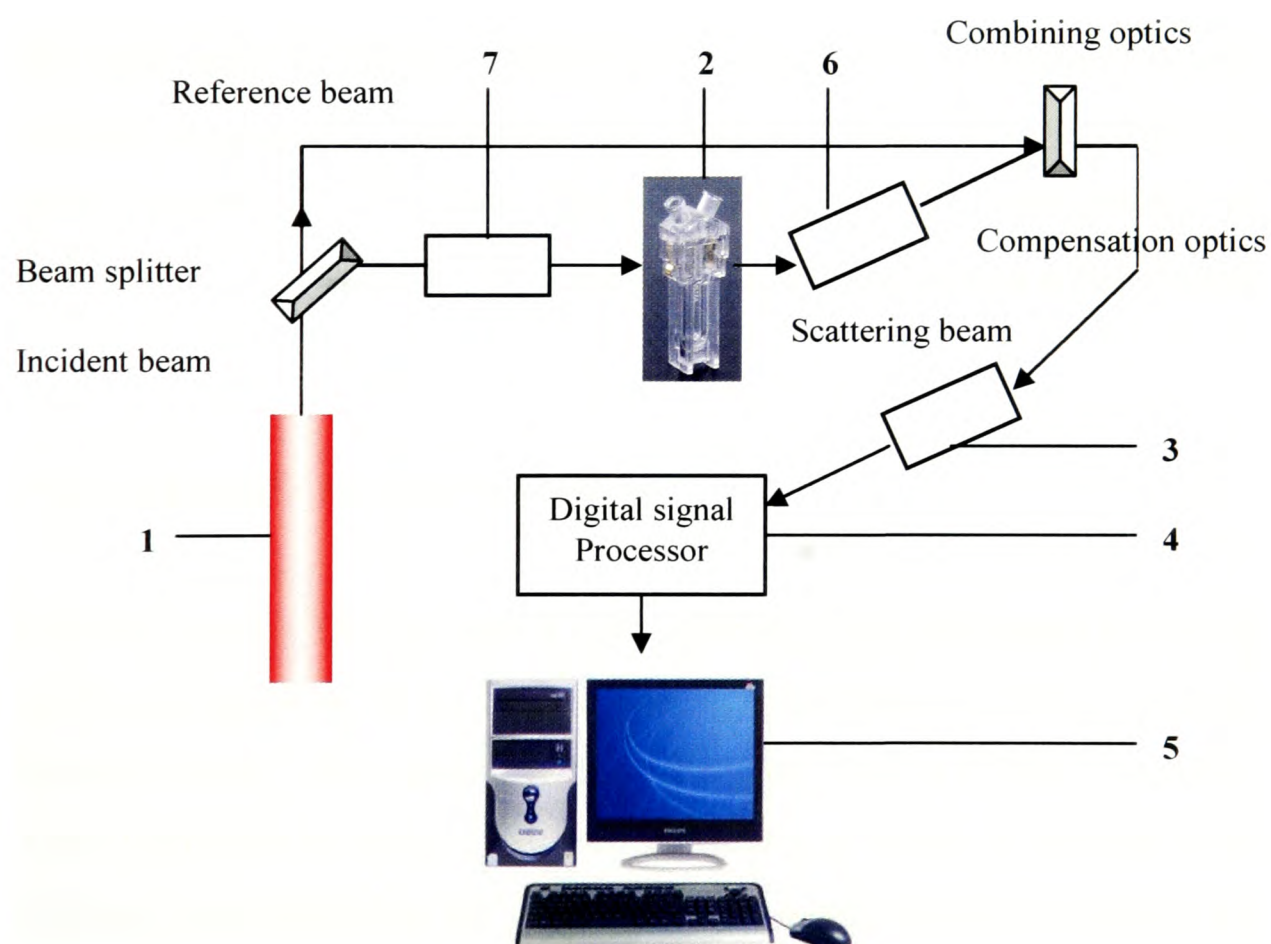


Figure 3.8. Optical configuration of a Malvern Zetasizer Nano instrument for measurement of electrophoretic mobility.

Using the Smoluchowski (aqueous samples) approximation for Henry's function, the dielectric constant of the sample, the viscosity of the liquid phase, and finally the measured electrophoretic mobility, the ζ -potential of the particles within the colloid is calculated. The intensity of the detected, scattered light must be within a specific range for the detector to successfully measure it. For this purpose, an attenuator (6) is employed. Compensation optics (7) are installed for the optimum alignment of the instrument to avoid differences in the cell wall thickness and dispersant refraction¹¹⁻¹².

3.15. *Ab initio* Calculations (Density functional theory (DFT))

Ab initio calculations were performed using the *Gaussian 98* program¹³ on a PC workstation using the hybrid SCF-DFT method B3-LYP, which incorporates Becke's three parameter hybrids functional¹⁴ and the Lee, Yang and Parr correlation functional¹⁵. DFT calculations were performed using the cc-pVTZ basis set¹⁶ in the protonated and deuterated solid state for the three molecules. Geometry optimisation in the case of Rd was conducted assuming C_s symmetry. On the other hand, the two derivatives were computed by assuming C_1 symmetry. Similarly, Rd dimer was computed by employing cc-pVTZ basis set. However, for the dimers of the Rd derivatives a D95 basis set was used.

3.15.1. Normal Coordinate Analysis (NCA)

The vibrational spectra (Raman and FT-IR spectra) were calculated at the optimised geometry. For computation of the potential energy distributions (PEDs) associated with the vibrational modes, the Cartesian force constants obtained from the *Gaussian 98* output were converted to force constants expressed in terms of internal coordinates. Scaling factors were applied to the force constants before input to a normal coordinate analysis program derived from those of Schachtsneider¹⁷. A full set of internal coordinates, including all bond angles and torsional angles, was reduced to a set of $3N-6$ symmetry-adapted internal coordinates, by construction of local symmetry coordinates where appropriate, e.g. for methyl and methylene groups and also for the in-plane and

out-of-plane deformations of the heterocyclic five-membered ring¹⁸. Scaling is necessary to match the calculated harmonic vibrations with the observed vibrations, which are anharmonic. Scaling of force constants, expressed in internal coordinates, was applied according to the following formula:

$$f_{ij}^{scaled} = f_{ij}^{calc} \sqrt{s_i s_j}$$

where s_i and s_j are scale factors relating to internal coordinates i and j . In these calculations the scale factors were as follows:

	Rd and derivatives	Rd dimer	Dimers of Rd derivatives
Basis set	cc-pVTZ	cc-pVTZ	D95
Vibration	Scale factors		
NH str	0.90	0.90	0.90
CH str	0.90	0.92	0.92
C=O str	0.92	0.905	0.905
C=C str	n/a	0.86	0.86
other str	0.97	0.97	0.97
NH def	0.92	0.92	0.92
CH def	0.95	0.95	0.95
other def	0.98	0.97	0.97

IR and Raman intensities were computed from the dipole and polarizability derivatives of the *Gaussian 98* output. Since the dipole and polarizability derivatives are expressed in terms of Cartesian coordinates they were transformed to internal coordinates and subsequently to normal coordinates. Scaling of force constants causes some redistribution of internal coordinates within the normal coordinates and therefore also some small changes in IR and Raman intensities with respect to those listed in the *Gaussian 98* output.

3.16. UV/vis Absorption Spectroscopy

Electronic absorption spectra were obtained using a Varian Inc., Cary 100 Bio UV-visible spectrophotometer. Ag and Au colloids were diluted (1:10) using deionized water. The preparation of samples was the same as that described above for SERS studies.

3.17. Transmission Electron Microscopy (TEM)

The size measurement of Ag colloid was carried out by Dr George Fern and Dr Ian Slipper at the School of Science, University of Greenwich, using a JEOL JEM 200CX TEM at a magnification of 50,000. The size measurement was obtained by placing 10 μ L aliquot of the dispersion onto the carbon coated copper grids of the instruments and allowing them to dry. The micrograph negatives were scanned onto a PC using a backlit scanner. TEM measurements revealed a mean diameter of 55 nm.

3.18. References

- [1] Labram User Manual, ISA, Dilor, Jobin Yvon, France, (1998).
- [2] CCD Detection User Manual, Spectrum One, (1996).
- [3] C. Rodger, W. E. Smith, G. Dent and M. Edmondson, *J. Chem. Soc. Dalton Trans.*, **5**, (1996), 791.
- [4] P. C. Lee and D. Meisel, *J. Phys. Chem.*, **86**, (1982), 3391.
- [5] C. H. Munro, W. E. Smith, D. R. Armstrong and P. C. White, *J. Phys. Chem.*, **99**, (1995), 879.
- [6] L. E. Camefeita, S. Sanchez-Cortez and J. V. Garcia-Ramos, *J. Raman. Spectrosc.*, **24**, (1993), 745.
- [7] J. D. Womack, T. J. Vickers and C. K. Mann, *Appl. Spectrosc.*, **41**, (1987), 117.
- [8] Text, courtesy of Perkin-Elmer, UK.
- [9] Photo and diagram courtesy of Perkin-Elmer, UK.
- [10] Particle sizing by DLS for the Zetasizer Nano series and HPPS training courses, presentation from Malvern website, www.malvern.co.uk
- [11] Zetasizer Nano series, user manual, (2005).
- [12] Zetasizer Nano technical note, www.malvern.co.uk
- [13] Gaussian 98, Revision A.6, M. J. Frisch, G. W. Trucks, H. B. Schlegel, G. E. Scuseria, M. A. Robb, J. R. Cheeseman, V. G. Zakrzewski, J. A. Montgomery, Jr., R. E. Stratmann, J. C. Burant, S. Dapprich, J. M. Millam, A. D. Daniels, K. N. Kudin, M. C. Strain, O. Farkas, J. Tomasi, V. Barone, M. Cossi, R. Cammi, B. Mennucci C. Pomelli, C. Adamo, S. Clifford, J. Ochterski, G. A. Petersson, P. Y. Ayala, Q. Cui, K. Morokuma, D. K. Malick, A. D. Rabuck, K. Raghavachari, J. B. Foresman, J. Cioslowski, J. V. Ortiz, B. B. Stefanov, G. Liu, A. Liashenko, P. Piskorz, Komaromi, R. Gomperts, R. L. Martin, D. J. Fox, T. Keith, M. A. Al-Laham, C.Y. Peng, A. Nanayakkara, C. Gonzalez, M. Challacombe, P. M.W. Gill, B. Johnson, W. Chen, M. W. Wong, J. L. Andres, C. Gonzalez, M. Head. Gordon, E. S. Replogle, and J. A. Pople, Gaussian, Inc., Pittsburgh PA, (1998).
- [14] A. D. Becke, *J. Chem. Phys.*, **98**, (1993), 5648.
- [15] C. Lee, W. Yang and R. G. Parr, *Phys. Rev. B* **37**, (1988), 785.

- [16] T. H. Dunning Jr., *J. Chem. Phys.*, **90**, (1989), 1007.
- [17] J. A. Schachtschneider, *Vibrational Analysis of Polyatomic Molecules*, Parts V and VI, Technical Report Nos. 231 and 57, Shell Development Co., Houston TX, (1964) and (1965).
- [18] P. Pulay, G. Fogarasi, F. Pang and J. E. Boggs, *J. Am. Chem. Soc.*, **101**, (1979), 2550.

Chapter Four

DFT Calculations and Vibrational Spectroscopic Investigations of Rhodanine and its Derivatives in the Solid State

4.1. Introduction

Despite the fact that Rd and its derivatives have been extensively studied there is a paucity of data relating to the vibrational spectroscopic properties of these species. Although, (limited) information can be found regarding the infrared (IR) spectra of Rd and its derivatives, the reports lack detailed assignments of vibrational bands¹⁻². Accordingly, in the present work, detailed Raman ($\lambda_0 = 632.8$ nm) and IR studies have been carried out for Rd, H₂NRd and MeRd, in the solid state, for both protonated and deuteriated species. The vibrational studies of deuteriated species have revealed a very interesting feature of these molecules. Not only are the protons of the N-H and NH₂ groups subject to deuteration, but also the protons of the methylene group. The foregoing discovery is also supported by NMR data (Appendix: Figs.1.3-1.6). The theoretical evaluation of vibrational spectra in terms of vibrational band assignments has been performed by utilization of *ab initio* calculations. The structures (for the isolated molecules in the gaseous state) and vibrational spectra of the three molecules have been computed employing density functional theory (DFT), in conjunction with the cc-pVTZ basis set. Of the three molecules, only the crystal structure of Rd has previously been determined by X-ray crystallography³.

4.2. Experimental

4.2.1. Chemical Reagents

See section, 3.1 in Chapter three.

4.2.2. Vibrational Spectroscopy

See sections, 3.2, 3.3, and 3.4, in Chapter three.

4.2.3. *Ab initio* Calculations

See sections 3.15, and 3.15.1, in Chapter three.

4.3. Results and Discussion

4.3.1. Geometry Optimization

The atom numbering schemes for Rd, H₂NRd, and MeRd are shown in Fig.4.1 and the optimized geometry parameters for the three molecules are tabulated in Table 4.1.

The calculated minimum energy structures of H₂NRd and MeRD are planar. The X-ray structure³ of Rd, retrieved from the Cambridge structural database, is compared with the computed molecular geometry in Fig.4.2. Likewise, the calculated bond distances, valence bond angles, and torsional angles for Rd are compared with experimental X-ray structural data in Table 4.1. The calculated minimum energy structure of Rd is planar, which is consistent with the experimental X-ray data. Deviations in the calculated data from the experimental data are found for the bond lengths and dihedral angles of C1-O4, N5-H6, S7-C3, H10-C2, O4-C1-C2, H9-C2-H10, C1-C2-H10, and C1-N5-H6. The C1-O4, N5-H6, and H10-C2 bonds are 0.02, 0.06 and 0.01 Å shorter, respectively, whereas S7-C3 is 0.02 Å higher in the calculated data. The calculated dihedral angles for O4-C1-C2, H9-C2-H10, C1-C2-H10, and C1-N5-H6 are 1.55, 18.32, 17.13, and 12.97° higher, respectively compared to the experimental data. The other major difference between the calculated and experimental geometry of Rd is that the latter shows the N-H moiety to be out of plane. Slight differences can also be observed between the calculated and experimental ring torsional angles, but on the whole there is a good correlation between experimental and calculated data. The aforementioned deviations in the calculated geometry in relation to the experimental could be attributed to resonance effects; a significant positive charge would be expected to reside on the nitrogen atom making the attached hydrogen atom acidic in nature. Likewise, a considerable negative charge will reside on the S8 atom while a smaller positive charge will be found on S7 and a small negative charge on O2 (see appendix Fig.1.7 for the possible resonating structures of Rd). The lone pair on the sulphur atom (S7, in the ring) conjugates with the C=S (thiocarbonyl) which is an inevitable consequence of the double bond character of S7-C3. The lone pair on the nitrogen atom can conjugate with C=O and/or C=S groups, so each of these two functional groups has a bond length shorter than the calculated values. The only functionality which is not involved in any resonating structure in the molecule is the methylene moiety. This is supported by both experimental and calculated data. For example, the bond length for S7-C2 is higher in relation to that of S7-C3 which agrees very well with the expected single bond length. It is worth noting that the calculated structure is based on a single molecule in the gas phase and does not take into account intermolecular forces such as hydrogen bonding, which are present in the solid state.

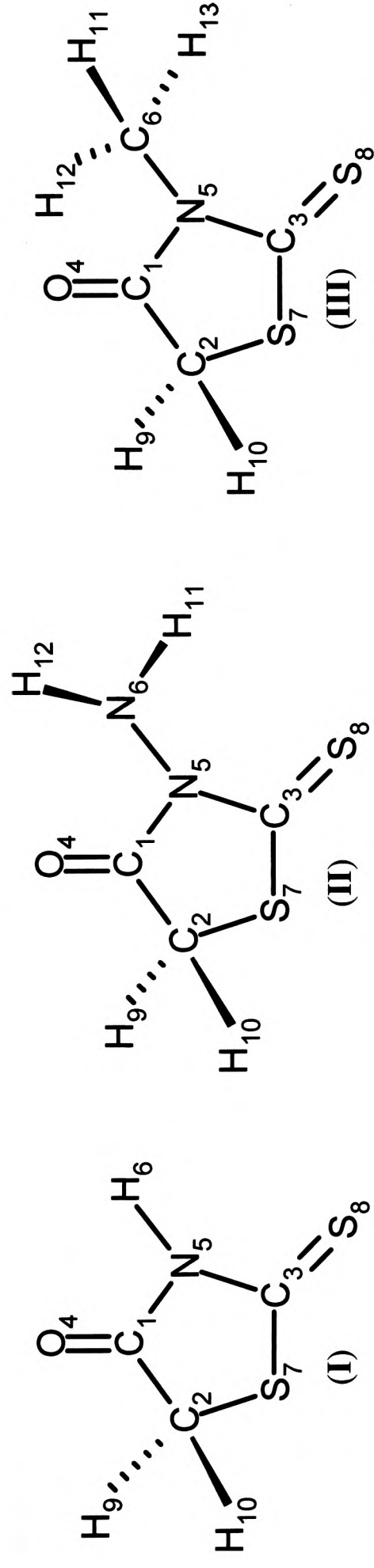


Figure 4.1. Schematic representation showing the chemical structure and atom number labelling used in normal coordinate analysis (NCA) for Rd (I), H₂NRd (II), and MeRd (III).

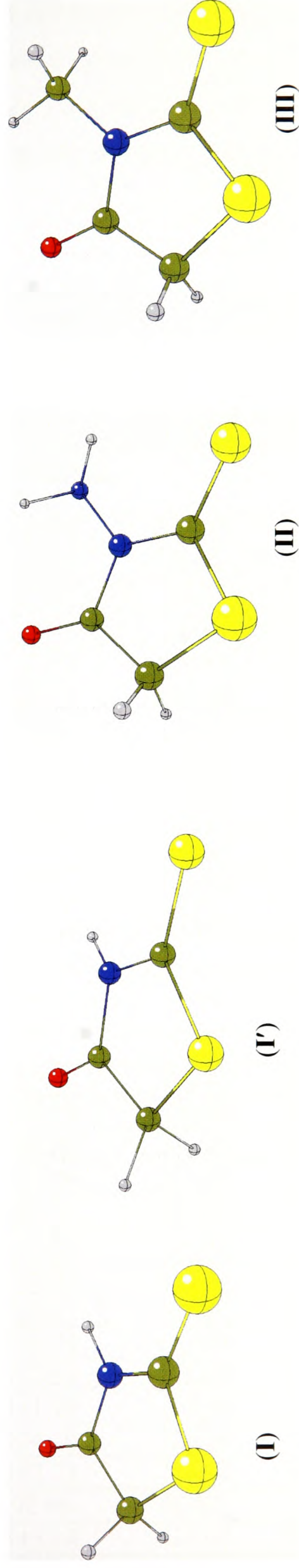


Figure 4.2. The computed molecular geometries at cc-pVTZ/B3LYP level (in gas phase) of: Rd (I), H₂NRd (II), and MeRd (III); together with the X-ray crystallographic structure of Rd (I').

Furthermore, there are four molecules per unit cell in the crystal structure of Rd³. The molecule in the plane forms a pair with the related molecule via a center of symmetry in the same plane. The two molecules interact via hydrogen bonding between N-H and C=O moieties. The other two molecules lie in the symmetry related plane (appendix Fig.1.8).

Table 4.1. Comparison of calculated and experimental geometries for Rd together with the calculated geometries for H₂NRd and MeRd. Bond distances are quoted in Å, bond angles and torsion angles in degrees.

Bond distances	Rd		MeRd	H ₂ NRd
	Calc.	(Monoclinic) Expt.		
r(C1-O4)	1.2034	1.2268	1.2056	1.2078
r(C2-H9)	1.0883	1.0954	1.0883	1.0887
r(C2-C1)	1.5211	1.5112	1.5165	1.5122
r(C3-N5)	1.3726	1.3719	1.3766	1.3679
r(N5-C1)	1.3860	1.3767	1.3944	1.3864
r(N5-X ^a 6)	1.0105	1.0791	1.4589	1.4011
r(S7-C2)	1.8281	1.8192	1.8212	1.8266
r(S7-C3)	1.7639	1.7433	1.7628	1.7639
r(S8-C3)	1.6356	1.6440	1.6396	1.6418
r(H10-C2)	1.0883	1.0999	1.0883	1.0880
r(H11-C6)			1.0880	
r(C6-H13)			1.0880	
r(C6-H12)			1.0854	
r(N6-H11)				1.0174
r(N6-H12)				1.0158
r(N5-N6)				1.4011
Interbond angles				
θ(O4-C1-C2)	125.43	123.88	124.25	126.29
θ(O4-C1-N5)	124.46	123.81	124.30	123.00
θ(H9-C2-C1)	109.44	106.09	109.29	109.49
θ(H9-C2-S7)	111.11	111.89	111.30	110.96
θ(H9-C2-H10)	108.73	90.41	108.69	108.82
θ(C2-C1-N5)	110.11	112.31	111.44	110.71
θ(C1-C2-S7)	106.98	106.27	106.92	106.95
θ(C1-C2-H10)	109.44	126.57	109.29	109.64
θ(C3-N5-C1)	120.22	116.94	117.82	119.34
θ(C3-N5-X6)	119.59	132.39	121.82	121.82
θ(N5-C3-S7)	109.45	111.76	110.88	110.01
θ(N5-C3-S8)	125.65	124.10	126.08	125.26
θ(C1-N5-X6)	120.19	107.22	120.36	118.79
θ(C2-S7-C3)	93.24	92.68	92.93	92.88
θ(S7-C2-H10)	111.11	113.88	111.30	110.95

$\theta(\text{S7-C3-S8})$	124.89	124.14	123.04	124.72
$\theta(\text{N5-C6-H13})$			109.87	
$\theta(\text{N5-C6-H12})$			107.20	
$\theta(\text{N5-C6-H11})$			109.87	
$\theta(\text{H13-C6-H12})$			110.66	
$\theta(\text{H13-C6-H11})$			108.58	
$\theta(\text{H12-C6-H11})$			110.66	
$\theta(\text{N5-N6-H11})$				106.77
$\theta(\text{N5-N6-H12})$				106.58
$\theta(\text{H11-N6-H12})$				111.55
Torsional angles				
$\tau(\text{O4-C1-C2-H9})$	59.53	-61.3125	59.41	62.77
$\tau(\text{O4-C1-C2-S7})$	180.00	179.4535	180.00	-176.93
$\tau(\text{O4-C1-C2-H10})$	-59.53	41.5886	-59.41	-56.55
$\tau(\text{O4-C1-N5-C3})$	180.00	179.3632	180.00	175.69
$\tau(\text{O4-C1-N5-X6})$	0.00	17.6830	0.00	-6.81
$\tau(\text{H9-C2-C1-N5})$	-120.47	117.9236	-120.59	-117.81
$\tau(\text{H9-C2-S7-C3})$	119.40	-113.7148	119.29	118.58
$\tau(\text{S7-C2-C1-N5})$	0.00	-1.3104	0.00	2.49
$\tau(\text{H10-C2-C1-N5})$	120.47	-139.1753	120.59	122.87
$\tau(\text{C2-C1-N5-C3})$	0.00	0.1265	0.00	-3.75
$\tau(\text{C2-C1-N5-X6})$	180.00	-161.5537	180.00	173.75
$\tau(\text{C1-C2-S7-C3})$	0.00	1.6518	0.00	-0.78
$\tau(\text{S7-C3-N5-C1})$	0.00	1.2154	0.00	3.10
$\tau(\text{S8-C3-N5-C1})$	180.00	-179.1038	180.00	-176.13
$\tau(\text{S7-C3-N5-X6})$	180.00	157.2313	180.00	-174.32
$\tau(\text{S8-C3-N5-X6})$	0.00	-23.0879	0.00	6.45
$\tau(\text{N5-C3-S7-C2})$	0.00	-1.6841	0.00	-1.12
$\tau(\text{H10-C2-S7-C3})$	-119.40	145.5509	-119.29	-120.32
$\tau(\text{C2-S7-C3-S8})$	180.00	178.6352	180.00	178.11
$\tau(\text{C3-N5-C6-H13})$			59.70	
$\tau(\text{C3-N5-C6-H12})$			180.00	
$\tau(\text{C3-N5-C6-H11})$			-59.70	
$\tau(\text{H13-C6-N5-C1})$			-120.30	
$\tau(\text{H12-C6-N5-C1})$			0.00	
$\tau(\text{H11-C6-N5-C1})$			120.30	
$\tau(\text{C1-N5-N6-H11})$				152.54
$\tau(\text{C1-N5-N6-H12})$				33.20
$\tau(\text{C3-N5-N6-H11})$				-30.03
$\tau(\text{C3-N5-N6-H12})$				-149.37

^aX = H, N or C for Rd, H₂NRd, and MeRd, respectively

4.3.2. Vibrational Spectroscopic Assignments

Simulated IR and Raman spectra, calculated by convolution with a Lorentzian lineshape (full-width-half-maximum = 10 cm^{-1}), are compared with the solid state experimental data (Raman $\lambda_0 = 632.8\text{ nm}$) for the Rds and their deuteriated derivatives, in Figs. 4.3-4.8. The scaled vibrational wavenumbers, together with their PEDs are compared with the experimental data for protonated Rd, H₂NRd and MeRd in Tables 4.2, 4.4, and 4.6, and with the deuteriated species in Tables 4.3, 4.5, and 4.7, respectively. Generally, the calculated (simulated) spectral profiles show good agreement with the experimentally derived spectra. However, differences are highlighted with respect to the discrepancies involved with calculated bond lengths, as mentioned above. Some of the vibrational modes associated with the N-H group are subject to slight errors. Generally, the calculated PEDs are less accurate for predicting modes with N-H group due to hydrogen bonding involving these groups. The vibrational band assignments have been made on the basis of comparison with previous literature values for other cyclic *cis* amide/thioamide moieties, group frequency considerations, comparisons of protonated and deuteriated samples and with reference to the calculated wavenumbers for Rd and its derivatives.

The 3N-6 rule suggests that Rd, H₂NRd, and MeRd should display 24, 30, and 33 internal vibrational bands, respectively. The computed structure for Rd has C_s symmetry, therefore in-plane (ip) and out-of-plane (op) modes are designated as A' and A'', respectively. As expected, the Raman and IR results also show that the rule of mutual exclusion does not hold for these three molecules because they lack a centre of symmetry.

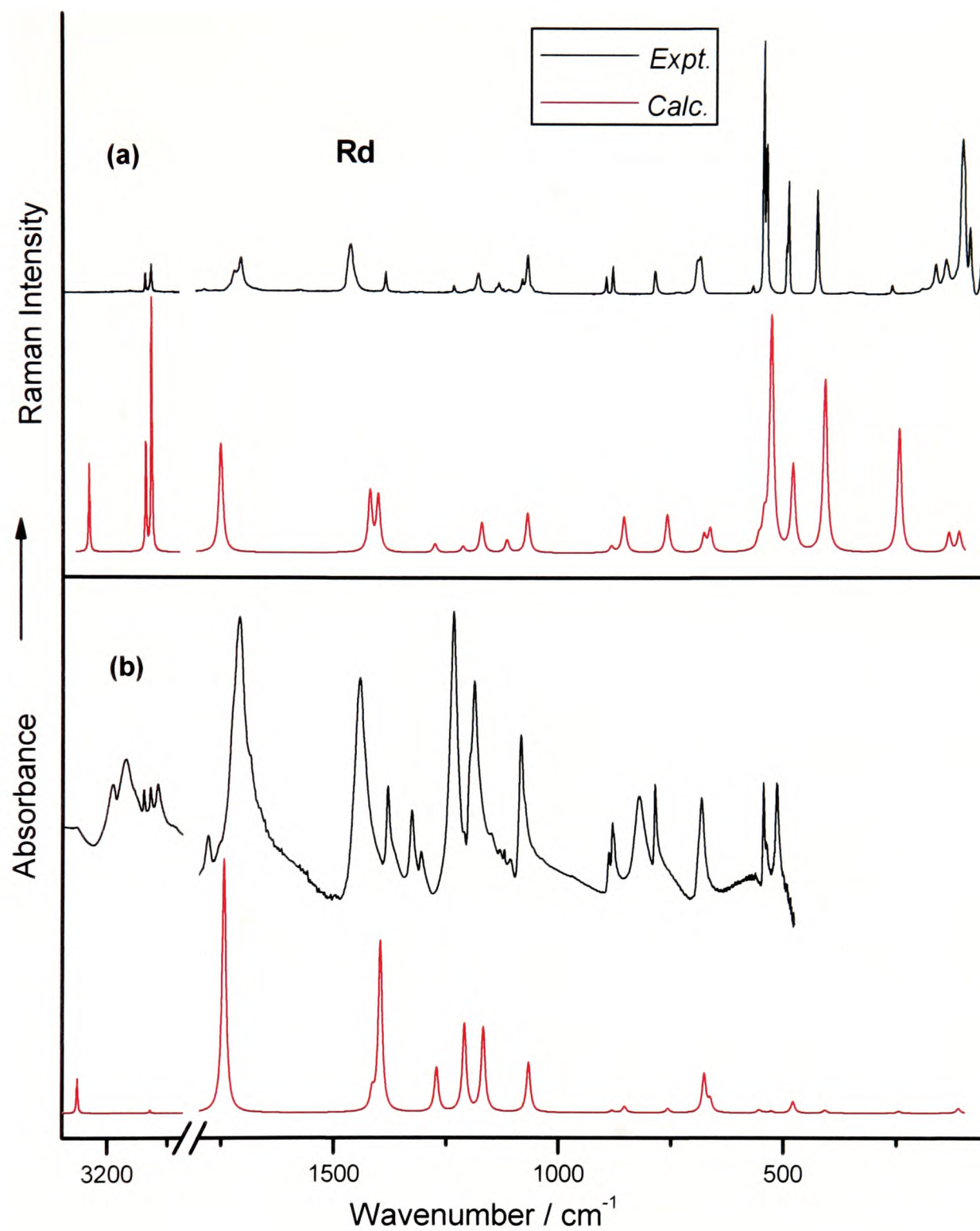


Figure 4.3. Experimental and calculated (a) Raman and (b) IR spectra for Rd (protonated).

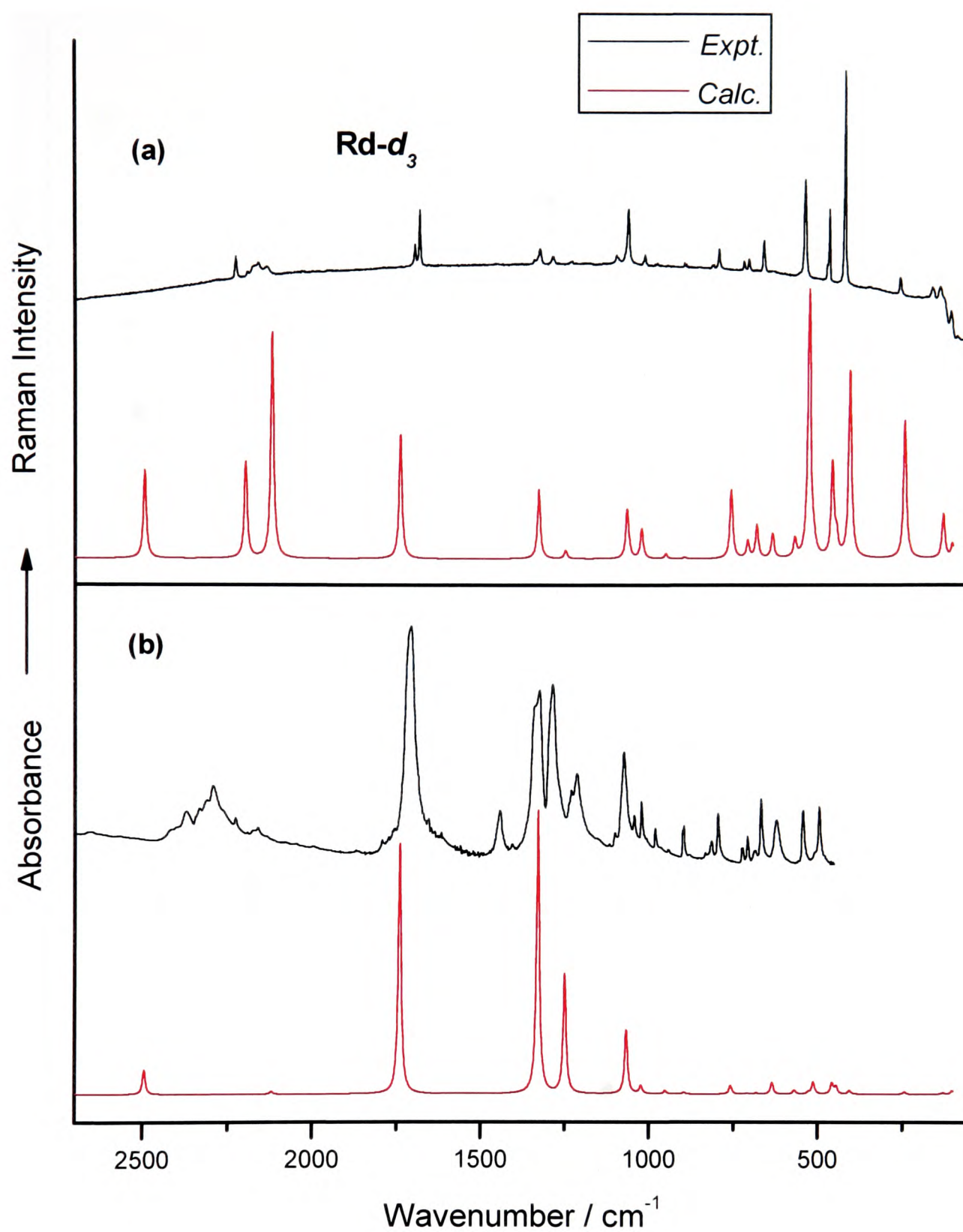


Figure 4.4. Experimental and calculated (a) Raman and (b) IR spectra for Rd (deuteriated).

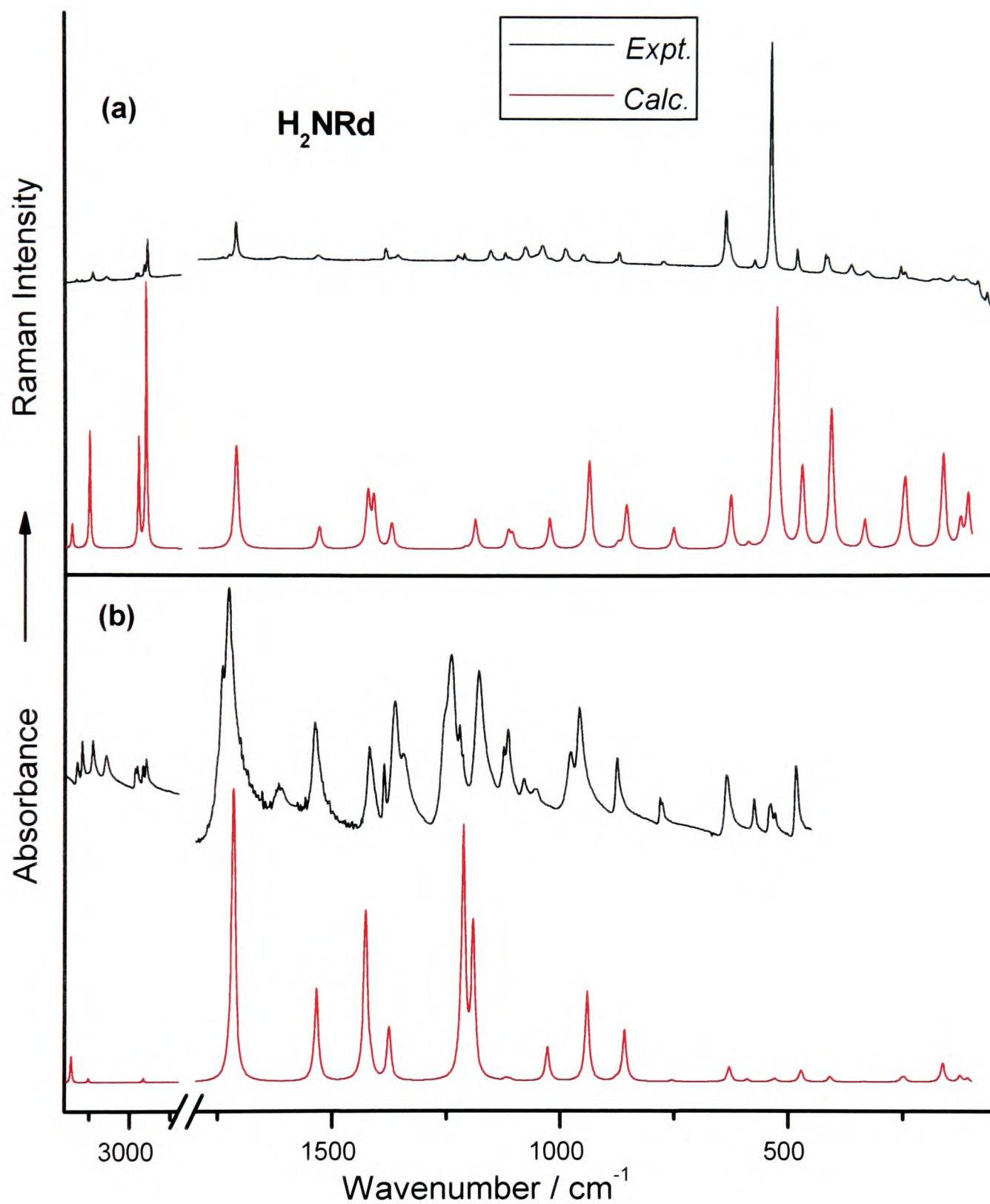


Figure 4.5. Experimental and calculated (a) Raman and (b) IR spectra for H_2NRd (protonated).

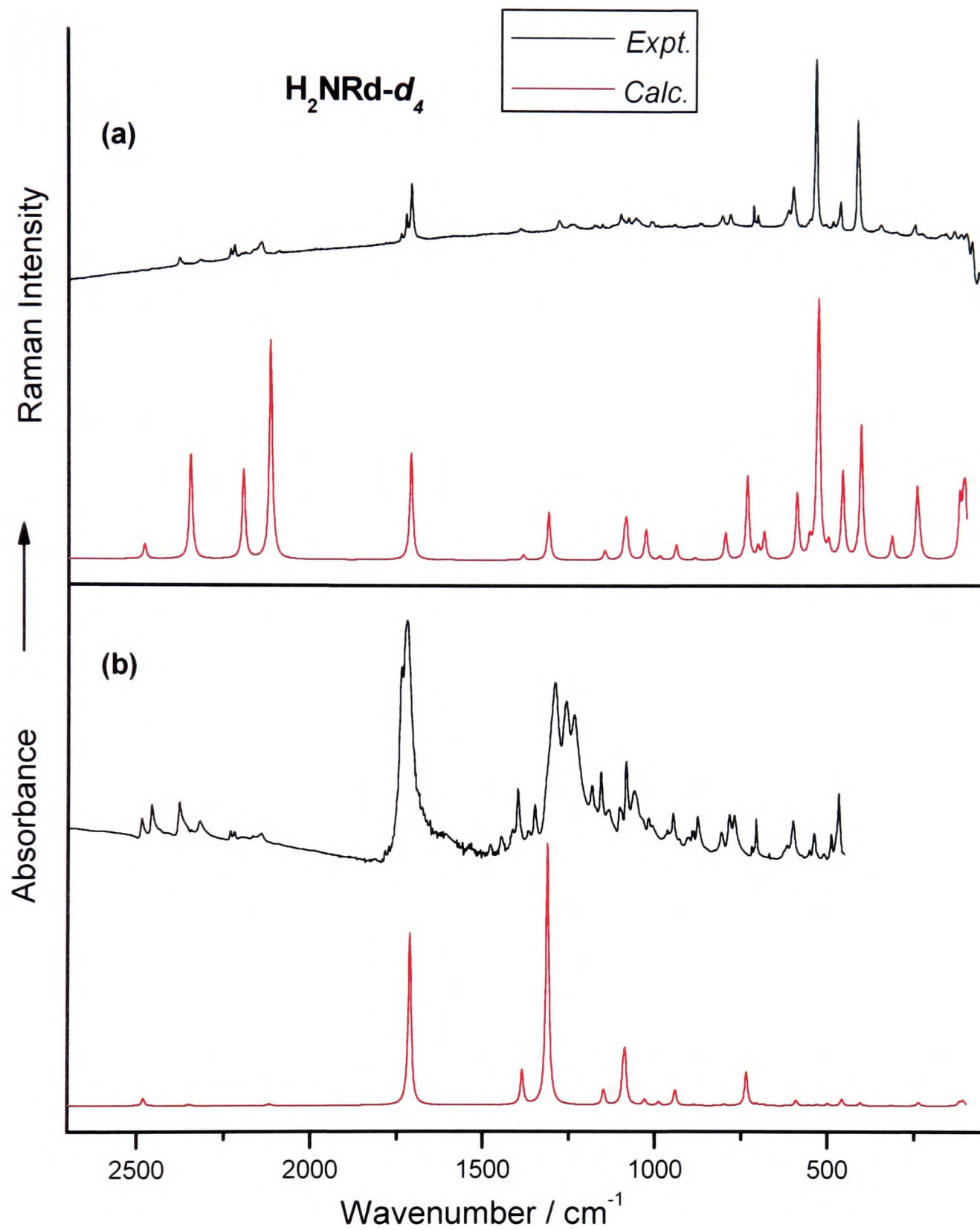


Figure 4.6. Experimental and calculated (a) Raman and (b) IR spectra for H_2NRd (deuteriated).

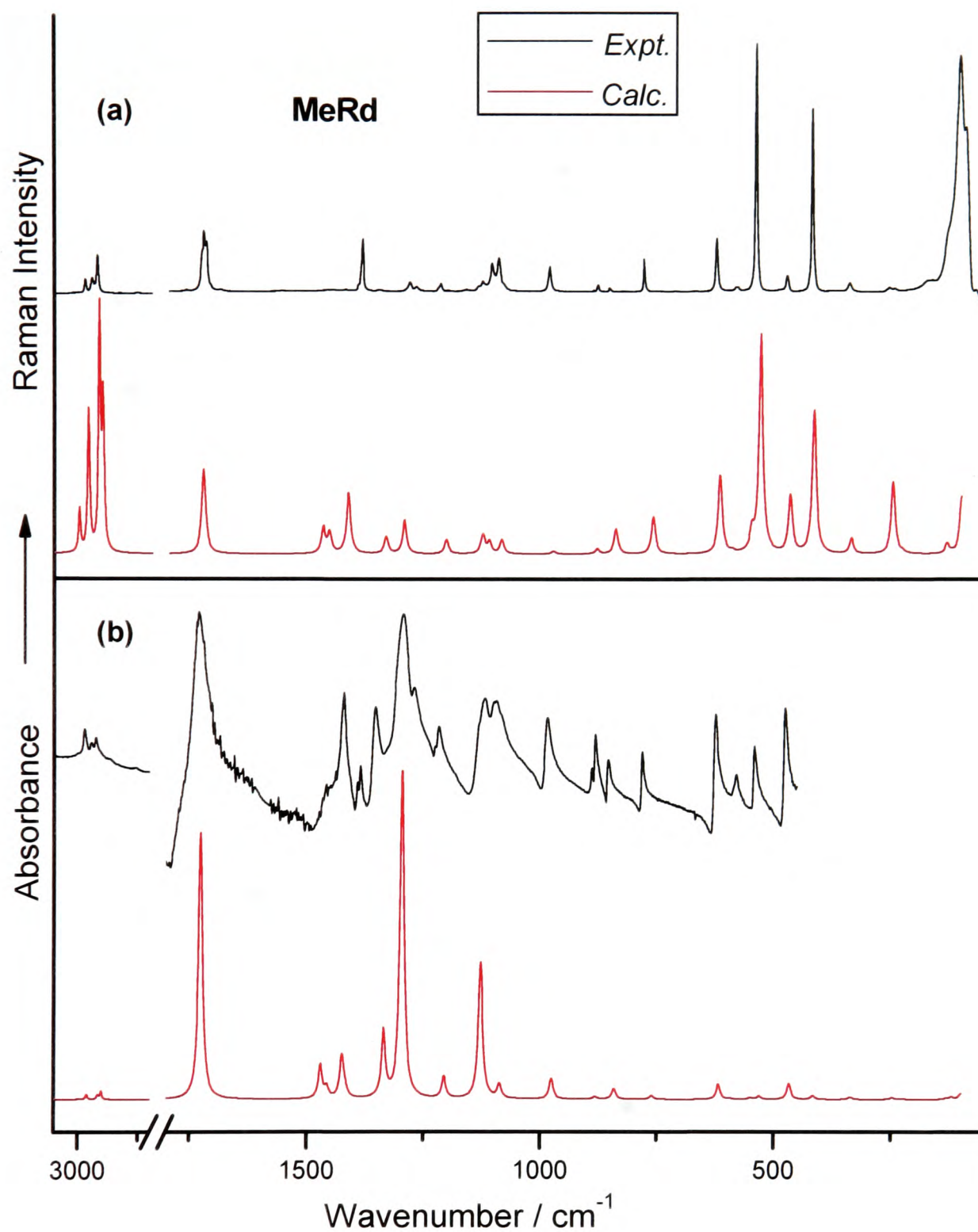


Figure 4.7. Experimental and calculated (a) Raman and (b) IR spectra for MeRd (protonated).

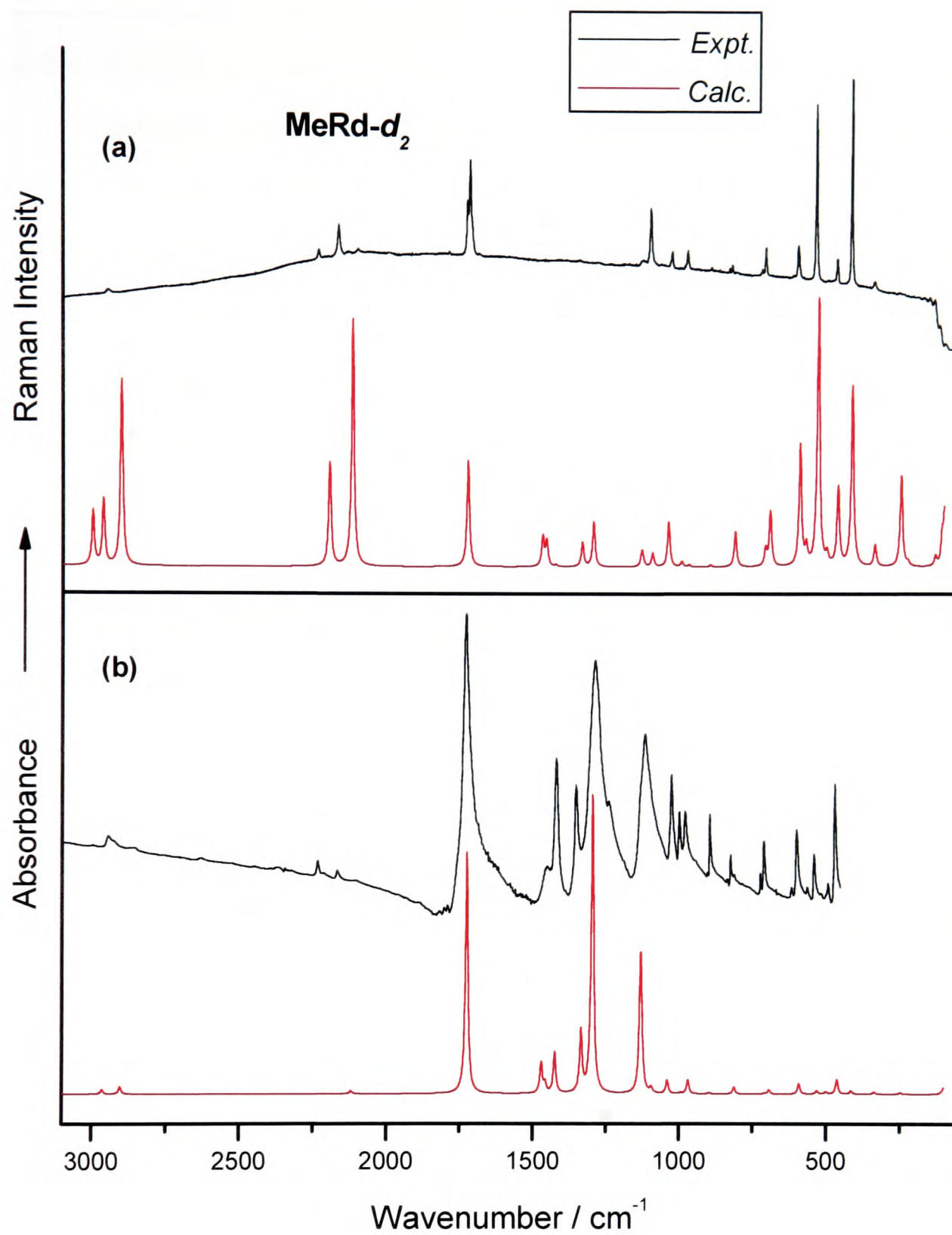


Figure 4.8. Experimental and calculated (a) Raman and (b) IR spectra for MeRd (deuteriated).

4.3.2.1. N-H and NH₂ Vibrations

The vibrations associated with the NH₂ group are usually found in the 3330-3550 cm⁻¹ (asymmetric stretch, ν_{as}) and 3250-3450 cm⁻¹ (symmetric stretch, ν_s) wavenumber regions. It is unlikely that these vibrations are coupled with any other fundamental. Therefore, ν_s is a realistic function of the N-H stretching force constant⁴, and indeed falls close to the value of ν_s (N-H) in related secondary amines and amides. Bellamy and Williams⁵ have developed a relationship relating to the two bands, namely: $\nu_s = 0.876\nu_{as} + 345.5(\text{cm}^{-1})$. This consideration applies to NH₂ groups, where both the N-H bonds are equivalent and does not take into account the relationship between ν (N-H) and bond angle. A different relationship has been described by Kreuger⁶, where ν_s is equated as $1023.3(\text{cm}^{-1}) + 0.682\nu_{as}$. In the present work the latter relationship provides a better fit, with an error of -2 and -4 cm⁻¹ for the Raman and IR spectra, respectively for H₂NRd. The ip N-H bending modes and the resonance stiffened C-N bond stretching modes interact in mono-substituted *trans* amides, giving rise to a strong band at ~1550 cm⁻¹⁷⁻⁸. However, in the case of (cyclic) mono-substituted *cis* amides there is much less interaction between corresponding modes. The *cis*-N-H bending vibration gives rise to a band in the region spanning 1440-1490 cm⁻¹.

For Rd, the band at 3079 cm⁻¹ (in both Raman and IR spectra) is assigned to an N-H stretch; this band is more intense and broader in the IR spectrum. The calculated value for the aforementioned band is 3402 cm⁻¹. The apparent discrepancy is the inevitable consequence of hydrogen bonding in the solid state, which complements the reported X-ray structure, where the N-H moiety is involved in hydrogen bonding. A weaker band - at 3165 and 3176 cm⁻¹ in the Raman and IR spectra, respectively - can be assigned to a combination of C=O and N-H deformation modes. A strong band at 1457 cm⁻¹ in Raman, and the relatively more intense band at 1442 cm⁻¹ in IR, appears to be due to a vibration of mixed character, involving contributions from ip N-H deformation (47 %) and C3N5 stretch (27%). Similarly, a strong band at 685 cm⁻¹ in Raman (681 cm⁻¹ in the IR spectrum) is assigned to an op N-H deformation mode. After deuteration, the N-D stretch is shifted towards lower wavenumber and appears

at 2282 cm^{-1} in the Raman spectrum, and at 2292 cm^{-1} in the IR spectrum. Subsequently, bands associated with ip and op N-D deformation modes are also shifted downward. According to the calculated PEDs, these vibrations also have contributions from other types of motion. For example, the band at 1326 cm^{-1} in Raman, and 1327 cm^{-1} in IR, has much less N-H (13 %) character and is assigned to a vibration which has a contribution (~59%) from a C3-N5 stretch.

For H_2NRd the ν_s and ν_{as} NH_2 modes are observed at 3295 and 3328 cm^{-1} in the Raman spectrum, whereas their counterparts in the IR spectrum are located at 3295 and 3325 cm^{-1} , respectively. In the calculated spectra, the bands at 3256 and 3362 cm^{-1} are associated with the corresponding modes. However, two additional bands are present in this region at 3149 and 3233 cm^{-1} in both Raman and IR spectra, which could be assigned to a combination band of the C=O stretching and NH_2 bending modes and an overtone of the 1539 cm^{-1} band, respectively⁹. A strong band at 1539 cm^{-1} in the IR, and relatively weak band at 1535 cm^{-1} in the Raman spectrum is assigned to an ip NH_2 deformation mode. The bands at 954 and 977 cm^{-1} in the Raman and IR spectra, respectively are assigned to the op NH_2 deformation mode but with a contribution (13 %) from C-C stretching. This band is more intense in Raman than its counterpart in the IR spectrum. After deuteration, the corresponding modes have been shifted towards the lower wavenumber region. The bands at 2380 and 2490 cm^{-1} in Raman (2378 and 2487 cm^{-1} in the IR spectra) are assigned to the ν_s and ν_{as} NH_2 stretching modes, respectively. It is worth noting that additional bands are observed in the 1157-1291 cm^{-1} region in the IR spectrum of the deuteriated species compared to the Raman spectrum. For example, bands at 1234 and 1257 cm^{-1} present in the IR spectrum are absent in the Raman spectrum. The calculated PEDs reveal that the band at 1158 cm^{-1} , in both Raman and IR spectra, is attributable to a vibration that is quite mixed and involves coupling of ip NH_2 deformation with N-N stretching. The op NH_2 deformation mode has been shifted to lower wavenumber and is located at 720 and 783 cm^{-1} in Raman and IR spectra, respectively; which is in good agreement with the calculated values. The band is more intense in the IR spectrum.

4.3.2.2. CH₂ and CH₃ Vibrations

The ν_s and ν_{as} CH₃ vibrations are found in the 2880-2950 cm⁻¹ region and can be differentiated from the comparable CH₂ vibrations at about 2865-2915 cm⁻¹. The symmetric NCH₃ bending¹⁰ mode gives rise to a band at 1410 ± 20 cm⁻¹ and CH₂ bending modes are located at ~1440 cm⁻¹. The CH₂ wagging, twisting, and rocking modes are not independent CH₂ motions; all are coupled to various degrees with other types of motion.

For Rd, ν_s and ν_{as} vibrations of the CH₂ group appear as bands at 2916 and 2960 cm⁻¹ in Raman (2915 and 2963 cm⁻¹ in IR spectra, respectively). The band at 1380 cm⁻¹, in both Raman and IR, is assigned to a CH₂ deformation mode. The bands at 568 and 893 cm⁻¹ in Raman, and 880 cm⁻¹ in the IR spectra, are associated with CH₂ rocking coupled with other types of motion. For example, the band at 893 cm⁻¹ is assigned to a vibration which also involves CH₂ torsion. After deuteration, the ν_{as} C-D stretch is shifted to lower wavenumber, appearing at 2191 and 2174 cm⁻¹ in Raman and IR spectra, respectively. The corresponding symmetric stretching modes are observed at 2133 and 2160 cm⁻¹ in Raman and IR spectrum, respectively. The C-D deformation modes are located at 976 and 1016 cm⁻¹ in Raman; and at 1021 and 1041 cm⁻¹ in the IR spectra. The calculated PEDs suggest that these vibrations involve other types of motion. The CH₂ rocking mode also shows a deuterium shift, appearing at 706 and 705 cm⁻¹ in Raman and IR spectra, respectively.

In spectra of H₂NRd, three bands are found in the region spanning 2904-2960 cm⁻¹. The two bands observed at 2924 and 2960 in Raman (2921 and 2957 cm⁻¹, respectively in the IR spectrum) are assigned to ν_s and ν_{as} CH₂ modes. For the deuteriated species, the corresponding C-D₂ stretching modes are found at 2167 and 2194 cm⁻¹ in Raman (2167 and 2198 cm⁻¹ in the IR spectra, respectively). The assignment of a third band at ~ 2904 cm⁻¹ is ambiguous. It might be an overtone or a combination band, whose intensity is enhanced by Fermi resonance. This band is also shifted towards lower wavenumber upon deuteration and observed at 2144 and 2142 cm⁻¹ in Raman and IR spectra, respectively. The CH₂ deformation mode is observed as a medium intensity band at 1387 cm⁻¹ in both Raman and IR spectra. The

two medium intensity bands at 1082 and 1158 cm^{-1} in Raman spectra are assigned to CH_2 torsional and wagging modes, respectively. Their counterparts in the IR spectrum are observed at 1080 and 1179 cm^{-1} , although the former band is more intense in the IR spectrum. After deuteration, two additional bands are observed in the 1012-1061 cm^{-1} region, where only one band should appear due to CD_2 bending. However, the calculated PEDs suggest that bands at 1061 cm^{-1} (Raman) and 1058 cm^{-1} (IR) could be assigned to CD_2 deformation. It is evident, especially in the IR spectrum, that total deuteration has not been achieved, as there are still some N-H, C-H stretching and CH_2 deformation modes (*very weak in intensity*), post-deuteration. Repeated deuteration did not improve this situation. The CD_2 rocking and wagging modes are observed at 875, 707, and 997 cm^{-1} in Raman and 892, 707, and 1002 cm^{-1} in IR spectra, respectively. The observed values are in good agreement with calculated values. The quantum mechanical calculations predict, however, that these vibrations exhibit various degrees of coupling with other types of motion.

In this study deuteration offers a method to clearly discriminate between the bands associated with CH_2 and CH_3 vibrations. In MeRd, three bands are located in the C-H stretching region. The two bands at 2925 and 2974 cm^{-1} in Raman (2924 and 2972 cm^{-1} in the IR spectrum) are tentatively assigned to the ν_s and ν_{as} CH_2 modes, respectively. This assignment is solely based on the results obtained from deuteration studies. Upon deuteration, the corresponding modes are downward shifted and are observed at 2134 and 2167 cm^{-1} in Raman and 2102 and 2167 cm^{-1} in the IR spectra, respectively, which are in good agreement with the calculated values (Table 4.7). The third band, at 2946 cm^{-1} in Raman and at 2943 cm^{-1} in the IR spectrum has not been shifted after deuteration, indicative of a CH_3 stretching mode. In Raman spectra, a strong band at 1385 cm^{-1} is assigned to the CH_2 deformation mode, its counterpart in the IR spectrum is observed at 1391 cm^{-1} . Asymmetric and symmetric CH_3 deformations give rise to a strong band at 1419 cm^{-1} in the IR spectrum and a weak band at 1421 cm^{-1} in the Raman spectrum. The calculated PEDs suggest that a weak band at 1137 cm^{-1} in Raman, and relatively medium intensity band at 1119 cm^{-1} in the IR spectrum, could be assigned to an *op* CH_3 deformation mode. A strong band in the Raman spectrum at 1107 cm^{-1} is attributed to a CH_2 torsional mode, which is absent in the IR spectrum. The CH_2 wagging mode is observed as a weak band at 1217 and

1224 cm^{-1} in the Raman and IR spectra, respectively. The CD_2 deformation modes also show a downward deuterium shift and are observed at 1030 and 1000 cm^{-1} in the Raman and IR spectra, respectively. A weak band at 722 cm^{-1} in both Raman and IR spectra is attributed to a CD_2 torsional mode. The PED calculations show that this vibration involves coupling of CD_2 torsional (53 %) and rocking (36 %) modes. The bands at 538 and 895 cm^{-1} , in both Raman and IR spectra, are also assigned to vibrations which exhibit CD_2 torsional character, to some extent.

4.3.2.3. C=O Vibrations (Amide Group)

The characteristic bands describing the amide carbonyl stretch ($\text{C}=\text{O}$) are usually observed in the 1630-1695 cm^{-1} region. In the IR spectrum of Rd, Enchev *et al.*,² have observed a doublet at 1723 and 1759 cm^{-1} in solution (CHCl_3) and only one band at 1711 cm^{-1} in the solid state. They attributed this effect to resonance phenomena. In the current study, three bands are observed at 1699, 1713, and 1779 cm^{-1} in the Raman spectrum of Rd. The first band is weak, the second medium and the third is of relatively higher intensity. Likewise, a weak band at 1779 cm^{-1} and a very strong band at 1709 cm^{-1} in the IR spectrum are attributed to the corresponding modes. Deuteriation has subtle effects on the carbonyl stretching wavenumber in the IR spectrum. For example, the former band is absent and the latter band has not been shifted. However, the Raman spectrum clearly shows a deuterium shift of the order of $\sim 17 \text{ cm}^{-1}$ for the band at 1713 cm^{-1} , which upon deuteriation is of higher intensity; this finding suggests that a N-H stretching mode contributes to this band. In the Raman spectrum of the protonated species, the ip and op $\text{C}=\text{O}$ deformation modes are observed as bands at 427, 489 and 545 cm^{-1} . Their counterparts in the IR spectrum are observed at 515 and 544 cm^{-1} . All these observed bands are of high intensity. The calculated PEDs reveal that these bands are attributed to vibrations that are quite mixed and show a degree of coupling with other motions. For example, bands at 427, 489 and 545 cm^{-1} are assigned to vibrations that have 19, 37 and 29 % contribution from ip and op $\text{C}=\text{O}$ deformation, respectively (Table 4.3). After deuteriation, these bands are shifted downward by $\sim 5 \text{ cm}^{-1}$.

For H₂NRd, a strong band at 1716 cm⁻¹ and two weak bands at 1730 and 1744 cm⁻¹ in the Raman spectrum are assigned to the carbonyl stretching mode. In the deuteriated species, the band at 1716 cm⁻¹ has been red-shifted by ~ 5 cm⁻¹ and the weak band at 1744 cm⁻¹ has disappeared. Nevertheless, the band at 1730 cm⁻¹ increases in intensity and is shifted downward by ~ 4 cm⁻¹. The corresponding bands in the IR spectrum are located at 1612 and 1727 cm⁻¹. Upon deuteration the former band disappears but the latter shifts to 1720 cm⁻¹. The bands attributed to ip and op C=O deformations are observed at 422, 648 and 953 cm⁻¹ in the Raman and 634 and 958 cm⁻¹ in the IR spectra, respectively. Upon deuteration, these appear at 419, 577, and 875 cm⁻¹ in Raman and 598 and 895 cm⁻¹ in IR. The calculated values are in good agreement with the experimental values.

For MeRd, two weak bands and one strong band are observed at 1688, 1761, and 1724 cm⁻¹ in the Raman spectrum. A strong band at 1729 cm⁻¹ in the IR spectrum is assigned to the C=O stretch. The bands at 421, 626, and 1107 cm⁻¹ in Raman and 623 cm⁻¹ in the IR spectrum are assigned to the ip C=O deformation mode. The op C=O deformation mode gives rise to bands at 542 and 889 cm⁻¹ in Raman and 539 and 880 cm⁻¹ in the IR spectra. In the deuteriated species the band previously at 1688 cm⁻¹ in the protonated Raman spectrum has disappeared and two bands at 1719 and 1728 cm⁻¹ are assigned to the carbonyl stretching mode. However, only one strong band at 1728 cm⁻¹ is observed in the IR spectrum of the deuteriated species. The observation of additional bands in the carbonyl stretching region is most probably due to factor group splitting resulting from the two in-equivalent molecules in the crystallographic unit cell, and may also involve Fermi resonance. After deuteration, a medium band at 895 cm⁻¹ in both Raman and IR spectra is assigned as the op C=O deformation. The op C=O deformation mode also give rise to a strong band at 538 cm⁻¹ in Raman but a relatively less intense band at 538 cm⁻¹ in the IR spectrum. The calculated PEDs suggest that these vibrations involve various degrees of coupling with other motions but are predominantly of op C=O deformation in character. The bands associated with ip C=O deformation modes are observed at 419 and 468 cm⁻¹ in Raman and IR spectra, respectively.

4.3.2.4. N-C=S Vibrations (Thioamide Group)

The thiocarbonyl (C=S) group does not give rise to a characteristic band, unlike the C=O group. The C=S group is less polar than the C=O group and therefore gives rise to a much weaker band in the IR spectrum. Furthermore, it occurs at much lower wavenumber, where it is much more susceptible to coupling with other types of motion. Identification is therefore more difficult and uncertain in the IR spectrum but it can usually be detected more easily in the Raman spectrum, due to the greater polarizability of the C=S bond. In compounds where the C=S group is adjacent to a nitrogen atom C=S stretching motion is strongly coupled with other types of motion, *e.g.* in thioamides there may be interaction with NH₂ rocking¹¹⁻¹². As a consequence, there are a number of different vibrations, each of which contains a significant contribution from the C=S stretching mode. Assignment of these bands would be difficult if based solely on the group frequency concept and a detailed NCA is, therefore, essential. Thioamides and thiazole have been extensively studied in the past¹³⁻¹⁵ and all of these types of compound show three bands in the following wavenumber regions: 1395-1570; 1260-1420, and 940-1140 cm⁻¹; whilst most thioamides show one other band in the 700-800 cm⁻¹ region; these are normally designated as thioamide I, II, III, and IV modes, respectively. The first two have little C=S stretching involvement, and originate mainly from C=N and N-H deformation modes but the last two both have a significant C=S stretching content.

In Rd, a medium intensity band at 1176 cm⁻¹ and a relatively strong band at 1187 cm⁻¹ followed by a shoulder at 1197 cm⁻¹ are assigned to the thioamide II mode. In the Raman spectrum, two bands are observed at 1066 and 1078 cm⁻¹ instead of the single one expected in this region. The first band is of medium intensity, whereas the second band has a higher intensity. In the IR spectrum, a very strong band is found at 1083 cm⁻¹ followed by a shoulder at 1073 cm⁻¹ which is consistent with a previous study². These bands could be attributed to the thioamide III mode. According to the PED values the bands at 1066 and 1073 cm⁻¹ appear to be assigned to vibrations which are quite mixed, but predominantly involve a C=S stretching (48 %) mode. Another strong band at 427 cm⁻¹ in the Raman spectrum, which is absent in the IR spectrum, is attributed to C=S stretching (15%). In the Raman spectrum a band at 261 cm⁻¹ is assigned to ip C=S deformation and a very strong band at 538 cm⁻¹ is

assigned to a vibration involving *op* C=S and C=O deformations. The latter is much weaker in the IR spectrum, and absent in the spectrum of the deuteriated species. Enchev *et al.*,² have assigned this band to a vibration involving C-N stretching coupled with *ip* ring deformation. Post deuteriation, the bands at 1078 and 1083 cm⁻¹ disappear and only bands at 1064 and 1074 cm⁻¹ remain in the Raman and IR spectra, respectively. The calculated PEDs suggest that these vibrations have 46 % contribution from C=S stretching.

In the case of H₂NRd, the thioamide II vibration is attributed to the band at 1158 cm⁻¹ in Raman and its counterpart in IR is observed at 1179 cm⁻¹. A strong band at 1044 cm⁻¹ in the Raman and a relatively weak band at 1074 cm⁻¹ in IR is assigned to the C=S stretch (thioamide mode III). After deuteriation, this band is shifted upwards by ~16 cm⁻¹ due to strong coupling with other motions (Table 4.5). Calculations suggest that the C=S deformation contributes little towards the vibrations responsible for the bands at 248, 542, 577, and 877 cm⁻¹ in the Raman and 575 and 875 cm⁻¹ in the IR spectrum.

For MeRd, a strong band at 1127 cm⁻¹ in the Raman spectrum is assigned to the thioamide II, which is observed at 1116 cm⁻¹ in the IR spectrum. The bands at 984 cm⁻¹ in Raman and 983 cm⁻¹ in IR are attributable to vibrations which have very little $\nu(\text{C}=\text{S})$ involvement and could be ascribed to the thioamide III. The band at 583 cm⁻¹ in Raman and 578 cm⁻¹ in the IR spectra is attributed to a vibration which is predominantly an *op* C=S deformation. After deuteriation, the band at 578 cm⁻¹ in the IR spectrum is downward shifted by ~16 cm⁻¹ and is absent in the Raman spectrum.

4.3.2.5. C-N and N-N vibrations

In the thiazolidine ring the nitrogen atom is directly linked with the C=O and C=S moieties for Rds. The lone pair on the nitrogen atom could therefore conjugate with either of these groups (due to resonance effects, as discussed in section 4.3.1). Such delocalization of electrons would weaken the C=O and C=S bonds, whilst stiffening the C-N bond. As a consequence, the $\nu(\text{C}=\text{O})$ and/or $\nu(\text{C}=\text{S})$ bands become less intense, and shift to lower wavenumber, such that coupling with other types of motion becomes more likely. A complete vibrational assignment of C-N and N-N vibrations is difficult due to interactions with other motions and for the diversity of regions to

which they could be assigned. However, calculated PEDs have been exploited to facilitate the detailed assignments.

In Rd spectra the bands at 878, 1176, 1230, and 1380 cm^{-1} in Raman (and 820, 1187, and 1234 cm^{-1} in the IR spectrum) are assigned to vibrations which are predominantly of C-N stretching character, but also involve other types of motion. For the deuteriated species, these bands are only slightly shifted in relation to the protonated species (Table 4.3).

The substitution of an amino group at position 3 in H_2NRd perturbs electronic structure, relative to Rd, due to its involvement in the resonance effect by donation of a lone pair to the ring nitrogen atom. This changes the charge on the nitrogen atom which becomes more polar in nature, and consequently alters the wavenumbers of vibrations involving motion of the ring nitrogen atom. A medium intensity IR band at 1420 cm^{-1} is assigned to a mode which has 25 % C3N5 stretching character. This band is absent in the Raman spectrum. A weak band at 1373 cm^{-1} in Raman and relatively strong band at 1363 cm^{-1} in the IR spectrum is attributed to a mode which has significant contribution from C1N5 (24%), C3N5 (11 %), and N-N (23%) stretching. In the Raman spectrum, bands at 648, 877, 1044, 1126, 1158, and 1230 cm^{-1} and their counterparts at 634, 875, 1050, 1115, 1179, and 1255 cm^{-1} in the IR spectrum have C-N and N-N contributions, to some extent. For example, a medium intensity doublet at 1115 and 1126 cm^{-1} in both the Raman and IR spectra is assigned to a vibration involving C1N5, C1C2, and N-N stretching. The ip N-N deformation mode gives rise to a band at 575 and 577 cm^{-1} in Raman and IR spectra, respectively. The bands at 184 and 257 cm^{-1} in the Raman spectrum are tentatively assigned to op N-N deformation and torsional modes. In the deuteriated species, bands at 540, 557, 997, 1158, 1388, and 1396 cm^{-1} in the Raman spectrum, and bands at 551, 598, 1002, 1155, 1367, and 1399 cm^{-1} in the IR spectrum are, to some extent, associated with C-N and N-N stretching motion. For instance, the doublet at 1396 and 1399 cm^{-1} in both Raman and IR spectra is attributed to a mode whose predominant contributions are C-N (48 %) and N-N (20 %) stretching (Table 4.4). The ip, op N-N deformation and torsional modes are accounted for by the bands at 351, 207, 104 cm^{-1} in the Raman spectrum.

For MeRd, three bands at 984, 1283, and 1348 cm^{-1} in the Raman (983, 1292, and 1353 cm^{-1} in the IR spectrum) appear to be quite mixed and have major contributions from C-N stretching. The ip C-N mode gives rise to a band at 340 and 336 cm^{-1} in the Raman and IR spectra, respectively. The bands at 242 and 172 cm^{-1} in the Raman and IR spectra, respectively, are tentatively assigned to op C-N deformation and torsional modes. Deuteriation has negligible effects on the C-N vibrations. For example, the observed bands at 976, 1282, and 1345 cm^{-1} in the Raman and 978, 1288, and 1352 cm^{-1} in the IR spectrum are attributed to C-N stretching modes. Similarly, the C-N deformation and torsional modes have not shifted significantly (Table 4.7). However, the band at 336 cm^{-1} is absent in the Raman spectrum of the deuteriated species.

4.3.2.6. C-C and C-S vibrations

C-C stretching vibrations usually give rise to bands in the region spanning the 920-965 and 850-890 cm^{-1} regions in aliphatic and aromatic compounds, respectively. The C-S stretching mode is weak in IR, but strong in Raman and resides in the 550-700 cm^{-1} region.

For Rd, a medium intensity band at 878 cm^{-1} in the Raman spectrum and its strong counterpart at 820 cm^{-1} in the IR spectrum is assigned to a C-C stretching mode. The calculated PEDs suggest that this vibration involves coupling with other motions, but is mainly C-C stretch (53%). The C-S stretching coordinate contributes significantly to a medium intensity band at 785 cm^{-1} in both Raman and IR spectra. C-S stretching is also involved, to some extent, in the vibrations which give rise to the following bands: 427 and 545 cm^{-1} in Raman and 544 cm^{-1} in IR spectra, respectively. For the deuteriated species, two strong bands at 620 and 666 cm^{-1} in IR are assigned to the C3S7 and C2S7 stretching modes. The second band is absent in the Raman spectrum. Nevertheless, a medium intensity band at 662 cm^{-1} in the Raman spectrum is attributed to the C2S7 stretch.

In H₂NRd spectra, C-C stretching modes are associated with two bands at 648 and 1126 cm^{-1} in the Raman and at 634 and 1115 cm^{-1} in the IR spectra. The calculated values of 629 and 1119 cm^{-1} are consistent with experimental values. A weak band at 776 cm^{-1} in the Raman and relatively strong band at 780 cm^{-1} in the IR is accounted

for by a C3S7 stretch. Theoretical calculations show that this vibration involves strong coupling with ring deformation. The bands at 485, 648, 877, and 1044 cm^{-1} in the Raman spectrum and their counterparts at 483, 634, 977, and 1050 cm^{-1} in the IR are assigned to vibrations that have C-S character, to some extent. Upon deuteration, the band at 1126 cm^{-1} is shifted downward by $\sim 21 \text{ cm}^{-1}$. The bands at 618 and 787 cm^{-1} in the Raman and 615 and 805 cm^{-1} in the IR spectrum are mainly assigned to the C2S7 and C3S7 stretching modes, respectively.

For MeRd, a strong band at 1093 cm^{-1} in Raman and a medium band at 1092 cm^{-1} in the IR spectra is mainly of C-C stretching character (33%). After deuteration, this band is shifted to 1065 cm^{-1} in the Raman spectrum and appears to be of weak intensity. Nevertheless, its counterpart in the IR spectrum is observed as a medium intensity band at 1025 cm^{-1} . The bands at 626 and 855 cm^{-1} in Raman and 623 and 853 cm^{-1} in IR have much less C-C character. A medium intensity band at 782 cm^{-1} in both the Raman and IR spectra is assigned to the C2S7 stretching mode which is in good agreement with a calculated value of 761 cm^{-1} . Upon deuteration this band is shifted to lower wavenumber region and is located at 710 cm^{-1} in both the Raman and IR spectra. According to calculated PEDs, this vibration involves coupling with CH_2 wagging and ip ring deformation motion but is mainly C2S7 stretching (58%).

4.3.2.7. Thiazolidine Ring Vibrations

In the Raman spectrum of Rd three strong bands at 427, 489, and 545 cm^{-1} are assigned to op and ip ring deformation modes, respectively. The first of these is the most intense band in the Raman spectrum. Two bands at 515 and 544 cm^{-1} in the IR spectrum are attributed to ring deformation. DFT calculations predict that ring deformation is coupled with other types of motion. Ring deformation also contributes partially to the vibrations which give rise to the bands at 878, 1066, and 1078 cm^{-1} in the Raman and 820, 1073, and 1083 cm^{-1} in the IR spectrum. The ring torsional modes give rise to the bands at 108 and 142 cm^{-1} in the Raman spectrum. After deuteration, ring deformation vibrations are observed at 423, 467, and 540 cm^{-1} in the Raman spectrum. The first band is of medium intensity and the other two bands are very strong. Only two bands, at 493 and 541 cm^{-1} , are observed in the IR spectrum, compared to the three bands in the Raman spectrum and are assigned to vibrations

which are predominantly due to ring deformation. The bands due to ring torsional modes show a downward shift of $\sim 3 \text{ cm}^{-1}$.

For H_2NRd , the three bands at 422, 485, and 542 cm^{-1} in the Raman spectrum are attributed to the op and ip ring deformation modes. The first band is very strong and shifts to 540 cm^{-1} upon deuteration, the second band is downward shifted by $\sim 20 \text{ cm}^{-1}$, whereas the third band does not show any shift. The two bands at 538 and 466 cm^{-1} in the IR spectrum are accounted for by op and ip ring deformation modes, respectively which are located at 466 and 537 cm^{-1} for the deuterated species. The ring torsional modes give rise to the bands at 89 and 113 cm^{-1} in the Raman spectrum.

In the case of MeRd three bands, at 421, 473, and 542 cm^{-1} , in the Raman spectrum are assigned to ring deformation. The first band is very strong and shifted down by $\sim 12 \text{ cm}^{-1}$ upon deuteration. The other two bands are also shifted upon deuteration and located at 419 and 466 cm^{-1} , respectively. In the IR spectrum, two bands at 474 and 539 cm^{-1} are associated with ring deformation. The calculated PEDs suggest that these vibrations are quite mixed but predominantly involve ring deformation. The ring torsional modes gives rise to two bands in the Raman spectrum, a very strong band at 105 cm^{-1} and weak band at 93 cm^{-1} . After deuteration, only one band is observed at 151 cm^{-1} in the Raman spectrum.

Having assigned the most important features of the Raman and IR spectra of Rd and its 3-amino and 3-methyl derivatives, we are able to compare the corresponding spectra of the three molecules in order to provide a spectroscopic methodology to differentiate them and to attain some insight into the substitution effects on the vibrational wavenumbers of related functional groups. The calculated structures of Rd, H_2NRd , and MeRd are illustrated in Fig.4.2. It is apparent from the computed structure that Rd is a mono-substituted cyclic thioamide/amide, with a *cis* conformation. This finding is confirmed by the appearance of a strong band at $\sim 1450 \text{ cm}^{-1}$ which is a characteristic band for cyclic amides (mode II). Moreover, this particular band is absent when the amide hydrogen atom is replaced with a NH_2 or CH_3 substituent. In the past, this band has been assigned to the CH_2 bending mode. However, a comparison of the vibrational spectra of the three molecules reveal that a band at $\sim 1380 \text{ cm}^{-1}$ is indeed due to the CH_2 bending mode, which is shifted

downward after deuteration. The substitution effect on the C=O stretching wavenumber is also apparent. In Rd, the corresponding mode is shifted to lower wavenumber by $\sim 20 \text{ cm}^{-1}$ in relation to the other two molecules. A very intense band at $\sim 542 \text{ cm}^{-1}$ could be used as a marker band in the vibrational spectra for these molecules, which is attributed to ring deformation. This band is split into two components, 545 and 538 cm^{-1} in the case of Rd. It is worth noting that in the vibrational spectra more than one band is found in specific regions where only one band is expected. These bands arise from factor group splitting in the solid state. It should be emphasized that the relative intensities of theoretical vibrational spectra follow the pattern of experimental vibrational spectra. Furthermore, the calculated band wavenumbers show almost one-to-one correspondence with the bands observed. Therefore, the quantum mechanical calculations performed during this study, allow detailed assignment of the protonated and deuterated spectra in the solid state.

Table 4.2. Experimental and theoretical calculations (NCA) for Rd in the solid state (protonated).

Expt.		Calc.		Assignments (% PEDs)
Raman $\tilde{\nu} / \text{cm}^{-1}$	IR			
		A'		
3176 vw	3165 w	3402	$\nu(\text{NH})$ (100)	
3079 vb	3079 m			
2916 m	2915 w	2918	$\nu_s(\text{CH}_2)$ (100)	
2856 vw	2865 w			
1779 w	1779 w	1745	$\nu(\text{C}=\text{O})$ (86)	
1713 m	1709 vs			
1699 s				
1567 vv				
1457 s	1442 vs	1398	$\nu(\text{C}_3\text{N})$ (27), $\delta_{\text{ip}}(\text{NH})$ (47)	
1380 m	1380 m	1416	$\delta(\text{CH}_2)$ (92)	
1325 vw	1327 m			
1305 vw	1305 w			
1230 w	1234 vs	1272	$\nu(\text{C}_1\text{N})$ (33), $\nu(\text{C}_3\text{N})$ (18), $\nu(\text{C}_1\text{C}_2)$ (10), $\delta_{\text{ip}}(\text{C}=\text{O})$ (15)	
	1210 vw	1210	$\nu(\text{C}_1\text{C}_2)$ (12), $\omega(\text{CH}_2)$ (64)	
1176 m	1197 sh	1168	$\nu(\text{C}_3\text{N})$ (23), $\nu(\text{C}=\text{S})$ (10), $\omega(\text{CH}_2)$ (26), $\delta_{\text{ip}}(\text{NH})$ (28)	
	1187 s			
1078 m	1083 s	1067	$\nu(\text{C}_1\text{N})$ (13), $\nu(\text{C}=\text{S})$ (48), $\delta_{\text{ip}}(\text{ring})$ (10)	
1066 s	1073 sh			

878 m	820 s	853	$\nu(\text{C1N})$ (21), $\nu(\text{C1C2})$ (53), $\delta_{\text{ip}}(\text{ring})$ (11)
785 m	785 m	757	$\nu(\text{C2S})$ (67), $\delta_{\text{ip}}(\text{ring})$ (21)
735 vb		662	$\nu(\text{C3S})$ (59)
545 vs	544 s	527	$\nu(\text{C3N})$ (13), $\nu(\text{C2S})$ (19), $\nu(\text{C=S})$ (10), $\delta_{\text{ip}}(\text{ring})$ (37)
489 s	515 s	479	$\delta_{\text{ip}}(\text{C=O})$ (37), $\delta_{\text{op}}(\text{ring})$ (41)
427 s		408	$\nu(\text{C3S})$ (13), $\nu(\text{C=S})$ (15), $\delta_{\text{ip}}(\text{C=O})$ (19), $\delta_{\text{op}}(\text{ring})$ (26)
261 w		245	$\delta_{\text{ip}}(\text{C=S})$ (74)
A''			
2963	2960 w	2963	$\nu_{\text{as}}(\text{CH}_2)$ (100)
1135 w	1149 vw	1112	$\tau(\text{CH}_2)$ (87), $\delta_{\text{op}}(\text{C=O})$ (10)
1120 w	1131 vw		
893 w	880 w	881	$\rho(\text{CH}_2)$ (69), $\tau(\text{CH}_2)$ (10), $\delta_{\text{op}}(\text{C=O})$ (18)
691 sh	681 s	676	$\delta_{\text{op}}(\text{C=O})$ (11), $\delta_{\text{op}}(\text{NH})$ (100)
685 s			
568 w		555	$\rho(\text{CH}_2)$ (17), $\delta_{\text{op}}(\text{C=O})$ (32), $\delta_{\text{op}}(\text{C=S})$ (21), $\tau_{\text{ip}}(\text{ring})$ (14), $\tau_{\text{op}}(\text{ring})$ (12)
538 s	538 m	543	$\delta_{\text{op}}(\text{C=O})$ (29), $\delta_{\text{op}}(\text{C=S})$ (65)
142 m		135	$\tau_{\text{ip}}(\text{ring})$ (82), $\tau_{\text{op}}(\text{ring})$ (10)
108 s		113	$\tau_{\text{ip}}(\text{ring})$ (13), $\tau_{\text{op}}(\text{ring})$ (89)

Table 4.3. Experimental and theoretical calculations (NCA) for Rd- d_3 in the solid state (deuteriated).

Expt.		Calc.	Assignments (% PEDs)
Raman	IR		
$\tilde{\nu} / \text{cm}^{-1}$			
A'			
2941 vw	2939 vw		
2285 w	2292 m	2496	$\nu(\text{ND})$ (98)
2226 m	2226 w		
2133 w	2160	2120	$\nu_{\text{s}}(\text{CD}_2)$ (99)
1697 m	1709 vs	1740	$\nu(\text{C=O})$ (88)
1682 s			
1457 vb	1441 m		
1342 w	1338 sh	1329	$\nu(\text{C3N5})$ (59), $\nu(\text{C=S})$ (15), $\delta_{\text{ip}}(\text{ND})$ (13)
1326 w	1327 s		
1287 w	1284 s	1249	$\nu(\text{C1N5})$ (47), $\nu(\text{C1C2})$ (16), $\delta_{\text{ip}}(\text{C=O})$ (16)
1232 w	1229 sh		
	1212 m		
1100 w	1100 w	1067	$\nu(\text{C1N5})$ (14), $\nu(\text{C=S})$ (46)
1064 s	1074 vs		
1016 w	1041 w	1059	$\nu(\text{C1C2})$ (19), $\delta(\text{CD}_2)$ (37), $\omega(\text{CD}_2)$ (12)
982 vw	1021 m	1023	$\delta(\text{CD}_2)$ (50), $\omega(\text{CD}_2)$ (12), $\delta_{\text{ip}}(\text{ND})$ (14)
976 vw	980 w	951	$\omega(\text{CD}_2)$ (43), $\delta_{\text{ip}}(\text{ND})$ (29)

897 vw	941		
795 m	794 s 723 w	757	$\nu(\text{C1N5})$ (15), $\nu(\text{C1C2})$ (29), $\delta_{\text{ip}}(\text{ring})$ (23), $\delta_{\text{ip}}(\text{ND})$ (16)
662 m	666 s	681	$\nu(\text{C2S7})$ (52), $\nu(\text{C1C2})$ (10), $\omega(\text{CD}_2)$ (25)
638 vb	620 s	634	$\nu(\text{C3S7})$ (56), $\delta_{\text{op}}(\text{ring})$ (11), $\delta_{\text{ip}}(\text{ND})$ (11)
540 s	541 s	526	$\nu(\text{C3N5})$ (12), $\nu(\text{C2S7})$ (21), $\nu(\text{C=S})$ (10), $\delta_{\text{ip}}(\text{ring})$ (37)
475 sh 467 s	493 s	457	$\delta_{\text{ip}}(\text{ring})$ (42), $\delta_{\text{ip}}(\text{C=O})$ (35)
423 vs		406	$\nu(\text{C3S7})$ (13), $\nu(\text{C=S})$ (14), $\delta_{\text{op}}(\text{ring})$ (23), $\delta_{\text{ip}}(\text{C=O})$ (22)
259 w		243	$\delta_{\text{ip}}(\text{C=S})$ (75)
A''			
2191 w 2177 sh 2160 sh	2174 w 2160 w	2199	$\nu_{\text{as}}(\text{CD}_2)$ (100)
892 w 819 vw 811 vw	898 m 894 m 832 w	895	$\rho(\text{CD}_2)$ (18), $\tau(\text{CD}_2)$ (40), $\delta_{\text{op}}(\text{C=O})$ (40)
721 w 706 w	705 m	708	$\rho(\text{CD}_2)$ (36), $\tau(\text{CD}_2)$ (53)
		568	$\delta_{\text{op}}(\text{C=S})$ (65), $\delta_{\text{op}}(\text{ND})$ (34)
		512	$\rho(\text{CD}_2)$ (17), $\delta_{\text{op}}(\text{C=O})$ (30), $\delta_{\text{op}}(\text{C=S})$ (26), $\delta_{\text{op}}(\text{ND})$ (25)
		445	$\rho(\text{CD}_2)$ (18), $\delta_{\text{op}}(\text{C=O})$ (17), $\delta_{\text{op}}(\text{ND})$ (49)
163 w 139 w		129	$\delta_{\text{op}}(\text{C=S})$ (10), $\tau_{\text{ip}}(\text{ring})$ (65), $\tau_{\text{op}}(\text{ring})$ (30)
106 w		102	$\tau_{\text{ip}}(\text{ring})$ (30), $\tau_{\text{op}}(\text{ring})$ (72)

Table 4.4. Experimental and theoretical calculations (NCA) for H₂NRd in the solid state (protonated).

Raman	Expt. $\tilde{\nu} / \text{cm}^{-1}$	IR	Calc.	Assignments (% PEDs)
3328 vw	3325 w	3325 w	3362	$\nu_{\text{as}}(\text{NH}_2)$ (98)
3298 vw	3295 m	3295 m	3256	$\nu_{\text{s}}(\text{NH}_2)$ (98)
3233 w 3149 w	3230 m 3146 w	3230 m 3146 w		
2960 w	2957 w	2957 w	2962	$\nu_{\text{as}}(\text{CH}_2)$ (99)
2924 w	2921 w	2921 w	2918	$\nu_{\text{s}}(\text{CH}_2)$ (99)
2904 m	2901 w	2901 w		
1744 w 1730 w 1716 s	1740 sh 1727 vs 1612 w	1740 sh 1727 vs 1612 w	1717	$\nu(\text{C=O})$ (85)

1536 w	1539 s	1535	$\delta_{ip}(\text{NH}_2)$ (97)
	1420 m	1428	$\nu(\text{C3N5})$ (25), $\delta(\text{NH}_2)$ (46), $\delta(\text{CH}_2)$ (10)
1387 m	1387 m	1415	$\delta(\text{CH}_2)$ (87)
1373 w	1363 s	1376	$\nu(\text{C1N5})$ (24), $\nu(\text{C3N5})$ (11), $\nu(\text{NN})$
1361 w	1342 w		(23), $\rho(\text{NH}_2)$ (13)
1230 w	1255 sh	1214	$\nu(\text{C3N5})$ (11), $\nu(\text{C=S})$ (10), $\rho(\text{NH}_2)$
1215 w	1239 s		(12), $\omega(\text{CH}_2)$ (43)
	1218 w		
	1212 sh		
1158 m	1179 s	1192	$\nu(\text{C3N5})$ (10), $\nu(\text{C=S})$ (11), $\rho(\text{NH}_2)$
			(15), $\omega(\text{CH}_2)$ (49)
1126 m	1115 m	1119	$\nu(\text{C1N5})$ (10), $\nu(\text{C1C2})$ (27), $\nu(\text{NN})$
			(20), $\nu(\text{C=S})$ (12), $\delta_{op}(\text{NH}_2)$ (10)
1082 m	1080 w	1110	$\tau(\text{CH}_2)$ (83)
1044 s	1050 w	1028	$\nu(\text{C3N5})$ (13), $\nu(\text{C3S7})$ (13), $\nu(\text{C=S})$
			(26), $\delta_{op}(\text{NH}_2)$ (15)
954 s	977 m	941	$\nu(\text{C1C2})$ (13), $\delta_{op}(\text{NH}_2)$ (61)
953 m	958 s	877	$\rho(\text{CH}_2)$ (72), $\delta_{op}(\text{C=O})$ (17)
877 m	875 s	859	$\nu(\text{C3S7})$ (20), $\nu(\text{NN})$ (19), $\delta_{op}(\text{NH}_2)$
			(11), $\delta_{ip}(\text{C=S})$ (11)
776 w	780 m	755	$\nu(\text{C3S7})$ (68), $\delta_{ip}(\text{ring})$ (14)
	776 sh		
648 s	634 s	629	$\nu(\text{C3S7})$ (10), $\nu(\text{C1C2})$ (21), $\nu(\text{NN})$
631 sh			(13), $\delta_{ip}(\text{ring})$ (20), $\delta_{ip}(\text{C=O})$ (17)
577 w	575 m	590	$\rho(\text{CH}_2)$ (17), $\delta_{op}(\text{C=O})$ (51), $\delta_{op}(\text{C=S})$
			(17), $\delta_{op}(\text{NN})$ (24)
	528 m	537	$\delta_{op}(\text{C=O})$ (18), $\delta_{op}(\text{C=S})$ (63)
542 vvs	538 m	529	$\nu(\text{C3N5})$ (12), $\nu(\text{C3S7})$ (14), $\delta_{ip}(\text{ring})$
			(26), $\delta_{op}(\text{C=S})$ (12)
485 w	483 s	472	$\nu(\text{C3S7})$ (18), $\delta_{op}(\text{ring})$ (39)
422 s		409	$\nu(\text{C3S7})$ (13), $\nu(\text{C=S})$ (14), $\delta_{op}(\text{ring})$
			(21), $\delta_{ip}(\text{C=O})$ (24)
365 w		335	$\delta_{ip}(\text{C=O})$ (17), $\delta_{ip}(\text{NN})$ (57)
331 w			
257 w		252	$\delta_{op}(\text{NN})$ (92)
248 w		246	$\delta_{ip}(\text{C=S})$ (70), $\delta_{op}(\text{NN})$ (12)
184 w		163	$\tau(\text{NN})$ (94)
169 w			
113 vw		125	$\tau_{ip}(\text{ring})$ (43), $\tau_{op}(\text{ring})$ (59)
89 vw		109	$\tau_{ip}(\text{ring})$ (65), $\tau_{op}(\text{ring})$ (59)

Table 4.5. Experimental and theoretical calculations (NCA) for H₂NRd-*d*₄ in the solid state (deuteriated).

Expt.		Calc.	Assignments (% PEDs)
Raman $\tilde{\nu}$ /cm ⁻¹	IR		
2490 vw	2487 w 2458 m	2483	$\nu_{as}(\text{ND}_2)$ (99)
2380 w 2319 w	2378 m 2319 w	2350	$\nu_s(\text{ND}_2)$ (99)
2191 w	2198 w	2198	$\nu_{as}(\text{CD}_2)$ (100)
2167 w 2144 m	2167 w 2142 w	2120	$\nu_s(\text{CD}_2)$ (99)
1726 s 1711 s	1740 sh 1720 vs	1713	$\nu(\text{C}=\text{O})$ (88)
1396 w	1399 m	1386	$\nu(\text{C3N5})$ (48), $\nu(\text{NN})$ (20)
1388 w	1367 w 1349 w	1313	$\nu(\text{C1N5})$ (41), $\nu(\text{C3N5})$ (13), $\rho(\text{ND}_2)$ (12), $\delta_{ip}(\text{ring})$ (10)
	1291 s 1257 s 1234 w	1214	$\nu(\text{C3N5})$ (11), $\nu(\text{C}=\text{S})$ (10), $\rho(\text{ND}_2)$ (12), $\omega(\text{CH}_2)$ (43)
1285 w 1158 w	1182 m 1158 m	1149	$\nu(\text{NN})$ (12), $\delta_{ip}(\text{ND}_2)$ (66)
1105 w	1132 w	1093	$\nu(\text{C1C2})$ (35), $\rho(\text{ND}_2)$ (10), $\delta(\text{CD}_2)$ (15)
1082 w 1061 w	1084 m 1058 w	1087	$\nu(\text{C}=\text{S})$ (42), $\delta_{ip}(\text{ND}_2)$ (22)
1012 w 1017 w	1029 w 1019 w	1030	$\delta(\text{CD}_2)$ (79)
997 w	1002 w	989	$\nu(\text{NN})$ (14), $\omega(\text{CD}_2)$ (49)
948 w	947 m	942	$\nu(\text{C3N5})$ (15), $\nu(\text{C3S7})$ (13), $\nu(\text{NN})$ (11), $\rho(\text{ND}_2)$ (31)
875 w	892 w	887	$\delta(\text{CD}_2)$ (19), $\rho(\text{CD}_2)$ (43), $\delta_{op}(\text{C}=\text{O})$ (39)
787 w	887 w 875 m 805 m	799	$\nu(\text{C1N5})$ (14), $\nu(\text{C3S7})$ (12), $\rho(\text{ND}_2)$ (26)
720 m	783 s 768 s	735	$\delta_{op}(\text{ND}_2)$ (91)
707 w	719 w 706 s	704	$\rho(\text{CD}_2)$ (38), $\tau(\text{CD}_2)$ (49)
618 w	615 w 598 m	686 591	$\nu(\text{C2S7})$ (58), $\omega(\text{CD}_2)$ (19), $\delta_{ip}(\text{ring})$ (14) $\nu(\text{C3S7})$ (12), $\nu(\text{C1C2})$ (23), $\nu(\text{NN})$ (14), $\delta_{ip}(\text{ring})$ (18), $\delta_{ip}(\text{C}=\text{O})$ (15)
557 w	551 w	555	$\delta_{op}(\text{C}=\text{S})$ (70), $\delta_{op}(\text{NN})$ (22)
540 vs	537 m	530	$\nu(\text{C3N5})$ (14), $\nu(\text{C2S7})$ (19), $\nu(\text{C}=\text{S})$ (10), $\delta_{ip}(\text{ring})$ (30)
489 w	489 m	500	$\nu(\text{CD}_2)$ (27), $\delta_{op}(\text{C}=\text{O})$ (47), $\delta_{op}(\text{C}=\text{S})$ (20)
467 m	466 s	459	$\nu(\text{C3S7})$ (14), $\delta_{op}(\text{ring})$ (44)

419 s	406	$\nu(\text{C3S7})$ (14), $\nu(\text{C=S})$ (13), $\delta_{\text{op}}(\text{ring})$ (18), $\delta_{\text{ip}}(\text{C=O})$ (26)
351 w	316	$\delta_{\text{ip}}(\text{C=O})$ (16), $\delta_{\text{ip}}(\text{NN})$ (56)
252 w	244	$\delta_{\text{ip}}(\text{C=S})$ (65), $\delta_{\text{op}}(\text{NN})$ (13)
207 vb	237	$\delta_{\text{ip}}(\text{C=S})$ (11), $\delta_{\text{op}}(\text{NN})$ (90)
140 w	120	$\tau_{\text{ip}}(\text{ring})$ (25), $\tau(\text{NN})$ (64)
119 w	110	$\tau_{\text{op}}(\text{ring})$ (98), $\tau(\text{NN})$ (14)
104 w	105	$\tau_{\text{ip}}(\text{ring})$ (86), $\tau(\text{NN})$ (21)

Table 4.6. Experimental and theoretical calculations (NCA) for MeRd in the solid state (protonated).

Expt.		Calc.	Assignments (% PEDs)
Raman $\tilde{\nu} / \text{cm}^{-1}$	IR		
3028 vb		2999	$\nu_{\text{as}}(\text{CH}_3)$ (98)
2946 w	2943 w	2964	$\nu_{\text{as}}'(\text{CH}_3)$ (100)
2974 w	2972 m	2961	$\nu_{\text{as}}(\text{CH}_2)$ (100)
2925 m	2924 w	2918	$\nu_{\text{s}}(\text{CH}_2)$ (100)
		2903	$\nu_{\text{s}}(\text{CH}_3)$ (98)
2832	2867 vw		Overtone of $\delta(\text{CH}_2)$
2759 w	2757 vw		
1724 s	1729 vvs	1726	$\nu(\text{C=O})$ (87)
1719 sh	1717 sh		
1688 w			
1557 vb		1470	$\delta_{\text{s}}(\text{CH}_3)$ (26), $\delta_{\text{as}}(\text{CH}_3)$ (58), $\rho_{\text{ip}}(\text{CH}_3)$ (11)
1456 w	1456 vw	1457	$\delta_{\text{as}}'(\text{CH}_3)$ (88)
1421 vw	1419 s	1424	$\delta_{\text{s}}(\text{CH}_3)$ (69), $\delta_{\text{as}}(\text{CH}_3)$ (18)
1385 s	1391 w	1416	$\delta(\text{CH}_2)$ (98)
1389 sh	1383 w		
1395 sh			
1348 vw	1353 m	1335	$\nu(\text{C1N})$ (12), $\nu(\text{C3N})$ (27), $\nu(\text{NC})$ (21), $\delta_{\text{s}}(\text{CH}_3)$ (14)
1283 w	1292 s	1296	$\nu(\text{C1N})$ (24), $\nu(\text{C3N})$ (20), $\delta_{\text{as}}(\text{CH}_3)$ (15), $\delta_{\text{ip}}(\text{CH}_3)$ (15)
	1268 sh		
1217 w	1224 w	1206	$\omega(\text{CH}_2)$ (90)
	1216 w		
1137 w	1119 m	1130	$\delta_{\text{op}}(\text{CH}_3)$ (72)
1127 w	1116 s	1127	$\nu(\text{C=S})$ (30), $\delta_{\text{ip}}(\text{CH}_3)$ (31), $\delta_{\text{op}}(\text{CH}_3)$ (15)
1107 s			
		1113	$\tau(\text{CH}_2)$ (84), $\delta_{\text{ip}}(\text{C=O})$ (10)
1093 s	1092 m	1087	$\nu(\text{C1N})$ (12), $\nu(\text{CC})$ (33), $\nu(\text{NC})$ (19), $\delta_{\text{ip}}(\text{C=O})$ (10)
	1085 sh		
984 m	983 s	975	$\nu(\text{C1N})$ (11), $\nu(\text{C3N})$ (14), $\nu(\text{C3S})$ (13), $\nu(\text{NC})$ (23), $\nu(\text{C=S})$ (13), $\delta_{\text{ip}}(\text{CH}_3)$ (14)

889 vw	889 w	882	$\delta_{ip}(\text{CH}_2)$ (69), $\tau(\text{CH}_2)$ (10), $\delta_{op}(\text{C=O})$ (18)
880 w	880 m		
855 w	853 m	841	$\nu(\text{C1N})$ (15), $\nu(\text{C3S})$ (20), $\nu(\text{CC})$ (14), $\nu(\text{NC})$ (11), $\delta_{ip}(\text{C=S})$ (11)
782 m	782 m	761	$\nu(\text{C2S})$ (68), $\delta_{ip}(\text{ring})$ (15)
626 s	623 s	618	$\nu(\text{C3S})$ (13), $\nu(\text{CC})$ (19), $\nu(\text{NC})$ (13), $\delta_{ip}(\text{ring})$ (19), $\delta_{ip}(\text{C=O})$ (19)
583 w	578 w	592	$\delta(\text{CH}_2)$ (17), $\delta_{op}(\text{C=O})$ (39), $\delta_{op}(\text{C=S})$ (28), $\delta_{op}(\text{NC})$ (15)
		550	$\delta_{op}(\text{C=O})$ (33), $\delta_{op}(\text{C=S})$ (60)
542 vvs	539 m	530	$\nu(\text{C3N})$ (15), $\nu(\text{C2S})$ (16), $\delta_{ip}(\text{ring})$ (31)
473 w	474 s	467	$\nu(\text{C3S})$ (15), $\delta_{op}(\text{ring})$ (37), $\delta_{ip}(\text{C=O})$ (12)
421 vs		416	$\nu(\text{C=S})$ (15), $\delta_{op}(\text{ring})$ (25), $\delta_{ip}(\text{C=O})$ (24)
340 w		336	$\nu(\text{C3S})$ (11), $\delta_{ip}(\text{C=O})$ (10), $\delta_{ip}(\text{NC})$ (61)
255 vw		247	$\delta_{ip}(\text{C=S})$ (75), $\delta_{ip}(\text{NC})$ (10)
242 vw		227	$\delta_{op}(\text{NC})$ (96)
172 w		131	$\tau(\text{NC})$ (88)
105 s		120	$\tau_{ip}(\text{ring})$ (66), $\tau_{op}(\text{ring})$ (26)
93 w		100	$\tau_{ip}(\text{ring})$ (35), $\tau_{op}(\text{ring})$ (76)

Table 4.7. Experimental and theoretical calculations (NCA) for MeRd- d_2 in the solid state (deuteriated).

Expt.		Calc.	Assignments (% PEDs)
Raman	IR		
$\tilde{\nu} / \text{cm}^{-1}$			
	2995vw	2999	$\nu_{as}(\text{CH}_3)$ (98)
2946 w	2944 w	2964	$\nu_{as}'(\text{CH}_3)$ (100)
	2924 vw	2903	$\nu_s(\text{CH}_3)$ (98)
2235 m	2167 w	2197	$\nu_{as}(\text{CD}_2)$ (100)
2167 m			
2134 vw	2102 w	2120	$\nu_s(\text{CD}_2)$ (99)
1728 m	1728 vs	1726	$\nu(\text{C=O})$ (88)
1719 s			
	1449 vw	1470	$\delta_s(\text{CH}_3)$ (26), $\delta_{as}(\text{CH}_3)$ (58), $\tau_{ip}(\text{CH}_3)$ (11)
		1457	$\delta_{as}(\text{CH}_3)$ (88)
1418 vw	1418 s	1424	$\delta_s(\text{CH}_3)$ (61), $\delta_{as}(\text{CH}_3)$ (17)
1345 w	1352 m	1334	$\nu(\text{C1N5})$ (12), $\nu(\text{C3N5})$ (27), $\nu(\text{NC})$ (21), $\delta_s(\text{CH}_3)$ (14)
1282 w	1288 s	1296	$\nu(\text{C1N5})$ (24), $\nu(\text{C3N5})$ (20), $\delta_{as}(\text{CH}_3)$ (15), $\tau_{ip}(\text{CH}_3)$ (15)
1131 w	1116 s	1131	$\nu(\text{C=S})$ (24), $\tau_{ip}(\text{CH}_3)$ (28), $\tau_{op}(\text{CH}_3)$ (25)
1103 s			
1065 w	1025 m	1094	$\nu(\text{C1C2})$ (39), $\nu(\text{NC})$ (15)
1030 m	1000 w	1040	$\delta(\text{CD}_2)$ (79)
1036 sh			

		994	$\omega(\text{CD}_2)$ (55)
976 m	978 m	969	$\nu(\text{C3N5})$ (12), $\nu(\text{C3S7})$ (16), $\nu(\text{NC})$ (30), $\nu(\text{C=S})$ (11)
895 vw	895 m	896	$\tau(\text{CD}_2)$ (18), $\tau(\text{CD}_2)$ (40), $\delta_{\text{op}}(\text{C=O})$ (40)
824 w	824 w	812	$\nu(\text{C1N5})$ (11), $\nu(\text{C3S7})$ (19), $\omega(\text{CD}_2)$ (11), $\delta_{\text{ip}}(\text{C=S})$ (11)
722 w	722 w	708	$\rho(\text{CD}_2)$ (36), $\tau(\text{CD}_2)$ (53)
710 m	710 m	692	$\nu(\text{C2S7})$ (58), $\omega(\text{CD}_2)$ (20), $\delta_{\text{ip}}(\text{ring})$ (14)
615 vw	615 w		
599 m	598 m	591	$\nu(\text{C3S7})$ (15), $\nu(\text{C1C2})$ (23), $\nu(\text{NC})$ (15), $\delta_{\text{ip}}(\text{ring})$ (16), $\delta_{\text{op}}(\text{C=O})$ (13)
538 vs	538 m	530	$\nu(\text{C3N5})$ (15), $\nu(\text{C2S7})$ (17), $\delta_{\text{ip}}(\text{ring})$ (34)
		499	$\tau(\text{CD}_2)$ (35), $\delta_{\text{op}}(\text{C=O})$ (49), $\delta_{\text{op}}(\text{C=S})$ (10)
	562 w	570	$\delta_{\text{op}}(\text{C=S})$ (79), $\delta_{\text{op}}(\text{NC})$ (13)
466 w	492 w	462	$\nu(\text{C3S7})$ (13), $\delta_{\text{op}}(\text{ring})$ (40), $\delta_{\text{ip}}(\text{C=O})$ (13)
419 vs	468 s	414	$\nu(\text{C=S})$ (14), $\delta_{\text{op}}(\text{ring})$ (23), $\delta_{\text{ip}}(\text{C=O})$ (26)
340 w		335	$\nu(\text{C3S7})$ (12), $\delta_{\text{ip}}(\text{C=O})$ (10), $\delta_{\text{ip}}(\text{NC})$ (61)
169 vw		130	$\tau(\text{NC})$ (95)
151 vw		108	$\tau_{\text{ip}}(\text{ring})$ (85), $\tau_{\text{op}}(\text{ring})$ (13)

Intensities have been classified semi quantitatively in terms of very strong (vs), strong (s), medium (m), weak (w) and very weak (vw), shoulder bands have been denoted by (sh).

ν = stretch, δ = deformation, ρ = rock, ω = wag, τ = twist, s = symmetric, as = asymmetric, ip = in-plane, op = out-of-plane

Ring deformations are defined (in Table III, reference 17) as:

$$\delta_{\text{ip}}(\text{ring}) = \theta(\text{N5C1C2}) - 0.809 \theta(\text{C1C2S7}) + 0.309 \theta(\text{C2S7C3}) + 0.309 \theta(\text{S7C3N5}) - 0.809 \theta(\text{C3N5C1})$$

$$\delta_{\text{ip}}(\text{ring}) = -1.118 \theta(\text{C1C2S7}) + 1.809 \theta(\text{C2S7C3}) - 0.809 \theta(\text{S7C3N5}) + 1.118 \theta(\text{C3N5C1})$$

$$\delta_{\text{op}}(\text{ring}) = 0.309 \tau(\text{C2C1N5C3}) - 0.809 \tau(\text{C1N5C3S7}) + \tau(\text{N5C3S7C2}) - 0.809 \tau(\text{C3S7C2C1}) + 0.309 \tau(\text{S7C2C1N5})$$

$$\delta_{\text{op}}(\text{ring}) = -1.809 \tau(\text{C2C1N5C3}) + 1.118 \tau(\text{C1N5C3S7}) - 1.118 \tau(\text{C3S7C2C1}) + 1.809 \tau(\text{S7C2C1N5})$$

4.3.2.8. Electronic structure

Atomic charges were computed by employing Mulliken population analysis. This scheme computes atomic charges by dividing orbital overlap evenly between the two atoms involved. It is an arbitrary scheme for assigning charges. Atomic charges, unlike electron density, are not a quantum mechanical observable and are not unambiguously predictable from first principles. The net Mulliken electric charges (q_0) of sulfur, oxygen and carbon atoms for Rd, H₂NRd and MeRd are tabulated in

Table 4.8. The Mulliken scheme places the negative charge more or less evenly on oxygen and sulfur atoms, and splits the positive charge among three carbon atoms. The calculated dipole moment for Rd, H₂NRd and MeRd are 2.05, 2.109, and 1.76 D, respectively.

Table 4.8. Partial charge on different atoms in Rd, H₂NRd, and MeRd calculated at the B3LYP level, using cc-pVTZ basis set.

Atom numbering	Fragments	Atomic Charges (e)		
		Rd	H ₂ NRd	MeRd
1	C	0.1874	0.1974	0.1959
2	C	0.0846	0.0919	0.0880
3	C	0.0427	0.0518	0.0435
4	O	-0.2712	-0.2990	-0.2906
5	N	0.1147	0.0223	-0.0187
6	R ^a		0.1335	0.1664
7	S	0.0651	0.0533	0.0546
8	S	-0.2235	-0.2513	-0.2392

^aR=N,

4.4. Conclusions

A detailed experimental and theoretical study of the vibrational spectra of Rd, H₂NRd, and MeRd has provided an insight into the molecular structure of these molecules, and their deuteriated derivatives in the solid state. The “active” methylene group at position 5 is readily deuteriated and therefore enables discrimination between the vibrations associated with CH₂ and CH₃ groups. Herein, deuteriation also provides a comprehensive method to assign the bands. The vibrational assignments are supported by NCA utilizing force constants from DFT calculations. Overall there is a good correlation between theoretical and experimental data. Due to strong coupling of the C=S stretching vibrations to other modes, it is virtually impossible to obtain reliable vibrational assignment of the spectra of thioamides without calculation of the PEDs. The theoretical spectra presented together with the vibrational assignments can assist in the interpretation of the vibrational spectra of all the family of compounds containing thioamide groups.

4.5. References

- [1] A. C. Fabretti and P. Giorgio, *Transition Met. Chem.*, **2**, (1977), 224.
- [2] V. Enchev, S. Chorbadjiev and B. Jordanov, *Chem. Heterocycl. Compd.*, **38**, (2002), 1110.
- [3] D. Van der Helm, A. E. Lessor and L. L. Merritt, *Acta . Cryst.*, **15**, (1962), 1227.
- [4] H. J. Bernstein, *Spectrochim. Acta*, **18**, (1962), 161.
- [5] L. J. Bellamy, *The Infrared Spectra of Complex Molecules*, 2nd Ed., Chapman and Hall, London, (1980), 299.
- [6] P. J. Kreuger, *Nature*, **194**, (1962), 1077.
- [7] T. Miyazawa, T. Shimanouchi, and S. Mizushima, *J. Mol. Spectrosc.*, **24**, (1956), 408.
- [8] C. G. Cannon, *Spectrochim. Acta*, **16**, (1960), 302.
- [9] T. Miyazawa, *J. Mol. Spectrosc.*, **4**, (1960), 155.
- [10] N. B. Clothup, L. H. Daly and S. E. Wiberley, *Introduction to Infrared and Raman Spectroscopy*, 3rd Ed, Academic press, London, (1990),
- [11] I. Suzuki, *Bull. Chem. Soc. Jap.*, **35**, (1962), 1286.
- [12] A. Yamaguchi, R. B. Penland, S. Mizuzhima, T. J. Lane, C. Curran and J. V. Quagliano, *J. Amer. Chem. Soc.*, **80**, (1958), 527.
- [13] B. Thorn, *Can. J. Chem.*, **38**, (1960), 1439.
- [14] L. J. Bellamy and P. E. Rogasch, *J. Chem. Soc.*, (1960), 2218.
- [15] E. Spinner, *J. Org. Chem.*, **23**, (1958), 2037.
- [16] G. Herzberg, *Infrared and Raman Spectra of Polyatomic molecules*, Van Nostrand Reinhold, Princeton, New Jersey, (1945).
- [17] P. Pulay, G. Fogarasi, F. Pang and J. E. Boggs, *J. Am. Chem. Soc.*, **101**, (1979), 2550.

Chapter Five

Surface Enhanced Raman Spectroscopic Studies of Rhodanine and its Derivatives

5.1. Introduction

Surface enhanced Raman spectroscopy (SERS) is one of the most convenient and sensitive techniques, amongst various other interfacial spectroscopic methods (e.g. EELS), to investigate the adsorption mechanism of analytes on metal surfaces¹⁻⁵. SERS enhancement is a combination of both a long range electromagnetic effect (EM) and a short range chemical effect (CT)⁶⁻⁹. Generally, it is accepted that the major signal enhancement contribution observed in SERS results from the EM effect. Thus, on the basis of electromagnetic surface selection rules, the interfacial structures of adsorbates on Ag and Au nanoparticle (NP) substrates can be explained in a more quantitative way¹⁰⁻¹¹. The total SERS enhancement (compared to dispersive solution state Raman) depends on a number of factors, the most important include: nature of ligand (analyte) and adsorption mechanism¹²⁻¹⁴ (*i.e.*, physi-adsorbed or chemi-sorbed); synthesis, chemical, optical, and morphological properties of the substrate¹⁵⁻¹⁶; environmental solution conditions, and the nature/properties of the exciting radiation¹⁷⁻¹⁸.

This chapter reports investigations on the solution state (in methanol) Raman spectra of Rd and its derivatives and SER(R)S studies *i.e.*, Raman spectra of the interaction of Rd and its derivatives adsorbed on citrate-reduced Ag and Au colloidal NPs. Preliminary studies revealed that Au NPs afford a weak (intensity) SER spectrum. Therefore, pH dependent studies were conducted using Ag NPs to optimize experimental conditions used for SER(R)S. SER spectra are dominated by a vibrational band at $\approx 1566/1575/1572 \text{ cm}^{-1}$ (Rd/H₂NRd/MeRd, respectively), which is (tentatively) attributed to a C=C stretching mode. This band is very weak in intensity in solid state spectra and is not present in the methanol solubilized solution Raman spectra. It is hypothesized that Rd and its derivatives are subject to “a photo-reaction” on Ag and Au surfaces in the presence of laser excitation, resulting in the formation of dimers. DFT calculations have, therefore, been performed on dimers [*i.e.*, *Z (cis)* and *E (trans)* isomers] of Rd and its

derivatives by employing a B3LYP/cc-pVTZ basis set in the case of Rd, and B3LYP/D95 basis sets for the 3-substituted derivatives.

5.2. Experimental

5.2.1. Chemical Reagents

See section, 3.1 in Chapter three.

5.2.2. Vibrational Spectroscopy

See sections, 3.3, 3.5, 3.6, and 3.7 in Chapter three.

5.2.3. Synthesis and Aggregation of Ag Colloid

See sections 3.8, 3.9, and 3.10 in Chapter three.

5.2.4. SERS pH Dependence

See section 3.12 in Chapter three.

5.2.5. UV/vis Absorption Spectroscopy

See section 3.16 in Chapter three.

5.2.6. DFT Calculations

See sections 3.15 and 3.15.1 in Chapter three.

5.3. Results and Discussion

5.3.1. Solution State Spectra

Solution state Raman studies of Rd, H₂NRd and MeRd have been conducted in methanol (Fig.5.1) due to the low solubility of these compounds in aqueous solution. The most intense bands present in solution spectra are (obviously) due to the solvent (*i.e.*, methanol). Nevertheless, the weak intensity bands at 252, 417, 492, 537, 683, 780, 875, 1074, 1718, and 1757 cm⁻¹; 315, 418, 538, 637, 881, and 1744 cm⁻¹; 256, 336, 416, 475, 539, 625, 781, 853, 986, and 1740 cm⁻¹ are due to Rd, H₂NRd, and MeRd, respectively.

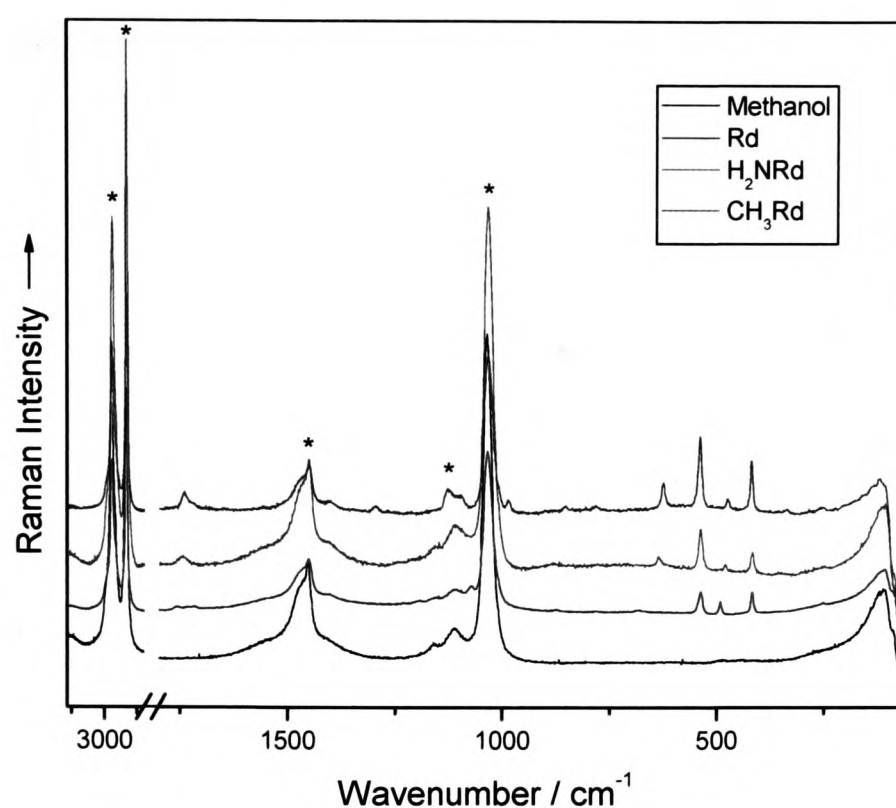


Figure 5.1. Solution state (in methanol) spectra of Rd and its derivatives ($\lambda_0 = 632.8$ nm); *represent bands due to the solvent.

5.3.2. SERS pH Dependent Studies

In order to optimize the experimental conditions used for SERS studies, pH profiles of Rd and its derivatives have been conducted. Fig. 5.2a shows SER spectra of Rd in the presence of 0.01 % PLL under acidic, neutral and basic (*i.e.*, alkaline) conditions. It is worth noting that the spectral profile changes significantly under acidic conditions compared to basic conditions. For pH values ≤ 6 the SER spectra are dominated by the bands at 556, 1191, 1382 and 1566 cm^{-1} . The band at 1566 cm^{-1} decreases in intensity towards neutral pH, increases in intensity at pH 7.3, and then remains constant under basic conditions. This band is also blue shifted by ~ 10 cm^{-1} under basic conditions, compared to acidic conditions. Similarly, the bands at 1191 and 1382 cm^{-1} are more intense under acidic conditions in relation to basic pH values. Whereas, at pH ≥ 7.3 values the bands at 1267 and 1312 cm^{-1} are enhanced. A weak band at 1313 cm^{-1} is enhanced at alkaline pH values and concomitantly blue shifted by ~ 5 cm^{-1} . A new band appears at 1478 cm^{-1} at pH ≥ 7.3 , this band is absent at acidic pH. The band at 556 cm^{-1} , which is the strongest band at pH 2.3, does not shift in wavelength with increasing

(alkaline) pH values; nevertheless, there is a considerable decrease in band intensity with increasing pH. The 556 cm^{-1} band was used to obtain the optimum conditions for SERS studies of Rd by plotting the log intensity (peak area) vs pH, as illustrated in Fig.5.2.b. The changes in spectral profile as a function of pH suggest either changes in the state of ionization, re-orientation of the molecule with respect to the Ag surface or the adsorption of Rd through a different binding site to the substrate or a combination of all three effects.

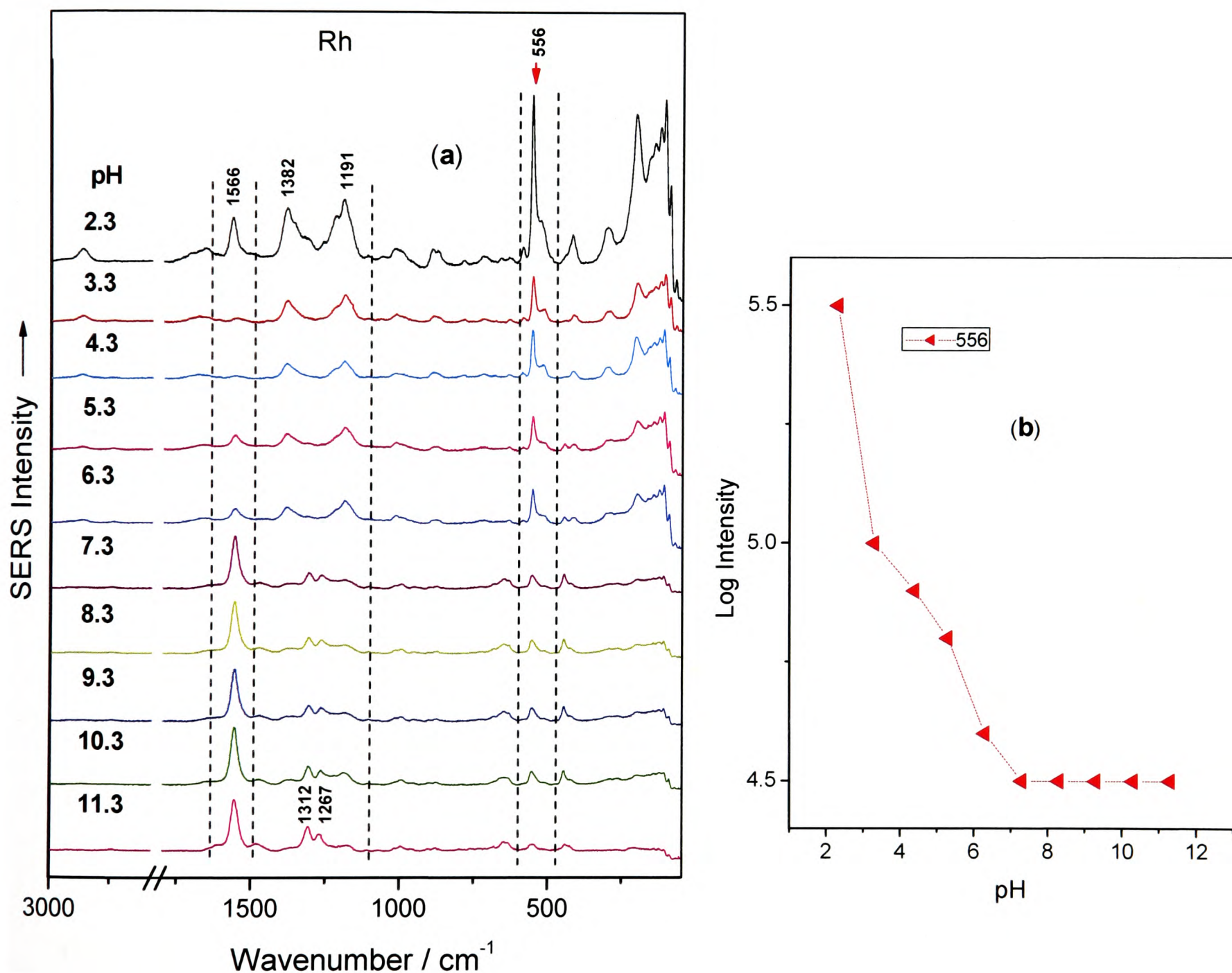


Figure 5.2. (a) SER spectra of Rd ($1.0 \times 10^{-3}\text{ mol dm}^{-3}$) adsorbed on the Ag colloid in the presence of 0.01 % (w/v) PLL and HCl in the pH range 2.3 to 11.3, (b) SERS pH profile for the vibrational band at 556 cm^{-1} (highlighted with red arrow); ($\lambda_0 = 632.8\text{ nm}$).

Fig.5.3. displays the SER spectra of H₂NRd in the presence of 0.01% PLL under acidic, neutral and basic conditions. There is a significant change in spectral profile in changing from acidic to alkaline pH values. SER spectra at pH \geq 2.3 are dominated by the bands at 436, 526, 1064, 1166, 1355, 1389, 1500, and 1575 cm⁻¹.

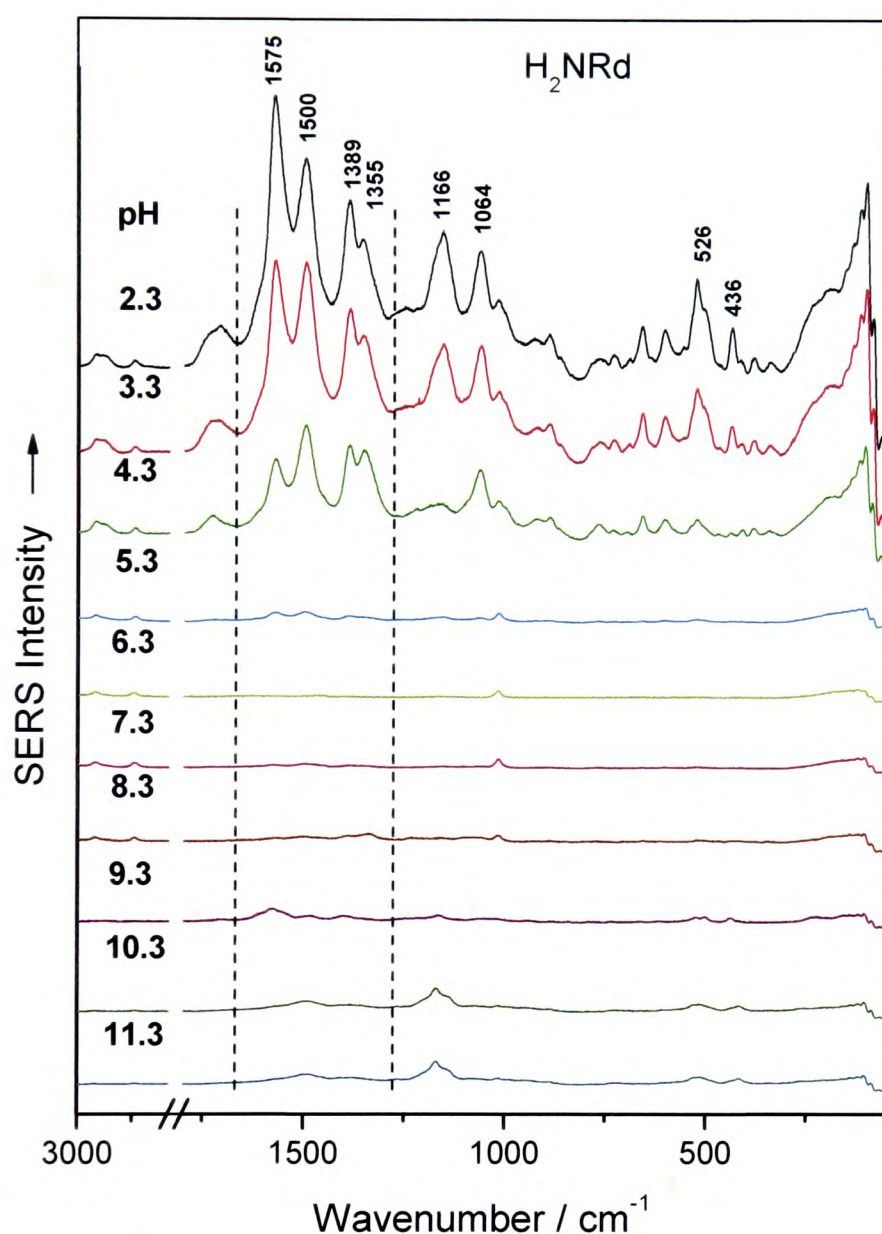


Figure 5.3. SER spectra of H₂NRd (8.6×10^{-4} mol dm⁻³) adsorbed on the Ag colloid in the presence of 0.01% PLL and HCl in the pH range from 2.3 to 11.3; ($\lambda_0 = 632.8$ nm).

Band intensities decrease towards neutral pH and no SERS signals are observed at pH 6.3. Under basic conditions the SERS signals are very weak, and bands are either blue-shifted or red-shifted (compared to acidic conditions). For example, a strong band at 1575 cm⁻¹ is red-shifted, observed at 1571 cm⁻¹, and is very weak in intensity. On the other hand, the band at 1166 cm⁻¹ is blue shifted, and found at 1174 cm⁻¹. It is intriguing to note

that the ratio of intensities of the bands at 1500 and 1575 cm^{-1} change at pH values > 2.3 ; the intensities of the two bands decrease with increasing pH and these bands are not detectable at neutral pH.

SER spectra of MeRd in the presence of 0.01 % PLL under acidic, neutral and basic conditions are shown in Fig. 5.4a. No significant changes in spectral profile are observed across the pH range examined. The major differences in spectral profile are attributed to the ratio of intensities of different bands. Intense bands are observed at 433, 503, 535, 885, 966, 1171, 1255, 1503, 1541, and 1572 cm^{-1} . The intensity of the band at 1572 cm^{-1} decreases with increasing (alkaline) pH and then increases again at pH 11.3. Conversely, the relative intensity of the band at 1503 cm^{-1} increases towards neutral pH and becomes very weak at pH 6.5. The bands at 503, 535, 885, 966, 1171, and 1255 cm^{-1} behave in the same fashion under acidic and basic conditions with the exception of a band at 433 cm^{-1} , which decreases in intensity in going from acidic to neutral pH, then increases in intensity until pH 8.3 before stabilizing at higher pH values. However, the relative intensity of this band is comparatively weak under basic conditions, for example at pH 11.3. These changes in the spectral profile could be attributed to changes in the re-orientation of the molecule with respect to the Ag surface, or the adsorption of MeRd via a different coordinating site to the substrate, or a combination of these effects. The band at 1255 cm^{-1} was used to obtain the optimum conditions for SERS studies of MeRd by plotting log intensity (peak area) vs. pH, as illustrated in Fig.5.4.b.

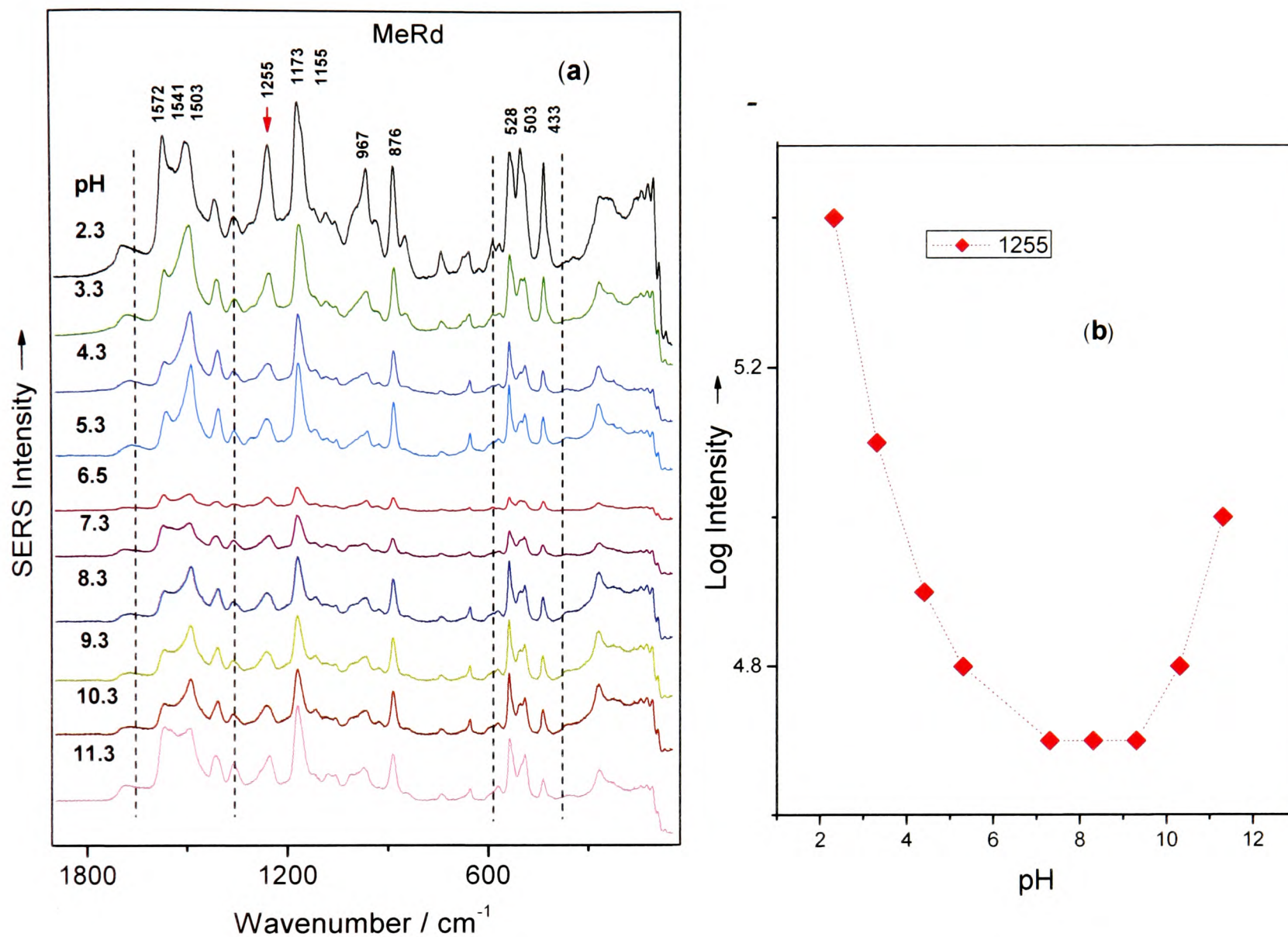


Figure 5.4. (a) SER spectra of MeRd (8.7×10^{-4} mol dm⁻³) adsorbed on the Ag colloid in the presence of 0.01 % (w/v) PLL and HCl at pH values ranging from 2.3 to 11.3, (b) SERS pH profile for the vibrational band at 1255 cm⁻¹ (highlighted with red arrow); ($\lambda_0 = 632.8$ nm).

5.3.3. SER Spectra of Rd

SERS pH studies of Rd demonstrate that the optimum condition, in the presence of 0.01% PLL, for undertaking SERS experiments is pH 2.3. However, a comparison of the SER spectra of Rd under optimized conditions ($\lambda_0 = 632.8$ nm) with solid state Raman spectra reveal that the band at 1566 cm⁻¹ is extremely intense in the SER spectrum, whereas it is very weak in the solid state spectrum. This necessitates further investigation

in order to shed light on the adsorption behavior on or chemical reaction with the Ag colloid. For this purpose, SERS studies have been performed by using a different SERS substrate (*i.e.*, Au colloidal NPs) and excitation wavelength (*i.e.*, 514.5 nm).

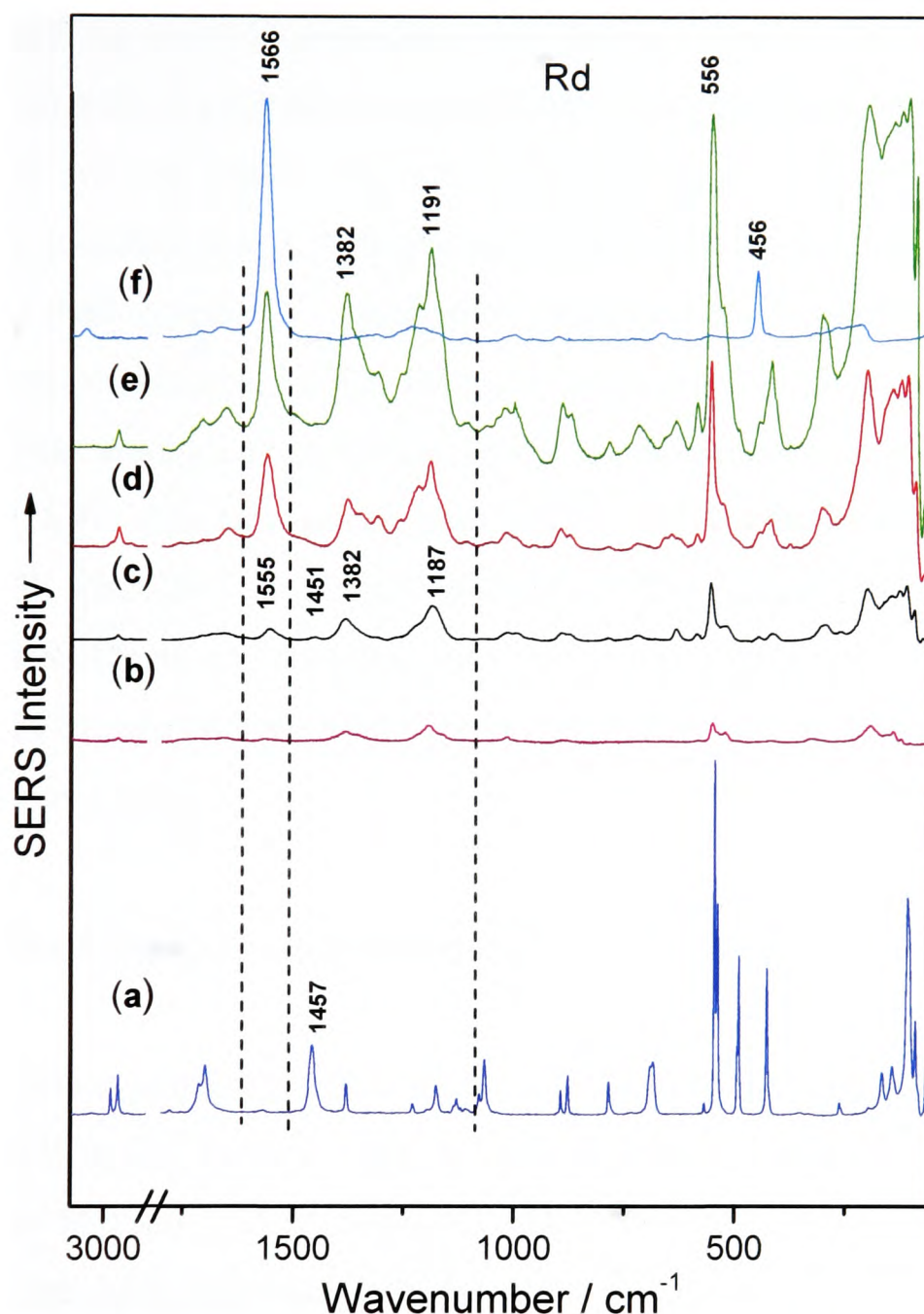


Figure 5.5. (a) Raman spectrum of Rd in the solid state ($\lambda_o = 632.8$ nm), (b) SER spectrum of Rd adsorbed on a Au colloid at pH 6.12 ($\lambda_o = 632.8$ nm); SER spectra of Rd adsorbed on Ag colloids: (c) at pH 6.12, (d) in the presence of HCl at pH 2.3, (e) in the presence of PLL, and HCl at pH 2.3 ($\lambda_o = 632.8$ nm) and (f) in the presence of PLL and HCl at pH 2.3 ($\lambda_o = 514.5$ nm). The concentration of Rd, for all the SER spectra, was 1.0×10^{-3} mol dm $^{-3}$.

Fig.5.5. shows a comparison of the Raman spectrum of Rd in the solid state with SER spectra of Rd under different experimental conditions. These spectral profiles show that SERS signals are obtained for Rd using both Ag and Au substrates in the absence of any aggregating. This observation suggests that the reaction (adsorption and/or chemical reaction) of Rd with Ag and Au substrates is very similar. However, the SERS signals are more enhanced using the Ag substrate compared to the Au substrate; the rationale behind this finding is, as yet, not known. Rd may potentially bond with Ag and Au NPs via nitrogen, oxygen, or sulfur atoms. Nitrogen and sulfur have a higher binding affinity for Ag and Au atoms than oxygen¹⁹⁻²⁰. Apparently, addition of HCl acid to Ag NPs does not change the adsorption behavior of Rd; instead it enhances the SERS signals. It is well known that chloride anions can be chemisorbed on the colloid surface owing to their high affinity for Ag²¹. Chloride anions can result in the aggregation of Ag NPs, thus enhancing the SER spectrum¹³. In a similar fashion, addition of both PLL and HCl further enhances the SERS signals. On the other hand, following addition of either HCl alone or a combination of PLL and HCl the SERS signals for Rd, obtained using the Au substrate, remain comparatively weak.

5.3.4. Effect of 514.5 nm Excitation Wavelength

This wavelength has a significant effect on the SER spectrum of Rd adsorbed on the Ag surface, in contrast to 632.8 nm excitation, in the presence of 0.01 % PLL and HCl, Fig.5.5f. The band at 1566 cm⁻¹ is enhanced, using 514.5 nm excitation, and is the most intense band in the SER spectrum. On the other hand, the intensity of the band at 556 cm⁻¹, which is an intense band using $\lambda_0 = 632.8$ nm, is dramatically decreased. In contrast, a weak band at 450 cm⁻¹ is also enhanced. Generally, it is accepted that SERS enhancement is predominantly due to excitation of localized surface plasmons²². Moreover, different laser excitation wavelengths provide enhancement from different sized colloidal aggregates and, to some extent, this has been shown to be related to the particle size and shape which, in turn, determines the plasmon resonance frequency²³. In the case of Ag and Au colloidal NPs, not all particles and aggregates will be SERS active at a given excitation wavelength. Due to the fact that only a number of particles will be

SERS active at any one time, the detected signal is an average over a number of particles, and therefore more stable. The SERS effect could also be enhanced when the molecular resonance of adsorbed analyte coincides with the laser excitation wavelength (*i.e.*, surface enhanced resonance Raman (SERRS)). The foregoing, may in part, account for the differences observed in the SER spectral profiles of Rd using different excitation wavelengths.

5.3.5. SER Spectra of H₂NRd

As is the case for the parent compound, SERS pH studies of H₂NRd suggest that the optimum condition for performing SERS experiments is under an acidic environment. Fig.5.6. shows a comparison of the Raman (solid state) and SER spectra obtained under optimized conditions. A band occurs at 1575 cm⁻¹, the most intense band in the SER spectrum, but this band is absent in the solid state spectrum. An attempt was made to interrogate the origin of this band, by obtaining SER spectra under different experimental conditions. Unlike Rd, this derivative does not give SER spectra in the absence of any aggregating agent when adsorbed on Ag NPs (Fig.5.6.c). Addition of HCl “activates” the Ag surface and SERS signals are observed (Fig.5.6.d). Furthermore, the addition of both PLL and HCl enhances the signals significantly by inducing the aggregation of Ag colloidal NPs. This feature highlights the importance of aggregation for SERS enhancement. The current findings complement previous studies published in the literature²⁴⁻²⁵, which demonstrate that large signal enhancements associated with aggregation occur at particle junctions.

Fig.5.6b displays the SER spectrum of H₂NRd using a Au NP substrate; the SERS signals are weak. Addition of HCl and PLL has subtle effects on SERS enhancement. Most of the observed bands do not shift in relation to the SER spectrum obtained using a Ag substrate. In particular the band at 1575 cm⁻¹ is still present, which suggests the same or similar adsorption behaviour and/or chemical reaction with the Au substrate as with the Ag substrate. It is important to note that H₂NRd gives a SER spectrum when using Au

NPs in the absence of any aggregating agent. On the other hand, in the case of Ag NPs addition of an aggregating agent is required to obtain a SER spectrum.

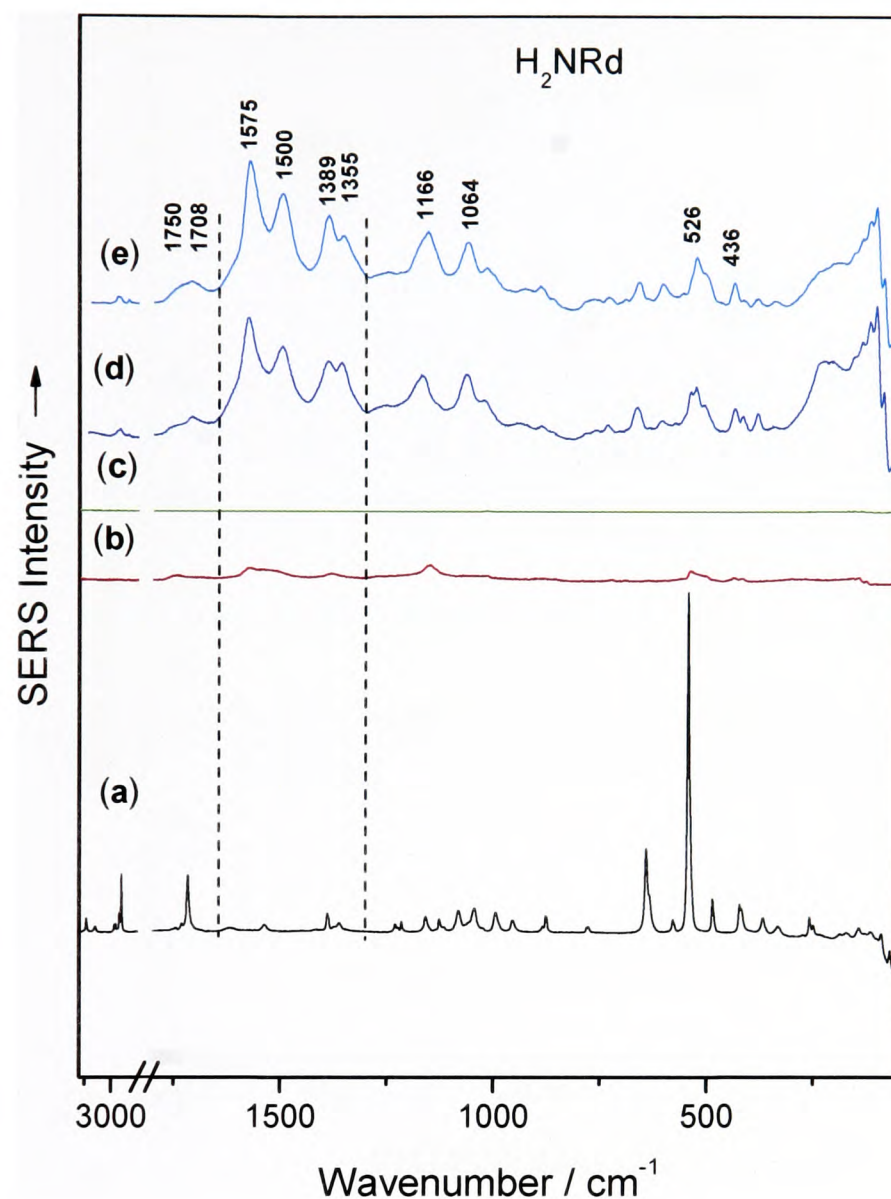


Figure 5.6. (a) Raman spectrum of H_2NRd ($8.6 \times 10^{-4} \text{ mol dm}^{-3}$) in the solid state ($\lambda_0 = 632.8 \text{ nm}$). SER spectra of H_2NRd : (b) adsorbed on the Au colloid at pH 7.70, (c) adsorbed on the Ag colloid at pH 7.70, (d) in the presence of HCl at pH 2.3, and (e) in the presence of PLL and HCl at pH 2.3; ($\lambda_0 = 632.8 \text{ nm}$).

5.3.6. SER Spectra of MeRd

SERS pH profiles of MeRd shows that the optimum condition for SERS studies is under acidic conditions in the presence of PLL and HCl. Fig.5.7 shows a comparison of the

solid state spectrum with the SER spectrum for MeRd under optimized condition ($\lambda_0 = 632.8$ nm).

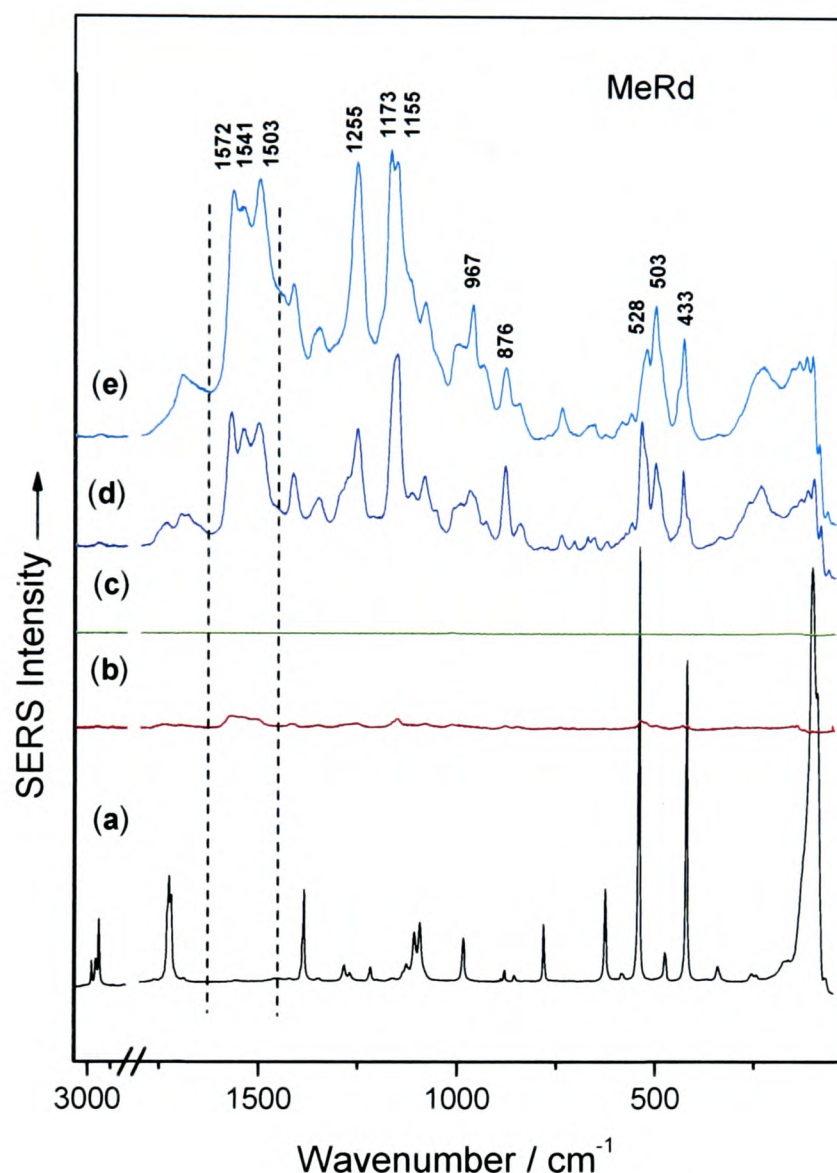


Figure 5.7. (a) Raman spectrum of MeRd (8.7×10^{-4} mol dm $^{-3}$) in the solid state ($\lambda_0 = 632.8$ nm). SER spectra of MeRd: (b) adsorbed on the Au colloid at pH 7.62, (c) adsorbed on the Ag colloid at pH 7.62, (d) in the presence of HCl at pH 2.3, and (e) in the presence of both PLL and HCl at pH 2.3; ($\lambda_0 = 632.8$ nm).

The SER spectra are dominated by three bands at 1503, 1541, and 1572 cm $^{-1}$, which are absent from the solid state spectra; whereas a majority of the bands in the SER spectrum correspond to bands in the solid state spectrum, as is the case for Rd and H $_2$ NRd. In order to understand the reasons for the occurrence of the aforementioned bands, SER spectra have been performed on Au surface as well as on Ag surface under different experimental conditions. For example, as stated above, no SERS signals are observed in the absence of

aggregating agent (Fig.5.7c). Nevertheless, addition of HCl enhances the signals as shown in Fig. 5.7d and more intense signals are observed upon the addition of both PLL and HCl. This aspect reflects the fact that aggregation is crucial for SERS enhancement.

Fig. 5.7b shows the SER spectrum of MeRd using a Au substrate. Despite the weak intensity of the SER spectrum, the bands at 1503, 1541, and 1572 cm^{-1} are easily detectable in the SER spectrum. Moreover, the addition of both HCl and PLL does not enhance the MeRd SERS signals as much as for the Rd and the amino derivative. These results suggest that MeRd is behaving in the same manner with respect to both Ag and Au substrates, but the SERS signals are more intense when using the Ag substrate.

5.3.7. Electronic Absorption Spectra

Fig.5.8.a. shows the electronic absorption spectra of Ag colloid, after the addition of 0.01% PLL only, and after the addition of both PLL and HCl (1 mol dm^{-3}). The plasmon absorption band for the Ag colloid is observed at 430 nm. The addition of PLL and HCl induces the aggregation of colloidal NPs particles, which is apparent from the electronic absorption spectra as indicated by the arrow in Fig. 5.8a. The broader band at longer wavelengths is attributed to small aggregates of Ag NPs. It has been reported in the literature that enhanced aggregation produces a broader peak further into the red, indicating the formation of larger NP clusters²⁶⁻²⁷. The electronic absorption spectra of Rd ($1 \times 10^{-3} \text{ mol dm}^{-3}$) and MeRd ($8.6 \times 10^{-4} \text{ mol dm}^{-3}$) show absorption maxima at 380 and 378 nm, respectively (Fig.5.8b, c). Addition of Rd and MeRd to the Ag colloid does not result in the appearance of a broader band at longer wavelength, indicative of non-aggregated Ag NPs. Nevertheless, upon the addition of HCl and PLL the plasmon absorption band of the Ag colloid has been red-shifted by ~ 10 nm, to 440 nm. This suggests an interaction between Ag NPs and Rd. Similarly, addition of Rd and MeRd to the aggregated colloidal NPs (*i.e.*, in the presence of PLL and HCl) also results in a red-shift of the plasmon absorption band of Ag colloid. Absorption spectra for H_2NRd in the presence of the Ag colloid are the same as those obtained for Rd.

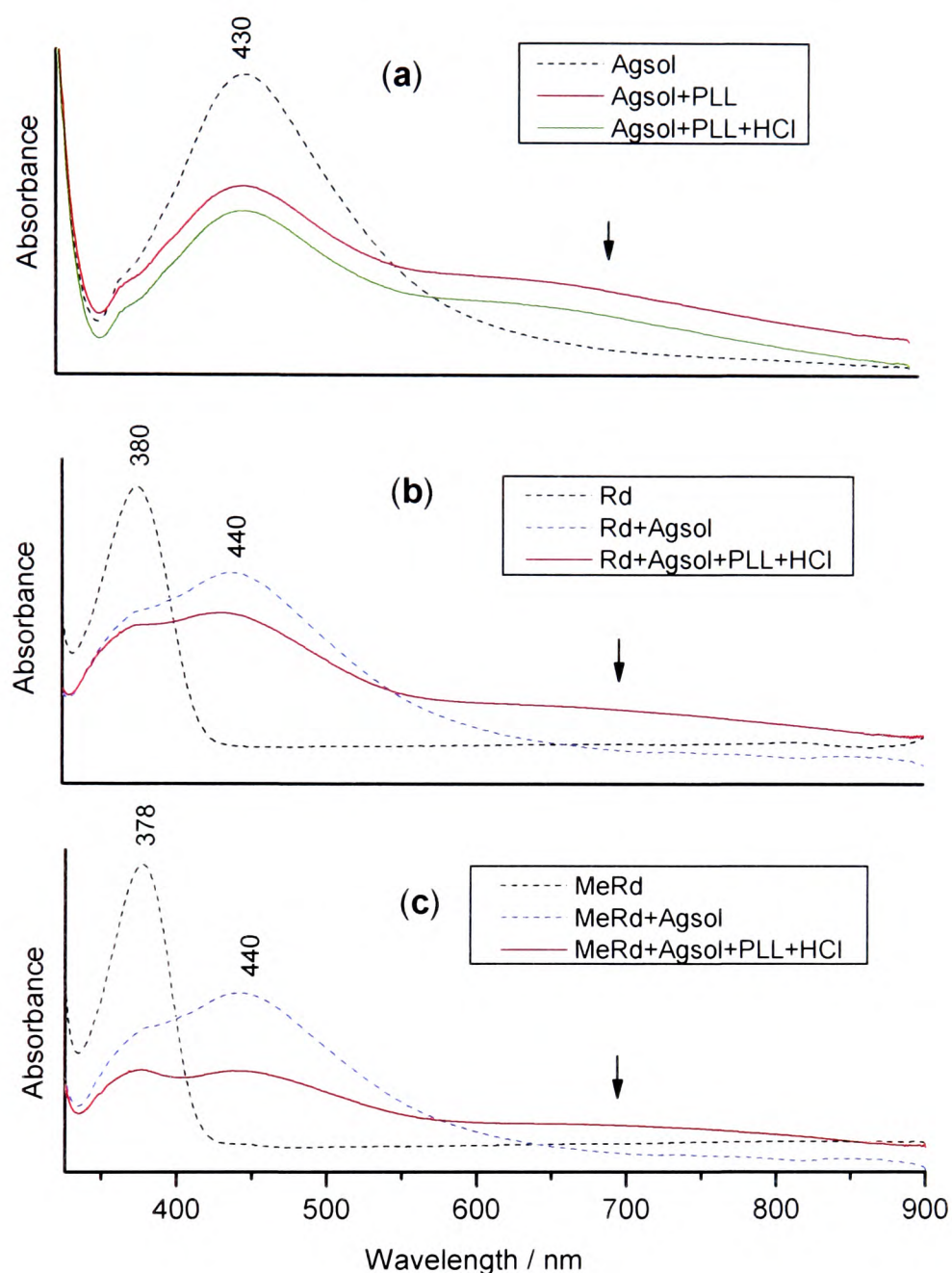


Figure 5.8. Electronic absorption spectra of (a) non-aggregated and aggregated Ag colloid, (b) Rd ($1 \times 10^{-3} \text{ mol dm}^{-3}$), and (c) MeRd ($8.7 \times 10^{-4} \text{ mol dm}^{-3}$) under different experimental conditions.

5.3.8. Origin of the Vibrational Band at $\approx 1566/1575/1572 \text{ cm}^{-1}$ in SER Spectra

A recurring characteristic of Rd and its derivatives observed during the SERS experiments with both Ag and Au NPs is the appearance of an intense vibrational band at $\approx 1566/1575/1572 \text{ cm}^{-1}$. A number of possible explanations can be put forward to assign the foregoing vibrational band in the SER spectra.

One explanation is that on Ag and Au surfaces Rd adopts either one of its other tautomeric forms or two forms exist in equilibrium. Tautomerism of Rd has been widely studied²⁸⁻²⁹. Five potential forms of Rd have been reported in the literature (as explained in Chapter one). The most prevalent form in the solid and solution state is tautomer **a** (*i.e.*, thione/keto form), which is further supported by NMR data (see appendix Fig.1.1-1.7). However, the possibility of tautomerism seems to be implausible due to the following consideration. The Rd derivatives cannot exist in the same tautomeric forms as does Rd. In particular, MeRd lacks the imino-proton to facilitate tautomerism. Possible tautomeric forms of MeRd and H₂NRd are shown in Fig.5.9. The presence of the bands at 1696 cm⁻¹ in MeRd as well as 1708 and 1750 cm⁻¹ in H₂NRd SER spectra, which are attributed to the C=O stretching mode, exclude the possibility of tautomer **b**.

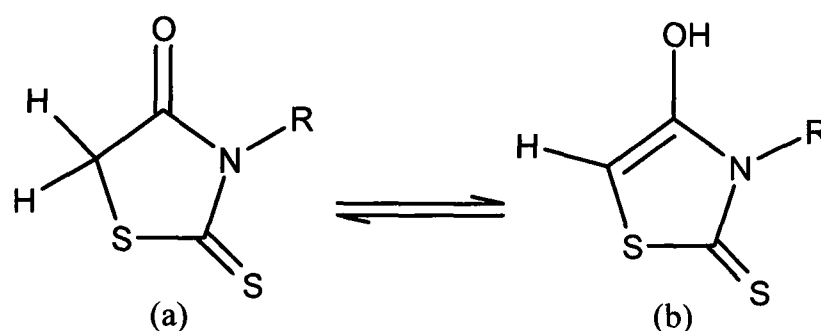


Figure 5.9. Possible tautomeric forms of Rd derivatives, R = Me or H₂N.

A second possible explanation is the formation of Ag and Au complexes owing to the electron donating nature of Rd and derivatives towards metal ions. These molecules have a propensity to form coordinate ion complexes with metals³⁰⁻³¹. It is generally accepted that Rd coordinates to Ag⁺ ions through the thiocarbonyl sulphur (C=S) and ring nitrogen atoms by forming a polymeric structure³²⁻³⁴, as shown in Fig.5.10. This explanation can also be ruled out due to the fact that metal complex formation is an inevitable consequence of de-protonation of the imino-hydrogen of Rd, whilst 3-substituted derivatives are not prone to deprotonation even in the solution state, particularly MeRd.

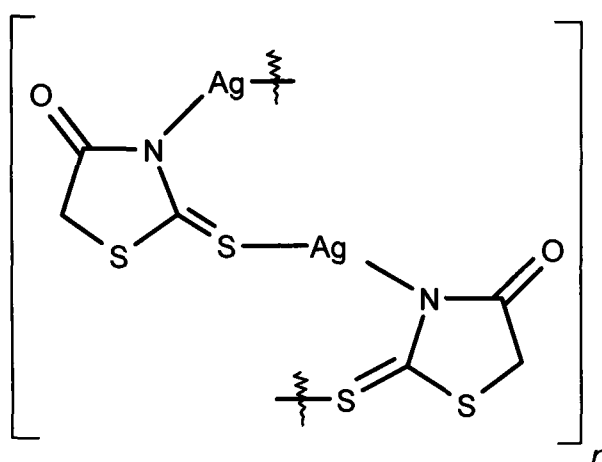


Figure 5.10. Chemical structure representing Ag complex formation with Rd³².

Thirdly, Rd could undergo polymerization in the presence of Ag and Au. Recently, Kardas *et al.* have conducted electropolymerization of Rd on Pt electrodes³⁵. FT-IR analysis of Rd polymer in the solid state revealed new vibrational bands at 1182, 1400, and 1638 cm^{-1} which were attributed to $\text{C}=\text{C}$, $\text{C}=\text{N}^+$, and $\text{C}-\text{O}^-$ stretching modes, respectively. Polymer formation proceeds by an autocatalytic mechanism and the polymer chain is formed via the carbon and nitrogen atoms. In addition to redistribution of electrons, an electrochemical coupling of Rd molecules also takes place. The oxidation process involves monomer oxidation at the amino group via cation-radical formation and coupling of cation-radicals followed by deprotonation. During further oxidation steps, molecular rearrangement takes place and further deprotonization occurs. This possibility is unlikely for the following reasons. FT-IR studies of poly(Rd) did not reveal a band at 1566 cm^{-1} (in the solid state). Moreover, it is not possible for MeRd to undergo the same mechanism of polymerization.

A fourth possibility is that ring scission of Rd and its derivatives could take place upon the addition of HCl. However, this seems implausible due to the fact that the band at 1566 cm^{-1} is also present in the SER spectrum of Rd even in the absence of HCl when adsorbed on Ag and Au substrates. Moreover, during the synthesis of Rd, HCl and high temperature are used to effect ring closure (as explained in Chapter one). In addition, bands associated with thiazolidine ring vibrations can also be observed in the SER spectra. This assertion is further supported by NMR and mass spectroscopy data, where

addition of HCl to the methanolic solution of Rd did not cause any changes in the NMR spectra compared to the absence of HCl (see appendix Fig.1.4, 1.9, 1.10, and 1.11).

Interestingly, laser irradiation could initiate a self-condensation reaction of Rd and its derivatives adsorbed to Ag and Au substrates *i.e.*, photocatalyzed condensation reactions. It is well documented that Rd and its derivatives partake in aldol condensation reactions³⁶⁻⁴¹. A review of these reactions shows that there is a nucleophilic addition of “active” methylene (at C₅ of Rd) to the corresponding aldehyde or ketone in the presence of catalyst, which is governed by the Knoevenagel reaction. It has also been established, that merocyanin dyes with a Rd nucleus have a narrow first absorption band and thus, could serve as photoelements⁴² and photosensors⁴³. Dimers of Rd derivatives have been reported in the literature; Mourad *et al*, have synthesized H₂NRd dimers by reacting H₂NRd with sulphuric acid⁴⁴. On the other hand, Nagase has prepared MeRd dimers using acetonitrile solvent at 20 °C for 48 hrs⁴⁵. The structure of the dimers of the amino/methyl derivatives prepared by the aforementioned methods is illustrated in Fig.5.11.

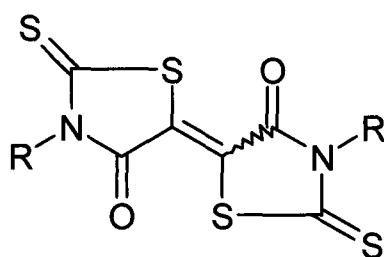
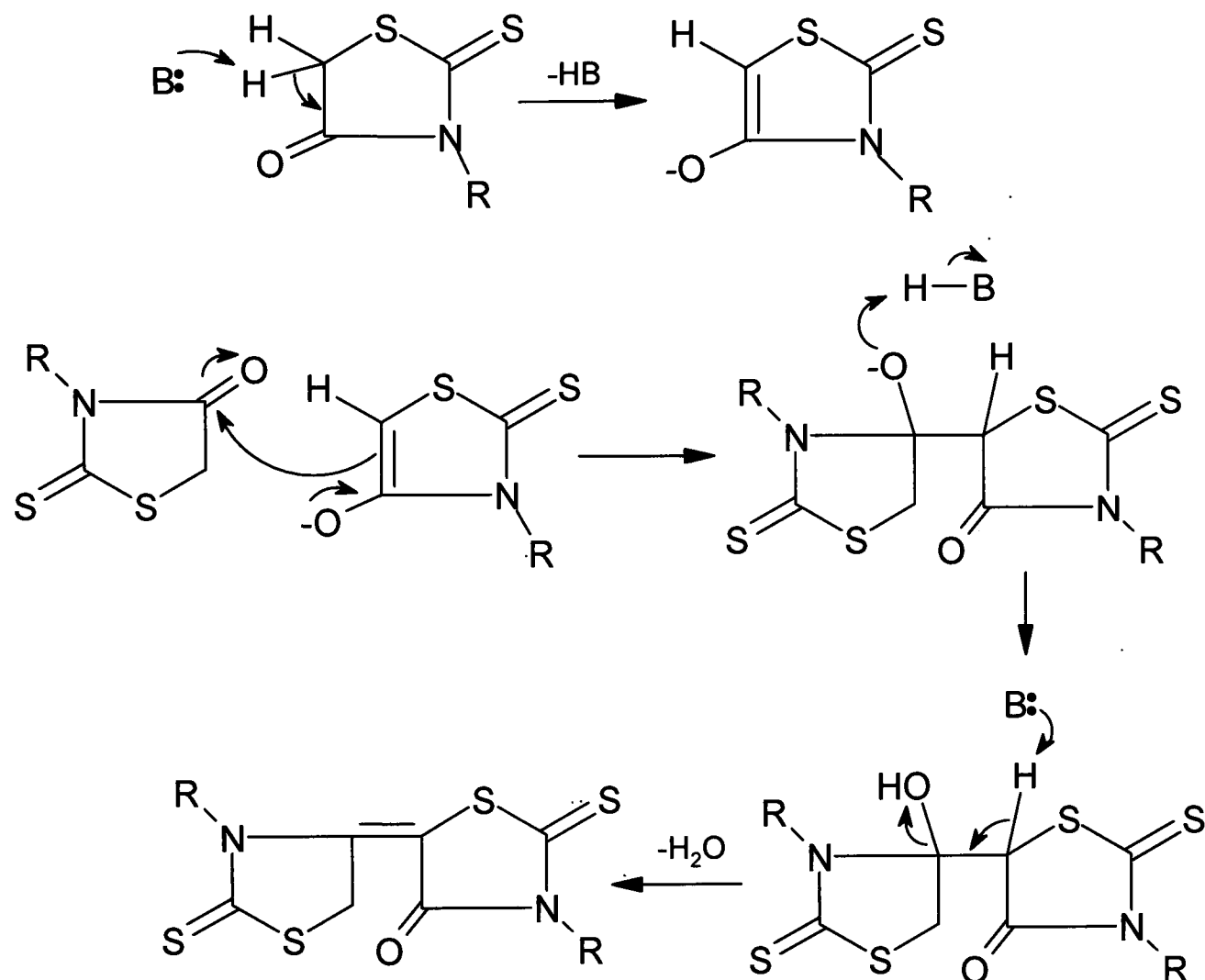


Figure 5.11. Chemical structure of dimer, R = Me or H₂N.

This explanation seems to be plausible due to the fact that Rd and its derivatives contain an active methylene group and a carbonyl group which can partake in self-condensation reaction followed by a dehydration reaction. Consequently, formation of *Z* and *E* isomers could occur. A proposed scheme for dimer formation is illustrated in Scheme 1. The mechanism proposed for the formation of dimer is different from those of Mourad *et al*, and Nagase due to the fact that bands associated with CH₂ vibrations are present in the SER spectra of these molecules. It is assumed that addition of acid results in the catalysis of the condensation reaction via the formation of C=C (OH) as opposed to C=C (O⁻), in the final step.



Scheme 1: Hypothetical photocatalyzed addition reaction of Rd and its derivatives on Ag or Au surfaces ($R=H$, CH_3 , and NH_2).

5.3.9. DFT studies: Geometry Optimization

The optimized geometries together with an atom numbering scheme for Rd, H_2NRd , and $MeRd$ dimers (E and Z isomers) are shown in Figs.5.12, 5.13, and 5.14, respectively. The optimized geometry parameters for the three molecules are tabulated in Tables 5.1, 5.2, and 5.3, respectively. DFT calculations suggest that the E -isomer of the Rd dimer is $-11.3 \text{ kJ mol}^{-1}$ more stable than the Z -isomer due to intramolecular hydrogen bonding between NH and $C=O$ moieties. On the other hand, the Z -isomers of H_2NRd and $MeRd$ are -18.5 and -15 kJ mol^{-1} more stable, respectively than the E -isomers. The calculated geometries of Rd (E -isomer), H_2NRd (Z -isomer), and $MeRd$ (Z -isomer) dimers are planar.

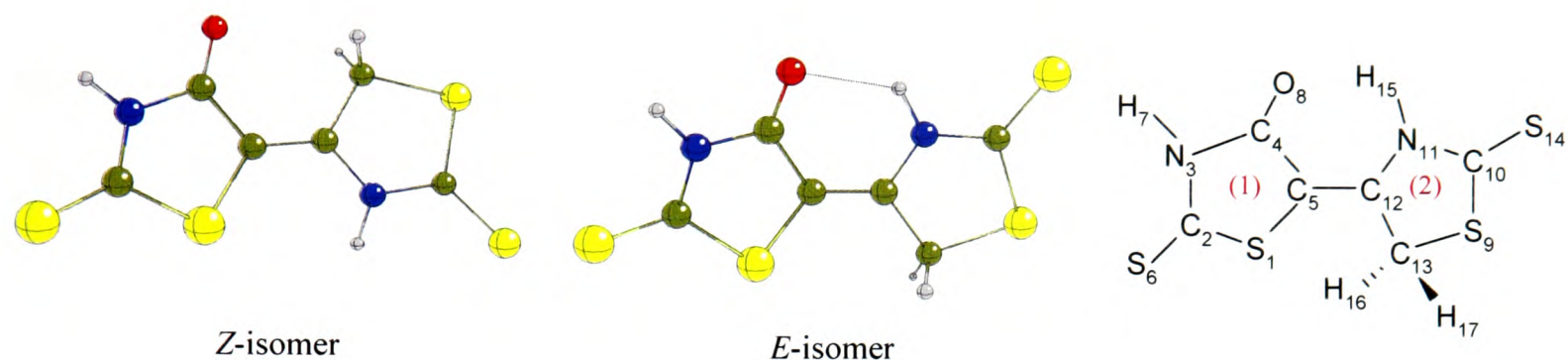


Figure 5.12. Calculated (B3LYP/ cc-pVTZ) molecular geometries (in the gas phase) of Rd dimers, and atom number labeling of the *E*-isomer.

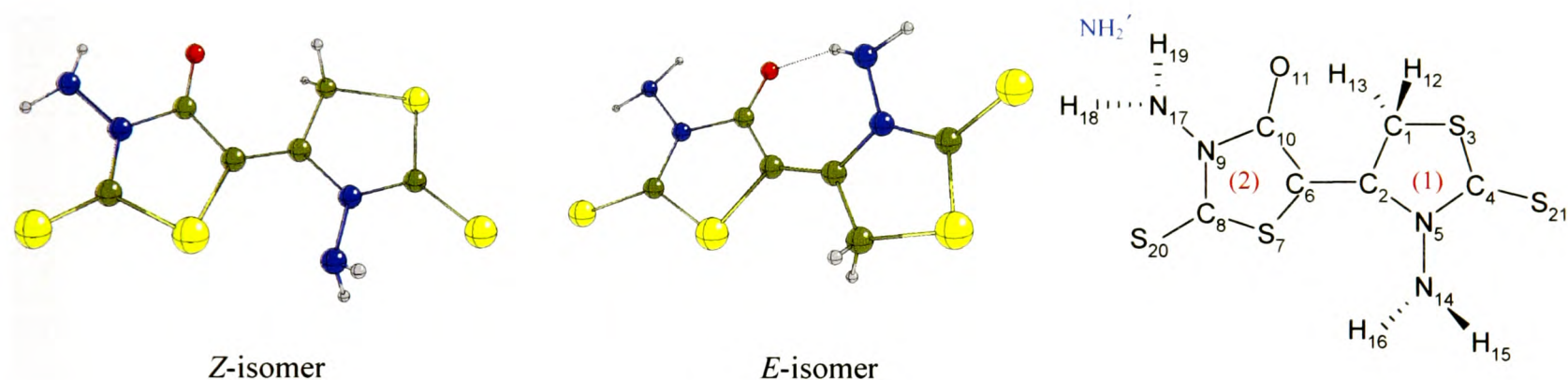


Figure 5.13. Calculated (B3LYP/ D95) molecular geometries (in the gas phase) of H₂NRd dimers and atom number labeling of the *Z*-isomer.

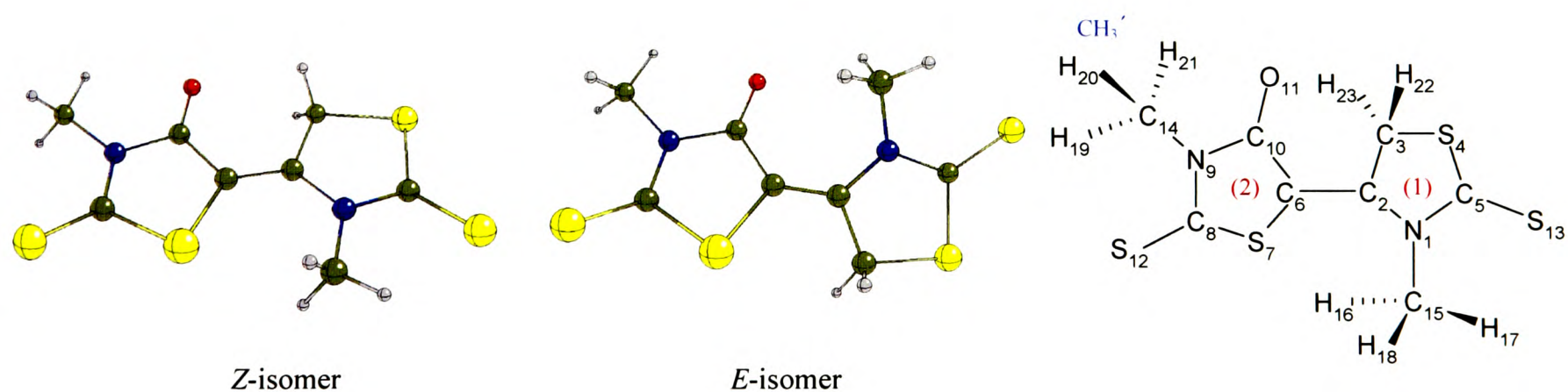


Figure 5.14. Calculated (B3LYP/ D95) molecular geometries (in the gas phase) of MeRd dimer, and atom number labeling of the *Z*-isomer.

Table 5.1. Optimized geometry parameters for *Z* and *E* isomers of Rd. Bond distances are quoted in Å; bond angles and torsion angles in degrees.

Bond distances	Z	E	Torsional angles	Z	E
r(S1-C5)	1.773	1.768	τ (C4-C5-S1-C2)	0.0	0.0
r(C2-S1)	1.771	1.769	τ (C12-C5-S1-C2)	180.0	180.0
r(C2-N3)	1.364	1.368	τ (C5-S1-C2-N3)	0.0	0.0
r(N3-C4)	1.396	1.390	τ (C5-S1-C2-S6)	180.0	180.0
r(C4-O8)	1.215	1.220	τ (S1-C5-C4-N3)	0.0	0.0
r(C4-C5)	1.463	1.459	τ (S1-C5-C4-O8)	180.0	180.0
r(C5-C12)	1.354	1.356	τ (S1-C5-C12-C13)	180.0	0.0
r(S6-C2)	1.636	1.637	τ (S1-C5-C12-N11)	0.0	180.0
r(H7-N3)	1.010	1.010	τ (S1-C2-N3-C4)	0.0	0.0
r(C10-S9)	1.755	1.767	τ (S1-C2-N3-H7)	180.0	180.0
r(C10-S14)	1.637	1.635	τ (S6-C2-N3-C4)	180.0	180.0
r(N11-C10)	1.377	1.371	τ (C2-N3-C4-O8)	180.0	180.0
r(C12-C13)	1.507	1.503	τ (C2-N3-C4-C5)	0.0	0.0
r(C12-N11)	1.369	1.365	τ (H7-N3-C2-S6)	0.0	0.0
r(C13-S9)	1.836	1.833	τ (H7-N3-C4-O8)	0.0	0.0
r(C13-H17)	1.087	1.090	τ (H7-N3-C4-C5)	180.0	180.0
r(H15-N11)	1.010	1.017	τ (N3-C4-C5-C12)	180.0	180.0
r(H16-C13)	1.087	1.090	τ (O8-C4-C5-C12)	0.0	0.0
r(H15-O8)		2.036	τ (C4-C5-C12-C13)	0.0	180.0
Interbond angles			τ (C4-C5-C12-N11)	180.0	0.0
θ (C5-S1-C2)	92.2	92.0	τ (C5-C12-C13-S9)	180.0	180.0
θ (S1-C5-C4)	110.5	110.6	τ (C5-C12-C13-H17)	-59.8	-60.3
θ (S1-C5-C12)	126.0	126.0	τ (C5-C12-C13-H16)	59.8	60.3
θ (S1-C2-N3)	108.5	108.7	τ (C5-C12-N11-C10)	180.0	180.0
θ (S1-C2-S6)	124.6	124.7	τ (C5-C12-N11-H15)	0.0	0.0
θ (C2-N3-C4)	119.9	119.4	τ (C13-S9-C10-S14)	180.0	180.0
θ (N3-C2-S6)	126.8	126.5	τ (C13-S9-C10-N11)	0.0	0.0
θ (C2-N3-H7)	119.9	119.9	τ (S9-C10-N11-C12)	0.0	0.0
θ (N3-C4-O8)	123.3	123.7	τ (S9-C10-N11-H15)	180.0	180.0
θ (N3-C4-C5)	108.7	109.0	τ (C10-S9-C13-C12)	0.0	0.0
θ (C4-N3-H7)	120.1	120.5	τ (C10-S9-C13-H17)	-120.7	-120.2
θ (O8-C4-C5)	127.8	127.1	τ (C10-S9-C13-H16)	120.7	120.2
θ (C4-C5-C12)	123.4	123.2	τ (S14-C10-N11-C12)	180.0	180.0
θ (C5-C12-C13)	124.6	124.9	τ (S14-C10-N11-H15)	0.0	0.0
θ (C5-C12-N11)	123.9	122.8	τ (C10-N11-C12-C13)	0.0	0.0
θ (S9-C10-S14)	126.3	125.1	τ (S9-C13-C12-N11)	0.0	0.0
θ (S9-C10-N11)	109.0	109.1	τ (H17-C13-C12-N11)	120.1	119.6
θ (C10-S9-C13)	93.5	93.2	τ (H16-C13-C12-N11)	-120.1	-119.6
θ (S14-C10-N11)	124.6	125.7	τ (C13-C12-N11-H15)	180.0	180.0
θ (C10-N11-C12)	120.0	119.5	τ (N3-C4-O8-H15)		180.0

$\theta(\text{C10-N11-H15})$	117.2	121.2	$\tau(\text{C5-C4-O8-H15})$	0.0
$\theta(\text{C13-C12-N11})$	111.4	112.2	$\tau(\text{C4-O8-H15-N11})$	0.0
$\theta(\text{C12-C13-S9})$	105.9	105.8	$\tau(\text{O8-H15-N11-C12})$	0.0
$\theta(\text{C12-C13-H17})$	111.4	111.1	$\tau(\text{C10-N11-H15-O8})$	180.0
$\theta(\text{C12-C13-H16})$	111.4	111.1	$\tau(\text{C4-C5-S1-C2})$	0.0
$\theta(\text{C12-N11-H15})$	122.6	119.1	$\tau(\text{C12-C5-S1-C2})$	180.0
$\theta(\text{S9-C13-H17})$	110.4	110.2	$\tau(\text{C5-S1-C2-N3})$	0.0
$\theta(\text{S9-C13-H16})$	110.4	110.2	$\tau(\text{C5-S1-C2-S6})$	180.0
$\theta(\text{H17-C13-H16})$	107.2	108.3	$\tau(\text{S1-C5-C4-N3})$	0.0
$\theta(\text{C4-O8-H15})$		100.4	$\tau(\text{S1-C5-C4-O8})$	180.0
$\theta(\text{N11-H15-O8})$		127.1	$\tau(\text{S1-C5-C12-C13})$	180.0

Table 5.2. Optimized geometry parameters of *Z* and *E* isomers of H₂NRd. Bond distances are quoted in Å, bond angles and torsion angles in degrees.

Bond distances	<i>Z</i>	<i>E</i>	Interbond angles	<i>Z</i>	<i>E</i>
r(C1-C2)	1.518	1.518	$\theta(\text{N9-N17-H18})$	111.58	110.74
r(C1-S3)	1.897	1.884	$\theta(\text{N9-N17-H19})$	111.02	111.92
r(C1-H12)	1.092	1.092	$\theta(\text{H15-N14-H16})$	111.69	117.44
r(C1-H13)	1.094	1.094	$\theta(\text{H18-N17-H19})$	119.25	119.39
r(C2-N5)	1.402	1.387	$\theta(\text{C10-O11-H15})$		105.22
r(C2-C6)	1.367	1.386	$\theta(\text{N14-H15-O11})$		150.42
r(S3-C4)	1.804	1.811	Torsional angles		
r(C4-N5)	1.405	1.404	$\tau(\text{N5-C2-C1-S3})$	0.02	-7.61
r(C4-S21)	1.678	1.686	$\tau(\text{C6-C2-C1-S3})$	179.95	172.77
r(N5-N14)	1.413	1.414	$\tau(\text{C2-C1-S3-C4})$	0	4.73
r(C6-S7)	1.837	1.844	$\tau(\text{N5-C2-C1-H12})$	-119.4	-126.76
r(C6-C10)	1.466	1.454	$\tau(\text{C6-C2-C1-H12})$	60.52	53.63
r(S7-C8)	1.836	1.828	$\tau(\text{N5-C2-C1-H13})$	119.42	-126.76
r(C8-N9)	1.377	1.377	$\tau(\text{C6-C2-C1-H13})$	-60.64	-68.78
r(C8-S20)	1.682	1.682	$\tau(\text{C1-C2-N5-C4})$	-0.04	7.73
r(N9-C10)	1.409	1.411	$\tau(\text{C1-C2-N5-N14})$	179.84	-163.24
r(N9-N17)	1.407	1.405	$\tau(\text{C1-C2-C6-S7})$	179.75	10.92
r(C10-O11)	1.269	1.269	$\tau(\text{C1-C2-C6-C10})$	-0.19	-164.26
r(N14-H15)	1.021	1.094	$\tau(\text{C4-S3-C1-H12})$	121.09	125.31
r(N14-H16)	1.021	1.031	$\tau(\text{C4-S3-C1-H13})$	-121.09	-115.56
r(N17-H18)	1.017	1.017	$\tau(\text{C1-S3-C4-N5})$	-0.01	-0.96
r(N17-H19)	1.017	1.017	$\tau(\text{C1-S3-C4-S21})$	179.98	177.02
r(H15-O11)	1.764		$\tau(\text{C4-N5-C2-C6})$	-179.97	-172.69
Interbond angles			$\tau(\text{N14-N5-C2-C6})$	-0.08	16.32
$\theta(\text{C2-C1-S3})$	106.69	106.9	$\tau(\text{N5-C2-C6-S7})$	-0.32	-168.61
$\theta(\text{C2-C1-H12})$	111.86	111.37	$\tau(\text{N5-C2-C6-C10})$	179.73	16.2
$\theta(\text{C2-C1-H13})$	111.86	111.42	$\tau(\text{C2-N5-C4-S3})$	0.03	-3.76

$\theta(\text{C1-C2-N5})$	111.79	112.26	$\tau(\text{C2-N5-C4-S21})$	-179.96	178.26
$\theta(\text{C1-C2-C6})$	123.19	120.55	$\tau(\text{C2-N5-N14-H15})$	-117.01	-49.12
$\theta(\text{S3-C1-H12})$	109.25	109.14	$\tau(\text{C2-N5-N14-H16})$	118.21	178.7
$\theta(\text{S3-C1-H13})$	109.23	108.53	$\tau(\text{C2-C6-S7-C8})$	-179.96	-178.8
$\theta(\text{C1-S3-C4})$	92.17	91.35	$\tau(\text{C2-C6-C10-N9})$	-179.06	179.77
$\theta(\text{H12-C1-H13})$	107.88	109.36	$\tau(\text{C2-C6-C10-O11})$	1.57	4.34
$\theta(\text{N5-C2-C6})$	125	127.18	$\tau(\text{S3-C4-N5-N14})$	-179.84	167.48
$\theta(\text{C2-N5-C4})$	119.59	118.53	$\tau(\text{N14-N5-C4-S21})$	0.15	-10.48
$\theta(\text{C2-N5-N14})$	119.3	121.9	$\tau(\text{C4-N5-N14-H15})$	62.86	139.93
$\theta(\text{C2-C6-S7})$	127.9	119.64	$\tau(\text{C4-N5-N14-H16})$	-61.9	7.76
$\theta(\text{C2-C6-C10})$	121.53	130.53	$\tau(\text{C8-S7-C6-C10})$	-0.01	-2.68
$\theta(\text{S3-C4-N5})$	109.73	110.41	$\tau(\text{S7-C6-C10-N9})$	0.98	4.22
$\theta(\text{S3-C4-S21})$	125.39	124.37	$\tau(\text{S7-C6-C10-O11})$	-178.37	-171.21
$\theta(\text{N5-C4-S21})$	124.87	125.18	$\tau(\text{C6-S7-C8-N9})$	-0.97	0.43
$\theta(\text{C4-N5-N14})$	121.09	118.96	$\tau(\text{C6-S7-C8-S20})$	178.72	179.68
$\theta(\text{N5-N14-H15})$	110.95	112.36	$\tau(\text{C6-C10-N9-C8})$	-1.92	-4.34
$\theta(\text{N5-N14-H16})$	110.92	109.23	$\tau(\text{C6-C10-N9-N17})$	174.52	174.9
$\theta(\text{S7-C6-C10})$	110.55	109.68	$\tau(\text{S7-C8-N9-C10})$	1.88	2.17
$\theta(\text{C6-S7-C8})$	90.3	91.16	$\tau(\text{S7-C8-N9-N17})$	-174.4	2.17
$\theta(\text{C6-C10-N9})$	110.41	110.67	$\tau(\text{C10-N9-C8-S20})$	-177.81	-177.06
$\theta(\text{C6-C10-O11})$	128.5	129.77	$\tau(\text{N17-N9-C8-S20})$	5.89	3.71
$\theta(\text{S7-C8-N9})$	109.23	108.19	$\tau(\text{C8-N9-C10-O11})$	177.48	
$\theta(\text{S7-C8-S20})$	124.83	125.25	$\tau(\text{C8-N9-N17-H18})$	-24.52	-24.41
$\theta(\text{N9-C8-S20})$	125.92	126.54	$\tau(\text{C8-N9-N17-H19})$	-160.18	-160.33
$\theta(\text{C8-N9-C10})$	119.45	120.11	$\tau(\text{O11-C10-N9-N17})$	-6.06	-9.11
$\theta(\text{C8-N9-N17})$	122.2	121.96	$\tau(\text{C10-N9-N17-H18})$	159.13	156.35
$\theta(\text{C10-N9-N17})$	118.23	117.92	$\tau(\text{C10-N9-N17-H19})$	23.47	20.43
$\theta(\text{N9-C10-O11})$	121.07	119.4	$\tau(\text{N9-C10-O11-H15})$		158.62

Table 5.3. Optimized geometry parameters of *Z* and *E* isomers of MeRd. Bond distances are quoted in Å; bond angles and torsion angles in degrees.

Bond distances	<i>Z</i>	<i>E</i>	Interbond angles	<i>Z</i>	<i>E</i>
r(N1-C5)	1.409	1.404	$\theta(\text{H19-C14-H21})$	108.67	109.9
r(C2-C3)	1.523	1.521	$\theta(\text{H20-C14-N9})$	107.48	107.49
r(C2-N1)	1.401	1.399	$\theta(\text{H20-C14-H21})$	110.5	110.32
r(C3-H23)	1.091	1.095	$\theta(\text{N9-C14-H21})$	109.83	109.9
r(C3-S4)	1.881	1.883	$\theta(\text{H16-C15-H17})$	109	108.83
r(C5-S4)	1.804	1.819	$\theta(\text{H16-C15-N1})$	110.31	108.46
r(C5-S13)	1.682	1.677	$\theta(\text{H17-C15-N1})$	107.83	107.71
r(C6-C2)	1.377	1.375	$\theta(\text{H17-C15-H18})$	109.02	110.18
r(S7-C6)	1.843	1.842	$\theta(\text{N1-C15-H18})$	110.28	111.28
r(C8-S7)	1.827	1.829	$\theta(\text{H19-C14-H21})$	108.67	109.9

r(C8-N9)	1.381	1.381	Torsional angles		
r(N9-C10)	1.422	1.429	τ (S4-C5-N1-C2)	0.05	-5.61
r(C10-O11)	1.257	1.252	τ (S13-C5-N1-C2)	-179.94	174.79
r(C10-C6)	1.473	1.472	τ (C5-N1-C2-C3)	-0.13	15.35
r(S12-C8)	1.677	1.677	τ (C5-N1-C2-C6)	179.85	-165.43
r(C14-H19)	1.094	1.094	τ (C15-N1-C5-S4)	-179.92	168.86
r(C14-H20)	1.091	1.091	τ (N1-C5-S4-C3)	0.03	-4.22
r(C14-N9)	1.475	1.475	τ (C15-N1-C5-S13)	0.07	-10.73
r(C15-H16)	1.093	1.092	τ (C5-N1-C15-H16)	-118.7	-143.02
r(C15-H17)	1.091	1.091	τ (C5-N1-C15-H17)	0.22	-23.59
r(C15-N1)	1.481	1.485	τ (C5-N1-C15-H18)	119.17	97.27
r(H18-C15)	1.093	1.089	τ (H23-C3-C2-N1)	119.95	101.38
r(H21-C14)	1.094	1.094	τ (S4-C3-C2-N1)	0.14	-16.91
r(H22-C3)	1.091	1.095	τ (H22-C3-C2-N1)	-119.65	-135.87
Interbond angles			τ (C3-C2-N1-C15)	179.84	15.35
θ (C5-N1-C2)	118.05	117.31	τ (C6-C2-C3-H23)	-60.03	-77.9
θ (N1-C5-S4)	110.65	110.57	τ (C6-C2-C3-S4)	-179.84	163.79
θ (N1-C5-S13)	126.84	126.71	τ (C2-C3-S4-C5)	-0.09	11.62
θ (C5-N1-C15)	119.2	119.21	τ (H22-C3-C2-C6)	60.35	44.83
θ (C3-C2-N1)	112.46	112.18	τ (C3-C2-C6-S7)	179.89	11.47
θ (C2-C3-H23)	111.65	111.73	τ (C3-C2-C6-C10)	-0.06	-162.66
θ (C2-C3-S4)	106.84	106.08	τ (C15-N1-C2-C6)	-0.16	20.33
θ (C3-C2-C6)	120.56	119.7	τ (N1-C2-C6-S7)	-0.09	-167.68
θ (C2-C3-H22)	111.64	111.41	τ (N1-C2-C6-C10)	179.94	18.17
θ (N1-C2-C6)	126.97	128.11	τ (C2-N1-C15-H16)	61.31	31.1
θ (C2-N1-C15)	122.74	123.22	τ (C2-N1-C15-H17)	-179.75	150.53
θ (H23-C3-S4)	109.59	108.69	τ (C2-N1-C15-H18)	-60.8	-88.58
θ (H23-C3-H22)	107.5	109.42	τ (H23-C3-S4-C5)	-121.22	-108.66
θ (C3-S4-C5)	91.99	91.27	τ (H22-C3-S4-C5)	121.02	131.91
θ (S4-C3-H22)	109.58	109.38	τ (C3-S4-C5-S13)	-179.97	175.38
θ (S4-C5-S13)	122.49	122.7	τ (C2-C6-S7-C8)	-179.94	-179.11
θ (C2-C6-S7)	129.16	119.37	τ (C2-C6-C10-N9)	179.95	179.15
θ (C2-C6-C10)	121.72	130.73	τ (C2-C6-C10-O11)	-0.04	2.85
θ (C6-S7-C8)	91.42	91.25	τ (C10-C6-S7-C8)	0.01	-3.82
θ (S7-C6-C10)	109.11	109.25	τ (C6-S7-C8-N9)	-0.01	2.1
θ (S7-C8-N9)	109.41	109.25	τ (C6-S7-C8-S12)	179.98	-178.22
θ (S7-C8-S12)	123.11	123.24	τ (S7-C6-C10-N9)	-0.01	4.57
θ (C8-N9-C10)	118.55	118.92	τ (S7-C6-C10-O11)	179.98	-171.71
θ (N9-C8-S12)	127.48	123.24	τ (S7-C8-N9-C10)	0.01	0.26
θ (C8-N9-C14)	121.41	121.23	τ (S7-C8-N9-C14)	-179.99	177.43
θ (N9-C10-O11)	121.65	121.27	τ (S12-C8-N9-C10)	-179.98	-179.4
θ (N9-C10-C6)	111.48	110.69	τ (C8-N9-C10-O11)	179.99	173.32
θ (C10-N9-C14)	120.02	119.77	τ (C8-N9-C10-C6)	0	-3.25
θ (O11-C10-C6)	126.85	127.92	τ (C14-N9-C8-S12)	0	-2.23

$\theta(\text{H19-C14-H20})$	110.49	107.49	$\tau(\text{C8-N9-C14-H19})$	-59.83	62.07
$\theta(\text{H19-C14-N9})$	109.84	109.83	$\tau(\text{C8-N9-C14-H20})$	179.91	-177.53

5.3.10. Vibrational Band Assignments

Simulated Raman spectra of Rd dimers (*E* and *Z*-isomers), calculated by convolution with a Lorentzian lineshape (full-width-half-maximum=10 cm^{-1}), are compared with the experimental SER spectra adsorbed on Ag surface under optimized SERS conditions, at both excitation wavelengths (514.5 and 632.8 nm), in Fig.5.15. Similarly, simulated Raman spectra of H₂NRd and MeRd dimers are compared with the experimental SER spectra adsorbed on Ag surface under optimized SERS conditions using $\lambda_o = 632.8$ nm (Figs.5.16-5.17). The scaled vibrational wavenumbers, together with their PED values are compared with the experimental SER spectra, adsorbed on Ag and Au surfaces under different experimental protocols using both 514.5 and 632.8 nm excitation wavelengths for the Rd dimer in Table 5.4. However, for the Rd derivatives the scaled vibrational wavenumbers, together with their PEDs are contrasted with the experimental SER spectra, adsorbed on Ag and Au surfaces under optimized conditions at an excitation wavelength of 632.8 nm only. Generally, the calculated (simulated) spectral profiles show good agreement with the experimentally derived spectra. However, some of the vibrational modes associated with N-H group are subject to small errors in wavenumber, as a consequence of hydrogen bonding.

5.3.11. Rd Dimer (*E*-Isomer)

The vibrational band assignments for Rd in the solid state have been discussed in Chapter four. The three intense bands at 427/489, and 545 cm^{-1} in the solid state spectrum are predominantly assigned to in-plane (ip) and out-plane (op) ring deformation modes, respectively. The first and third bands are red-shifted and found at 417 and 537 cm^{-1} , respectively in the solution spectrum; the second band is blue shifted by ~ 3 cm^{-1} . Conversely, in SER spectra the first band has been blue-shifted by ~ 11 cm^{-1} and is observed at 556 cm^{-1} followed by a shoulder at 521 cm^{-1} and is mainly attributed to the ip

ring-2 deformation mode of the dimer. This band is weak in intensity using 514.5 nm excitation as opposed to 632.8 nm excitation. The second band is $\approx 44 \text{ cm}^{-1}$ red-shifted and found at 444 cm^{-1} followed by a shoulder at 430 cm^{-1} and attributed to an ip ring-2 deformation mode. Its counterpart, using 514.5 nm excitation, is observed at 452 cm^{-1} and enhanced compared to 632.8 nm excitation. The third band occurs at $\sim 420 \text{ cm}^{-1}$ in SER spectra, and appears to be a heavily mixed mode. The calculated PEDs suggest that the main contribution is due to ip ring-1 deformation, C=S stretching, and C-S stretching modes. C=O stretching vibrations are associated with the bands at 1649, 1706, and 1760 cm^{-1} in the Ag SER spectrum under optimized conditions. The C=O deformation modes are observed at 584, and 722 cm^{-1} , respectively. It is worth noting that in the C=O stretching region more than one band is observed in the solid, solution and SER spectra. The appearance of additional bands could be attributed to intramolecular hydrogen bonding.

The intense band at $\approx 1566 \text{ cm}^{-1}$ is attributed to the C=C stretching mode of the (hypothetical) Rd dimer. In the absence of any aggregating agent, under neutral conditions using a Ag colloid and 632.8 nm excitation, the corresponding band is $\approx 10 \text{ cm}^{-1}$ red-shifted. On the other hand, in an acidic environment using 514.5 nm excitation this band is significantly enhanced and is the most intense band in the SER spectrum. The SER spectra also show band shifts in comparison to the solid state Raman spectrum, in the $1206\text{-}1480 \text{ cm}^{-1}$ region, which are associated with C-N stretching, N-H ip deformation, and CH_2 deformation modes. For example, a band at 1457 cm^{-1} in the solid state spectrum is red-shifted in the Ag colloid SER spectrum under neutral and optimized conditions (632.8 nm) and observed at 1451 and 1485 cm^{-1} , respectively. According to the DFT calculations, this band can be assigned to C-N stretching and ip N-H deformation modes. The CH_2 deformation is attributed to the band at $\sim 1382 \text{ cm}^{-1}$. It is interesting to note that additional bands found in the above-mentioned region are absent in solid state spectra. For example, two medium intensity bands at 1312 and 1347 cm^{-1} in the Ag colloid SER spectra (*i.e.*, under optimized and neutral conditions using 632.8 nm excitation) are absent in the solid state spectra. The calculated PEDs

reveal that these vibrations involve more than one type of motion but the major contribution is from C-N stretching.

The bands associated with the thioamide (N-C=S) modes are observed at 1066, 1078, and 1176 cm^{-1} in the solid state spectrum. The band at 1176 cm^{-1} in the solid state spectrum is blue-shifted and observed at $\sim 1191 \text{ cm}^{-1}$ in SER spectra using 632.8 nm excitation, both under optimized and neutral pH conditions; and is assigned to C-N stretching, C=S stretching, and NH ip deformation modes (thioamide II). Its counterpart using 514.5 nm excitation occurs at 1177 cm^{-1} and is relatively weak in intensity. In the solid state spectrum the major contribution to the bands at 1066 and 1078 cm^{-1} is due to the C=S stretching mode (thioamide III). Nevertheless, in SER spectra the former band is blue shifted by $\sim 23 \text{ cm}^{-1}$ and the latter band is weak in intensity. In the solution spectrum a weak band at 1074 cm^{-1} is assigned to the thioamide III mode. The shift in frequency for the bands associated with thioamide groups in SER spectra suggest that the dimer is coordinating to the Ag surface and Au surface through the sulfur atom. According to the DFT calculations the bands observed in the 903-1015 cm^{-1} region in SER spectra are predominantly assigned to the C-C stretching modes. These bands are absent in the solid state spectrum. The C-S stretching modes are attributed to the bands at 649, 722, and $\sim 784 \text{ cm}^{-1}$ in the SER spectra. A medium intensity band at 325 cm^{-1} is assigned to a ip C-S deformation mode coupled to ip and op C-C and C=O deformation modes. Assignment of the band at $\sim 203 \text{ cm}^{-1}$ is ambiguous due to the fact that bands associated with Ag-N, Ag-O, Ag-S, and Ag-Cl vibrations will occur in almost the same wavenumber region.

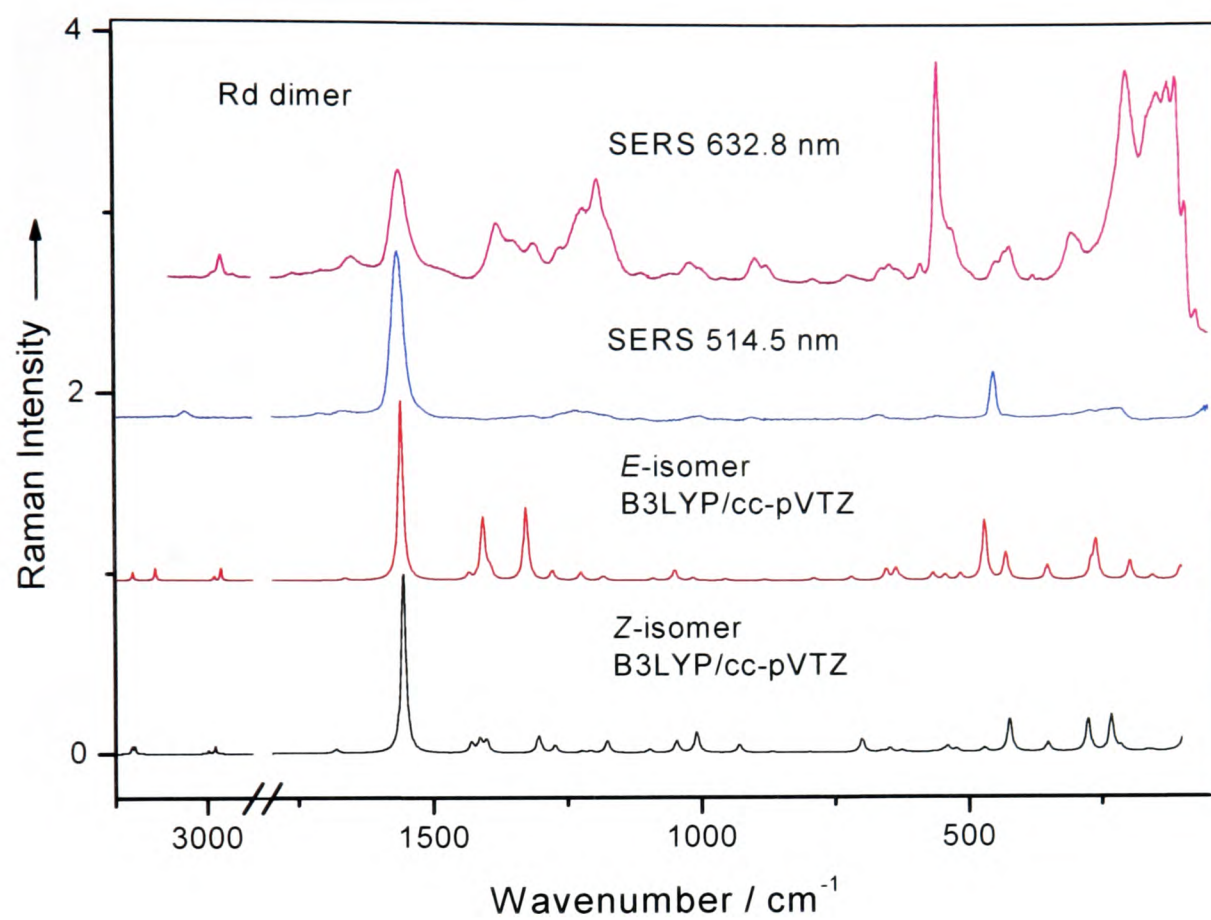


Figure 5.15. Experimental and calculated SER spectra of the Rd dimer (*E*-isomer) under optimized experimental conditions using (a) $\lambda_o = 514.5$ and (b) $\lambda_o = 632.8$ nm.

Table 5.4. Experimental and theoretical calculations (NCA) for Rd dimer.

Ag SERS ^a	Ag SERS ^b	Ag SERS ^c	Au SERS ^d	Calc.	Assignments (% PEDs)	
Expt. $\tilde{\nu} / \text{cm}^{-1}$						
3126 w				3407	$\nu_{\text{as}}(\text{N3H7})$ (100)	
2957 w				3283	$\nu_{\text{s}}(\text{N11H15})$ (100)	
2918 w	2922 m	2921 w	2922 w	2925	$\nu_{\text{as}}(\text{CH}_2)$ (100)	
2841 w	2847 w	2849 w	2847 vw		$\nu_{\text{s}}(\text{CH}_2)$ (100)	
1711 w	1706 w	1760 w	1706 w	1664	$\nu_{\text{s}}(\text{C=O})$ (75)	
1673 vw	1683 w	1706 w	1660 w			
1649 vw	1655 m	1649 w				
1566 vs	1555 m	1566 s	1566 m	1560	$\nu_{\text{s}}(\text{C=C})$ (53), $\delta_{\text{ip}}(\text{N11H15})$ (15)	
1445 w	1451 w	1480 w	1474 vw	1408	$\nu_{\text{s}}(\text{C10N11})$ (190), $\nu_{\text{s}}(\text{N11C12})$ (10), $\nu_{\text{s}}(\text{C=C})$ (10), $\delta_{\text{ip}}(\text{N11H15})$ (27), $\delta(\text{CH}_2)$ (12)	
1375 vw	1382 s	1380 m		1434	$\delta(\text{CH}_2)$ (86)	
		1347 m		1395	$\nu_{\text{s}}(\text{C2N3})$ (32), $\delta_{\text{ip}}(\text{N3H7})$ (44)	
1312 m	1309 w	1312 m		1328	$\nu_{\text{s}}(\text{C10N11})$ (10), $\nu_{\text{s}}(\text{N11C12})$ (35), $\nu_{\text{s}}(\text{C12C13})$ (13), $\delta_{\text{ip}}(\text{C12C5})$ (15)	
1265 vw	1271 w	1259 m		1279	$\nu_{\text{s}}(\text{C2N3})$ (11), $\nu_{\text{s}}(\text{N3C4})$ (31), $\nu_{\text{s}}(\text{C4C5})$ (12), $\delta_{\text{ip}}(\text{C=O})$ (12)	
1208 m		1217 m	1220 vw	1225	$\omega(\text{CH}_2)$ (73)	
1177 w	1187 s	1191 s	1192 s	1185	$\nu_{\text{s}}(\text{C10S14})$ (10), $\nu_{\text{s}}(\text{C10N11})$ (23), $\delta_{\text{ip}}(\text{N3H7})$ (10), $\delta_{\text{ip}}(\text{N11H15})$ (18), $\omega(\text{CH}_2)$ (13)	
				1181	$\nu_{\text{s}}(\text{C2N3})$ (19), $\nu_{\text{s}}(\text{C10N11})$ (13), $\delta_{\text{ip}}(\text{N3H7})$ (21), $\delta_{\text{ip}}(\text{N11H15})$ (15)	
1114 w	1106 w	1109 w	1106 vw	1116	$\tau(\text{CH}_2)$ (92)	
			1098 vw	1091	$\nu_{\text{s}}(\text{C10S14})$ (40), $\delta_{\text{ip}}(\text{ring-2})$ $\delta_{\text{op}}(\text{ring-2})$ (17)	
	1075 w	1055 w	1055 vw	1050	$\nu_{\text{s}}(\text{C2S6})$ (46), $\nu_{\text{s}}(\text{C2N3})$ (10), $\delta_{\text{ip}}(\text{ring-1})$ 14	

1015 w	1015 m	1016 m	1017 vw	1016	$\nu_s(\text{N3C4})$ (18), $\nu_s(\text{C4C5})$ (25), $\nu_s(\text{C5S1})$ (18), $\delta_{ip}(\text{C5C12})$ (10)
960 vw	994 m	994 w		954	$\nu_s(\text{N11C12})$ (13), $\nu_s(\text{C12C13})$ (41)
903 w	992 w	992 w			
	896 m	896 m	896 vw	882	$\rho(\text{CH}_2)$ 82
	874 m	870 w	870 vw		
	787 w	787 w	787 vw	789	$\nu_s(\text{C12C13})$ (10), $\nu_s(\text{C13S9})$ (12), $\delta_{ip}(\text{ring-2})$ (36)
724 vw	720 w	722 w	730 vw	719	$\nu_s(\text{C13S9})$ (64)
665 m		645 m	649 w	654	$\nu_s(\text{S1C2})$ (59), $\delta_{ip}(\text{ring-1})$ (14)
627 w	633 m			636	$\nu_s(\text{S9C10})$ (62), $\delta_{ip}(\text{ring-2})$ (12)
				625	$\delta_{op}(\text{N3H7})$ (100)
	585 m	584 w	584 w	566	$\nu_s(\text{C13S9})$ (12), $\delta_{ip}(\text{ring-1})$ (26), $\delta_{ip}(\text{C=O})$ (23)
556 m	555 vs	556 w	555 s	557	$\nu_s(\text{C10S14})$ (31), $\delta_{op}(\text{C12C5})$ (24), $\delta_{ip}(\text{ring-2})$ (17)
534 w	521 sh	521 sh	521 sh		
				543	$\nu_s(\text{C2S6})$ (11), $\nu_s(\text{C5S1})$ (24), $\delta_{op}(\text{ring-1})$ (31)
452 s	445 w	444 m	448 w	469	$\nu_s(\text{C10S14})$ (11), $\delta_{op}(\text{ring-2})$ (53)
		430 sh			
421 w	413 w	419 m	418 vw	429	$\nu_s(\text{C2S6})$ (14), $\nu_s(\text{S1C2})$ (11), $\nu_s(\text{C5S1})$ (12), $\delta_{op}(\text{ring-1})$ (12), $\delta_{ip}(\text{C=O})$ (14)
325 vw		376 w	325 m	351	$\nu_s(\text{S9C10})$ (12), $\delta_{op}(\text{C=O})$ (10), $\delta_{op}(\text{C10S14})$ (17), $\delta_{ip}(\text{C12C5})$ (19)
		325 m			
270 w	296 m			293	$\delta_{op}(\text{C5C12})$ (43), $\tau_{ip}(\text{ring-1})$ (11), $\tau_{op}(\text{ring-1})$ (12)
	261 w			261	$\nu_s(\text{C=C})$ (10), $\tau_{ip}(\text{ring-1})$ (16), $\delta_{ip}(\text{C2S6})$ (35)
216 s	200 s	203 s	195 s		
				197	$\nu_s(\text{C5S1})$ (10), $\delta_{ip}(\text{C2S6})$ (15), $\delta_{ip}(\text{C10S14})$ (30)
	147 w	147		154	$\tau_{ip}(\text{ring-1})$ (12), $\tau_{op}(\text{ring-1})$ (27), $\tau_{op}(\text{ring-2})$ (23), $\tau(\text{C=C})$ 25
	128 s	128 s		102	$\tau_{op}(\text{ring-1})$ 27, $\tau_{ip}(\text{ring-2})$ (59)
	94 m	110		86	$\delta_{ip}(\text{C5C12})$ (42), $\delta_{ip}(\text{C12C5})$ (39)

^a With acid and PLL (514.5 nm laser); ^b without acid and PLL; ^c with acid and PLL; and ^d without acid and PLL (632.8 nm laser).

5.3.12. H₂NRd Dimer (Z-Isomer)

A very intense band at 542 cm⁻¹ in the solid state spectrum of H₂NRd is assigned to a ip ring deformation mode. This band is red-shifted in the solution spectrum and observed at 538 cm⁻¹. Whereas, in SER spectra the band at 526 cm⁻¹ (followed by shoulders at 504 and 539 cm⁻¹) is attributed to the ip ring-2 deformation mode. The DFT calculation suggests that this band is mainly due to a combination of C-S stretching and ip ring-2 modes. The bands for op ring deformation modes in the solid state spectrum are observed at 422 and 485 cm⁻¹. These bands are red-shifted by ~4 cm⁻¹ in the solution spectrum; and in the Ag SER spectrum by ~5 and ~ 45 cm⁻¹ and found at 415 and 436 cm⁻¹, respectively. The former band is absent in the Au SER spectrum. The calculated PEDs predict that these bands are predominantly assigned to op ring-1 and ring-2 deformation modes. The C=O stretching mode is attributed to the bands at 1708 and 1750 cm⁻¹ in the Ag SER spectrum. The former band is absent in the Au SER spectrum. A weak band at 763 cm⁻¹ is attributed to a C=O deformation mode.

In SER spectra, the intense band at 1575 cm⁻¹ is assigned to the C=C stretching mode of the (hypothetical) H₂NRd dimer, which is in good agreement with the calculated value at 1563 cm⁻¹. This band is absent in the solid state spectrum. A weak band at 1536 cm⁻¹ in the solid state spectrum is attributed to a NH₂ deformation mode, which is 36 cm⁻¹ red-shifted and observed at 1500 cm⁻¹ in the SER spectra. The CH₂ deformation mode is assigned to a strong band at 1389 cm⁻¹ in the Ag SER spectrum. Whereas, its counterpart in the Au SER spectrum is 10 cm⁻¹ red-shifted and found at 1378 cm⁻¹. A band at 1355 cm⁻¹ appears to be mixed and is ascribed to C-N and N-N deformation modes; it is absent in the Au SER spectrum. The C-N stretching mode is also assigned to a weak band at 1252 cm⁻¹ in the SER spectra.

The bands for thioamide mode II are observed at 1126 and 1158 cm⁻¹ in the solid state spectrum. Whereas, in the SER spectra -instead of two bands- only one band is observed at 1166 cm⁻¹. The calculated PEDs show that this band is heavily mixed and assigned to C=S, C-N, N-N stretching and NH₂ rocking modes. The thioamide mode III

is attributed to the bands at 1044 and 1082 cm^{-1} in the solid state spectrum. Both bands are red-shifted and observed at 1021 and 1064 cm^{-1} in SER spectra. The bands associated with C-S stretching modes are found in the 665-947 cm^{-1} region. For example, a medium intensity band at 666 cm^{-1} is predominantly assigned to a C-S stretching mode in the Ag colloid SER spectrum. Its counterpart in the Au colloid spectrum is weak and observed at 635 cm^{-1} . In the solid state spectrum, two bands at 331 and 365 cm^{-1} are attributed to the ip C=O and ip N-N deformation modes. These bands are blue-shifted by ~ 15 and ~ 18 cm^{-1} , respectively in the Ag SER spectrum. For H_2NRd , enhancement of bands due to thioamide and C-N stretching modes suggests coordination via the C=S moiety. As for Rd, the assignments of the bands at 208 and 224 cm^{-1} are ambiguous due to the fact that bands associated with Ag-N, Ag-O, Ag-S, and Ag-Cl vibrations will occur in almost the same wavenumber region.

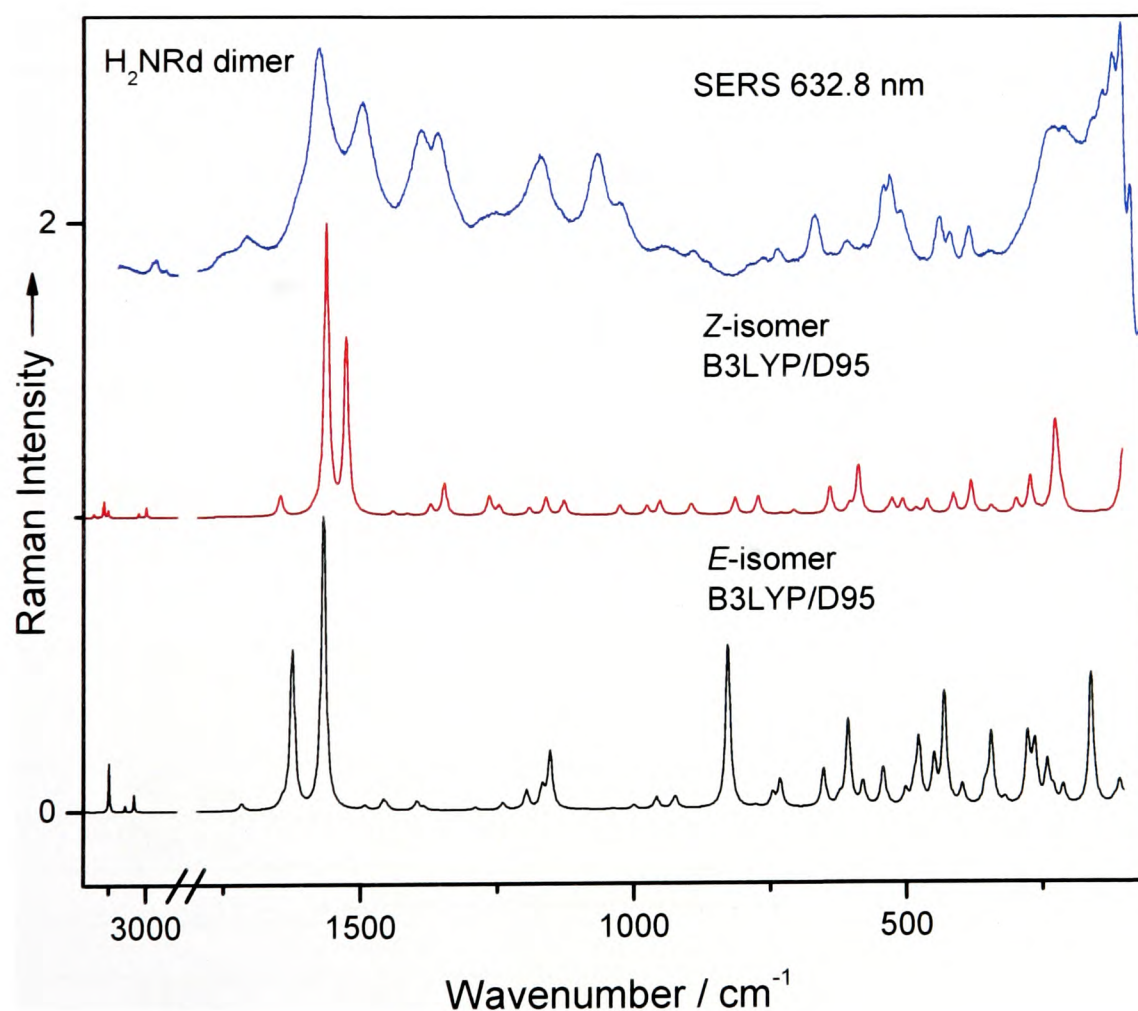


Figure 5.16. Experimental and calculated SER spectra of H_2NRd dimer (Z-isomer) under optimized experimental conditions ($\lambda_0 = 632.8$ nm).

Table 5.5. Experimental and theoretical calculations (NCA) for H₂NRd dimer.

Ag SERS	Expt. $\tilde{\nu}$ /cm ⁻¹		Calc.	Assignments (% PEDs)
	Au SERS			
			3494	$\nu_{as}(\text{NH}_2')$ (100)
			3420	$\nu_{as}(\text{NH}_2)$ (100)
			3342	$\nu_s(\text{NH}_2')$ (99)
			3308	$\nu_s(\text{NH}_2)$ (100)
			3062	$\nu_{as}(\text{CH}_2)$ (100)
2925 m			3001	$\nu_s(\text{CH}_2)$ (100)
1750 w	1750 w			
1708 w				
			1647	$\delta(\text{NH}_2)$ (94)
			1587	$\nu_s(\text{CO})$ (31), $\delta(\text{NH}_2')$ (53)
1575 vs	1575 s		1563	$\nu_s(\text{C}=\text{C})$ (57), $\delta(\text{NH}_2')$ (13)
1500 s	1500 s		1527	$\nu_s(\text{CO})$ (39), $\nu_s(\text{C6C10})$ (11), $\delta(\text{NH}_2')$ (33)
1389 s	1378 m		1442	$\delta(\text{CH}_2)$ (91)
			1415	$\nu_s(\text{C8N9})$ (44), $\nu_s(\text{N9N17})$ (13), $\rho(\text{NH}_2')$ (24)
			1373	$\nu_s(\text{C10N9})$ (28), $\nu_s(\text{N9N17})$ (16), $\rho(\text{NH}_2')$ (24)
1355 s			1347	$\nu_s(\text{C2N5})$ (31), $\nu_s(\text{N5N14})$ (25)
1252 w	1252 w		1265	$\nu_s(\text{C4N5})$ (31), $\omega(\text{CH}_2)$ (13)
			1259	$\rho(\text{NH}_2)$ (96)
			1247	$\nu_s(\text{C4N5})$ (12), $\omega(\text{CH}_2)$ (72)
			1192	$\nu_s(\text{N5N14})$ (10), $\nu_s(\text{C1C2})$ (13), $\nu_s(\text{C6C10})$ (15), $\rho(\text{NH}_2')$ (11)
1166 s	1151 s		1161	$\nu_s(\text{C8S20})$ (18), $\nu_s(\text{C8N9})$ (12), $\nu_s(\text{N9N17})$ (10), $\rho(\text{NH}_2')$ (20)
			1134	$\rho(\text{CH}_2)$ (93)
			1128	$\nu_s(\text{C4}=\text{S21})$ (22), $\nu_s(\text{N5N14})$ (12), $\nu_s(\text{C1C2})$ (15), $\delta_{ip}(\text{ring-1})$ 10
1064 s	1073 w		1025	$\nu_s(\text{C4}=\text{S21})$ 21, $\nu_s(\text{C10N9})$ 17
1021 m	1021 w		976	$\nu_s(\text{C8S20})$ (27), $\nu_s(\text{C8S7})$ (10)
947 vw	900 vw		952	$\nu_s(\text{C1C2})$ (17), $\nu_s(\text{C6S7})$ (22)
889 vw	889 vw		895	$\nu_s(\text{C4N5})$ (13), $\nu_s(\text{N5N14})$ (13), $\nu_s(\text{C4S3})$ (15)
			891	$\rho(\text{CH}_2)$ (83)
			813	$\nu_s(\text{N5N14})$ (12), $\omega(\text{NH}_2)$ (57), $\delta_{ip}(\text{N5N14})$ (10)
787 vw	792 w		771	$\omega(\text{NH}_2)$ (21), $\delta_{ip}(\text{CO})$ (13)
763 vw			729	$\delta_{op}(\text{CO})$ (78), $\delta_{op}(\text{C6}=\text{C2})$ (14)
733 w	724 m		705	$\nu_s(\text{C1S3})$ (34), $\delta_{ip}(\text{CO})$ (13), $\delta_{ip}(\text{ring-1})$ (18)
666 m	635 w		638	$\nu_s(\text{C1S3})$ (39), $\omega(\text{NH}_2')$ (14), $\delta_{ip}(\text{ring-2})$ (13)
606 w			603	$\omega(\text{NH}_2')$ (35), $\delta_{ip}(\text{ring-1})$ (10)

		588	$\delta_{op}(C2=C6)$ (37)
574 vw		586	$\omega(NH_2')$ (35)
		533	$\delta_{op}(N9N17)$ (13), $\delta_{op}(C4=S21)$ (41), $\delta_{op}(C8=S20)$ (33)
539 sh 526 s 504 sh	539 sh 526 s 504 sh	524	$\nu_s(C6S7)$ (26), $\delta_{ip}(ring-2)$ (15), $\delta_{op}(ring-2)$ (18)
		505	$\delta_{op}(C4=S21)$ (33), $\delta_{op}(C8=S20)$ (39), $\delta_{op}(C2=C6)$ (15)
436 m	436 m	480	$\nu_s(C4S3)$ (15), $\nu_s(C8S7)$ (13), $\delta_{op}(ring-1)$ (23), $\delta_{op}(ring-2)$ (10)
415 m		460	$\delta_{ip}(ring-1)$ (15), $\delta_{op}(ring-2)$ (15), $\delta_{op}(ring-2)$ (13)
		411	$\nu_s(C8S20)$ (15), $\nu_s(C6S7)$ (17), $\nu_s(C8S7)$ (20), $\delta_{ip}(CO)$ (16)
		379	$\nu_s(C4=S21)$ (16), $\nu_s(C4S3)$ (23), $\delta_{ip}(N5N14)$ (17), $\delta_{ip}(ring-1)$ (22)
383 m		342	$\delta_{ip}(CO)$ (27), $\delta_{ip}(N9N17)$ (44)
346 w	302 vw	334	$\delta_{op}(N9N17)$ (28), $\delta_{ip}(C6=C2)$ (31), $\rho(N5N14)$ (15)
		296	$\delta_{ip}(N5N14)$ (31), $\delta_{ip}(C4=S21)$ (27), $\delta_{ip}(C2=C6)$ (22)
		270	$\delta_{ip}(C8=S20)$ (29), $\delta_{op}(ring-2)$ (10)
	269 vw	267	$\delta_{op}(N5N14)$ 14, $\delta_{op}(ring-2)$ (12), $\rho(N5N14)$ (57)
		253	$\delta_{op}(N9N17)$ (51), $\tau(N5N14)$ (25)
		236	$\delta_{op}(N5N14)$ (55), $\rho(C=C)$ (13)
		225	$\delta_{ip}(C8=S20)$ (28), $\delta_{op}(ring-2)$ (10)
		219	$\delta_{ip}(C4=S21)$ (26), $\delta_{ip}(C6=C2)$ (11), $\rho(N9N17)$ (10)
224 s 208 s			
		211	$\tau(N9N17)$ (68)
	143 w	141	$\tau_{ip}(ring-1)$ (18), $\tau_{op}(ring-1)$ (50), $\tau(C=C)$ 20
		111	$\tau_{ip}(ring-1)$ (52), $\tau_{op}(ring-2)$ (49)

5.3.13. MeRd Dimer (Z-Isomer)

In the solid state spectrum of MeRd, three bands at 421, 473, and 542 cm^{-1} are assigned to ring deformation modes. The first and third bands are red-shifted by $\sim 3 \text{ cm}^{-1}$ in the solution spectrum, whereas the second band is blue-shifted by $\sim 2 \text{ cm}^{-1}$. However, in the Ag colloid SER spectrum, the bands at 435 and 503; 528 and 566 cm^{-1} are attributed to ring-1 and ring-2 deformation modes of the dimer, respectively. Their counterparts in the Au colloid SER spectrum are observed at 416 and 435; 500 and 539 cm^{-1} . The calculated PEDs suggest that these vibrations involve coupling of ring deformation with C-S and C-N stretching. The C=O stretching vibration appears at 1740 cm^{-1} in the solution spectrum and 1697 cm^{-1} in the Ag colloid SER spectrum. The corresponding mode gives rise to two bands at 1745 and 1691 cm^{-1} in the Au colloid spectrum. The weak bands at 591 and 706 cm^{-1} are accounted for by the C=O deformation mode in Ag and Au SER spectra, respectively.

In SER spectra, the intense bands at 1503, 1541, and 1572 cm^{-1} are assigned to the C=C stretching, CH_3 , and CH_3' asymmetric deformation modes of the (hypothetical) dimer, which are in good agreement with the calculated values. These bands are absent in the solid and solution state spectra. A medium intensity band at 1419 cm^{-1} in the SER spectra is also attributed to CH_3' asymmetric deformation. The bands at 1255 and 1351 cm^{-1} are ascribed to C-N stretching. It is noteworthy that bands associated with C-N stretching modes are more enhanced in SER spectra in contrast to bands in the solid state spectrum.

The thioamide bands II and III are observed at 1107 and 984 cm^{-1} , respectively in the solid state spectrum. On the other hand, in Ag colloid SER spectrum a doublet occurs at 1155 and 1173 cm^{-1} . According to the calculated PEDs, these bands are attributed to C=S stretching and *op* CH_3 deformation modes of dimer. Conversely, in the Au colloid SER spectrum a single band is observed at 1155 cm^{-1} . A medium intensity band at 1002 cm^{-1} is assigned to the thioamide III in Ag colloid SER spectrum. Its counterpart in the Au colloid SER spectrum is found at 1016 cm^{-1} . The C-C stretching modes are ascribed to the bands at 967 and 1084 cm^{-1} . The former band is absent in the Au colloid SER

spectrum of MeRd. The bands observed in the 658-847 cm^{-1} region are mainly assigned to C-S stretching. For example, a medium intensity band at 658 cm^{-1} appears to be mixed and is predominantly attributed to a C-S stretching mode. This band is blue-shifted in the Au colloid SER spectrum and found at 706 cm^{-1} . A band at 346 cm^{-1} in the Ag colloid SER spectrum is assigned to the C=S deformation mode. This band is red-shifted in the Au colloid SER spectrum and observed at 303 cm^{-1} .

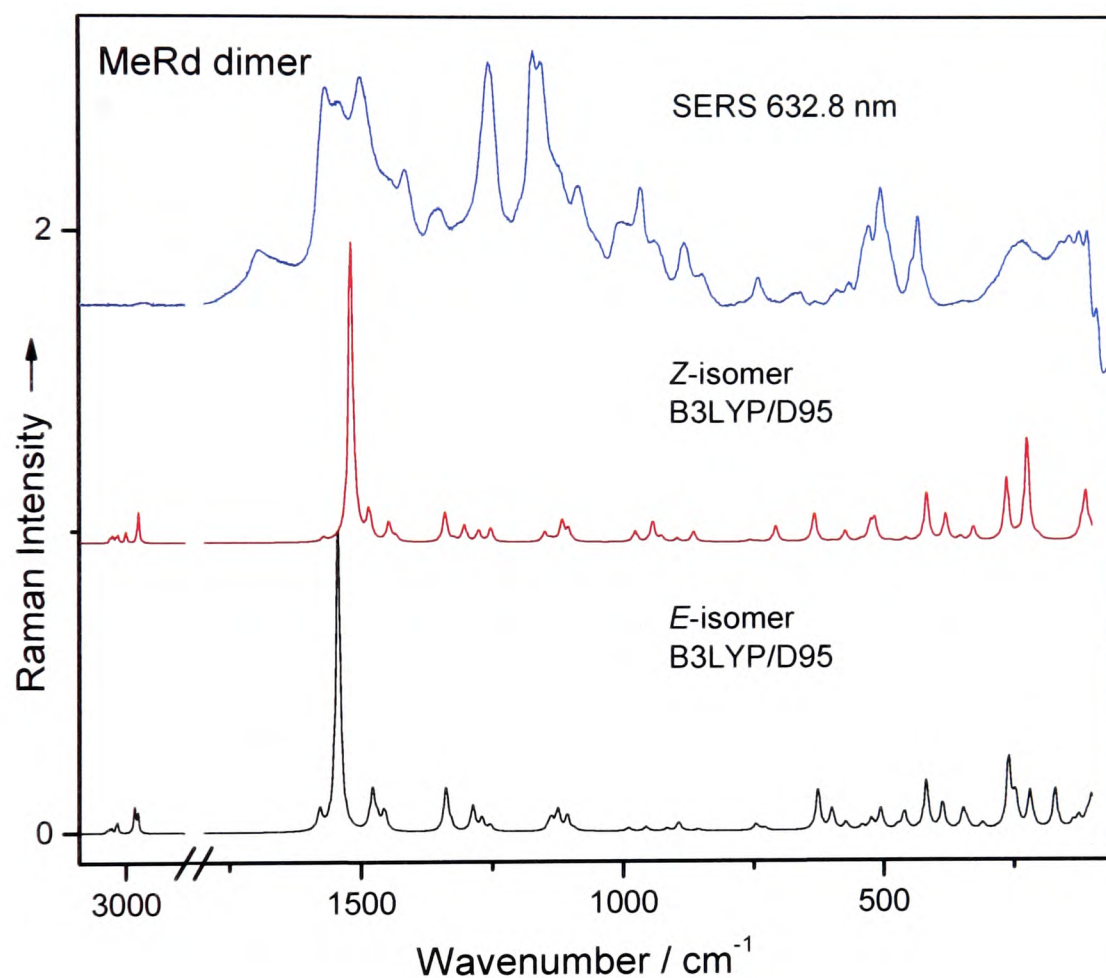


Figure 5.17. Experimental and calculated SER spectra of MeRd dimer (Z-isomer) under optimized experimental conditions ($\lambda_0 = 632.8 \text{ nm}$).

Table 5.6. Experimental and theoretical calculations (NCA) for MeRd dimer.

Expt. $\tilde{\nu} / \text{cm}^{-1}$		Assignments (% PEDs)	
Ag SERS	Au SERS	Calc.	
		3072	$\nu_{\text{as}}(\text{CH}_3')$ (25), $\nu_{\text{as}}(\text{CH}_3')$ (74)
		3062	$\nu_{\text{as}}(\text{CH}_2)$ (100)
		3058	$\nu_{\text{as}}(\text{CH}_3)$ (24), $\nu_{\text{as}}(\text{CH}_3)$ (75)
		3046	$\nu_{\text{as}}(\text{CH}_3)$ (76), $\nu_{\text{as}}(\text{CH}_3)$ (24)
		3038	$\nu_{\text{as}}(\text{CH}_3')$ (75), $\nu_{\text{as}}(\text{CH}_3')$ (25)
		3003	$\nu_{\text{s}}(\text{CH}_2)$ (100)
		2951	$\nu_{\text{s}}(\text{CH}_3')$ (74)
2952 vw	2942 w	2950	$\nu_{\text{s}}(\text{CH}_3)$ (98)
1697 m	1745 m 1691 m	1572	$\nu_{\text{s}}(\text{CO})$ (63), $\nu_{\text{s}}(\text{C}=\text{C})$ (10), $\delta_{\text{ip}}(\text{ring-2})$ (10)
1572 vs	1572 vs	1520	$\nu_{\text{s}}(\text{CO})$ (10), $\nu_{\text{s}}(\text{C}=\text{C})$ (50)
1541 s	1543 s	1504	$\delta_{\text{as}}(\text{CH}_3)$ (70), $\delta_{\text{as}}(\text{CH}_3)$ (24)
1503 s	1503 s	1487	$\delta_{\text{as}}(\text{CH}_3)$ (13), $\delta_{\text{as}}(\text{CH}_3)$ (36), $\delta_{\text{as}}(\text{CH}_3')$ (23)
1419 m	1419 m	1486	$\delta_{\text{as}}(\text{CH}_3')$ (27), $\delta_{\text{as}}(\text{CH}_3')$ (31)
		1482	$\delta_{\text{as}}(\text{CH}_3')$ (71), $\delta_{\text{as}}(\text{CH}_3')$ (22)
		1450	$\delta_{\text{s}}(\text{CH}_3')$ (66)
		1448	$\delta_{\text{s}}(\text{CH}_3)$ (79)
		1435	$\delta(\text{CH}_2)$ (84)
1351 m	1351 m	1341	$\nu_{\text{s}}(\text{C8N9})$ (47), $\nu_{\text{s}}(\text{N9C14})$ (10), $\delta_{\text{s}}(\text{CH}_3')$ (12)
		1324	$\nu_{\text{s}}(\text{C2N1})$ (32)
		1304	$\nu_{\text{s}}(\text{C5N1})$ (20), $\nu_{\text{s}}(\text{N1C15})$ (13)
1255 s	1255 m	1277	$\nu_{\text{s}}(\text{C5N1})$ (11), $\nu_{\text{s}}(\text{C10N9})$ (20), $\nu_{\text{s}}(\text{N9C14})$ (11), $\rho_{\text{op}}(\text{CH}_3')$ (10)
		1254	$\omega(\text{CH}_2)$ (88)
		1151	$\nu_{\text{s}}(\text{C6C10})$ (30), $\rho_{\text{op}}(\text{CH}_3')$ (11)
		1141	$\rho(\text{CH}_2)$ (93)
		1139	$\rho_{\text{ip}}(\text{CH}_3')$ (67), $\rho_{\text{op}}(\text{CH}_3')$ (22)
		1132	$\rho_{\text{ip}}(\text{CH}_3)$ (69), $\rho_{\text{op}}(\text{CH}_3)$ (23)
1173 s		1117	$\nu_{\text{s}}(\text{C8S12})$ (19), $\rho_{\text{op}}(\text{CH}_3')$ (20)
1155 s	1155 s	1105	$\nu_{\text{s}}(\text{C5}=\text{S13})$ (29), $\rho_{\text{op}}(\text{CH}_3)$ (17)
1084 w	1084 w	1096	$\nu_{\text{s}}(\text{N1C15})$ (18), $\nu_{\text{s}}(\text{C2C3})$ (17), $\rho_{\text{op}}(\text{CH}_3)$ (11), $\delta_{\text{ip}}(\text{ring-1})$ (10)
1055 vw 1002 m	1016 m	977	$\nu_{\text{s}}(\text{C8S12})$ (17), $\nu_{\text{s}}(\text{C10N9})$ (26)
967 s		944	$\nu_{\text{s}}(\text{C2C3})$ (21), $\nu_{\text{s}}(\text{C6S7})$ (16)
930 m		927	$\nu_{\text{s}}(\text{N9C14})$ (19), $\nu_{\text{s}}(\text{C8S7})$ (10)
883 s	882 m	897	$\rho(\text{CH}_2)$ (83)

847 m	843 m	865	$\nu_s(\text{N1C15})$ (13), $\nu_s(\text{N9C14})$ (17), $\nu_s(\text{C5S4})$ (13)
735 m	735 w	757	$\nu_s(\text{C3S4})$ (12)
		744	$\delta_{\text{op}}(\text{CO})$ (77), $\delta_{\text{op}}(\text{C6=C2})$ (16)
658 m	706 w	708	$\nu_s(\text{C3S4})$ (41), $\delta_{\text{ip}}(\text{CO})$ (13)
631 w	631 vw	634	$\nu_s(\text{C3S4})$ (25), $\delta_{\text{ip}}(\text{ring-1})$ (13), $\delta_{\text{ip}}(\text{ring-1})$ (11)
		598	$\delta_{\text{op}}(\text{N1C15})$ (13), $\delta_{\text{op}}(\text{C5=S13})$ (13), $\delta_{\text{op}}(\text{C2=C6})$ (43)
591 w		574	$\nu_s(\text{C5=S13})$ (10), $\nu_s(\text{N1C15})$ (11), $\nu_s(\text{C5S4})$ (17), $\delta_{\text{ip}}(\text{N1C15})$ (13)
566 w		545	$\delta_{\text{op}}(\text{N9C14})$ (11), $\delta_{\text{op}}(\text{C5=S13})$ (26), $\delta_{\text{op}}(\text{C8=S12})$ (49)
528 s	539 s	526	$\nu_s(\text{C8N9})$ (10), $\nu_s(\text{C6S7})$ (21), $\nu_s(\text{C8S7})$ (10), $\delta_{\text{ip}}(\text{ring-2})$ (19), $\delta_{\text{op}}(\text{ring-2})$ (14)
		518	$\delta_{\text{op}}(\text{C5=S13})$ (43), $\delta_{\text{op}}(\text{C8=S12})$ (26), $\delta_{\text{op}}(\text{C2=C6})$ (19)
503 vs	500 m	487	$\nu_s(\text{C5S4})$ (12), $\nu_s(\text{C8S7})$ (14), $\delta_{\text{ip}}(\text{ring-2})$ (13), $\delta_{\text{op}}(\text{ring-2})$ (19)
435 s	435 m	458	$\nu_s(\text{C5S4})$ (10), $\delta_{\text{ip}}(\text{N1C15})$ (10), $\delta_{\text{ip}}(\text{ring-1})$ (230), $\delta_{\text{op}}(\text{ring-2})$ (10)
	416 m	418	$\nu_s(\text{C8S12})$ (14), $\nu_s(\text{C6S7})$ (17), $\nu_s(\text{C8S7})$ (10), $\delta_{\text{ip}}(\text{CO})$ (19), $\delta_{\text{ip}}(\text{ring-1})$ (12)
		382	$\nu_s(\text{C5=S13})$ (14), $\nu_s(\text{C5S4})$ (14), $\delta_{\text{ip}}(\text{N1C15})$ (27), $\delta_{\text{ip}}(\text{ring-1})$ (24)
		335	$\nu_s(\text{C8S7})$ (11), $\delta_{\text{ip}}(\text{CO})$ (14), $\delta_{\text{ip}}(\text{N9C14})$ (45)
346 vw	303 w	328	$\delta_{\text{ip}}(\text{N1C15})$ (25), $\delta_{\text{ip}}(\text{C5=S13})$ (46), $\delta_{\text{ip}}(\text{C2=C6})$ (19)
		321	$\delta_{\text{op}}(\text{N1C15})$ (10), $\delta_{\text{op}}(\text{N9C14})$ (12), $\delta_{\text{op}}(\text{C6=C2})$ (40)
237 m	247 w	265	$\delta_{\text{ip}}(\text{N9C14})$ (16), $\delta_{\text{ip}}(\text{C8=S12})$ (34), $\delta_{\text{op}}(\text{ring-2})$ (11)
		246	$\delta_{\text{op}}(\text{N1C15})$ (41), $\delta_{\text{op}}(\text{N9C14})$ (12), $\delta_{\text{op}}(\text{C2=C6})$ (12), $\tau(\text{C=C})$ (10)
		232	$\delta_{\text{op}}(\text{N9C14})$ (57), $\tau_{\text{ip}}(\text{ring-2})$ (14)
		231	$\delta_{\text{ip}}(\text{C5=S13})$ (27), $\delta_{\text{ip}}(\text{C8=S12})$ (17), $\delta_{\text{ip}}(\text{C2=C6})$ (18)
		225	$\nu_s(\text{C=C})$ (13), $\delta_{\text{ip}}(\text{C8=S12})$ (13), $\delta_{\text{ip}}(\text{ring-2})$ (14)
		204	$\delta_{\text{op}}(\text{N1C15})$ (15), $\tau(\text{N1C15})$ (87)
108 s	146 s	141	$\tau_{\text{ip}}(\text{ring-1})$ (40), $\tau_{\text{op}}(\text{ring-2})$ (21), $\tau(\text{C=C})$ (21)
		121	$\tau(\text{N9C14})$ (98)

5.4. Summary and Conclusions

The SER spectra of Rd, H₂NRd, and MeRd adsorbed on Ag and Au colloidal NPs have been reported for the first time. The Ag colloid SER spectra are more enhanced compared to the Au SER spectra, which suggest strong interaction of these molecules with Ag NPs. The pH dependent SERS studies reveal that the optimum conditions to obtain SER spectra are at pH 2.3 in the presence of PLL and HCl. This study further implies that the spectral changes under different pH values could be attributed to the different orientations of the adsorbate molecules on the Ag surface and/or change in the state of ionization. A detailed comparison of SER spectra, under different experimental conditions, with solid and solution state spectra show the appearance of band at $\approx 1566/1575/1572\text{ cm}^{-1}$. It has been tentatively assumed that on Ag and Au surfaces these molecules undergo a photo-initiated self-condensation reaction, which leads to the formation of dimers. DFT calculations have been performed on dimers to facilitate the vibrational band assignments of SER spectra. There is good agreement between the calculated and experimental spectra. The calculated PEDs predict that the band at $\approx 1566/1575/1572\text{ cm}^{-1}$ can be assigned to the C=C stretching mode of the dimers. It is very difficult to predict the coordination site on the Ag and Au surfaces due to three potential binding sites of these molecules (*i.e.*, N, O, and S). However, the frequency shifts in the bands associated with thioamide modes suggest that Rd and its derivatives are adsorbing on the Ag and Au surface through exo-sulfur. As a consequence, bands due to the C-N stretching modes are significantly enhanced, which suggests that the C-N moiety is in close proximity to the thiocarbonyl sulfur.

5.5. References

- [1] L. K. Jong and J. Sang-Woo, *J. Electroanal. Chem.*, **605**, (2007), 68.
- [2] I. C. N. Diogenes, I. M. M. de Carvalho, E. Longhotti, L. G. F. Lopes, M. L. A. Temperini, G. F. S. Andrade and I. S. Moreira, *J. Electroanal. Chem.*, **605**, (2007), 1.
- [3] M. Saavedra, M. Campos-Vallette, R.E. Clavijo, F. Mendizabal, G. Diazb, J. V. Garci-Ramosc and S. Sanchez-Cortes, *Vib. Spectrosc.*, **32**, (2003), 155.
- [4] R. Wen and Y. Fang, *Vib. Spectrosc.*, **39**, (2005), 106.
- [5] E. Podstawka, R. Borszowska, M. Grabowska, M. Drag, P. Kafarski, and L. M. Proniewicz, *Surf. Sci.*, **599**, (2005), 207.
- [6] M. Moskovits, *Rev. Mod. Phys.*, **57**, (1985), 783.
- [7] J. A. Creighton, *Surf. Sci.*, **124**, (1983), 209.
- [8] K. Kneipp, H. Kneipp, I. Itzkan, R. R. Dasari and M. S. Feld, *Chem. Rev.*, **99**, (1999), 2957.
- [9] G. A. Baker and D. S. Moore, *Anal. Bioanal. Chem.*, **382**, (2005), 1751.
- [10] S. J. Bae, C. R. Lee, I. S. Choi, C. S. Hwang, M. S. Gong, K. Kim and S.W. Joo, *J. Phys. Chem. B* **106**, (2002), 7076.
- [11] S. W. Joo, T. D. Chung, W. Jang, M. S. Gong, N. Geum and K. Kim, *Langmuir*, **18**, (2002), 8813.
- [12] N. Jaegeun, J. Soonmin, L. Donghyung, S. Seokmin, K.Y. Joon, I. Eisuke and J. Samg-Woo, *Curr. Appl. Phys.*, **7**, (2007), 605.
- [13] C. Y. Jing and Y. Fang, *Chem. Phys.*, **332**, (2007), 27.
- [14] Z. M. Li, N. Zhang, and F. T. Li, *Appl. Surf. Sci.*, **253**, (2006), 2870.
- [15] G. K. Liu, B. Ren, R. A. Gu and Z. Q. Tian, *J. Phys. Chem.*, **111**, (2007), 3417.
- [16] H. Chu, H. F. Yang, S. Y. Huan, W. Q. Lin, G. L. Shen and R. Q. Yu, *J. Raman Spectrosc.*, **38**, (2007), 295.
- [17] K. L. Kim, S. J. Lee, K. Kim, *J. Phys. Chem. B* **108**, (2004), 9216.
- [18] J. Chowdhury and M. Ghosh, *J. Colloid. Interf. Sci.*, **277**, (2004), 121.
- [19] R. G. Pearson, *J. Am. Chem. Soc.*, **79**, (1963), 3533.
- [20] R. G. Pearson, *Science*, **151**, (1966), 172.
- [21] M. Muniz-Miranda and G. Sbrana, *J. Raman Spectrosc.*, **27**, (1996), 105.

- [22] C. L. Haynes, C. R. Yonzon, X. Zhang and R. P. Van Duyne, *J. Raman Spectrosc.*, **36**, (2005), 471.
- [23] K. Faulds, R. E. Littleford, D. Graham, G. Dent, and W. E. Smith, *Anal. Chem.*, **76**, (2004), 592.
- [24] K. Kneipp and H. Kneipp, *Isr. J. Chem.*, **46**, (2006), 299.
- [25] L. Brus, *J. Am. Chem. Soc.*, **221**, (2001), 112.
- [26] H. Xu, J. Aizpurua, M. Käll, and P. Apell, *Phys. Rev. E* **62**, (2000), 4318.
- [27] C. McLaughlin, D. Graham, W.E. Smith. *J. Phys.chem. B* **106**, (2002), 5408.
- [28] R. Hilal, H. Ead and A.Osman, *Appl. Spectrosc.*, **32**, (1978), 557.
- [29] V. Enchev, S. Chorbadjiev and B. Jordanov, *Chem. Heterocycl. Compd.*, **38**, (2002), 1110.
- [30] M. F. El-Sherbiny, *Chem. Pap. Chem. Zvesti.*, **59**, (2005), 332.
- [31] E. Subasi, A. Ercag, S. Sert, and O. S. Senturk, *Synth. React. Inorg. Met. Org. Chem.*, **36**, (2006), 705.
- [32] W. I. Stephen and A. Townshend, *J. Chem. Soc.*, (1965), 3738.
- [33] A. C. Fabretti and P. Giorgio, *Transition Met. Chem.*, **2**, (1977), 224.
- [34] A. C. Fabretti, G. Franchini, G. Peyronel and M. Ferrari, *Polyhedron*, **1**, (1982), 633.
- [35] G. Kardas and R. Colloidmaz, *Appl. Surf. Sci.*, **253**, (2007), 33402.
- [36] F. C. Brown, *Chem. Rev.*, **61**, (1961), 463.
- [37] S. P. Singh, S. S. Parmar, K. V. Raman and I. Stenberg, *Chem. Rev.*, **81**, (1981), 175.
- [38] B. B. Lohray, V. Bhushan, P. B. Rao, G. R. Madhavan, N. Murali, K. N. Rao, K. A. Reddy, B. M. Rajesh, P. G. Reddy, R. Chakrabarti and R. Rajagopalan, *Bioorg. Med. Chem. Lett.*, **7**, (1997), 785.
- [39] C. L. Lee and M. M. Sim, *Tetrahedron Lett.*, **41**, (2000), 5729.
- [40] W. T. Sing, C. L. Lee, S. L. Yeo, S. P. Lim and M. M. Sim, *Bioorg. Med. Chem. Lett.*, **11**, (2001), 91.
- [41] K. Bourahla, A. Derdour, M. Rahmouni, F. Carreauxa and J. P. Bazureaua, *Tetrahedron Lett.*, (2007), in press.
- [42] I. Simon, J. J. Andre, in: J. M. Lehn, C.W. Rees (Eds.), *Molecular Semiconductors*, Springer, Berlin, (1985).
- [43] F. Nuesch and M. Gratzel, *Chem. Phys.*, **193**, (1995), 1.

- [44] A. E. Mourad, A. A. Hassan, A. A. Ashraf, N. K. Mohamed and B. A. Ali, *Phosphorus, Sulfur Silicon Relat. Elem.*, **182**, (2007), 321.
- [45] H. Nagase, *Chem. Pharm. Bull.*, **22**, (1974), 505.

Chapter Six

Semi-Quantitative Trace Analysis of Rd and its Derivatives Adsorbed on Citrate-Reduced Silver Colloids

6.1. Introduction

SERS is a well established analytical technique to detect and identify molecules quantitatively at very low limits of detection (*e.g.* atto and zepto molar) due to the unique combination of specificity, selectivity and sensitivity¹⁻². It produces very large enhancements in the effective Raman cross-section (comparable too or even better than fluorescence) of adsorbed species on noble metal nano-structured surfaces (*e.g.* colloidal NPs), due to the excitation of localized surface plasmon resonance (LSPR). In order to achieve the lowest limits of SERS detection, both the relationship between the surface nanostructure and laser excitation wavelength, as well as the analyte/surface binding chemistry, must be carefully optimized. The pioneering work of Nie and co-workers³⁻⁴, and Kneipp *et al.*,⁵⁻⁶ later corroborated by the work of Käll and co-workers⁷⁻⁹ and Brus and co-workers,¹⁰⁻¹¹ has brought SERS to the present state of the art (*i.e.*, “single molecule” (SM)-SERS). It is now understood that SERS signals from colloidal NPs can be attributed to the following two regimes: (a) SER spectra that are the product of an “average SERS” enhancement *i.e.*, the product of SER spectra from an ensemble of colloidal particles and aggregates and characterized by a stable average spectrum with well defined frequency and bandwidth; (b) SM-SER spectra obtained from a single particle and single aggregate of particles, where so called “hot spots” are the ultimate source of high enhancement (as much as $\sim 10^{14}$) and allow single molecule detection¹².

The current work demonstrates limits of detection (LOD) for the semi-quantitative trace analysis of the molecules Rd, H₂NRd, and MeRd using SERS. In order to determine and compare the extent of the linearity of the signal dependence on concentration, the aforementioned molecules were adsorbed on citrate-reduced silver colloidal nanoparticles (Ag NPs) and SER spectra were recorded. In the case of Rd two laser excitation wavelengths (*i.e.*, $\lambda_0 = 514.5$ and 632.8 nm) were used. In the case of the Rd derivatives SER spectra were investigated using a laser excitation wavelength of 632.8 nm only. A

pivotal feature observed during the present study is the adsorbate concentration dependence of SERS bands using Ag NPs.

6.2. Experimental

6.2.1. Chemical reagents

See section 3.1. in Chapter three.

6.2.2. Synthesis and aggregation of Ag colloids

See sections 3.8., and 3.9. in Chapter three.

6.2.3. Solutions of Rd and its derivatives

See section 3.6 in Chapter three.

6.2.4. SERS measurements

See section 3.7 in Chapter three.

6.2.5. Reproducibility/time dependence

See section 3.10 in Chapter three.

6.2.6. Concentration dependence

See section 3.11 in Chapter three.

6.3. Results and Discussion

6.3.1. Concentration-Dependent SER Spectra of Rd

SERS concentration studies of Rd and its derivatives have been performed to investigate the sensitivity of this technique as a probe for detection and semi-quantitative analysis, and to understand the adsorption behavior of these molecules on Ag NPs surfaces. For this purpose, SERS studies of Rd were carried out under minimal conditions (*i.e.*, in the absence of PLL and HCl using $\lambda_0 = 632.8$ nm), and under an acidic environment at pH 2.3 (*i.e.*, in the presence of PLL using $\lambda_0 = 514.5$ and 632.8 nm). Fig.6.1 depicts the SER spectra of Rd under minimal conditions as a function of concentration. Before addition of analyte the Ag colloid has a pH of 8; the addition of different concentrations of Rd changes the pH of the system (see Figure legends). Proceeding from a concentration of 1×10^{-3} mol dm⁻³, the SERS signal intensity is weak and increases slightly between 4.8×10^{-4} to 1.2×10^{-4} mol dm⁻³ before decreasing in intensity until only SERS signals

are barely observed at $3.7 \times 10^{-6} \text{ mol dm}^{-3}$. It is worth noting that at a concentration of $1.2 \times 10^{-4} \text{ mol dm}^{-3}$ the band at 1555 cm^{-1} is of medium intensity and the SER spectrum is dominated by bands at 555, 1187, and 1382 cm^{-1} . The band at 1382 cm^{-1} is ascribed to CH_2 deformation. The band at 1187 cm^{-1} is mainly attributed to C-N stretching and ip N-H deformation modes, whereas the band at 555 cm^{-1} is assigned to an ip ring deformation mode. Rd could adsorb to the Ag substrate via S, N or O atoms. However, detailed examination of solid state and SER spectra show that the band at 1457 cm^{-1} , attributed to a combination of C-N stretching and ip N-H deformation modes (amide II) in the solid state, has not been shifted significantly and is observed at 1451 cm^{-1} in the SER spectra. On the other hand, the C=S stretching vibration (thioamide III) gives rise to two bands at 1066 and 1078 cm^{-1} in the solid state spectrum. In the SER spectra the former band is $\approx 50 \text{ cm}^{-1}$ red shifted and the latter band is very weak in intensity. This large shift in the C=S stretching mode suggests that adsorption on the Ag surface is through exo-sulfur. Electromagnetic (EM) theory selection rules, for SERS, predict¹³⁻¹⁴ that vibrations with changes in polarizability perpendicular to the surface are expected to be more enhanced in contrast to vibrations with changes in polarizability parallel to the surface. Thus, ip vibration modes should be more enhanced than the op ones. If Rd dimer adsorbs perpendicular to the surface then the bands due to the ip vibrations would be more enhanced. In the present study, the bands due to the ip vibrations are more enhanced, which suggests that the Rd dimer lies in a perpendicular direction on the Ag surface, under minimal experimental conditions.

Fig.6.2a. shows the SER spectra of Rd at pH 2.3, in the presence of PLL, over the concentration range 1×10^{-6} to $1 \times 10^{-3} \text{ mol dm}^{-3}$ (SER spectra over the linear region will be discussed in a later section). The spectral profiles change significantly with decreasing concentration of Rd and no significant changes are observed below $1 \times 10^{-6} \text{ mol dm}^{-3}$. Nevertheless, the signals are weak in intensity. It is interesting to note that the intense band at 556 cm^{-1} decreases in intensity with concentration. Conversely, the band at 1566 cm^{-1} increases in intensity and reaches a maximum intensity at $1 \times 10^{-5} \text{ mol dm}^{-3}$, before decreasing in intensity, gradually, with concentration. Plots of intensities (areas) of SERS bands at 556 and 1566 cm^{-1} versus Rd concentration are shown in Fig.6.2b. The SER

spectra show very pronounced differences in the region spanning $1191\text{--}1382\text{ cm}^{-1}$. The bands at 1191 and 1382 cm^{-1} decrease in intensity; but, the bands at 1267 and 1312 cm^{-1} increase in relative intensity with decreasing concentration of Rd. The bands at 1191 and 1382 cm^{-1} are predominantly assigned to CH_2 deformation, and mixed C-N stretching/ip N-H deformation modes.

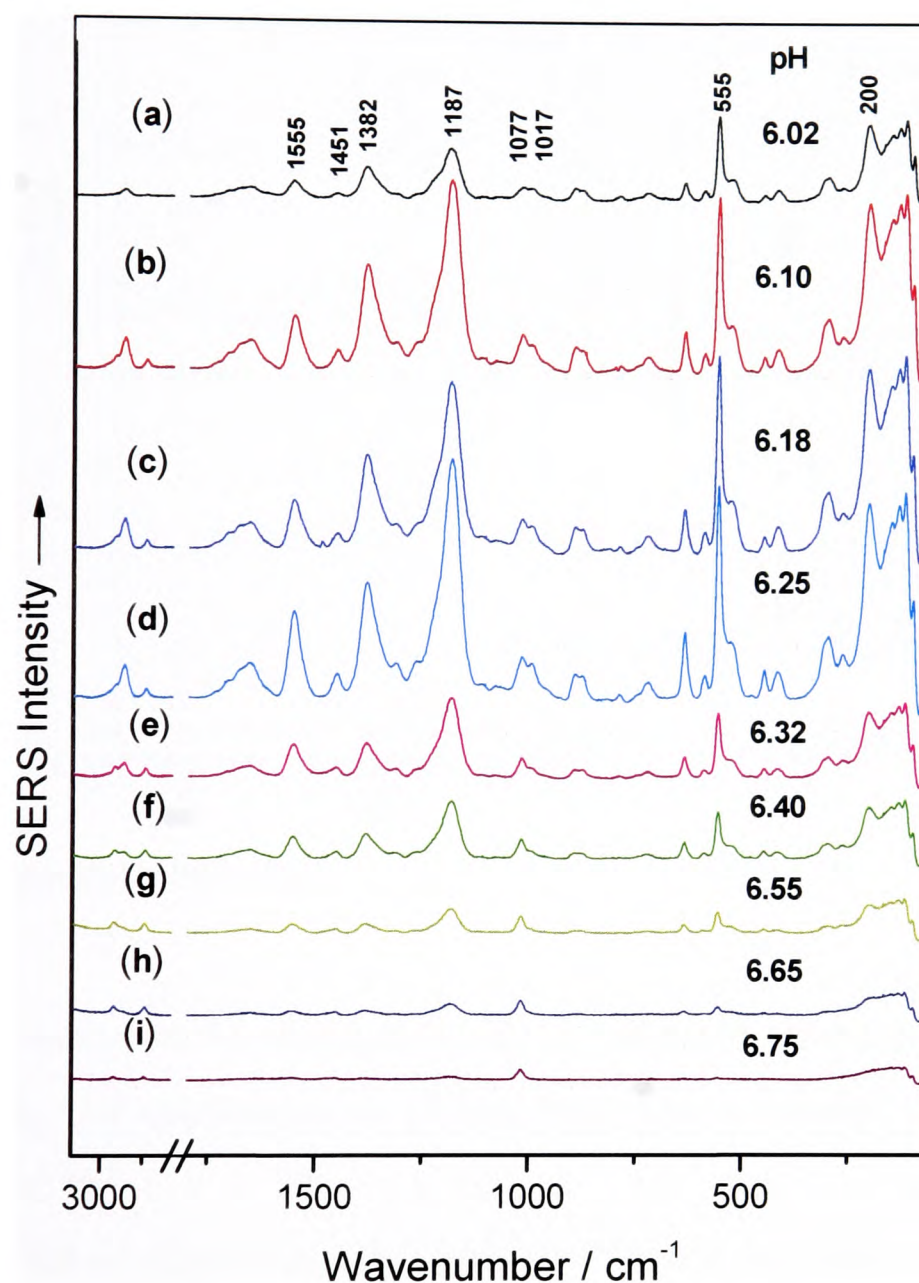


Figure 6.1. SER spectra of Rd adsorbed on the Ag colloid as a function of concentration ($\lambda_0 = 632.8\text{ nm}$). The concentrations of Rd are: (a) 1×10^{-3} , (b) 4.8×10^{-4} , (c) 2.4×10^{-4} , (d) 1.2×10^{-4} , (e) 6×10^{-5} , (f) 3×10^{-5} , (g) 1.5×10^{-5} , (h) 7.5×10^{-6} , and (i) $3.7 \times 10^{-6}\text{ mol dm}^{-3}$.

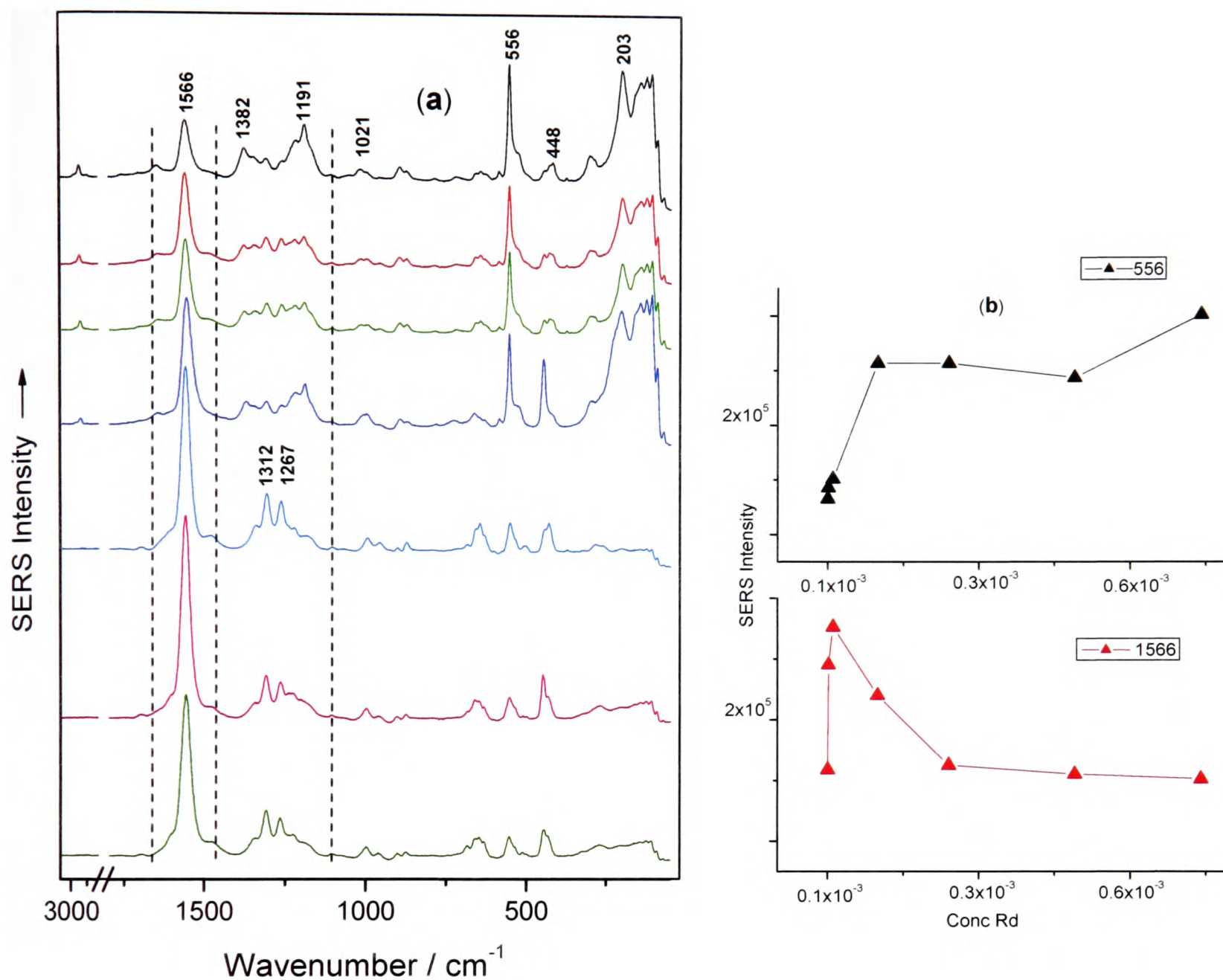


Figure 6.2. SER spectra of Rd adsorbed on the Ag colloid as a function of concentration ($\lambda_0 = 632.8$ nm). The concentrations of Rd, from top to bottom, are: (a) 1×10^{-3} , 7.4×10^{-4} , 4.9×10^{-4} , 2.4×10^{-4} , 1×10^{-4} , 1×10^{-5} , and 1×10^{-6} mol dm⁻³. (b) Concentration of Rd vs. signal intensity (peak area for non log data) for SERS bands at 556 (▲) and 1566 cm⁻¹ (▲).

It is apparent from the SER spectra of Rd under minimal and acidic conditions, that the bands at 556 and 1191 cm⁻¹ are less enhanced under acidic conditions. Conversely, the band at 1566 cm⁻¹ is enhanced significantly and becomes the most intense band at lower concentrations (pH 2.3). These changes could be a consequence of the re-orientation of the molecule on the Ag surface, which changes from a perpendicular to a tilted

orientation at low concentrations (as illustrated in Fig.6.3), the monolayer coverage effect or different coordination mechanism on the Ag surface.

At low concentrations (*i.e.*, submonolayer coverage) the SERS signal is weak as the surface coverage increases with increasing concentration of adsorbate, hence the SERS signal is enhanced and attains a maximum intensity at monolayer coverage, where both electromagnetic and charge transfer contributions to SERS are at a maximum. Further increases in concentration result in multilayer coverage of adsorbate on the surface, which causes a decrease in SERS signal intensity. This conjecture suggests that orientation of the adsorbate molecules does not change with surface coverage, and the predicted behavior holds for all the SERS bands. However, the opposite can also occur. A number of studies have been reported in the literature pertaining to changes in orientation of the adsorbed molecules with surface coverage, and therefore with adsorbate concentration in the colloid¹⁵⁻¹⁷.

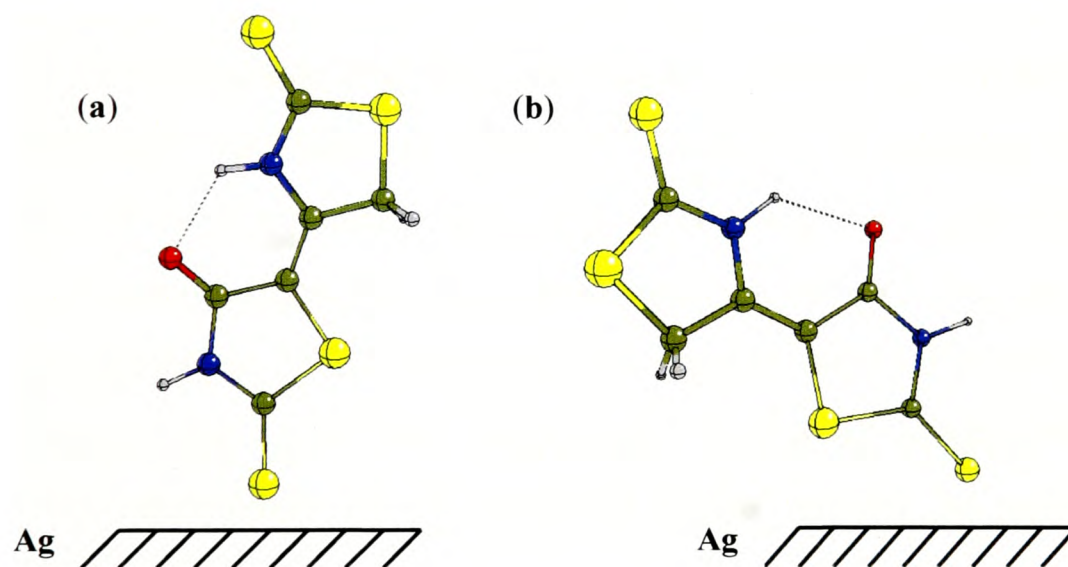


Figure 6.3. Plausible adsorption orientations of Rd dimer (*E*-isomer) on the Ag surface: (a) in the absence and (b) presence of PLL and HCl.

It is worth noting that SER spectra obtained at concentrations above $1 \times 10^{-5} \text{ mol dm}^{-3}$ resemble the SER spectra recorded under basic conditions at $1 \times 10^{-3} \text{ mol dm}^{-3}$, as discussed in chapter five. The rationale behind this is not clear. However, it is tentatively suggested that under acidic conditions, at low concentrations, the Rd dimer is adsorbed in a similar manner as under basic conditions at high concentrations. The effect of 514.5 nm

excitation on the SER spectra of Rd as a function of concentration is not significant. No changes in the spectral profiles are observed with changes in concentration. Nevertheless, there is a decrease in SERS signal intensity. A comparison of SER spectra, using exciting wavelengths at 514.5 and 632.8 nm, under optimized condition is discussed in Chapter five.

6.3.2. Concentration-Dependent SER Spectra of H₂NRd

Fig.6.4 shows SER spectra of H₂NRd over the concentration range of 8.6×10^{-8} to 8.6×10^{-4} mol dm⁻³ at pH 2.3 in the presence of PLL, using $\lambda_0 = 632.8$ nm. The spectral profiles change dramatically with decreasing concentration of H₂NRd. At a concentration of 8.6×10^{-4} mol dm⁻³ the spectral profile is dominated by bands at 526, 666, 1021, 1064, 1166, 1389, 1500, and 1575 cm⁻¹. The intense band at 1575 cm⁻¹ is assigned to the C=C stretching mode of the H₂NRd dimer, and decreases in intensity with decreasing concentration of the monomer. Similarly, bands at 1064, 1355, and 1389 cm⁻¹ (mainly arising from C=S stretching and CH₂ deformation modes) are behaving in the same manner. Conversely, the band at 1166 cm⁻¹ increases in intensity with decreasing concentration and is more enhanced at 8.6×10^{-6} mol dm⁻³, and then decreases in intensity. This band is assigned to vibrations which involve C-N, C=S and N-N stretching modes. The enhancement of the foregoing band suggests that C-N and N-N groups are in close proximity to the Ag surface, interacting with the Ag surface through the C=S moiety or that reorientation of the molecule occurs on the Ag surface (*i.e.*, from perpendicular to tilted orientation as shown in Fig.6.5). It is noteworthy that at a concentration of 8.6×10^{-4} mol dm⁻³ the band at 526 cm⁻¹ is accompanied by two shoulders at 506 and 540 cm⁻¹, which disappear leaving a single strong band at concentrations below 8.6×10^{-5} mol dm⁻³. This band is associated with an ip ring deformation mode. These changes in spectral profile could be accounted for by the reorientation of the molecule on the Ag surface, monolayer converge effects or different coordination mechanism on the Ag surface. Monolayer coverage on Ag colloid surface for H₂NRd is achieved at a concentration of 8.6×10^{-6} mol dm⁻³.

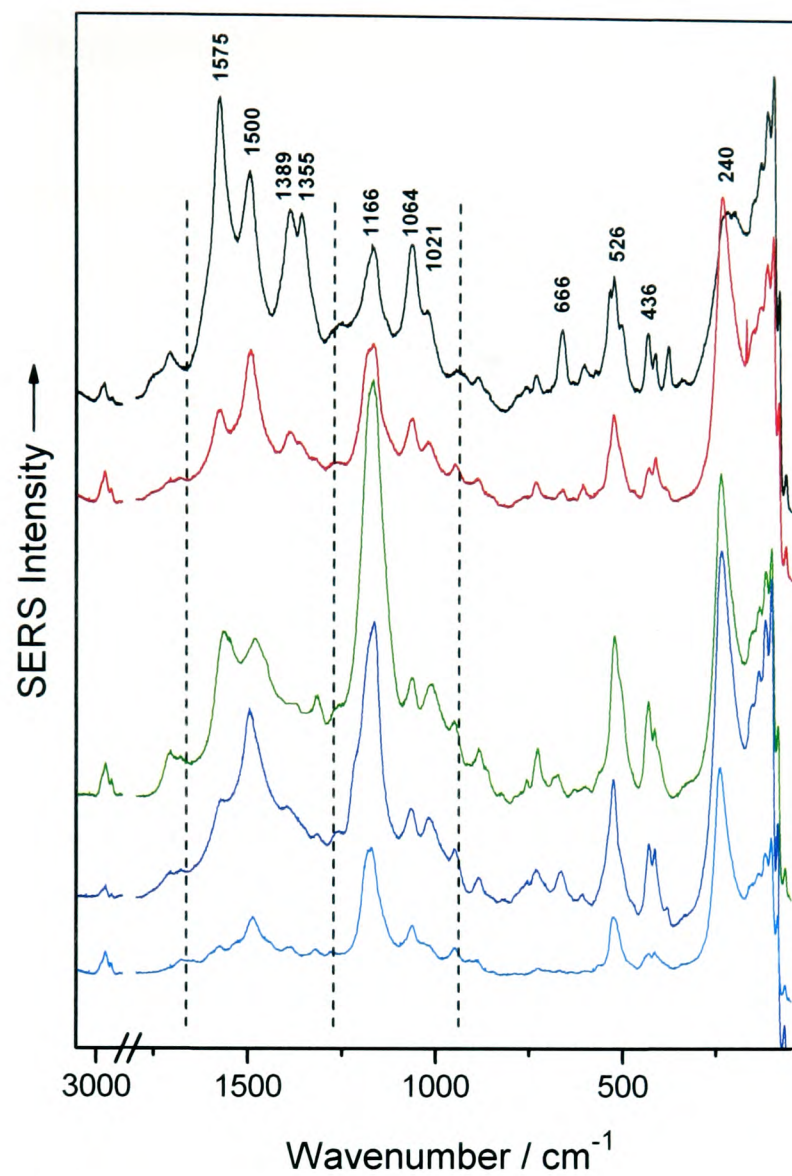


Figure 6.4. SER spectra of H_2NRd adsorbed on the Ag colloid as a function of concentration ($\lambda_0 = 632.8 \text{ nm}$). The concentrations of Rd from top to bottom are: 8.6×10^{-4} , 8.6×10^{-5} , 8.6×10^{-6} , 8.6×10^{-7} , and $8.6 \times 10^{-8} \text{ mol dm}^{-3}$.

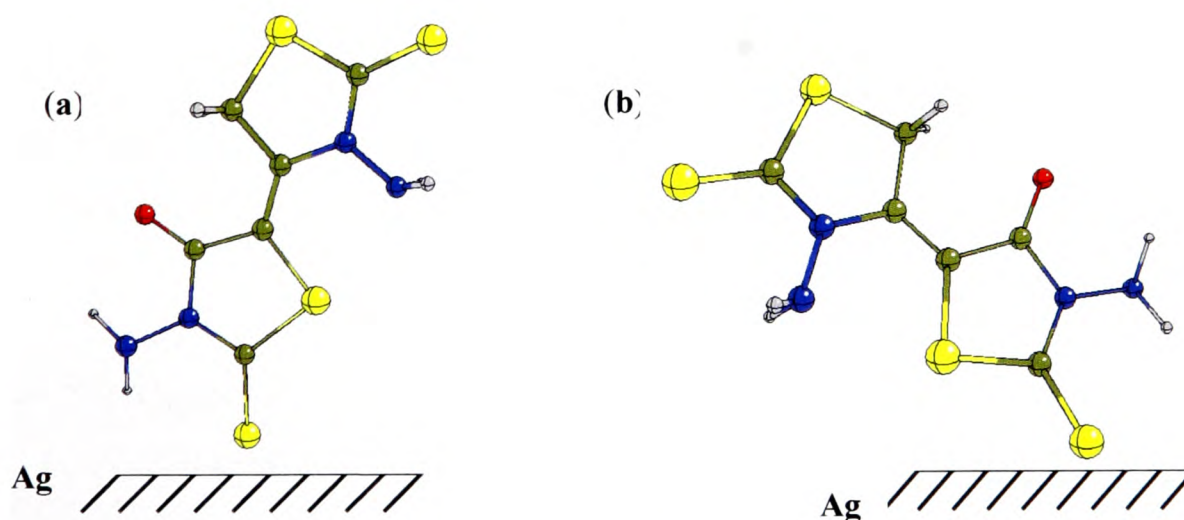


Figure 6.5. Plausible adsorption orientations of the H_2NRd dimer (*Z-isomer*) on the Ag surface: (a) at higher and (b) low concentrations in the presence of PLL and HCl.

6.3.3. Concentration-Dependent SER Spectra of MeRd

The SER spectra of MeRd over the concentration range 8.7×10^{-7} to 8.7×10^{-4} mol dm⁻³ are shown in Fig.6.6. Changes in the spectral profile with concentration are much less significant compared with Rd and H₂NRd. Nevertheless, there are noticeable changes in the 1400 to 1575 cm⁻¹ region. The bands found in this region are assigned to C=C stretching, CH₃ symmetric and asymmetric stretching modes. The band at 1572 cm⁻¹ decreases in intensity with decreasing concentration but the band at 1503 cm⁻¹ increases in intensity, becoming more enhanced at 8.7×10^{-7} mol dm⁻³ and then drops in intensity with further decrease in concentration. The doublet at 1155 and 1173 cm⁻¹ (mainly attributed to mixed CH₃ deformation and C=S stretching modes) also changes with decreasing concentration. For example at a concentration of 8.7×10^{-7} mol dm⁻³ the former is enhanced and the latter is observed as a shoulder.

In the case of MeRd, there are two possible sites for coordination to the Ag substrate: the thioamide sulphur and carbonyl oxygen atoms. By analogy with un-substituted Rd it is expected that MeRd is more likely to coordinate through the exo-sulfur atom. Apparently, in SER spectra the bands associated with C-N stretching at 1155, 1173 and 1255 cm⁻¹ are more enhanced compared with their relative intensities in the solid state spectrum, as discussed in Chapter four. The foregoing indicates that C-N groups are most likely to be perpendicular to the surface; band shifts show interaction with the surface or are in close proximity to the coordination site as depicted in Fig.6.7. At higher concentrations (*e.g.* 8.7×10^{-4} mol dm⁻³) of adsorbate the molecules adopt a perpendicular orientation on the surface, whereas at low concentration they re-orientate and adopt a tilted orientation.

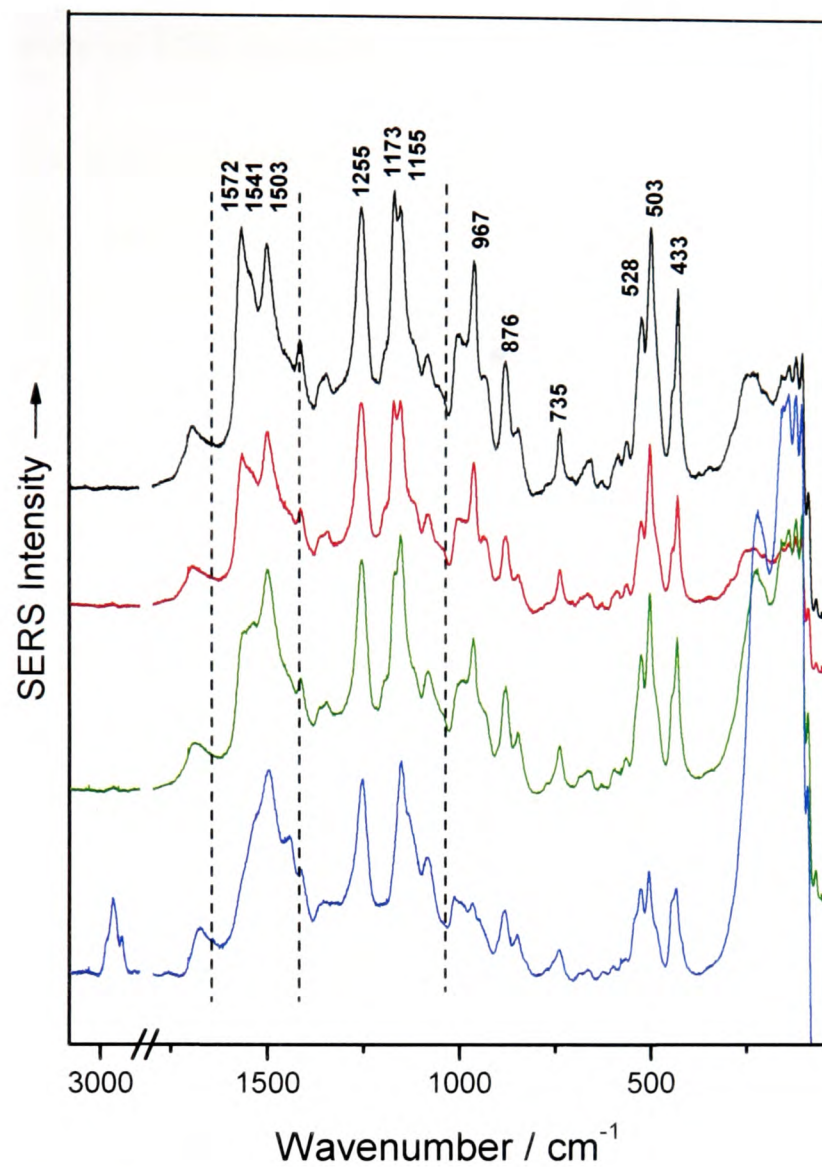


Figure 6.6. SER spectra of MeRd adsorbed on the Ag colloid as a function of concentration ($\lambda_0 = 632.8$ nm). The concentrations of MeRd from top to bottom are: 8.7×10^{-4} , 8.7×10^{-5} , 8.7×10^{-6} , and 8.7×10^{-7} mol dm $^{-3}$.

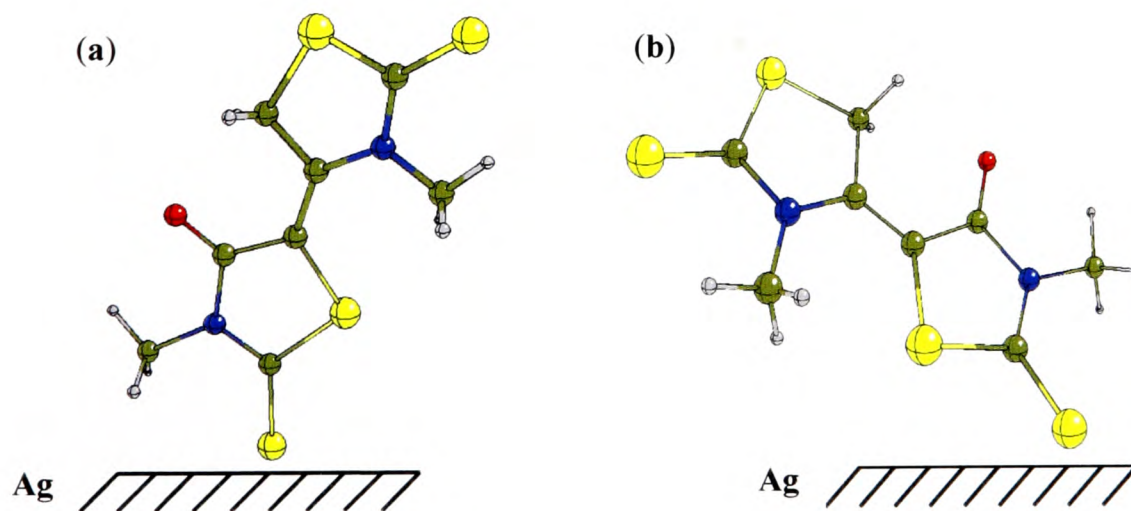
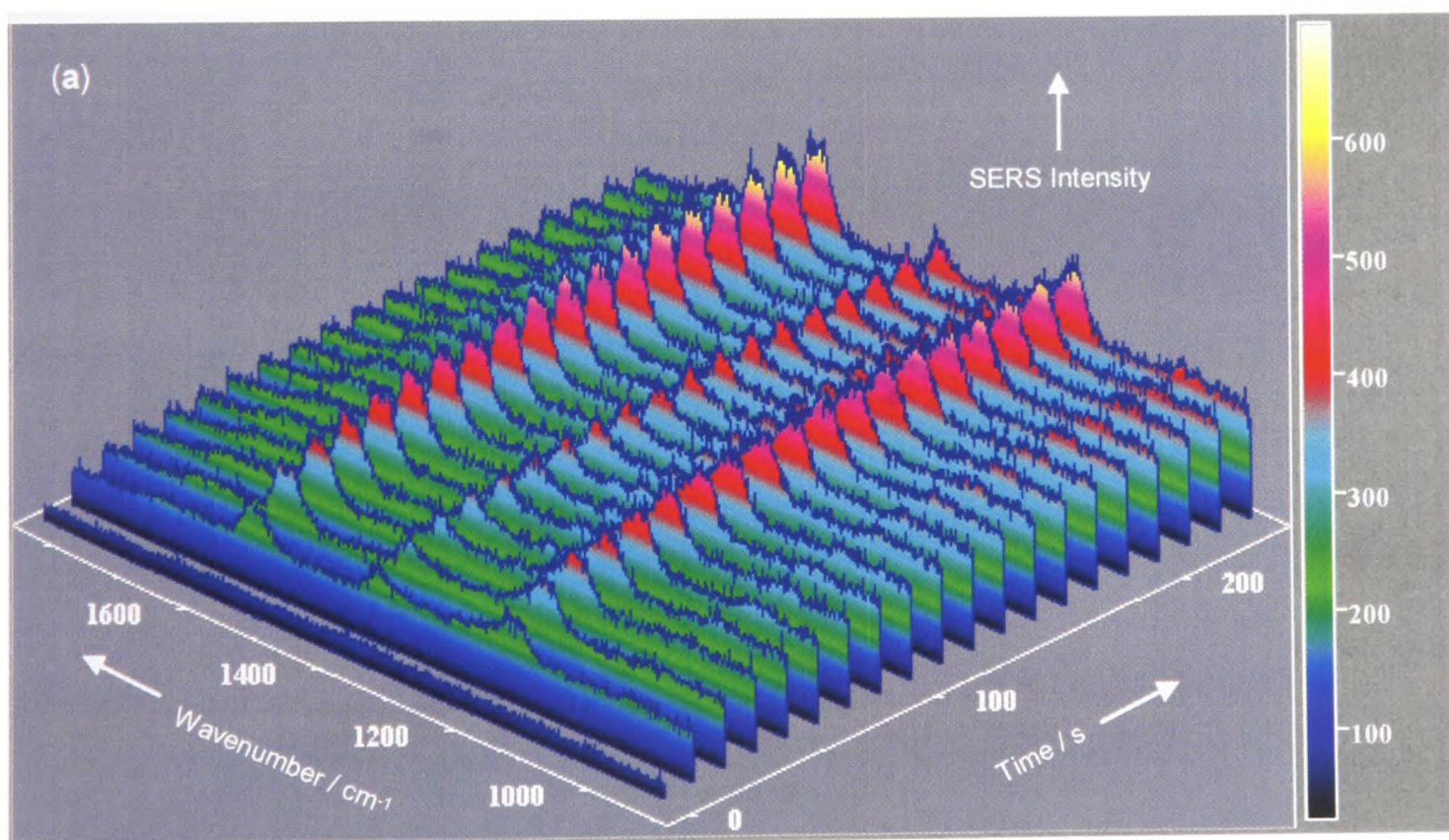
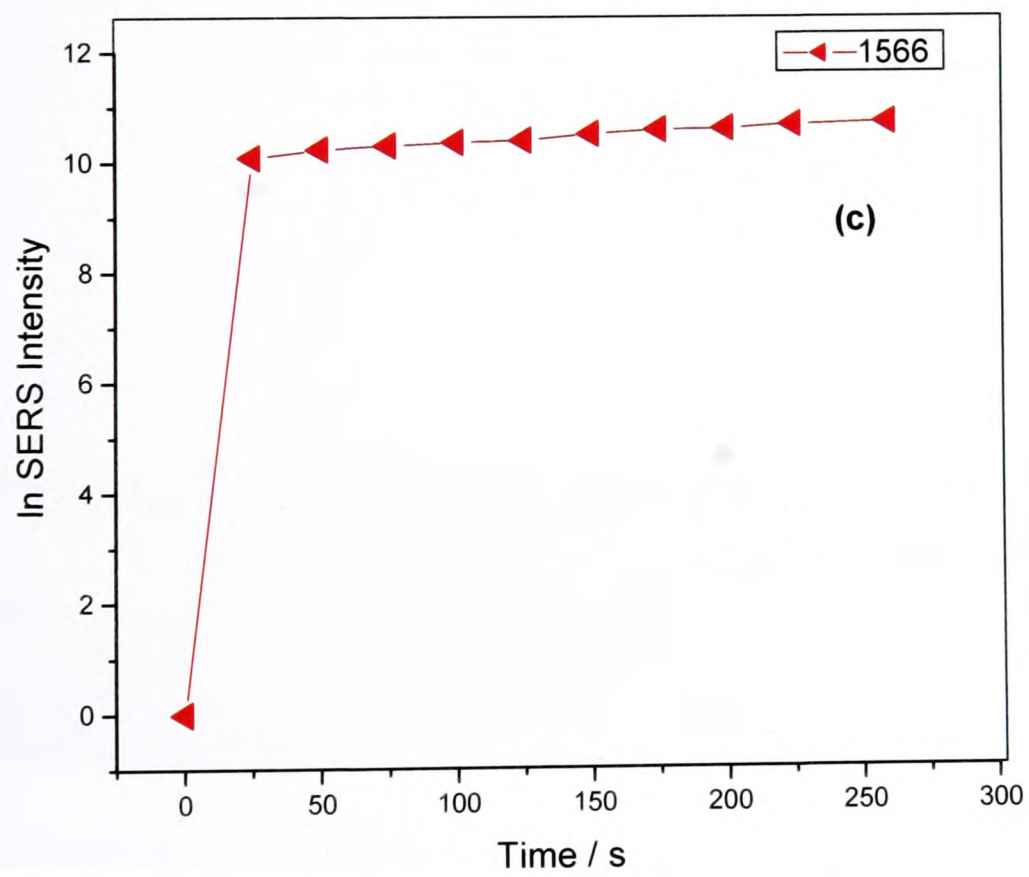
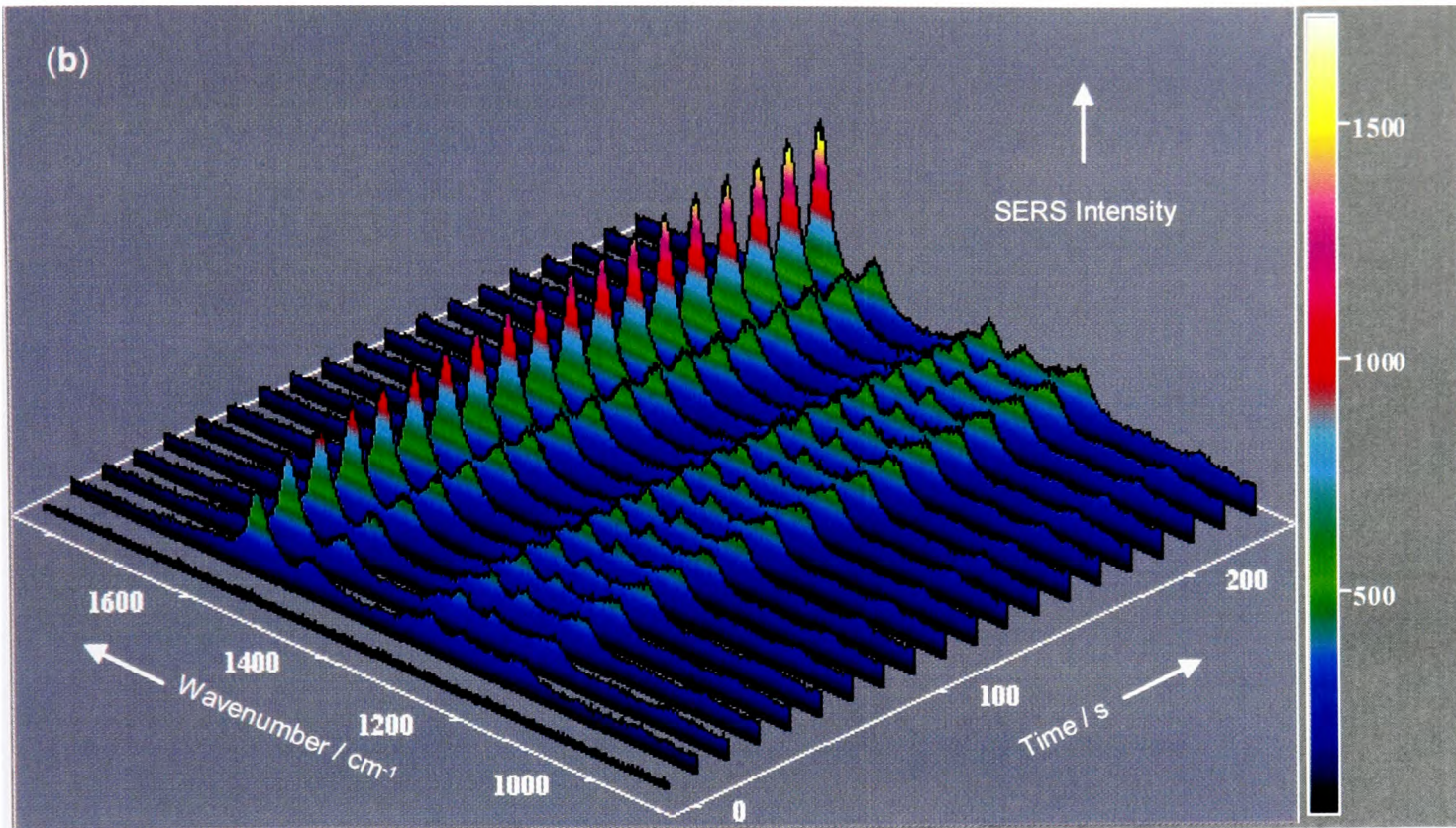


Figure 6.7. Plausible adsorption orientations of MeRd dimer (*Z-isomer*) on the Ag surface: (a) at higher and (b) low concentrations in the presence of PLL and HCl.

6.3.4. Time-Dependence of SER Spectra

Fig.6.8 (a,b) shows the time-dependent SER spectra of Rd dimer under optimized and minimal pH conditions, respectively using 632.8 nm excitation in the 900-1800 cm^{-1} region. A graph has been plotted for \ln SER intensity (peak area) of the band located at 1566 cm^{-1} vs. time (Fig.6.8c), which initially shows a dramatic increase in intensity followed by a linear dependence of SERS signal with time. Similarly, Figs.6.8 (d,e) displays the time-dependent SER spectra of H_2NRd and MeRd dimers following the addition of PLL and HCl, respectively. It is apparent from the SER spectra that there is a gradual increase in intensity of the band at $\approx 1566/1575/1572 \text{ cm}^{-1}$ with time. This indicates that the overall increase in the intensity of this band cannot be attributed to changes in molecular orientation with time. The increase in the intensity of SERS signal is probably due to the aggregation of Ag colloidal NPs and also due to the co-adsorption and replacement kinetics of Cl^- anions and Rd molecules on the Ag surface with time. After 30 minutes the intensity decreases due to the precipitation of Ag NPs.





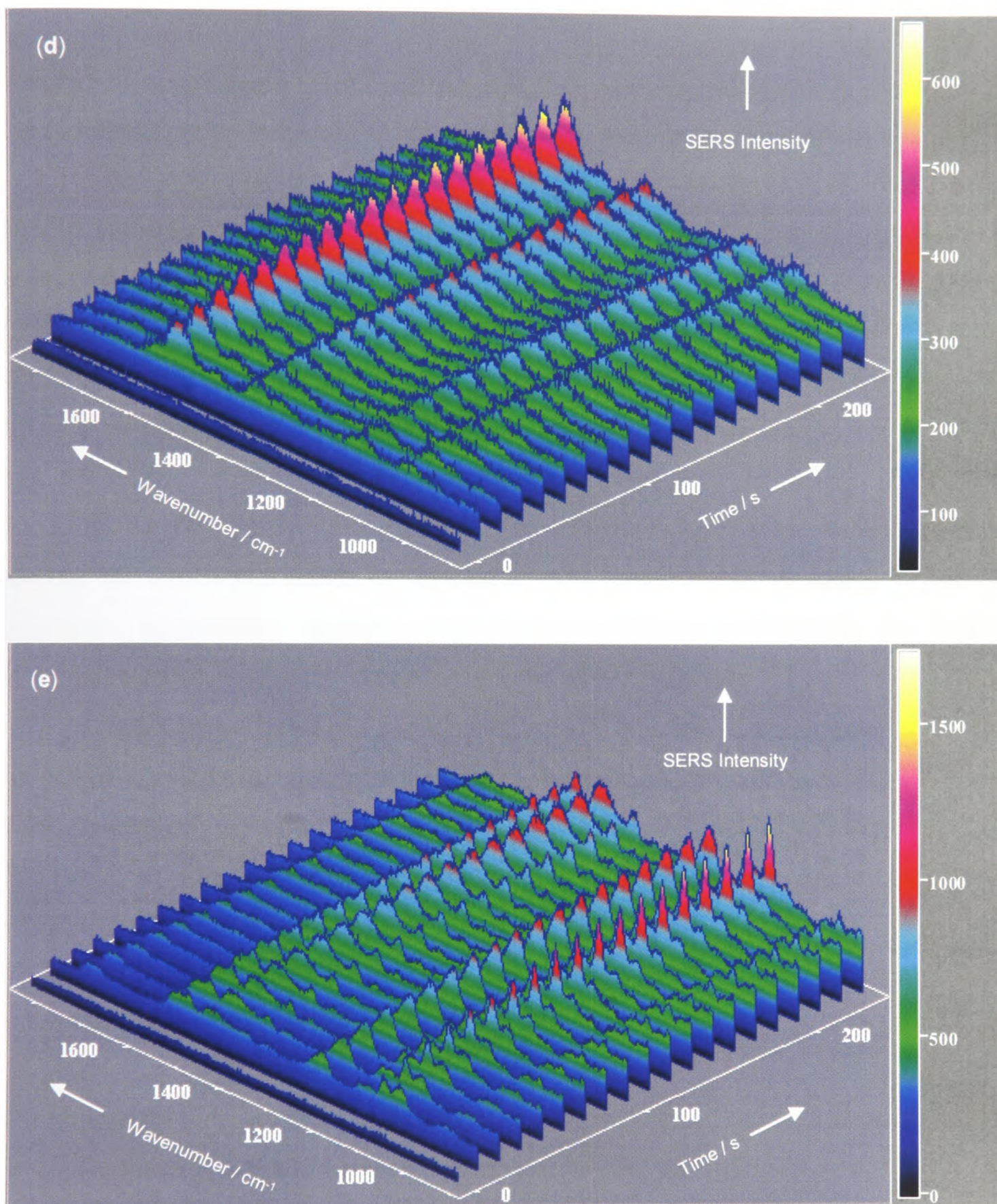


Figure 6.8. Time dependent SER spectra of: (a) Rd ($1 \times 10^{-3} \text{ mol dm}^{-3}$) in the absence of PLL and HCl, (b) Rd ($1 \times 10^{-4} \text{ mol dm}^{-3}$), (c) In [signal intensity (peak area)] vs. time for SERS band at 1566 cm^{-1} , (d) H₂NRd ($8.6 \times 10^{-5} \text{ mol dm}^{-3}$), and (d) MeRd ($8.7 \times 10^{-5} \text{ mol dm}^{-3}$) in the presence of PLL and HCl; ($\lambda_0 = 632.8 \text{ nm}$).

6.3.5. Linear correlations

The Rd SER spectra used for multi-linear regression analysis, and plots of log intensity vs log concentration for 514.4 and 632.8 nm excitation, are shown in Figs.6.9 (a, c) and 6.10 (a, c), respectively. Similarly, SER spectra and plots of log intensity vs concentration for H₂NRd and MeRd ($\lambda_0 = 632.8$ nm) are shown in Figs. 6.11 (a, c) and 6.12 (a, c), respectively. The linear correlation coefficients (R^2) for Rd, H₂NRd, and MeRd for the SERS signal intensities are given in Table 6.1. For Rd, good linear correlations are observed with 632.8 nm excitation for the bands at 1566 ($R^2 = 0.992$) and 556 cm^{-1} ($R^2 = 0.980$) and using 514.5 nm excitation for the bands at 1566 ($R^2 = 0.992$) and 452 cm^{-1} ($R^2 = 0.992$) over the concentration range 1×10^{-13} - 1×10^{-7} and 1×10^{-11} - 1×10^{-8} mol dm^{-3} , respectively. The quantifiable concentration range for SER spectra, for 514.5 and 632.8 nm excitation, was found to be ≈ 3 and 6 orders of magnitude, respectively. Similarly, good linear correlations are observed for H₂NRd using 632.8 nm excitation for the bands at 1166 ($R^2 = 0.978$) and 525 cm^{-1} ($R^2 = 0.995$) over the concentration range of 8.6×10^{-12} - 8.6×10^{-7} mol dm^{-3} . The calculated R^2 values for MeRd for the bands at 1255 and 433 cm^{-1} using 632.8 nm excitation are 0.977 and 0.990, respectively over the concentration range of 8.7×10^{-13} to 8.7×10^{-9} mol dm^{-3} . The linear concentration range for SER spectra of H₂NRd and MeRd, at 632.8 nm excitation, was found to be ≈ 5 and 4 orders of magnitude, respectively.

6.3.6. Multi-linear Regression Analysis

The plots of the dependence of SERS signals on concentration give good fits to sigmoidal curves for Rd (514 and 632.8 nm excitation) and its derivatives (632.8 nm) as shown in Figs. 6.9 (b), 6.10 (b), 6.11 (b) and 6.12 (b), respectively. The R.S.D., values obtained after the multi-linear regression analysis of SERS signal intensity vs concentration data are tabulated in Table 6.1. In the case of Rd, the calculated R.S.D. values using 514.5 nm excitation for SERS bands at 1566 and 452 cm^{-1} are ± 0.284 and ± 0.165 , respectively. Similarly, for the 632.8 nm excited SERS bands at 1566 and 556 cm^{-1} the calculated R.S.D. values are ± 0.114 and ± 0.169 , respectively. There is not much difference

between the R.S.D. values obtained, which implies that both excitation wavelengths can be employed for semi-quantitative analysis. The limits of detection (LOD) are calculated as the quotient of three times the standard deviation of intercept and the slope of the lines of best fit, as shown in Table 6.1. For Rd, the LODs are 1×10^{-11} (4.4 ppb) and 1×10^{-11} (6 ppb) mol dm^{-3} for the bands at 1565 and 452 cm^{-1} ($\lambda_0 = 515.4 \text{ nm}$); and 1×10^{-13} (6.6 ppt) and 1×10^{-13} mol dm^{-3} (5.8 ppt) for the bands at 1566 and 556 cm^{-1} ($\lambda_0 = 632.8 \text{ nm}$), respectively. In the case of H₂NRd the R.S.D. values for SERS bands at 1166 and 524 cm^{-1} are ± 0.059 and ± 0.177 using 632.8 nm excitation. Consequently, the calculated LOD for corresponding bands at 8.6×10^{-12} mol dm^{-3} concentration are 2.5 ppb and 4.6 ppb, respectively. On the other hand, R.S.D. values obtained for MeRd bands at 1255 and 433 cm^{-1} are ± 0.126 and ± 0.105 , respectively. The LOD's at 8.7×10^{-13} mol dm^{-3} concentration are 0.840 and 0.640 ppb for the corresponding bands.

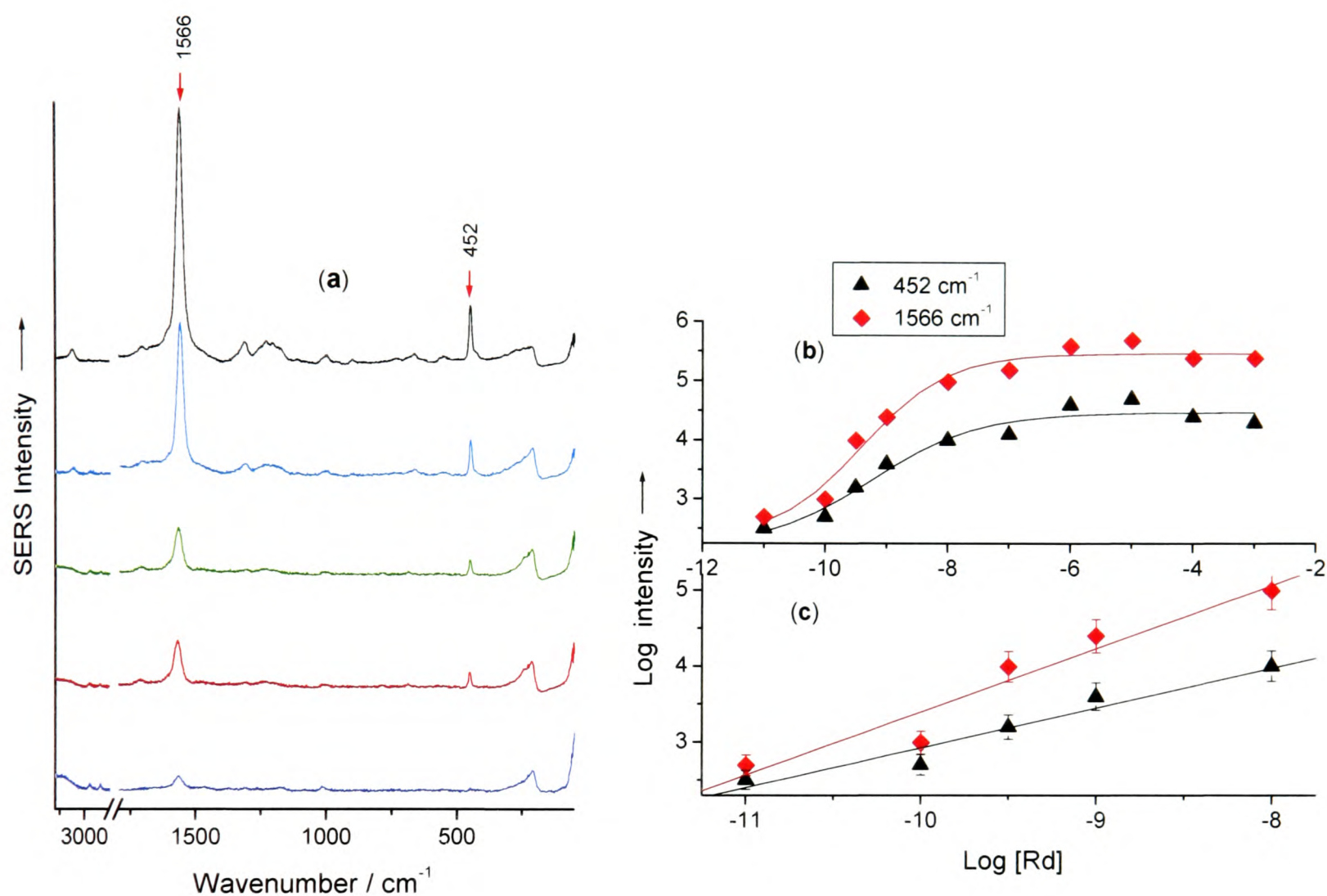


Figure 6.9. (a). Representative 514.5 nm excited SER spectra for Rd (at pH 2.3) in the linear signal vs. concentration region. Concentrations from top to bottom are 1×10^{-8} , 1×10^{-9} , 2.5×10^{-10} , 1×10^{-10} and 1×10^{-11} mol dm⁻³. The bands used for analysis are indicated with arrows. **(b).** Log (concentration) vs. log (signal intensity) (peak area) over the concentration range examined for 632.8 nm excited SERS bands at 452 (▲) and 1566 cm⁻¹ (◆). **(c).** Linear region of intensities of SERS bands of Rd at 452 (▲) and 1566 cm⁻¹ (◆) used for multi-linear regression analysis.

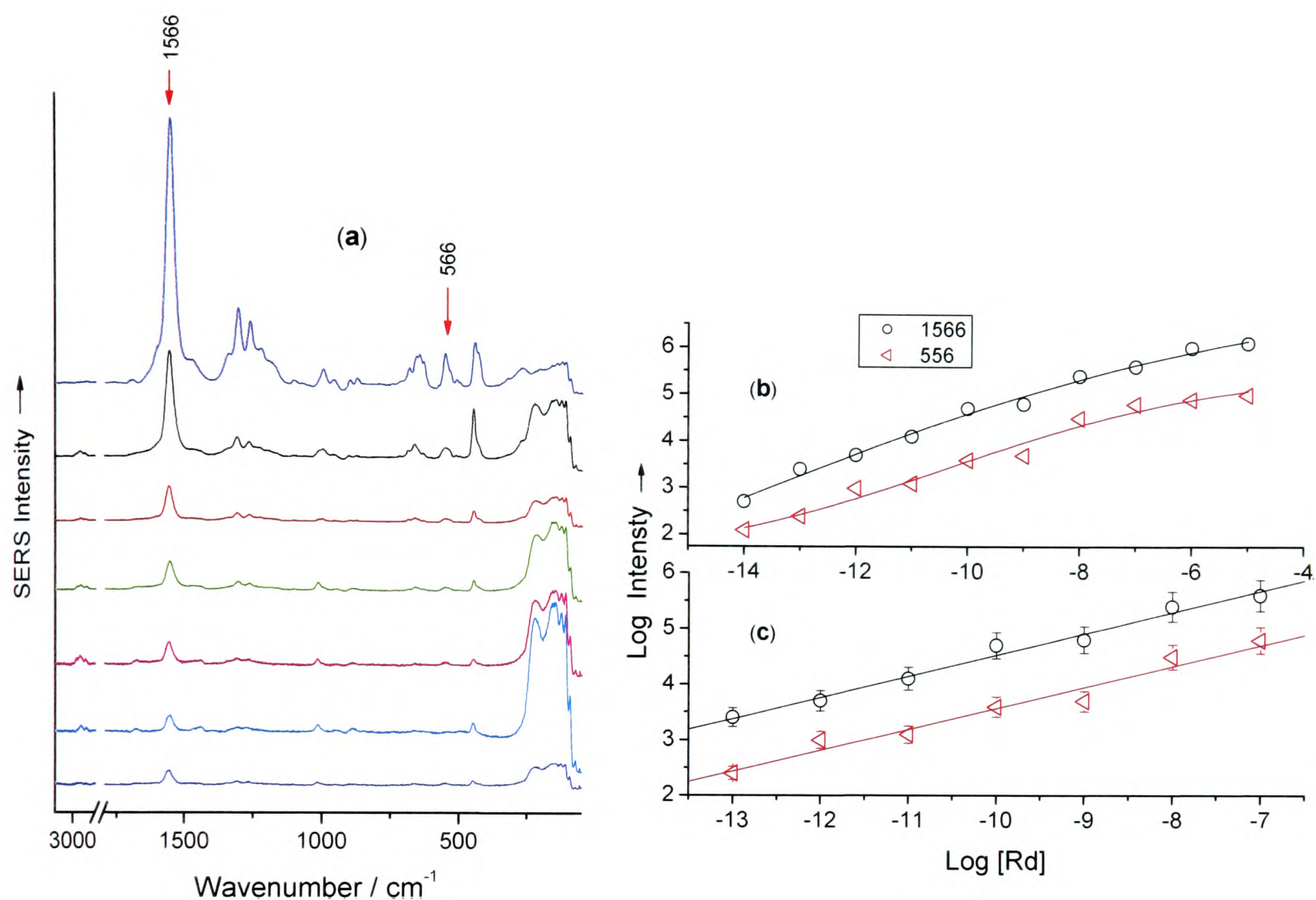


Figure 6.10. (a). Representative 632.8 nm excited SER spectra of Rd (at pH 2.3) in the linear signal vs. concentration region. Concentrations from top to bottom are 1×10^{-7} , 1×10^{-8} , 1×10^{-9} , 1×10^{-10} , 1×10^{-11} , 1×10^{-12} , and 1×10^{-13} mol dm⁻³. The bands used for analysis are indicated by arrows. **(b).** Log concentration Rd vs. log signal intensity (peak area) over the concentration range examined for 632.8 nm excited SERS bands at 556 (\blacktriangleleft) and 1566 cm⁻¹ (\circ). **(c).** Linear region of intensities of SERS bands of Rd at 556 (\blacktriangleleft) and 1566 cm⁻¹ (\circ) used for multi-linear regression analysis.

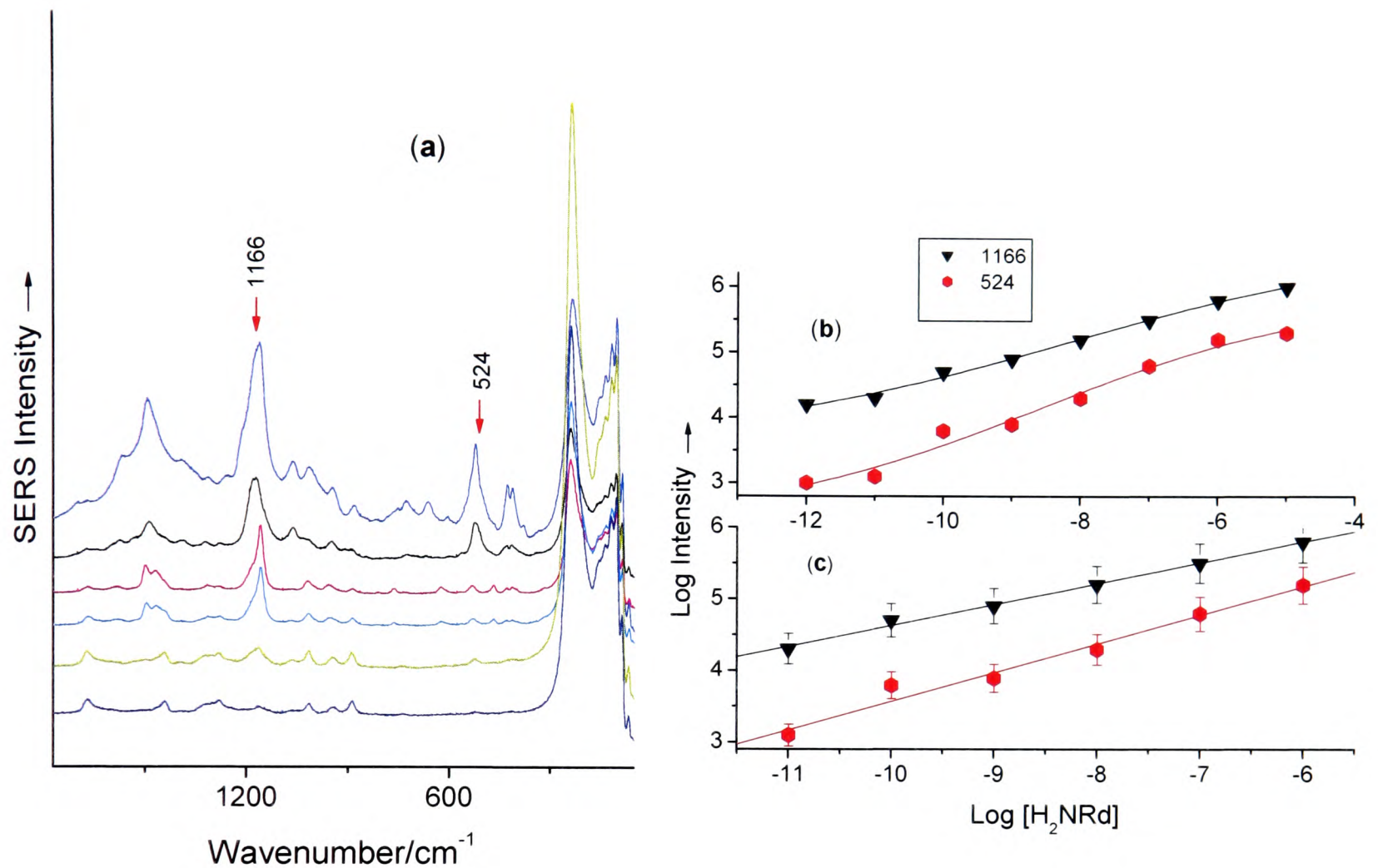


Figure 6.11. (a). Representative 632.8 nm excited SERS spectra for H₂NRd (at pH 2.3) in the linear signal vs. concentration region. Concentrations from top to bottom are 8.6×10^{-7} , 8.6×10^{-8} , 8.6×10^{-9} , 8.6×10^{-10} , 8.6×10^{-11} , and 8.6×10^{-12} mol dm⁻³. The bands used for analysis are indicated by arrows. (b). Log concentration Rd vs. log signal intensity (peak area) over the concentration range examined for 632.8 nm excited SERS bands at 524 (▼) and 1166 (●) cm⁻¹. (c). Linear region of intensities of SERS bands of Rd at 524 (▼) and 1166 cm⁻¹(●) used for multi-linear regression analysis.

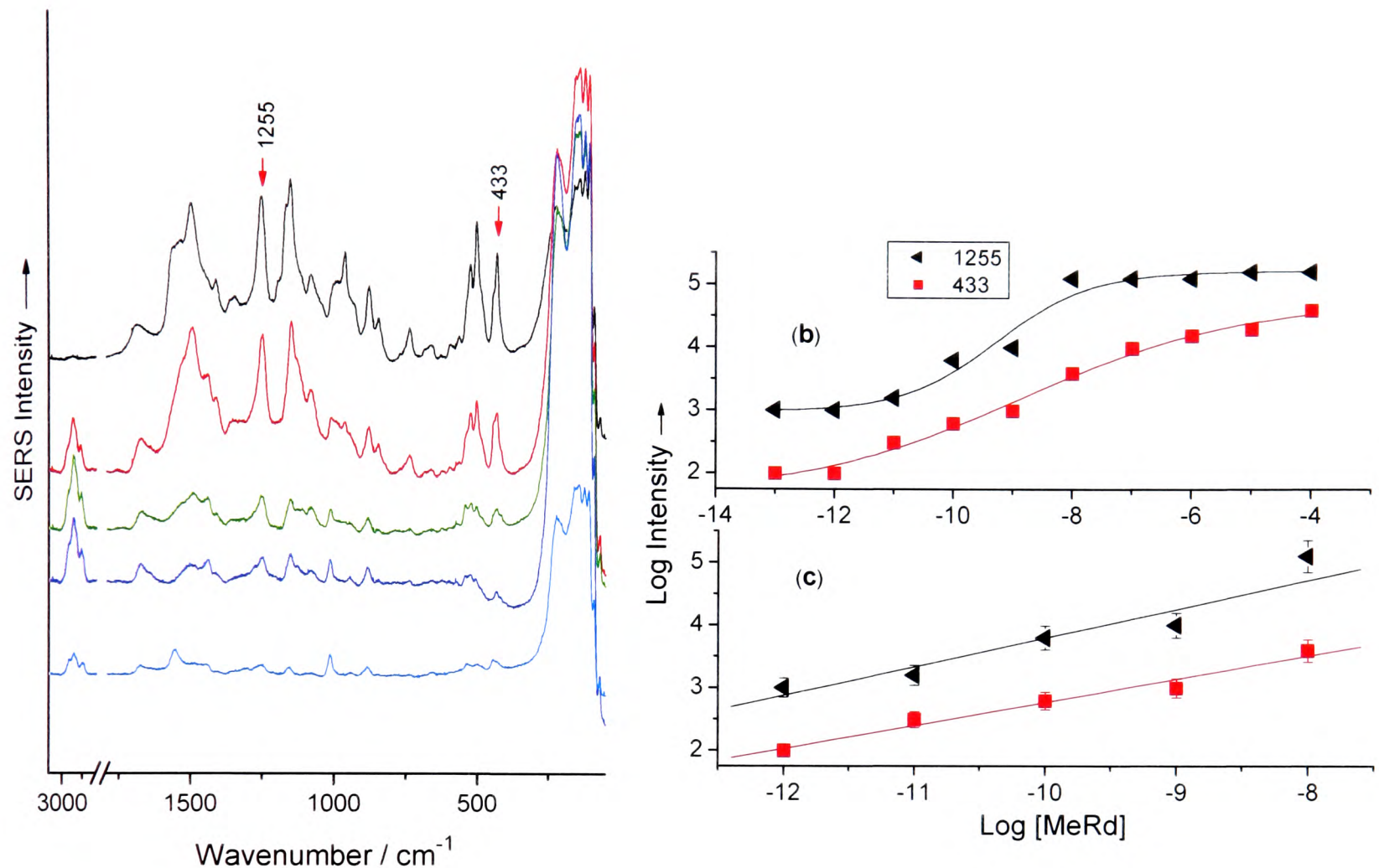


Figure 6.12. (a). Representative 632.8 nm excited SER spectra of MeRd (at pH 2.3) in the linear signal *vs.* concentration region. Concentrations from top to bottom are 8.7×10^{-9} , 8.7×10^{-10} , 8.7×10^{-11} , 8.7×10^{-12} , and 8.7×10^{-13} mol dm⁻³. The bands used for analysis are indicated by arrows. (b). Log concentration *vs.* log signal intensity (peak area) over the concentration range examined for 632.8 nm excited SERS bands at 433 (■) and 1255 cm⁻¹ (◄). (c). Linear region of intensities of SERS bands of Rd at 433 (■) and 1255 cm⁻¹ (◄) used for multi-linear regression analysis.

Table 6.1. Analytical parameters calculated from multi-linear regression analysis of Rd and its derivatives.

Technique	Molecules	Band (cm^{-1})	pH	Slope	Intercept	Correlation Coefficient (R^2)	Linear Region			χ^2	
							Conc. Range (mol dm^{-3})	RSD (\pm)	Orders of Magnitude		LOD* (ppb/ppt)
SERS (514.5 nm)	Rd	1566	2.3	0.83	11.76	0.961	10^{-12} - 10^{-9}	0.284	3	4.4 ppb	0.035
		452		0.54	8.33	0.976		0.165	3	6 ppb	0.042
SERS (632.8 nm)	Rd	1566	2.3	0.38	8.35	0.992	10^{-14} - 10^{-8}	0.114	6	6.6 ppt	0.031
		556		0.38	7.44	0.980		0.169	6	5.8 ppt	0.015
SERS (632.8 nm)	H ₂ NRd	1166	2.3	0.29	7.53	0.978	10^{-12} - 10^{-7}	0.059	5	2.5 ppb	0.016
		524		0.37	7.29	0.995		0.177	5	4.6 ppb	0.003
SERS (632.8 nm)	MeRd	1255	2.3	0.36	7.28	0.977	10^{-13} - 10^{-9}	0.126	4	0.84 ppb	0.031
		433		0.38	6.67	0.990		0.105	4	0.64 ppb	0.013

* Three times standard deviation of intercept/slope

6.4. Summary and Conclusions

The concentration-dependent SERS studies of Rd and its derivatives have encompassed both the adsorption behaviour on the Ag surface and semi-quantitative trace analysis. This study clearly demonstrates that changing the adsorbate concentration causes changes in molecular orientation or coordination of different adsorption sites, which have significant effects on the intensities of SERS bands. The monolayer coverage effect of adsorbate on the Ag surface is evident in the SER spectra for the three molecules. In particular, for Rd and H₂NRd certain bands exhibit maximum intensity at 1×10^{-5} and 8.6×10^{-6} mol dm⁻³, respectively, which are representative of monolayer coverage on the Ag surface. However, in addition to the foregoing effect orientation changes of the molecule on the surface are also apparent in the SER spectra of Rd and H₂NRd. The enhancement of bands due to C-N stretching modes reflect the fact that these molecules are adsorbed on the Ag surface through the exo-sulfur group, which in turn enhances the vibrations associated with the C-N moiety due to a combination of electromagnetic and charge transfer effects.

In this study low LOD values and good linear correlations have been achieved for the three molecules examined. In the case of Rd, two excitation wavelengths have been employed to conduct semi-quantitative analysis. However, using 632.8 nm excitation SER spectra have been detected at near femtomolar concentration in relation to 514.5 nm excitation wavelength (*i.e.*, picomolar concentration). Similarly, for H₂NRd and MeRd SER spectra were recorded at picomolar and femtomolar concentrations, respectively. The SERS data presented herein highlight the sensitivity and specificity of this technique as a probe for conducting semi-quantitative trace analysis.

6.5. References

- [1] P. Etchegoin, R. C. Maher, L. F. Cohen, H. Hartigan, R. J. Brown, M. J. T. Milton and J. C. Gallop, *Chem. Phys. Lett.*, **375**, (2003), 84.
- [2] M. Futamata, Y. Maruyama and M. Ishikawa, *Vib. Spectrosc.*, **35**, (2004), 121.
- [3] J. T. Krug, G. D. Wang, S. R. Emory and S. Nie, *J. Am. Chem. Soc.*, **120**, (1999), 9208.
- [4] S. Nie and S.R. Emery, *Science*, **275**, (1997), 1102.
- [5] K. Kneipp, Y. Wang, H. Kneipp, L. T. Perelman, I. Itzkan, R. R. Dasari and M. S. Feld, *Phys. Rev. Lett.*, **78**, (1997), 1667.
- [6] K. Kneip, H. Kneipp, I. Itzkan, R. R. Dasari and M. S. Feld, *Chem. Rev.*, **99**, (1999), 2957.
- [7] H. Xu, E. J. Bjerneld, M. Käll and L. Borjesson, *Phys. Rev. Lett.*, **83**, (1999), 4357.
- [8] E. J. Bjernald, Z. Foldes-Papp, M. Käll and R. Rigler, *J. Phys. Chem. B* **106**, (2002), 1213.
- [9] H. Xu, J. Aizpurua, M. Käll and P. Apell, *Phys. Rev. E* **62**, (2000), 4318.
- [10] A. M. Micheals, J. Jiang and L. E. Brus, *J. Phys. Chem. B* **104**, (2000), 11965.
- [11] K. A. Bosnick, J. Jiang and L. E. Brus, *J. Phys. Chem. B* **106**, (2000), 8096.
- [12] R. F. Aroca, R. A. Avarez-Puebla, N. Pieczonka, S. Sanchez-Cortez and J. V. Garcia, *Adv. Coll. Interf. Sci.*, **116**, (2005), 45.
- [13] M. Moskovits, *Rev. Mod. Phys.*, **57**, (1985), 783.
- [14] M. Moskovits, *J. Raman. Spectrosc.*, **36**, (2005), 485.
- [15] M. Moskovits, J. S. Suh, *J. Phys. Chem.*, **92**, (1988), 6327.
- [16] J. Chowdhury, M. Ghosh, P. Pal and T. N. Misra, *J. Coll. Interf. Sci.*, **263**, (2003), 318.
- [17] J. Chowdhury and M. Ghosh, *J. Coll. Interf. Sci.*, **277**, (2004), 121.

Chapter Seven

PCS Measurements: Influence of Aggregating Agents on Ag and Au Nanoparticles (NPs) Aggregation

7.1. Introduction

Aggregation of colloidal NPs is very important from the point of view of SERS, due to the fact that large enhancements are observed at the particle junctions of substrate aggregates¹⁻². Even single-molecule SERS has been reported on small Ag NP aggregates³. Despite the fact that aggregation is crucial for effective SERS enhancement, there are few in-depth studies in the literature pertaining to the kinetics of aggregation by employing photon correlation spectroscopy (PCS). Lecomte *et al.* have studied the ζ -potential of a Ag colloid prepared by citrate reduction method⁴⁻⁵ as a function of different analytes⁶⁻⁷, whilst Aroca *et al.*⁸ have carried out ζ -potential measurements as a function of pH for Ag and Au colloids prepared by citrate and borohydride reduction methods⁹⁻¹⁰. Faulds *et al.*¹¹ have investigated aggregated and non-aggregated NPs to obtain insight into the SER(R)S phenomenon.

The focus of the present study is predominantly on the state of aggregation of Ag and Au NPs, by employing a number of different aggregating agents as a function of concentration and time to optimize SERS experimental conditions, in terms of ζ -potential (surface charge), hydrodynamic diameter and electrophoretic mobility. Potassium chloride (KCl), sodium sulphate (Na₂SO₄), sodium thiosulfate (Na₂S₂O₃) and poly(L-lysine) [PLL] have been used to induce the aggregation of Ag and Au NPs. ζ -potential and hydrodynamic diameter measurements of Rd and its derivatives adsorbed on Ag and Au surfaces have also been investigated under different optimized SERS experimental conditions.

7.2. Experimental

7.2.1. Chemical reagents

See section 3.1. in Chapter three.

7.2.2. Synthesis and aggregation of Ag Colloid

See sections 3.8., and 3.9. in Chapter three.

7.2.3. Photon Correlaton Spectroscopy (PCS)

See sections 3.14., 3.14.1., and 3.14.2. in Chapter three.

7.2.4. UV/vis absorption Spectroscopy

See section 3.16. in Chapter three.

7.3. Results and Discussion

7.3.1. Characterization of Ag and Au Colloidal NPs

Ag and Au colloids were characterized by UV/vis spectra and PCS measurements. Plasmon absorption bands are observed for Ag and Au colloids at 425 ± 5 and 521 ± 5 nm, respectively; the foregoing values are consistent with those reported in the literature^{4, 10}. The full width at half maximum (FWHM) of the plasmon absorption band for Ag NPs is ≈ 89 nm, indicating a distribution of different size particles (Fig.7.1a).

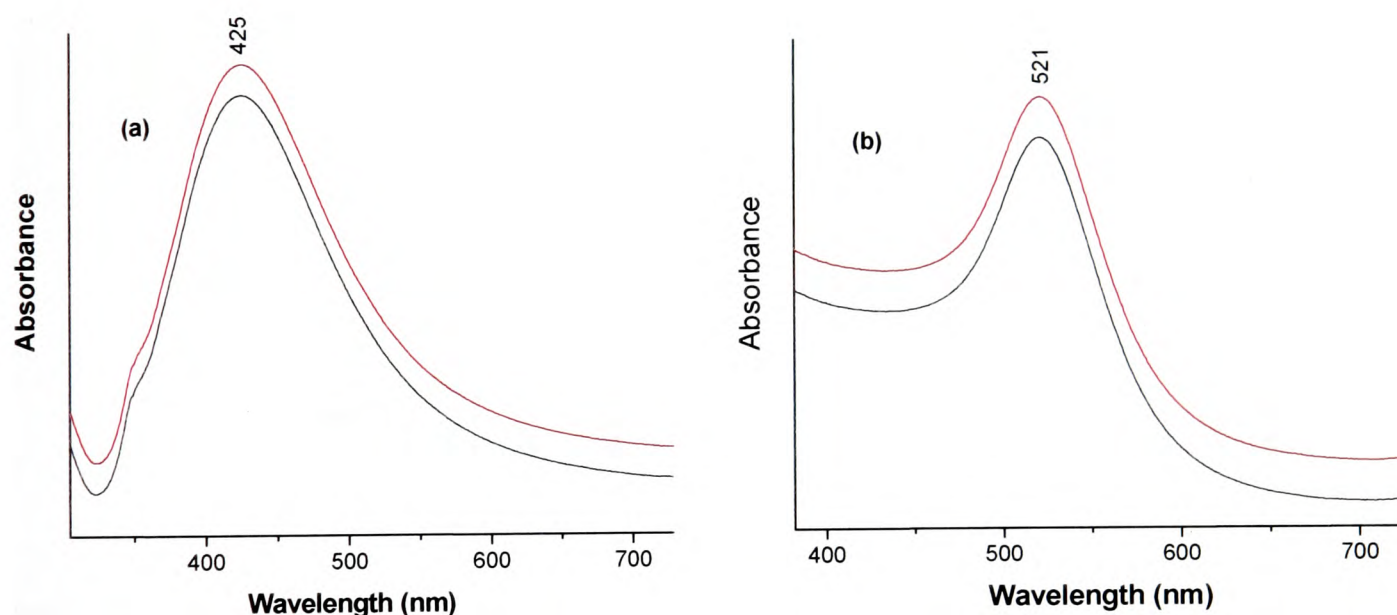


Figure 7.1. UV/Vis spectra of: (a) Ag and (b) Au NPs prepared by the chemical reduction method using tri-sodium citrate.

In the case of Au NPs, the FWHM of the plasmon band is ≈ 50 nm *i.e.*, a more homogeneous dispersion (the absorption at longer wavelengths was negligible indicative of the absence of larger particles), compared to the Ag colloid (Fig.7.1b). The hydrodynamic diameters (D_H) for Ag and Au NPs are 65 ± 5 and 50 ± 5 nm with ζ -potential values of -31 and -30 mV, respectively; the foregoing values are in good agreement with a previous report⁸. The size distribution of the Ag colloid, as measured by intensity fluctuations using PCS, indicates that the dispersion is not

monodisperse due to the presence of two peaks as shown in Fig.7.2a. Considering that the intensity distribution overestimates large particles, one can conclude that most of the Ag colloid particles are $\sim 65 \pm 5$ nm in diameter, with a small contribution from larger size particles. The size distribution is also confirmed by the TEM images, as shown in Fig.7.3.

Interestingly, only one peak is observed for the Au colloid in the particle size distribution graph representing a more homogenous colloidal dispersion, compared to the Ag colloid (Fig.7.2b).

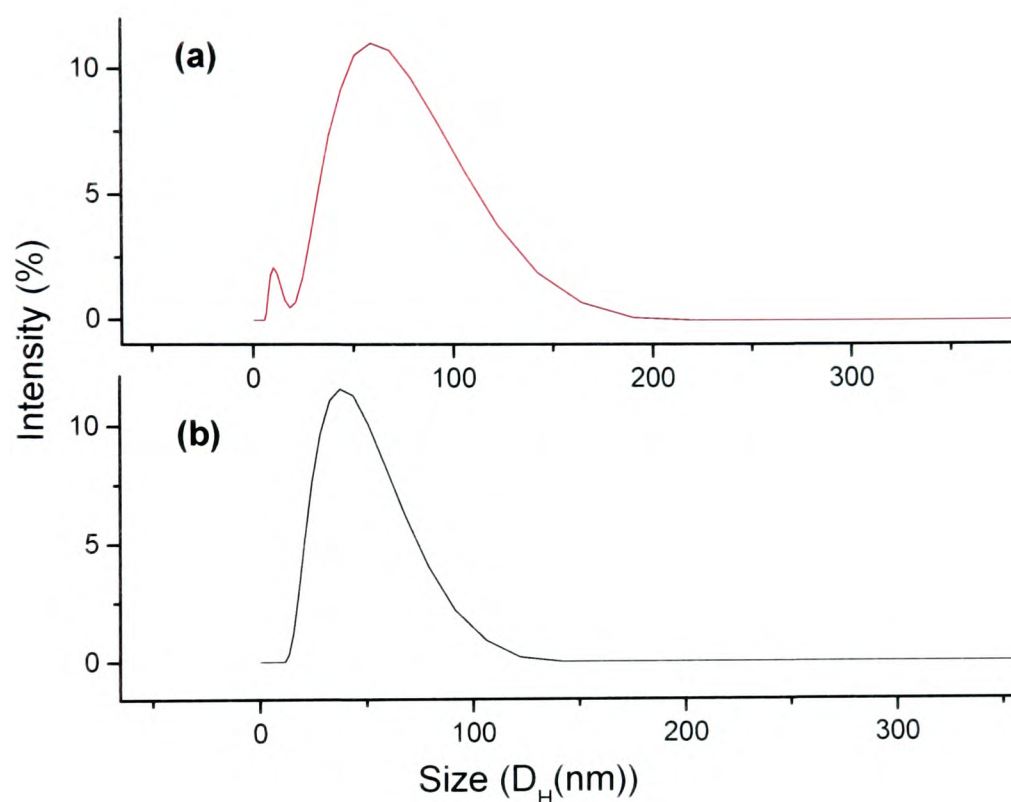


Figure 7.2. Size distribution analysis by intensity of (a) Ag and (b) Au NPs.

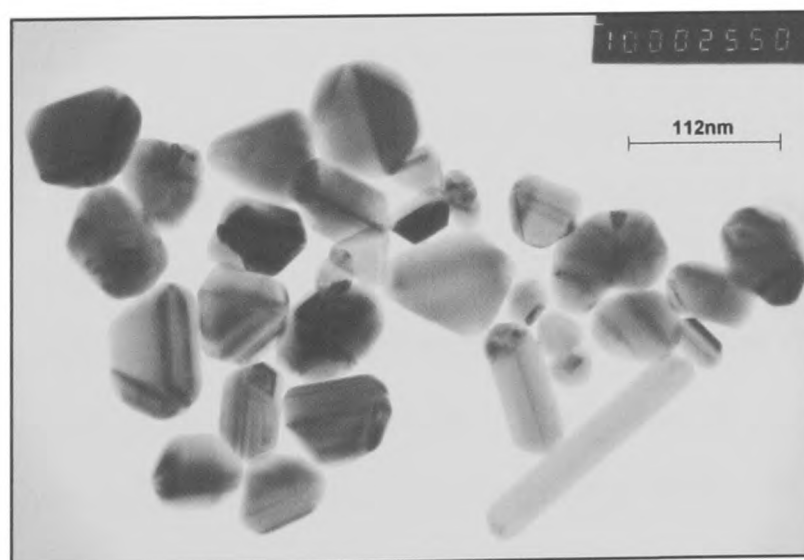


Figure 7.3. Transmission electron micrograph of citrate reduced colloidal silver particles at magnification of $\times 50,000$.

7.3.2. Size Measurements of Ag and Au Aggregates (Effect of Electrolyte Concentration)

In order to understand the effect of ionic concentrations on colloidal NPs aggregation, hydrodynamic diameter measurements have been carried out over a range of concentrations of KCl, Na₂SO₄, and Na₂S₂O₃, as illustrated in Fig.7.4. Generally, the rate of aggregation increases with electrolyte concentration until the so-called critical coagulation concentration (CCC) is reached. Above this concentration of added electrolyte, aggregation is controlled by the diffusion times of the aggregates only. All three electrolytes have significant effects on the average hydrodynamic diameter of Ag and Au aggregates at concentrations in the 7-35 mmol dm⁻³ range. However, at electrolyte concentrations in the range of 35-100 mmol dm⁻³ the hydrodynamic diameter remains fairly constant. For instance, at 53, 70, 84, and 100 mmol dm⁻³ concentrations of KCl, the Ag aggregates have hydrodynamic diameters of 618, 696, 678, and 671 nm, respectively. Almost the same trend is observed for Au NPs; however, the average hydrodynamic diameters of Au aggregates are larger than those of Ag aggregates at the same (53-100 mmol dm⁻³) KCl concentrations, as illustrated in Fig.7.4b.

Aggregates formed from colloidal particles will vary in shape according to the prevalent aggregation regime. Compact structures are formed when the aggregation is slow, whilst “loose” structures are formed when rapid (or diffusion limited) aggregation prevails. These structures can be fractal in nature, *i.e.*, there is a relationship between porosity and the number of primary particles making up the aggregate, and is described by the fractal dimension¹². Theoretical calculations carried out on the images of both the citrate-reduced Ag and Au systems by employing ImageJ software have revealed that in presence of 16 mmol dm⁻³ KCl the dispersions are mostly fractal-like (*i.e.*, fractal dimension closest to 1)¹³. This particular study showed that from 16-100 mmol dm⁻³ KCl, the fractal nature of both the Ag and Au systems appears to be more 2-dimensional (*i.e.*, fractal dimension closest to 2) in character. Based on the foregoing study, it can be tentatively concluded that aggregation of Ag or Au NPs induced by KCl follows the reaction limited aggregation (RLA) regime.

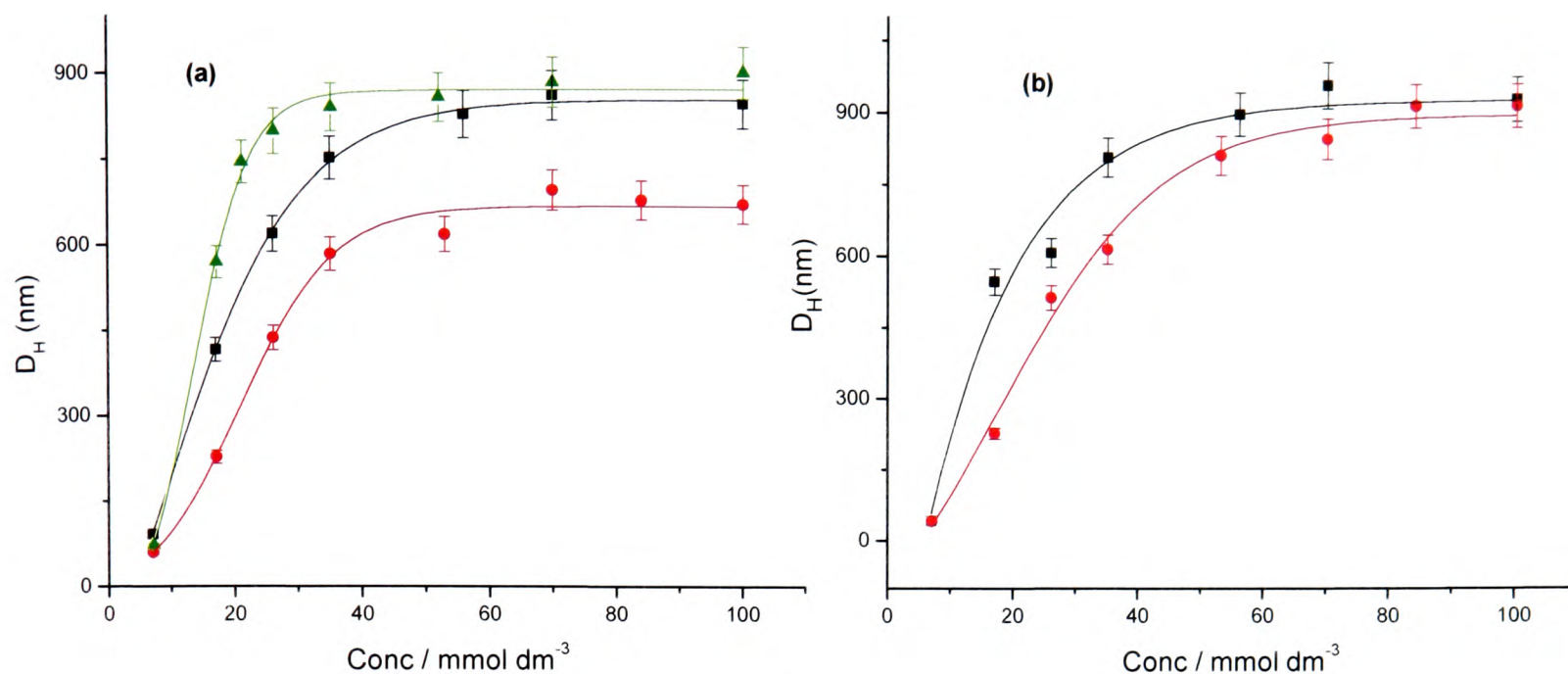


Figure 7.4. Hydrodynamic diameters (D_H) of: (a) Ag and (b) Au aggregates as a function of concentration of Na_2SO_4 (■), KCl (●), and $\text{Na}_2\text{S}_2\text{O}_3$ (▲).

The aggregation of colloidal NPs in the presence of aggregating agents leads to a multi-modal distribution of aggregate size. For example, the size distribution of Ag aggregates in the presence of 0.1 mol dm^{-3} KCl with time is shown in Fig.7.5. There are different size aggregates after 16.5 mins. Fig.7.6. displays the aggregation of Ag and Au NPs as a function of time over the concentration range of 7 to 100 mmol dm^{-3} KCl. The Ag and Au aggregates show a significant increase in hydrodynamic diameter between 0 and 4.5 mins (*i.e.*, from ~ 65 to ~ 300 and ~ 50 to ~ 350 nm for Ag and Au, respectively), then there is a gradual increase in hydrodynamic diameter with time by an increment of ~ 143 and 200 nm, every 3.5 mins, from 53 to 100 mmol dm^{-3} of KCl, respectively. At 17, 26, and 35 mmol dm^{-3} KCl, the hydrodynamic diameter of both Ag and Au aggregates increase with time by an increment of ~ 46 , 55, and 100 nm, respectively.

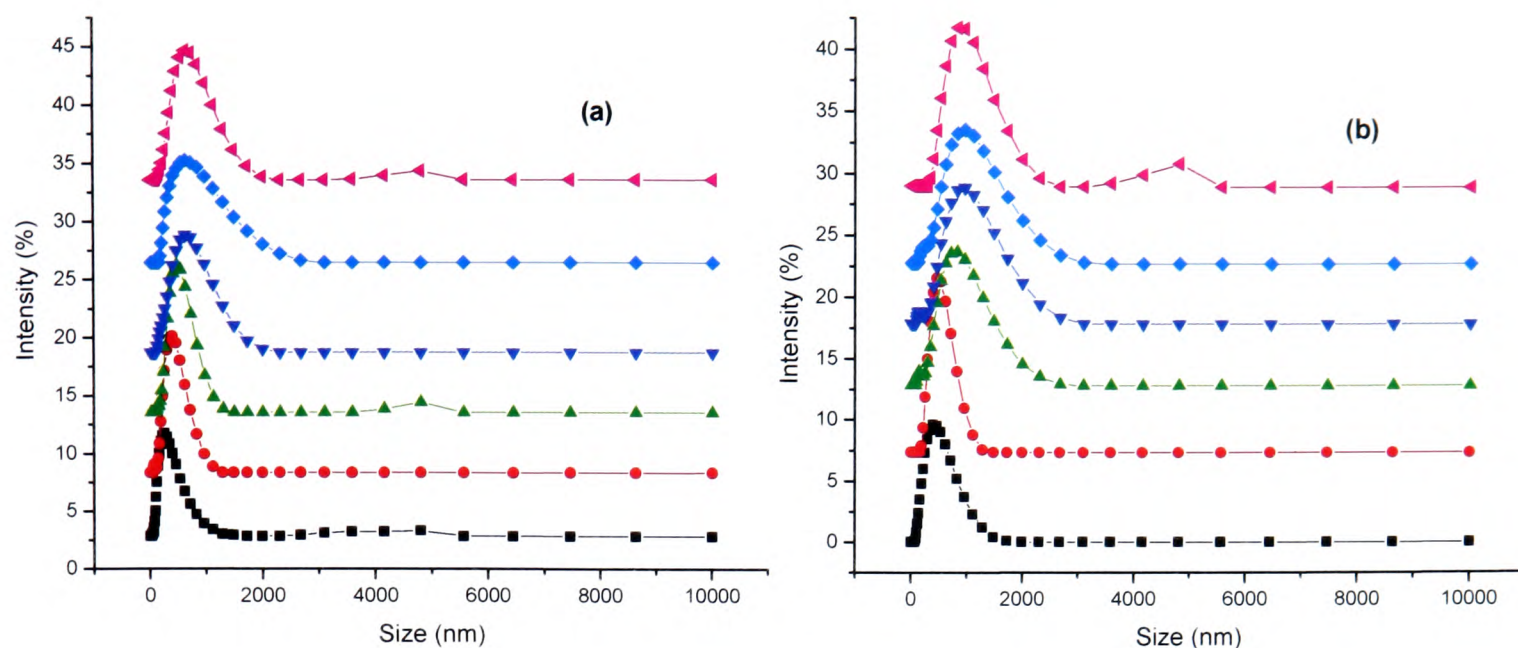


Figure 7.5. Size distribution analysis by intensity of Ag colloid in the presence of: (a) 100 mmol dm^{-3} KCl and (b) 100 mmol dm^{-3} Na_2SO_4 after 4.5 (■), 7.5 (●), 10.5 (▲), 13.5 (▼), 16.5 (◆), 19.5 (◄) mins.

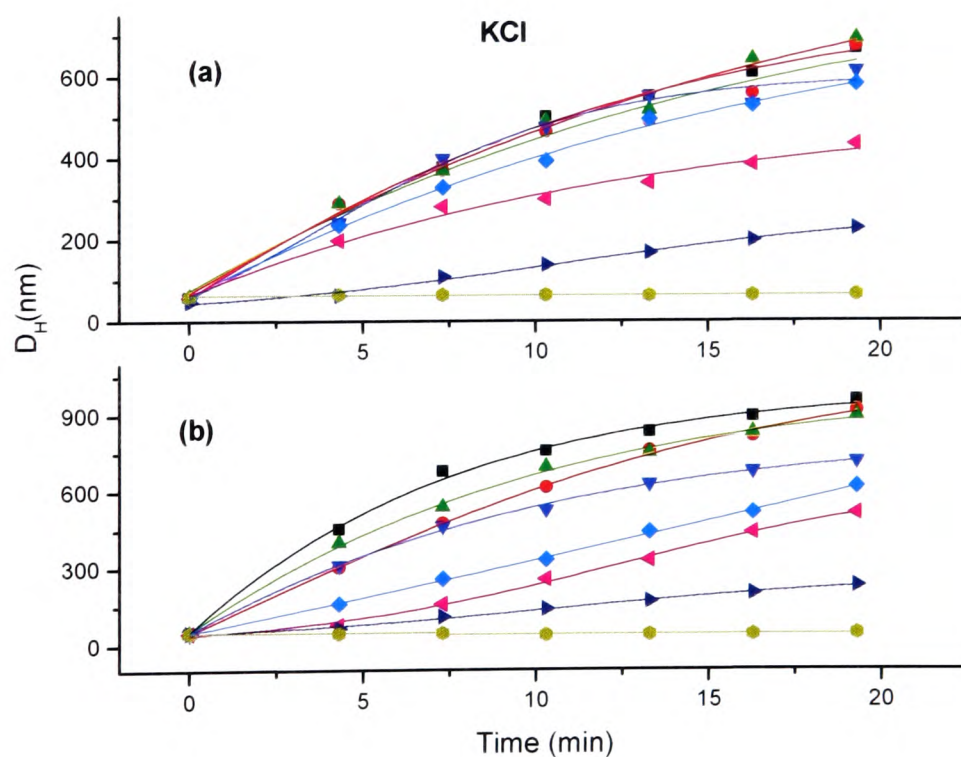


Figure 7.6. Hydrodynamic diameter (D_H) of: (a) Ag and (b) Au aggregates as a function of time at concentrations of KCl (mmol dm^{-3}) of 7 (●), 17 (►), 26 (◄), 35 (◆), 53 (▼), 70 (▲), 84 (●), and 100 (■).

Variation in the concentrations of added Na_2SO_4 has a more dramatic effect on the hydrodynamic diameters of Ag aggregates than KCl (Fig.7.4) as opposed to the Au aggregates where changes in concentration of both the aforementioned electrolytes have almost the same effect on Au NP aggregation. The aggregation of Ag and Au colloids gradually increases with increasing concentration of Na_2SO_4 . In the case of Ag NPs the difference observed in aggregation by varying the concentration of KCl and Na_2SO_4 could be attributed to the divalent anion (SO_4^{2-}) effect. The size distribution of Ag aggregates in the presence of $100 \text{ mmol dm}^{-3} \text{ Na}_2\text{SO}_4$, with time, is shown in Fig.7.5. The data from these graphs show that the distribution of aggregates is polydisperse.

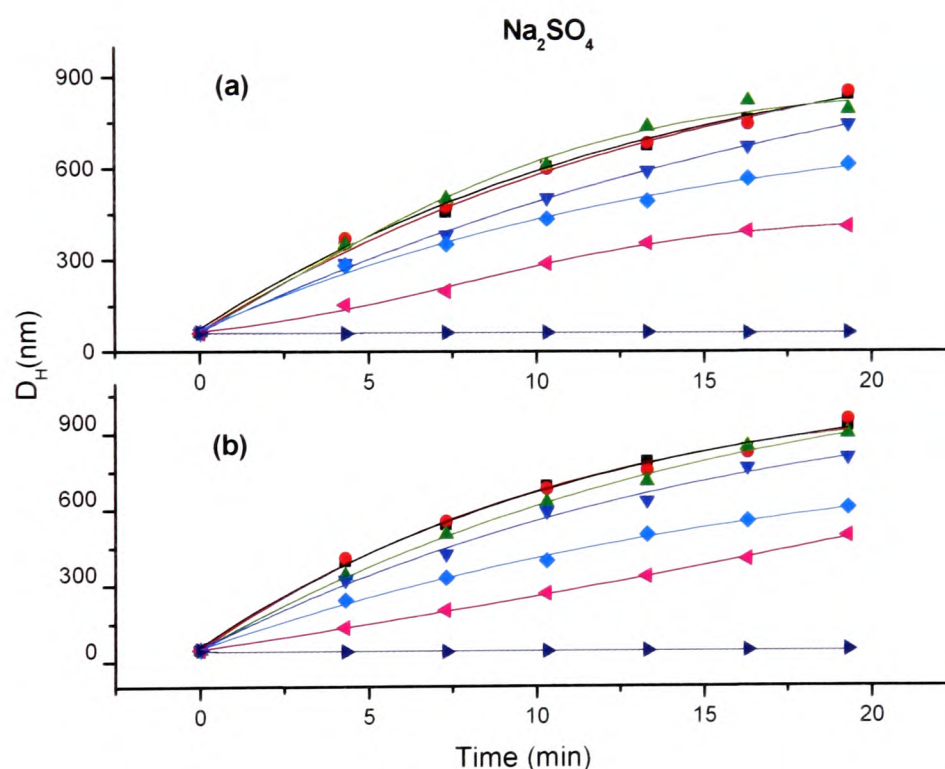


Figure 7.7. Hydrodynamic diameter (D_H) of: (a) Ag and (b) Au aggregates as a function of time at concentrations of Na_2SO_4 (mmol dm^{-3}) of: 7 (\blacktriangleright), 17 (\blacktriangleleft), 26 (\blacklozenge), 35 (\blacktriangledown), 53 (\blacktriangle), 70 (\bullet), and 100 (\blacksquare).

Fig.7.7. shows a comparison of the hydrodynamic diameter of Ag and Au aggregates as a function of time over the concentration range of 7 to 100 mmol dm^{-3} of Na_2SO_4 . The Ag and Au aggregates show a significant increase in hydrodynamic diameter between 0 and 4.5 mins (*i.e.*, ~ 300 and 350 nm for Ag and Au, respectively), then there is a gradual increase in hydrodynamic diameter with time by an increment of $\sim 200 \text{ nm}$ every 3.5 mins, between 53 and 100 mmol dm^{-3} of Na_2SO_4 , respectively. At

17, 26, and 35 mmol dm^{-3} Na_2SO_4 , the hydrodynamic diameter of both Ag and Au aggregates increases with time by an increment of ~ 100 , 150, and 200 nm, respectively.

Thiosulfate ions have been used to dissolve Ag^+ ions in a SERS study to quench the electronic interaction between Ag and rhodamine 6G molecules in the presence of Cl^- ions¹⁴. Therefore, it is intriguing to investigate the effect of thiosulfate ions on Ag NP aggregation. In the present study, concentrations of $\text{Na}_2\text{S}_2\text{O}_3$ from 7 to 100 mmol dm^{-3} induced the aggregation of Ag NPs in the same fashion as the other two electrolytes. There is an increase in hydrodynamic diameter of Ag aggregates over the concentration range of 7-56 mmol dm^{-3} and then the hydrodynamic diameter remains constant over the concentration range 56-100 mmol dm^{-3} of $\text{Na}_2\text{S}_2\text{O}_3$, as illustrated in Fig.7.4. A significant increase in hydrodynamic diameter of Ag aggregates between 0-4.5 mins (*i.e.*, ~ 350 nm) over the concentration range of 21-100 mmol dm^{-3} is observed, and then there is a gradual increase in hydrodynamic diameter with time; every 3.5 mins, by an increment of ~ 170 nm. At 17 mmol dm^{-3} , the hydrodynamic diameter of Ag aggregates increases with time every 3.5 mins, by an increment of ~ 94 nm (Fig.7.8).

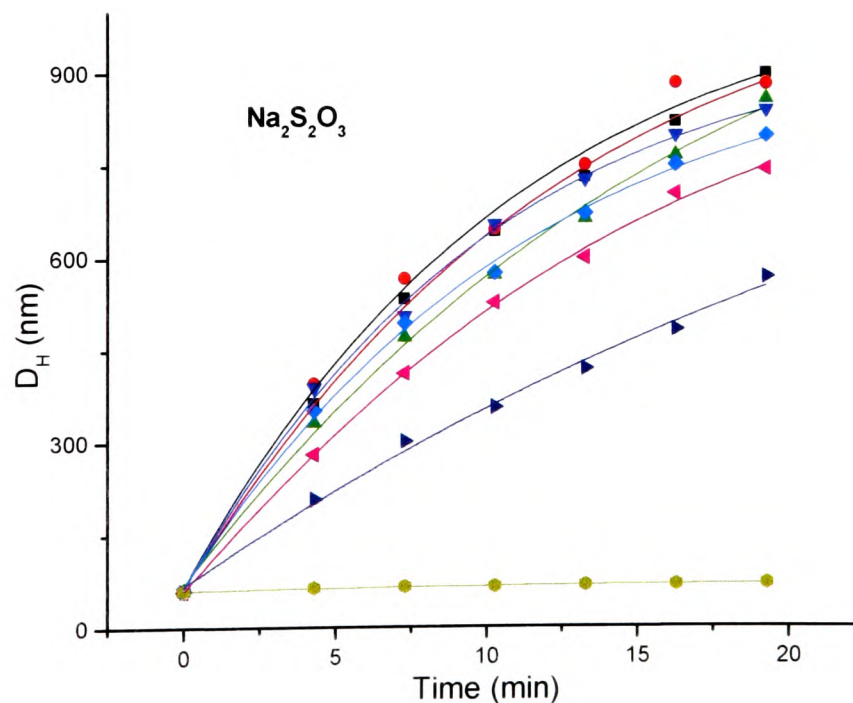


Figure 7.8. Hydrodynamic diameter (D_H) of Ag aggregates as a function of time in the presence of concentrations of $\text{Na}_2\text{S}_2\text{O}_3$ (mmol dm^{-3}) of 7 (\bullet), 17 (\blacktriangleright), 21 (\blacktriangleleft), 26 (\blacklozenge), 35 (\blacktriangledown), 56 (\blacktriangleup), 70 (\bullet), and 100 (\blacksquare).

7.3.3. Size Measurements of Ag and Au Aggregates (Effect of PLL Concentration)

The effect of PLL concentration on Ag and Au NPs are shown in Fig.7.9. The average hydrodynamic diameters of Ag and Au aggregates at 0.01% (w/v) PLL are 485 and 486 nm, respectively. In the case of PLL there is sharp increase in average hydrodynamic diameter with increase in concentration and the largest hydrodynamic diameters are observed for Ag (859 nm) and Au (786) NPs at a concentration of 1.2×10^{-3} w/v % followed by a gradual decrease in hydrodynamic diameter with increasing concentration of PLL. Fig.7.10. shows the hydrodynamic diameter of Ag and Au aggregates as a function of time over the concentration range of 1.2×10^{-4} to 0.01 w/v %. As for the three electrolytes, there is a significant increase in hydrodynamic diameter of Ag NPs between 0-4.5 mins (*i.e.*, ~300 nm) over the concentration range of PLL studied, and then a gradual decrease in hydrodynamic diameter with time is observed. Similarly, the hydrodynamic diameters of Au NPs also show a gradual increase with time over the concentration range of PLL studied. Time dependent size distributions of Ag aggregates in the presence of 1.2×10^{-3} and 0.01 w/v % PLL are shown in Fig.7.11. There are different size aggregates after 16.5 mins.

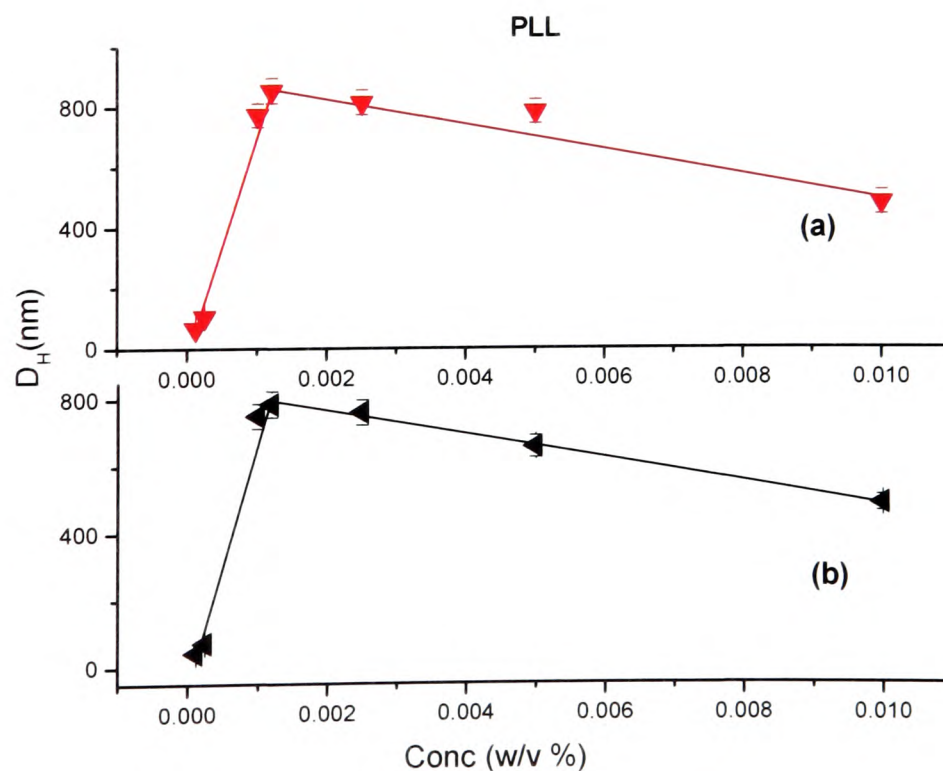


Figure 7.9. Hydrodynamic diameters (D_H) of: (a) Ag and (b) Au aggregates as a function of concentration of PLL.

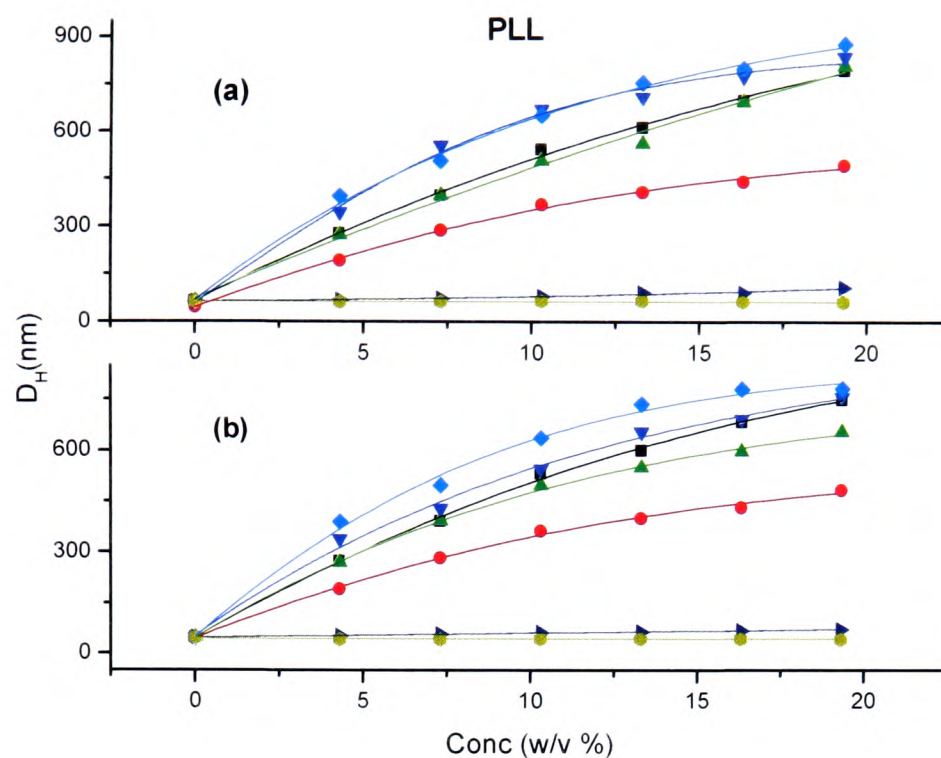


Figure 7.10. Hydrodynamic diameter (D_H) of: (a) Ag and (b) Au aggregates as a function of time in the presence of PLL at concentrations of 1×10^{-4} (■), 2.5×10^{-4} (▸), 5×10^{-4} (●), 1.2×10^{-3} (◆), 2.5×10^{-3} (▼), 5×10^{-3} (▲), and 0.01 (●) % (w/v).

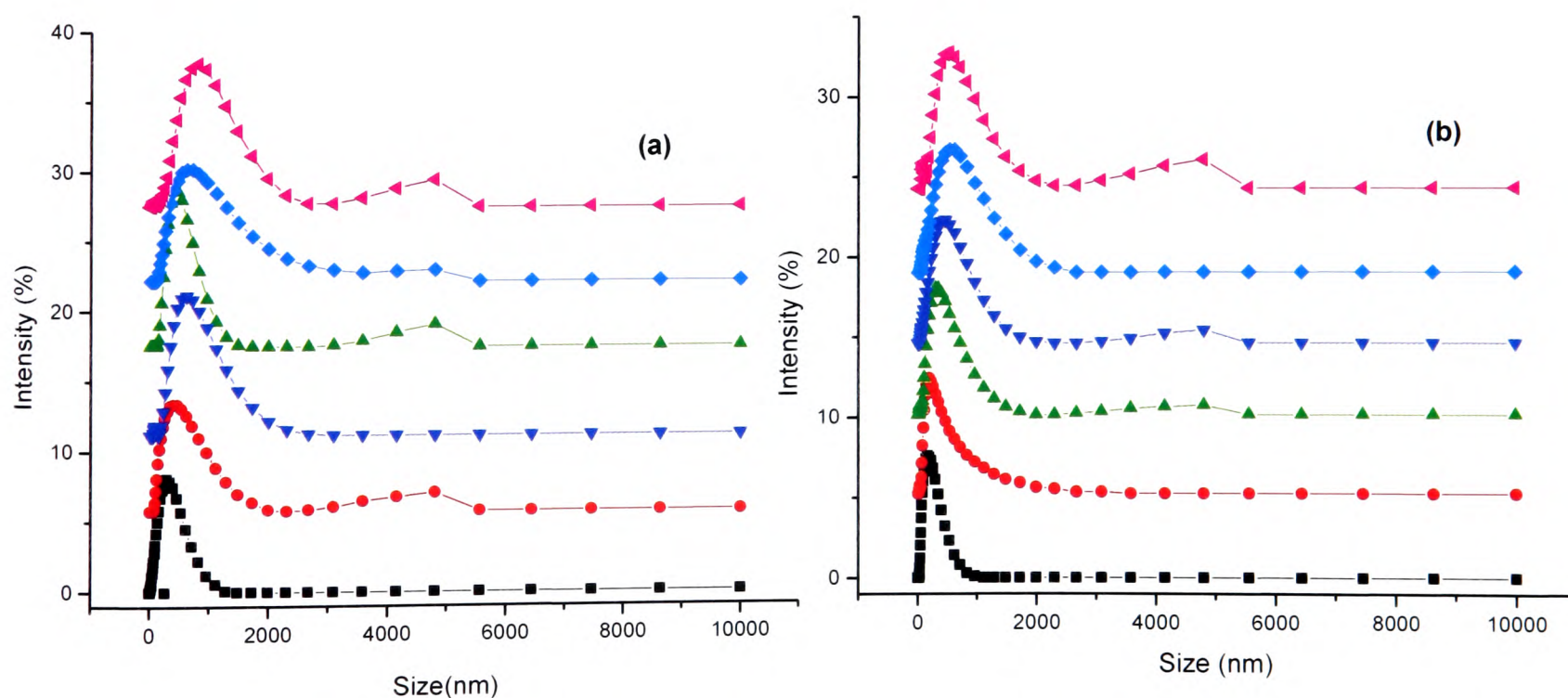


Figure 7.11. Size distribution analysis by intensity of Ag NPs in the presence of: (a) 1.2×10^{-3} and (b) 0.01% (w/v) after 4.5 (■), 7.5 (●), 10.5 (▼), 13.5 (▲), 16.5 (◆), 19.5 (◀) mins.

7.3.4. ζ -Potential of Ag and Au Aggregates (Effect of Electrolyte Concentration)

The ζ -potential values of Ag and Au NPs together with electrophoretic mobility values as a function of KCl concentration are illustrated in Fig.7.12. The effect of counter-ion concentration arises from at least two effects: (a) the counter-ion may be adsorbed to the surface, or incorporated into the Stern layer (and thereby change the net surface charge density that must be shielded by the diffuse region); (b) changing the thickness of the electrical double layer (EDL) changes the ζ -potential directly, even for a fixed surface charge density. Bell *et al.*¹⁵ have conducted displacement experiments monitored by SERS to elucidate the binding affinity of anions with citrated-reduced Ag colloid. Displacement experiments have revealed that Cl⁻ ions showed high affinity towards Ag by displacing the citrate layer. The residual citrate was observed when the colloids were aggregated with sulfate ions. Hence, the Cl⁻ ions in the EDL of Ag and Au NPs in the presence of KCl are accounted for by the negative ζ -potential values at the slipping plane. In the case of Ag NPs, there is a gradual decrease in the ζ -potential with increasing concentration of added KCl. Conversely, for Au NPs, the ζ -potential remains constant over the concentration range of 7-35 mmol dm⁻³, followed by a decrease in ζ -potential with increasing concentration of KCl. As a consequence, Ag and Au colloidal systems are more stable at lower concentration of KCl. The ζ -potential measurements did not show any time dependent changes using the above mentioned concentrations of KCl.

Fig.7.13 shows the ζ -potential and electrophoretic mobility of Ag and Au aggregates as a function of concentration of Na₂SO₄. The ζ -potential values of Ag aggregates at 56, 70 and 100 mmol dm⁻³ are -30, -29, and -27 mV, respectively. These values confirm that at higher concentrations of sulfate ions the Ag colloidal system is, arguably, marginally less stable. At lower concentration higher values of ζ -potential and electrophoretic mobility are observed and account for the more stable system. The same trend is observed in ζ -potential measurements of Au aggregates. At 56, 70, and 100 mmol dm⁻³ Na₂SO₄ the measured values of ζ -potential are -30, -26, and -26 mV, respectively. Conversely, at Na₂SO₄ concentrations of 7, 17, 26, and 35 mmol dm⁻³

the ζ -potential is -36, -35, -32, and -31 mV, respectively. It is obvious that the stability of the system decreases with higher concentrations of added electrolyte.

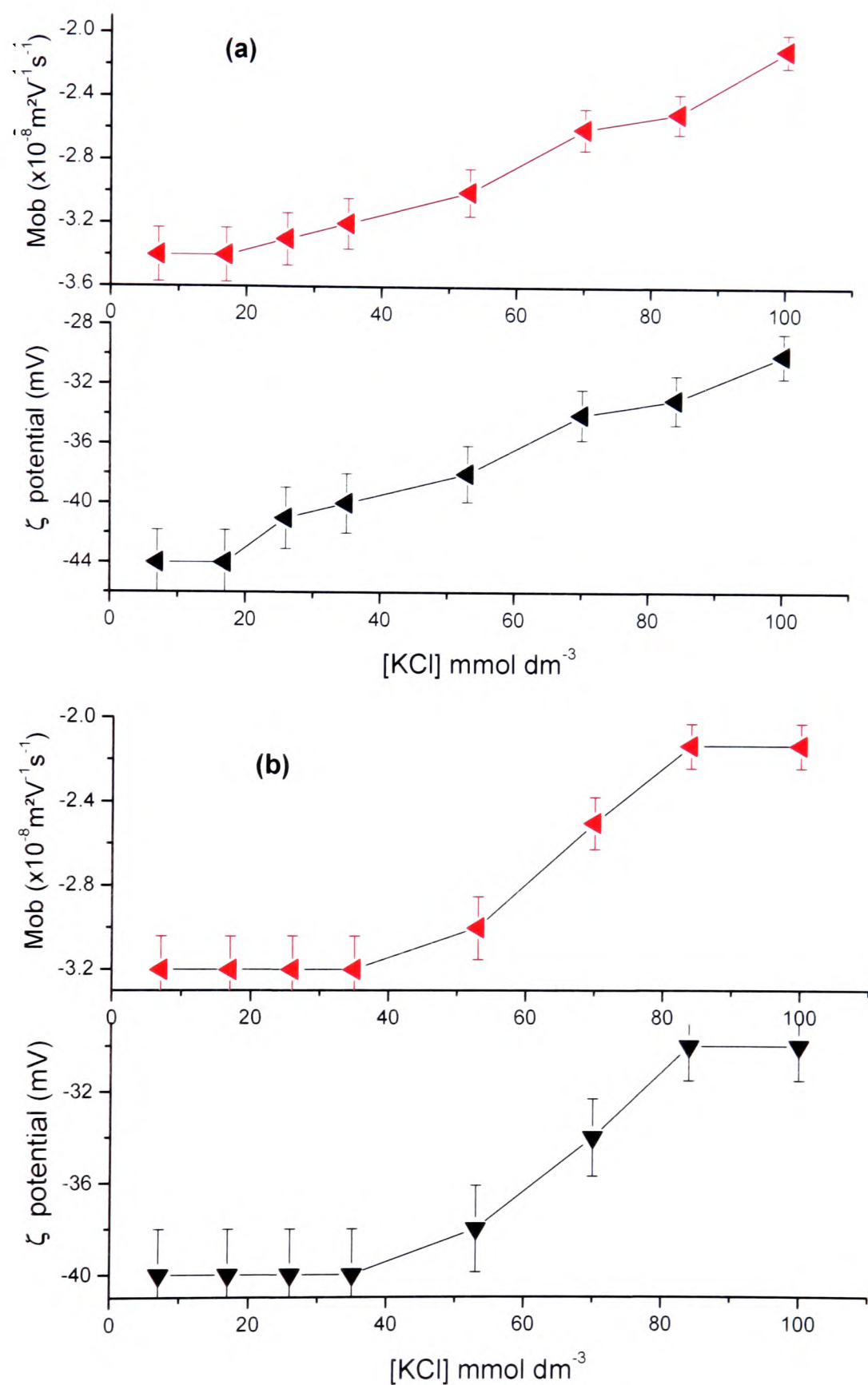


Figure 7.12. ζ -potential and electrophoretic mobility values of (a) Ag and (b) Au aggregates as a function of concentration of KCl.

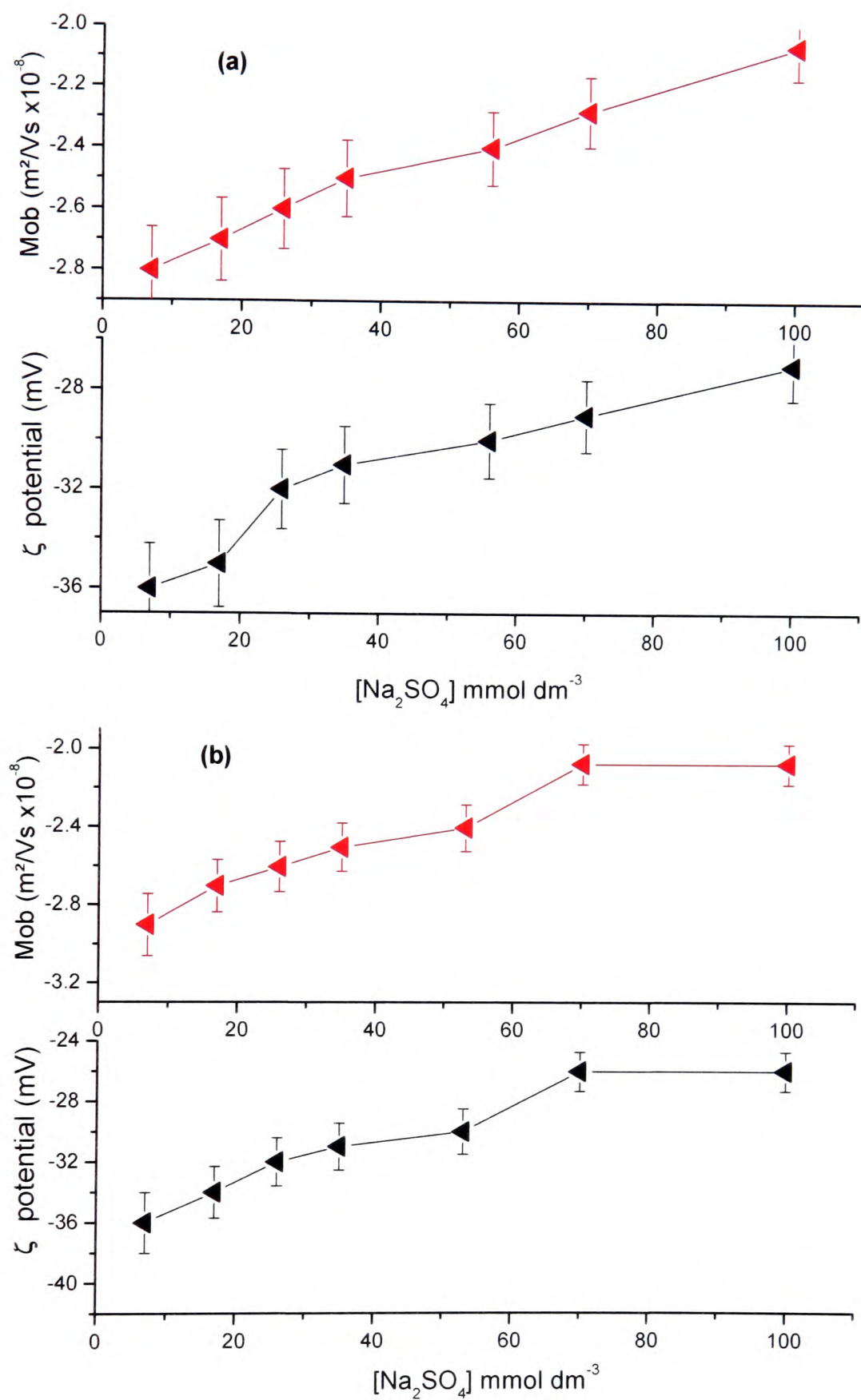


Figure 7.13. ζ -potential and electrophoretic mobility values of (a) Ag and (b) Au aggregates as a function of concentration of Na₂SO₄.

The sulfate ion does not replace the citrate layer¹⁵, therefore the negative ζ -potential at the slipping plane represents the presence of residual citrate ions in the electrical double layer in addition to sulfate ions. Counter-ion valency and size influence the ζ -potential by affecting surface adhesion equilibrium, changing the exact location of the outer Helmholtz plane (OHP) as well as the thickness of the diffuse double layer. The most easily modelled effect is the compression of the diffuse double-layer attendant with use of counter-ions of higher valency. Comparison of the ζ -potential of Ag and Au NPs suggest that there is a reduction in ζ -potential in the presence of SO_4^{2-} a divalent ion as compared to Cl^- a monovalent ion. Contrary to this, in the presence of $\text{Na}_2\text{S}_2\text{O}_3$ ($\text{S}_2\text{O}_3^{2-}$, divalent anion) higher values of ζ -potential are observed. Fig.7.14. shows the ζ -potential values of Ag aggregates as a function of concentration of $\text{Na}_2\text{S}_2\text{O}_3$. The ζ -potential remains constant over the concentration range of 7-35 mmol dm^{-3} , followed by a decrease in ζ -potential with increasing concentration of $\text{Na}_2\text{S}_2\text{O}_3$. An explanation for the higher ζ -potential values (when compared to KCl and Na_2SO_4) could be the higher affinity of thiosulfate anion towards the Ag^+ ; rather than physi-sorbing on the surface it may bind strongly to the Ag^+ .

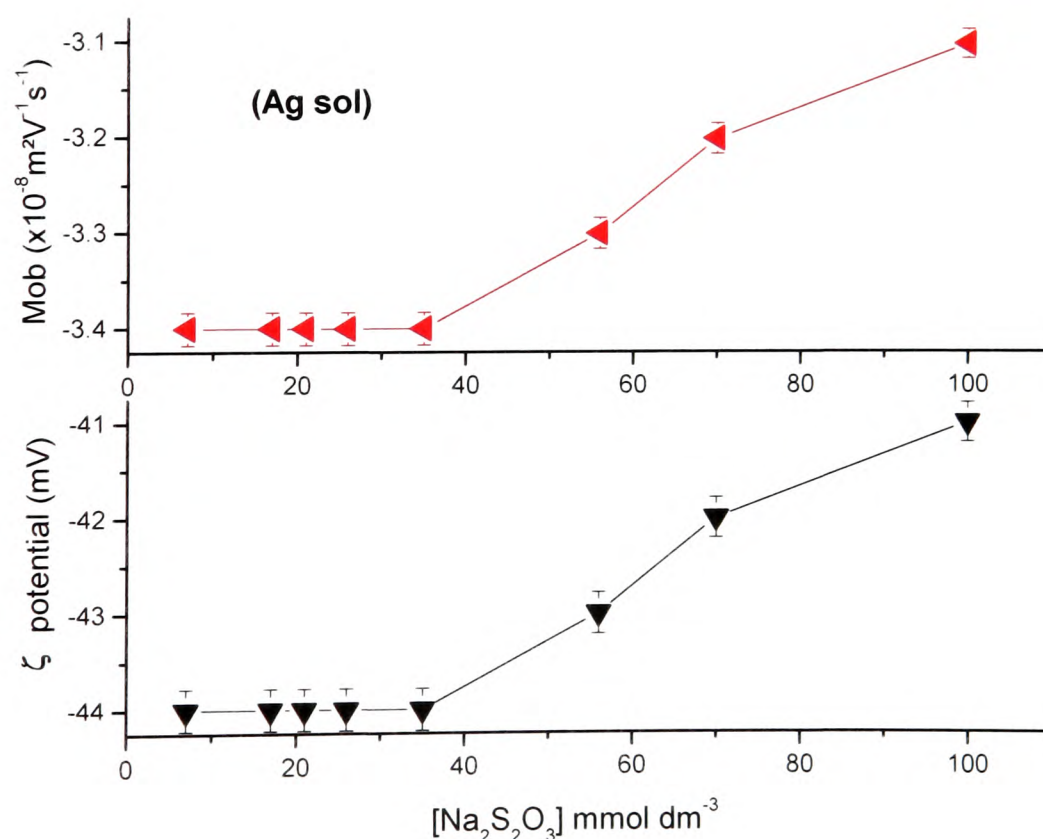


Figure 7.14. ζ -potential and electrophoretic mobility values of Ag aggregates as a function of concentration of $\text{Na}_2\text{S}_2\text{O}_3$.

7.3.5. ζ -Potential of Ag and Au Aggregates (Effect of PLL Concentration)

Fig.7.15 shows the ζ -potential and electrophoretic mobility values of Ag and Au aggregates as a function of concentration of PLL.

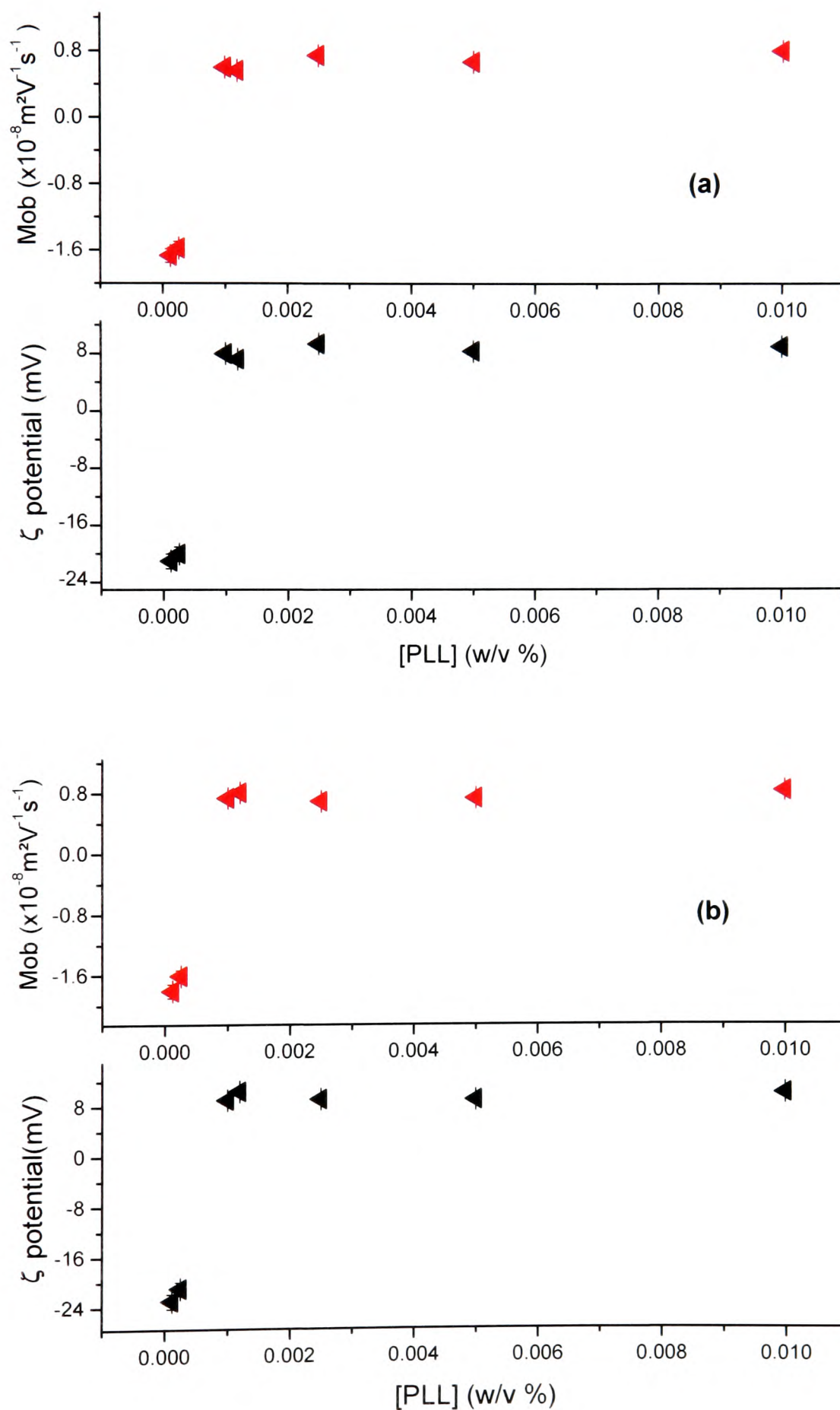


Figure 7.15. ζ -potential and electrophoretic mobility values of (a) Ag and (b) Au aggregates as a function of concentration of PLL.

The Ag aggregates exhibit ζ -potentials of 8 ± 1 mV in the presence of PLL at concentrations of 1.2×10^{-3} - 0.01 % (w/v). Similarly, the Au aggregates have measured ζ -potentials of 9 ± 1 mV at the same concentrations of PLL. The ζ -potential values clearly reflect the fact that aggregation induced by PLL makes the system very unstable. At lower concentrations of PLL, the measured ζ -potentials values of Ag and Au aggregates are $\sim -21 \pm 2$, representative of citrate ions in the EDL (Fig. 7.5). On the other hand at higher concentrations of PLL, measured values of ζ -potentials are positive indicative of adsorption of PLL via the amino group replacing the citrate layer of the Ag and Au NPs and/or coating of PLL with pendant positive charges.

7.3.6. Size and ζ -Potential Measurements under SERS Optimized Experimental Protocols

The work reported in this thesis is partly focused on the interaction of Rd, H₂NRd and MeRd with SERS substrates (*i.e.*, Ag and Au colloidal NPs). For this reason PCS measurements were carried out on Ag and Au colloids prepared under conditions that afforded optimized SERS enhancement, as described in Chapters 3 and 5, in order to gain insight into the SERS phenomenon. The results are tabulated in Table 7.1. The size and ζ -potential of Ag and Au NPs varies in the presence of different reagents due to aggregation and/or adsorption. When both PLL and HCl are added to the Ag and Au NPs the aggregation process is slow compared with when only one of these components is present. For example, average hydrodynamic diameters of Ag aggregates in the presence of 0.01 w/v % PLL and 1 mol dm^{-3} HCl are 801 and 786 nm, respectively, after 19.5 mins. The corresponding ζ -potential values are 7 and -30 mV, respectively. However, there is a reduction in average size when both are added together and the average size of Ag aggregates is 510 nm with a ζ -potential value of 33 mV. From a pragmatic standpoint, Table 7.1 shows that addition of HCl and PLL together has slowed down the process of aggregation, consequently increasing the stability of the colloidal system, as indicated by the measured ζ -potential. Au NPs exhibit similar behaviour. This could be attributed to either conformational changes in the PLL in the presence of HCl or the interaction of Cl⁻ ions with Ag or, importantly, a change in charge of the PLL, *i.e.*, going from the zwitterionic form to the acidic form. It is known that conformational changes of PLL

occur in solution. At neutral pH and room temperature PLL adopts a random-coil structure with some constraints due to the peptide bonds and repulsion between charges of the amine groups. It thus exhibits a very open random-coil structure. Increasing the solvent pH changes the charge on the amine groups inducing formation of an α -helix structure¹⁶⁻¹⁷. By increasing the temperature, hydrophobic interactions are increased and a β -sheet structure results¹⁸. The structure of PLL has been well characterized by vibrational spectroscopic techniques¹⁹⁻²². In the present study, it is very difficult to interrogate the structure of PLL adsorbed on the Ag or Au surface due to the very weak intensity or absence of vibrational bands in the SER spectra. The foregoing represents pivotal PLL characteristic (*i.e.*, weak interaction with Ag or Au surface) which is consistent with SERS studies carried out by Munro *et al.*,²³ where aggregation was induced by PLL and no SERS bands due to PLL were observed.

Rd adsorbed on Ag and Au surfaces gives SER spectra in the absence of any aggregating agent. However, its 3-methyl and 3-amino derivatives only give SER spectra in the presence of aggregating agents. The hydrodynamic diameter and ζ -potential measurements suggest that Rd itself causes the aggregation of Ag and Au NPs, to some extent, as shown in the Table 7.1. The addition of HCl to Rd/Ag colloid or Rd/Au colloid produced larger aggregates. Apparently, more extensive aggregation manifests itself by decreasing the stability of system in terms of low ζ -potential values. On the other hand, addition of both HCl and PLL result in smaller size aggregates and a more stable colloidal system. The same trend is also observed for H₂NRd and MeRd. For example, H₂NRd adsorbed on the Ag surface has an average hydrodynamic diameter and ζ -potential of 596 nm and 36 mV, respectively in the presence of both HCl and PLL. But, an average hydrodynamic diameter of 830 nm and ζ -potential of 14 mV is observed in the presence of HCl alone. Consequently, for MeRd the hydrodynamic diameter and ζ -potential in the presence of both HCl and PLL are 469 nm and 32 mV, respectively. But, the hydrodynamic diameter and ζ -potential in the presence of HCl only are 794 nm and 16 mV, respectively.

Table 7.1. Hydrodynamic diameter (D_H), ζ -potential, and electrophoretic mobility (Mob) values for Ag and Au NPs in the presence and absence of different experimental reagents.

Experimental Conditions	D_H (nm) (± 5)	ζ -potential (mV) (± 3)	Mob ($\times 10^{-8} \text{ m}^2 \text{ V}^{-1} \text{ s}^{-1}$)	pH
Ag NPs	65	-31	-2.45	8
Ag NPs/methanol	73	-19	-1.47	7.8
Ag NPs/PLL/HCl	510	33	2.60	2.3
Ag NPs/PLL/methanol	801	7	0.40	7
Ag NPs/HCl/methanol	786	-29	-2.36	2.3
Ag NPs/HCl + methanol/PLL	505	30	2.37	2.3
Ag NPs/Rd (methanol)	109	-23	-0.96	6.2
Ag NPs/H ₂ NRd (methanol)	72	-17	-1.34	7.6
Ag NPs/MeRd (methanol)	70	-29	-2.23	7.7
Ag NPs/Rd ^a	646	33	2.56	2.3
Ag NPs/H ₂ NRd ^a	596	36	2.78	-
Ag NPs/MeRd ^a	469	32	2.47	-
Ag NPs/Rd (methanol) + HCl	822	8	0.64	-
Ag NPs/H ₂ NRd (methanol) + HCl	830	14	1.06	-
Ag NPs/MeRd (methanol) + HCl	794	16	1.29	-
Au NPs	50	-30	-1.75	7
Au NPs/methanol	52	-23	-1.76	7
Au NPs/PLL/HCl	520	34	2.70	2.3
Au NPs/PLL/methanol	486	10	0.84	6.7
Au NPs/HCl/methanol	786	-29	-2.36	2.3
Au NPs/HCl + methanol/PLL	520	28	2.35	2.3
Au NPs/Rd (methanol)	110	-26	-2.04	5.0
Au NPs/H ₂ NRd (methanol)	49	-25	-2.00	6.6
Au NPs/MeRd (methanol)	45	-20	-1.48	6.4
Au NPs/Rd ^a	640	30	2.37	2.3
Au NPs/H ₂ NRd ^a	590	29	2.36	-
Au NPs/MeRd ^a	460	28	2.35	-
Au NPs/Rd (methanol) + HCl	820	7	0.40	-
Au NPs/H ₂ NRd (methanol) + HCl	810	13	1.04	-
Au NPs/MeRd (methanol) + HCl	790	12	1.03	-

^a In the presence of HCl/PLL. Solutions of Rd and its derivatives were made up in methanol.

7.4. Summary and conclusions

PCS measurements have been performed on citrate-reduced Ag and Au colloids in the presence of aggregating agents as a function of concentration of aggregating agents and time. The current study shows that hydrodynamic diameters of Ag and Au NPs at higher concentration of aggregating agent remain constant and then abruptly decrease with lower concentrations. This further implies that aggregation is a dynamic process due to increase in size with time and concentration of aggregating agent (such as in the case of PLL). Nevertheless, at higher concentration aggregation is fast and larger aggregates are produced, but ζ -potential measurements confirm that the colloidal system is less stable under such conditions. From a practical point of view, the optimum concentrations of aggregating agents for SERS experiment could be 17-26 mmol dm⁻³ for the three electrolytes investigated in the present study. In the case of PLL the particle size increases with time and concentration of PLL. The surface charge is positive and low values of ζ -potential are observed. Notably, the presence of both PLL and HCl in the colloidal system increases the stability and slows down the aggregation process.

Finally, the work described in this chapter highlights some key developments in understanding the effects of aggregating agents on the aggregation processes of Ag and Au colloids and chemical influence of the ionic environment that surround the resultant aggregates. This valuable information could be utilized to further optimize protocols used for SERS experiments.

7.5. References

- [1] H. X. Xu, E. J. Bjerneld, M. Käll and L. Borjesson, *Phys. Rev. Lett.*, **83**, (1999), 4357.
- [2] K. Kneipp and H. Kneipp, *Isr. J. Chem.*, **3**, (2006), 299.
- [3] K. Kneipp, Y. Wang, H. Kneip, L. T. Perelman, I. Itzkan and R. R. Dasari, *Phys. Rev. Lett.*, **78**, (1997), 1667.
- [4] C. Rodger, W.E. Smith, G. Dent and M. Edmondson, *J. Chem. Soc. Dalton Trans.*, **5**, (1996), 791.
- [5] P. C. Lee and D. Meisel, *J. Phys. Chem.*, **86**, (1982), 3391.
- [6] P. Matejka, S. Lecomte and M. H. Baron, *J. Mol. Struct.*, **410-411**, (1997), 197.
- [7] S. Lecomte, P. Matejka and M. H. Baron, *Langmuir*, **14**, (1998), 4373.
- [8] R. A. Alvarez-Puebla, E. Arceo, P. J. G. Goulet, J. J. Garrido and R. F. Aroca, *J. Phys. Chem. B* **109**, (2005), 3787.
- [9] J. A. Creighton, C. G. Blatchford and M. G. Albrecht, *J. Chem. Soc. Faraday Trans.*, **75**, (1978), 790.
- [10] L. E. Camefeita, S. Sanchez-Cortez and J. V. Garcia-Ramos, *J. Raman Spectrosc.*, **24**, (1993), 745.
- [11] K. Faulds, R. E. Littleford, D. Graham, G. Dent, and W. E. Smith, *Anal. Chem.*, **76**, (2004), 592.
- [12] A. J. Raper and R. Amal, *Particle and Particle Systems Characterization*, **5**, (1993), 239.
- [13]. Visit URL: www.npl.co.uk. *Chemical Optimisation Methodologies for SERS*.
- [14] M. Futamata and Y. Maruyama, *Analyt. Bioanalyt. Chem.*, **1**, (2007), 89.
- [15] S. E. J. Bell and N. M. S. Sirimuthu, *J. Phys. Chem. A* **109** (33), (2005), 7405.
- [16] M. Chittchang, N. Salamat-Miller, H. H. Alur, D. G. V. Velde, A. K. Mitra and T. P. Johnston, *J. Pharm. Pharmacol.*, **54**, (2002), 1497.
- [17] M. Muller, R. Buchet and U. P. Fringeli, *J. Phys. Chem.*, **100**, (1996), 10810.
- [18] S. D. Swanson and R. G. Bryant, *Biopolymers*, **31**, (1991), 967.
- [19] M. C. Chen and R. C. Lord, *J. Am. Chem. Soc.*, **96**, (1974), 4750.
- [20] L. J. Lippert, D. Tyminski and J. P. Desmeules, *J. Am. Chem. Soc.*, **98**, (1976), 707.
- [21] T. J. Yu, J. L. Lippert and W. L. Peticolis, *Biopolymers*, **12**, (1973), 2161.
- [22] M. Rozenberg and G. Shoham, *Biophys. Chem.*, **125**, (2007), 166.
- [23] C. H. Munro, W. E. Smith and P. C. White, *Analyst*, **120**, (1995), 993.
-

Chapter Eight

Summary and Future Research

8.1. Summary

The calculated molecular geometry (B3-LYP/cc-pVTZ) of Rd in the gas phase is planar, which is comparable with the X-ray crystallographic structure¹ in the solid state. Since the theoretical calculations (*i.e.*, DFT) have been carried out by modelling a single isolated molecule in the gaseous state, they do not account for crystal packing forces and hydrogen bonding between the molecules present in a unit cell. The significant differences observed in the bond lengths and bond angles of C-N, C-S, and C-O groups could be due to the delocalization of π -electron density from the thiocarbonyl (C=S) to the carbonyl group (C=O) via the ring nitrogen, in the solid state. No X-ray crystallographic structures exist in the literature for Rd derivatives; therefore their geometries are compared and contrasted with Rd.

Vibrational spectroscopic [IR and Raman ($\lambda_0 = 632.8\text{nm}$)] studies of Rd, H₂NRd and MeRd have been investigated for both the protonated and deuteriated forms of the molecules in the solid state. *Ab initio* calculations have been carried out on the aforementioned molecules. Normal coordinate analysis has also been conducted in order to predict the contribution of different vibrational modes for the assignment of bands. In nitrogen containing thiocarbonyl groups (N-C=S), the assignment of the C=S stretching mode is controversial²⁻³. However, the calculated PEDs suggest that the bands at 1176, and 1078/1066 cm⁻¹ in the Raman spectrum of Rd are attributed to thioamide II and III vibrations, respectively. Their counterparts in the IR spectrum are represented by the bands at 1187 and 1083 cm⁻¹, respectively. For H₂NRd, the corresponding modes are observed at 1126 and 1044 cm⁻¹ in Raman and 1230 and 1074 cm⁻¹ in IR spectra, respectively. For MeRd the assignment of the C=S group is difficult due to strong coupling with CH₃ ip and op deformation motion. Nevertheless, the bands at 1107 and 984 cm⁻¹ in the Raman and 1116 and 983 cm⁻¹ in IR spectra are tentatively assigned as thioamide II and III modes, respectively. These assignments are further confirmed by detailed studies of deuteriated spectra, where vibrations associated with the foregoing

have shown no (or subtle) frequency shifts. Theoretical assignments of the N-C=S moiety, achieved in this study, can be used as a guide to characterize molecules belonging to the thioamide family.

Examination of the vibrational spectra of Rd and its derivatives in the solid state has enabled the band at $\sim 1457\text{ cm}^{-1}$ to be re-assigned. Previously, this band has been assigned to the CH₂ deformation mode⁴. Herein, the foregoing band has been assigned to the C-N stretching and ip N-H deformation modes (amide mode II). The corresponding band is lacking in the vibrational spectra of H₂NRd and MeRd. One interesting observation is the hydrogen-deuterium exchange in the spectra of the deuteriated molecules, where the protons of the CH₂ moiety are exchanged with deuterium. This observation has obvious implications for the application of deuteriation to discriminate the bands associated with the N-H, NH₂, and CH₂ vibrations. In MeRd, particularly, this strategy allows explicit differentiation between the bands attributed to the CH₂/CH₃ stretching and deformation modes.

Thiazolidine ring vibrations give rise to characteristic bands in both Raman and IR spectra of Rd and its derivatives. The band at $\sim 545\text{ cm}^{-1}$ in the Raman spectra of all three molecules, associated with ip ring deformation, is of high intensity. Its counterpart in IR spectra is observed at $\sim 540\text{ cm}^{-1}$. For Rd a band at $\sim 489\text{ cm}^{-1}$ is found in both Raman and IR spectra, which is not present in the vibrational spectra of the Rd derivatives. However, after deuteriation the band at $\sim 489\text{ cm}^{-1}$ is not present, and the band at 545 cm^{-1} is red shifted by $\sim 5\text{ cm}^{-1}$; this could be attributed to factor group splitting or crystal lattice effects. The strong bands at 473, 485, and 490 cm^{-1} represent op ring deformation modes in both Raman and IR spectra for MeRd, Rd, and H₂NRd, respectively. Another strong band at $\sim 427\text{ cm}^{-1}$ also represents the op ring deformation mode in vibrational spectra of all three molecules. According to the DFT calculations the thiazolidine ring vibrations show a degree of contribution from other types of motion but the predominant contribution is from ring deformation. For example, the band at $\sim 545\text{ cm}^{-1}$ is attributed to vibrations with C-N, C=S, and C-S stretching contributions in addition to ip ring deformation.

Rd and its derivatives have been adsorbed on Ag and Au NPs to obtain SER spectra. SERS pH dependent studies suggest that the optimum condition to carry out SERS experiments is in the presence of PLL and HCl, at pH 2.3. This particular study highlights the seminal characteristic of these molecules on Ag and Au surfaces. From a pragmatic standpoint, the appearance of bands in SER spectra of Rd, H₂NRd and MeRd at ≈ 1566 , 1575 and 1572 cm⁻¹, respectively represent a chemical reaction on the Ag/Au surface. It has been tentatively concluded that these molecules undergo a photo-catalyzed Knoevenagel condensation reaction, where the nucleophilic CH₂ group (*i.e.*, active methylene) at position 5 of one monomer reacts with the C=O group at position 2 of another monomer followed by dehydration to form a dimer⁵⁻⁶. In order to assign the SER spectra, structures of the dimers of the above mentioned molecules have been computed at B3-LYP/cc-pVTZ (Rd) and B3-LYP/D95 (H₂NRd and MeRd) level of DFT. The calculated PEDs predict that the band at $\approx 1566/1575/1572$ cm⁻¹ may be attributed to the C=C stretching mode of the dimer.

Concentration-dependent SERS studies using Ag colloidal NPs have demonstrated that for Rd and H₂NRd changes in the SER spectral features are related to the concentration of adsorbate on the surface (*i.e.*, surface coverage effect), which could cause changes in the orientation or coordination site on the SERS substrate surface. Enhanced SERS signals are achieved at monolayer surface coverage. For example, in the case of H₂NRd monolayer coverage is attained at a concentration of 8.6×10^{-6} mol dm⁻³. It is also assumed that these molecules coordinate with the Ag surface through the exo-sulfur atom. The current work illustrates the potential of SERS as a technique for identifying reactions on SERS substrates, predicting the orientation of adsorbates as well as surface adsorption sites, and surface coverage. For semi-quantitative analysis good fits to correlation coefficients and sigmoidal fits are observed for Rd and its derivatives. In the case of Rd, two excitation wavelengths (514.5 and 632.8 nm) have been used to obtain SER spectra. However, 632.8 nm excited SER spectra give a relatively lower LOD in contrast to 514.5 nm excited spectra. The LOD's for Rd, H₂NRd, and MeRd ($\lambda_0 = 632.8$ nm) are 10^{-14} , 10^{-12} , and 10^{-13} mol dm⁻³, respectively. The acquired SERS data represents the sensitivity of this technique for semi-quantitative trace analysis.

PCS measurements reveal that aggregation of colloidal NPs is a dynamic process, which is dependent on the concentration of added aggregating agent as well as time. According to this study, the optimum concentration of the three electrolytes (KCl, Na₂SO₄, and Na₂S₂O₃) to achieve optimum SERS signals ranges from 17-26 mM. It is worth mentioning that the presence of both PLL and HCl in the colloidal system (in the absence of analyte molecules) increases the stability and slows down the aggregation process. This feature is also prevalent in the PCS measurements conducted for the three molecules adsorbed on Ag and Au colloids. The size and ζ -potential measurements suggest that Rd itself causes the aggregation of Ag and Au NPs, to some extent, which mirrors the observation of SER spectra for the Rd adsorbed on the Ag and Au surfaces without any aggregating agent.

8. 2. Future Research

A number of novel research projects can be proposed to enhance/shed further light on the studies reported in this thesis.

- As discussed in Chapter Six, re: the origin of the intense band at $\approx 1566/1575/1572\text{ cm}^{-1}$, Rd and its derivatives could partake in an addition reaction on the Ag and Au surface when irradiated with laser light. The main impetus behind this reaction is the presence of the active methylene moiety at position 5. It would be fruitful to conduct SERS studies using Rd derivatives which lack the active methylene group. Examples of the foregoing include 5-(*p*-dimethylaminobenzylidene) Rd (PDR) and 5-(4-pyridylmethylene) Rd. These are ylidene derivatives of Rd which contain C=C group at position 5. This would be especially significant from the viewpoint that dimer formation could not occur for these species. In addition, SERS studies of ylidene derivative could shed some light into the adsorption behavior on Ag surfaces. It would also be interesting to perform SERS concentration-dependent studies of the above mentioned two Rd derivatives, particularly PDR, in order to investigate the effect of adsorbate concentration on SERS spectral profile and intensity.

- Unfortunately, it was not possible to carry out mass and NMR spectroscopic studies of Rd and its derivatives adsorbed on the Ag and Au NPs. It would be useful to carry out the aforementioned studies to establish the exact origin and nature of the Rd species formed. It should be emphasized that such studies would need to be conducted in the presence and absence of laser irradiation. The reason for this is that dimer formation (or in fact the formation of some other molecular species which would account for the bands at $\approx 1566/1575/1572 \text{ cm}^{-1}$ in SER spectra) could be dependent upon the interaction and/or catalysis due to the presence of Ag ions and /or laser radiation.
- It would be interesting to synthesize the dimers of Rd derivatives (as reported in the literature⁷⁻⁸) and compare them with the hypothetical dimers (as proposed in this thesis) by employing Raman technique to find out the origin of bands at $1575/1572 \text{ cm}^{-1}$ in SER spectra.
- Further *ab initio* calculations could be performed in order to gain better insight into the orientation (*i.e.*, perpendicular or parallel or head on) and adsorption sites (either through sulfur, nitrogen, or oxygen atoms) of the dimers, of the three molecules, adsorbed on the Ag surface.
- Kinetics studies of the self-condensation reaction of Rd, H₂NRd, and MeRd could be further extended as a function of concentration and temperature.
- High resolution X-ray crystallographic studies of 3-amino and 3-methyl derivative could be performed in order to obtain information regarding the structure of these molecules, which could then be compared and contrasted with the calculated geometries.
- Unfortunately, it was not possible to conduct the SERS experiment under the optimized conditions achieved during the PCS studies. It would be interesting to carry out SERS studies under those optimized conditions. Furthermore, PCS studies have been performed with monovalent cations and monovalent/ divalent anions; investigations could be further extended by using divalent and trivalent cations. Static light scattering techniques could also be employed to understand the kinetics of aggregation as well as composition of the aggregates.

- It would be intriguing to conduct isothermal calorimetry (ITC) experiments, to examine the thermodynamics of the interaction of SERS substrates (*e.g.* Ag and Au colloids) with different analytes including Rd and its derivatives. A large number of techniques have been exploited to investigate and characterize SERS phenomenon. To date ITC has not, however, been used to reveal the thermodynamic parameters associated with the interaction of specific analytes with SERS substrates. In particular, the enthalpies of interaction of analytes with different substrates have not been examined as a function of analyte concentration and temperature.

8. 3. References

- [1] D. van der Helm, A. E. Lessor and L. L. Merritt, *Acta. Cryst.*, **15**, (1962), 1227.
- [2] L. J. Bellamy, *The Infrared Spectra of Complex Molecules*, Chapman & Hall, London, (1975).
- [3] C. N. R. Rao, *Chemical Applications of Infrared Spectroscopy*, Academic Press, New York, (1963), 249.
- [4] V. Enchev, S. Chorbadjiev and B. Jordanov, *Chem. Heterocycl. Compd.*, **38**, (2002), 1110.
- [5] C. L. Lee and M. M. Sim, *Tetrahedron Lett.*, **41**, (2000), 5729.
- [6] G. Ravindran, S. Muthusubramanian, S. Selvaraj and S. Perumal, *Phosphorous, Sulfur Silicon Relat. Elem.*, **182**, (2007), 321.
- [7] A. E. Mourad, A. A. Hassan, A. A. Ashraf, N. K. Mohamed and B. A. Ali, *Phosphorous, Sulfur Silicon Relat. Elem.*, **182**, (2007), 321.
- [8] H. Nagase, *Chem. Pharm. Bull.*, **22**, (1974), 505.

Appendix

1.1. Physico-chemical Properties of Rd and its Derivatives

	Rd	H ₂ NRd	MeRd
mp (°C)	165-169	100-103	69-71
Solubility (mol dm ⁻³)			
H ₂ O	7.5 x 10 ⁻³	6.7 x 10 ⁻³	6.7 x 10 ⁻³
Methanol	0.15	0.136	0.101
pK _a	5.18 ¹	-	9.32 ²

1.2. NMR Spectra of Rd and its Derivatives

1.2.1 Solid State Spectra

Solid state sample spectra were obtained using a Jeol Eclipse, 300 MHz FT-NMR, spectrometer incorporating a SH30T6/HS solid state probe. Samples were packed into a 6 mm o.d. zirconium oxide rotor and spun at the magic angle. The typical spinning speed used was ~6 KHz. ¹³C spectra were acquired using the cross-polarisation magic angle (CPMAS) pulse sequence. The relaxation delay was set to 10 secs, the number of spectral accumulations was 8192 (in order to obtain a suitable signal/noise ratio) and the 90° pulse width was 4 μs. Samples were referenced with respect to a separate solid state spectrum of DSS.

Fig.1.1 shows the ¹³C-NMR spectra of the three molecules in the solid state. The broad signals in the NMR spectra are background signals from the NMR probe. The NMR signals for Rd are very weak; the small peak at ~30 ppm is due to CH₂. The split signal at ~170 ppm is due to C=S. Unfortunately, it was not possible to detect the C=O signals. They are probably very weak and sit under the broad background signal at ~210 ppm. For Rd the split chemical shifts at 170 ppm are attributed to the fact that there is more than one inequivalent molecule per unit cell. This information is useful because it supports the experimental X-ray crystallographic structure findings for Rd (Appendix, section 1.5).

In the case of H₂NRd, the split peak at ~ 200 ppm is due to C=O. The split peak at ~175 ppm is due to the C=S moiety and the CH₂ is observed at ~ 40 ppm. The rest of the signals are either background or spinning side-bands. The NMR data indicates that there is more than one in-equivalent molecule per unit cell (*cf* Rd). This information is useful because there is no experimental X-ray crystallographic structure for H₂NRd.

For MeRd, single peaks at 175 and ~210 ppm are accounted for by C=S and C=O groups, respectively. Two peaks at ~40 ppm are assigned to CH₃ and CH₂ groups. It is worth nothing that no split peaks are observed in the NMR spectra of MeRd. This finding *suggests* that, in contrast to RD and H₂NRd, all the molecules in the unit cell are likely to be equivalent.

The NMR spectra also show that the most stable form of all three molecules, in the solid state, is tautomer **a** (*i.e.*, thioketone/ketone).

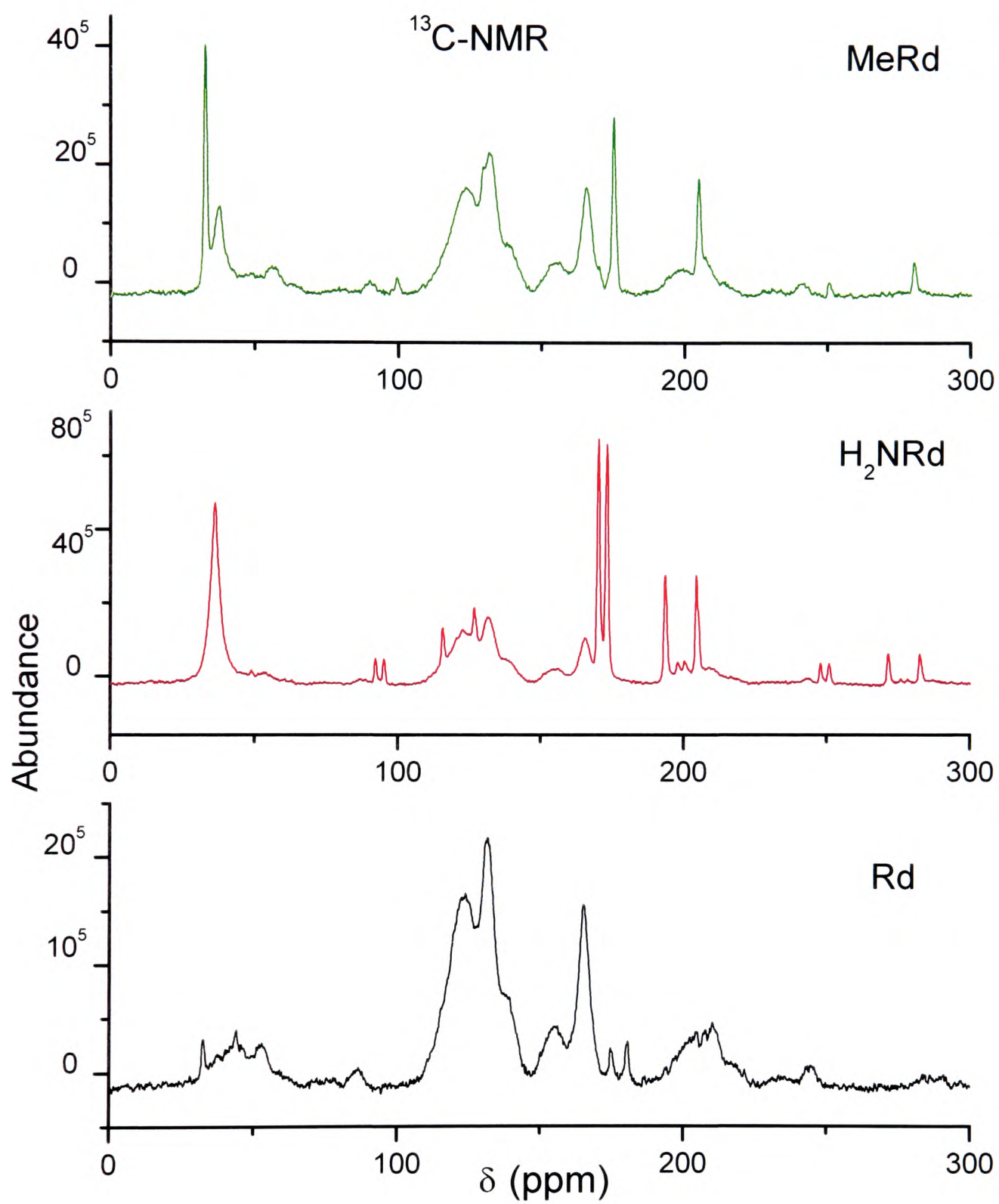


Figure 1.1. $^{13}\text{C-NMR}$ spectra of MeRd, H₂NRd, and Rd in the solid state.

1.2.2. Solution (Methanol Spectra)

The ^1H and ^{13}C -NMR solution state spectra of Rd and its derivatives were obtained in order to check the purity of the samples, and in order to gain insight into hydrogen-deuterium exchange of the methylene and amino moieties.

Solution state sample spectra were obtained using a Jeol ECA, 500 MHz FT-NMR spectrometer, incorporating a NM-50TH 5AT/FG2 probe. Solution samples were dissolved in $\text{DMSO-}d_6$ and placed into a 5 mm o.d. borosilicate glass NMR tube. Samples were spun at 15 Hz and locked with respect to the deuteriated solvent. ^1H spectra were acquired using a single pulse experiment, with a relaxation delay of 1 s, the number of spectral accumulations was 16 scans and the 90° pulse width was 14.5 μs . ^{13}C spectra were acquired using a standard ^1H -decoupled pulse sequence, with a relaxation delay of 1 s, the number of spectral accumulations was 10240 scans and the pulse width was 12.5 μs .

Chemical shifts from the ^1H -NMR spectra indicate that there are no other signals which can be related to impurities and thus it can be surmised that the purity of the compounds is at least $> 95\%$

^1H -NMR kinetic studies of the three molecules have been carried out in the solution state (CD_3OD). In addition to the foregoing, a ^{13}C -NMR kinetic study has also been conducted, but for Rd only. Figs.1.2 and 1.3. display the ^1H -NMR and ^{13}C -NMR spectra of Rd after 30, 120 mins and 7 days, respectively. The spectra clearly demonstrate that hydrogen-deuterium exchange is not complete, even after seven days. There is no evidence for CD_2 , but this species cannot be ruled out because of the poor intrinsic sensitivity of the ^{13}C -NMR experiment. With time $^1\text{J}_{\text{CD}}$ splitting is observed (as highlighted by the appearance of a triplet (at ~ 40 ppm)). No evidence of CD_2 can be observed due to the fact that this would appear as a quintet, yet no such signals are observed; the fact that it cannot be observed does not rule out its existence. In the case of ^1H -NMR spectra $^2\text{J}_{\text{HD}}$ splitting can be observed as a function of time but, of course, if

CD_2 had been formed it would not be observed in a ^1H -NMR experiment. For H_2NRd , the hydrogen-deuterium exchange has almost gone to completion after 24 hrs (Fig.1.5). NMR spectra for MeRd showed a hydrogen-deuterium exchange after 40 mins, as shown in Fig. 1.6. Furthermore, addition of DCl does not cause any change in the ^1H - NMR spectra of Rd (*i.e.*, there is no ring scission upon the addition of HCl in methanolic solution), as illustrated in Fig.1.4.

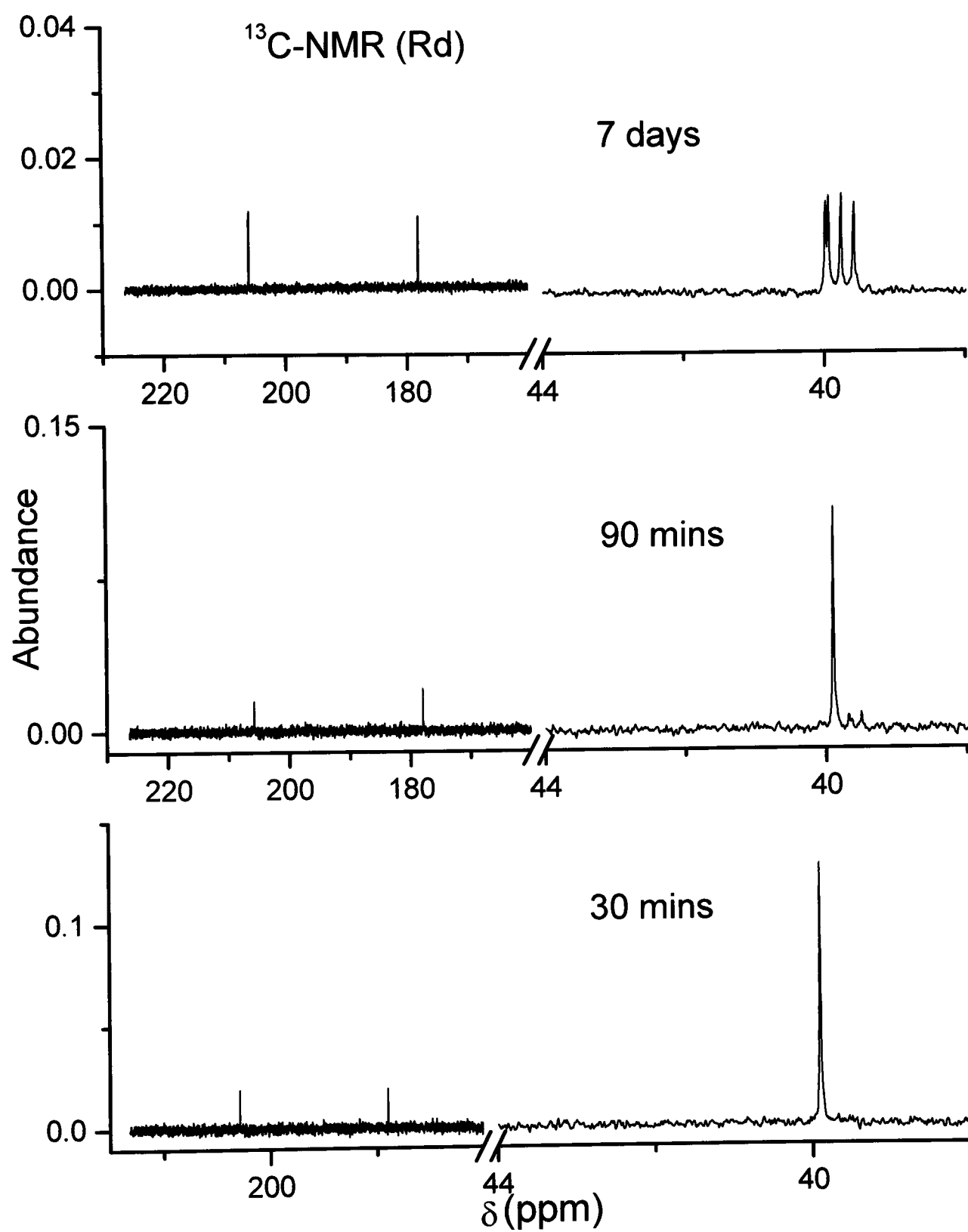


Figure 1.2. ^{13}C -NMR spectra of Rd, H_2NRd and MeRd in the solution state (CD_3OD).

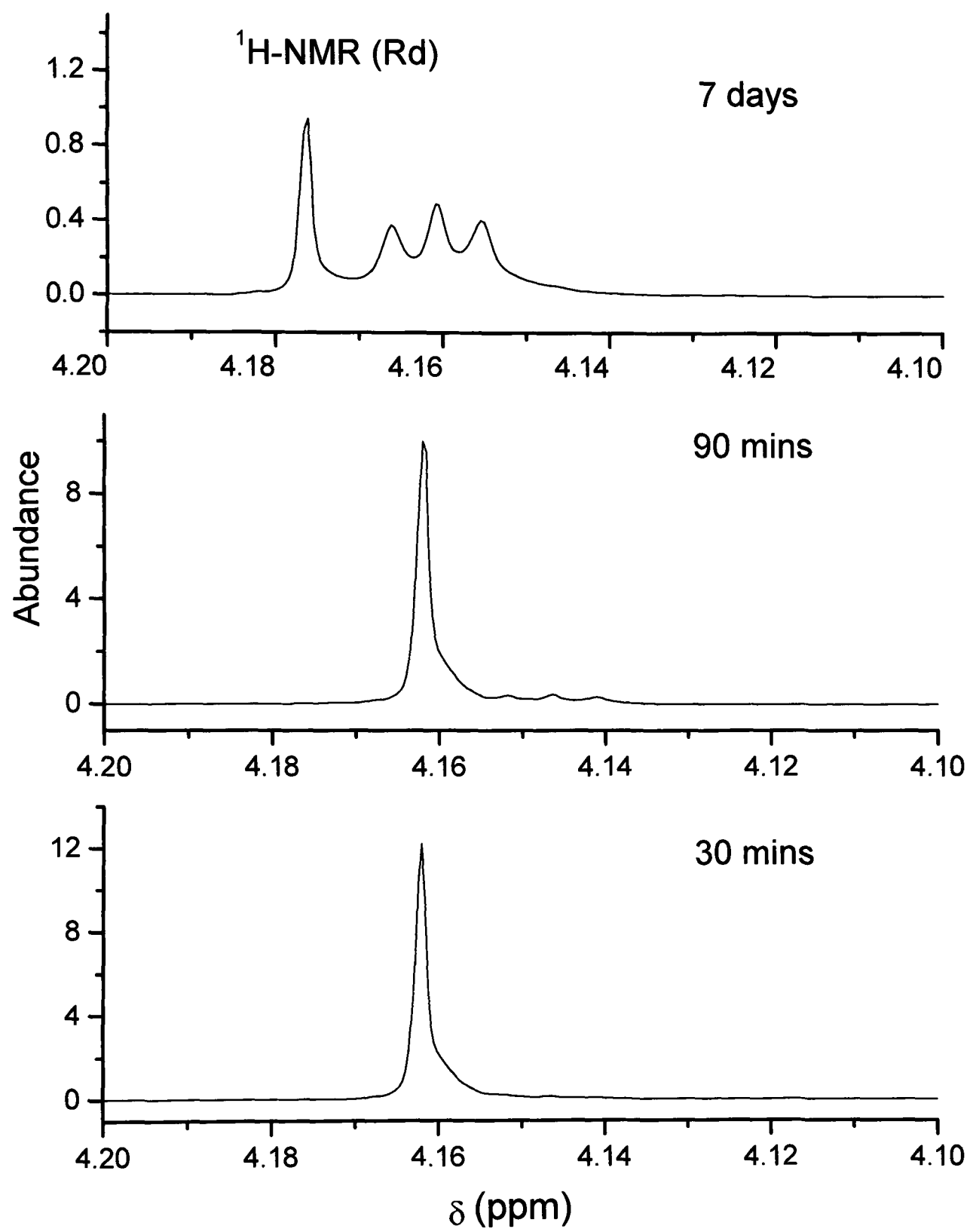


Figure 1.3. $^1\text{H-NMR}$ spectra of Rd in the solution state.

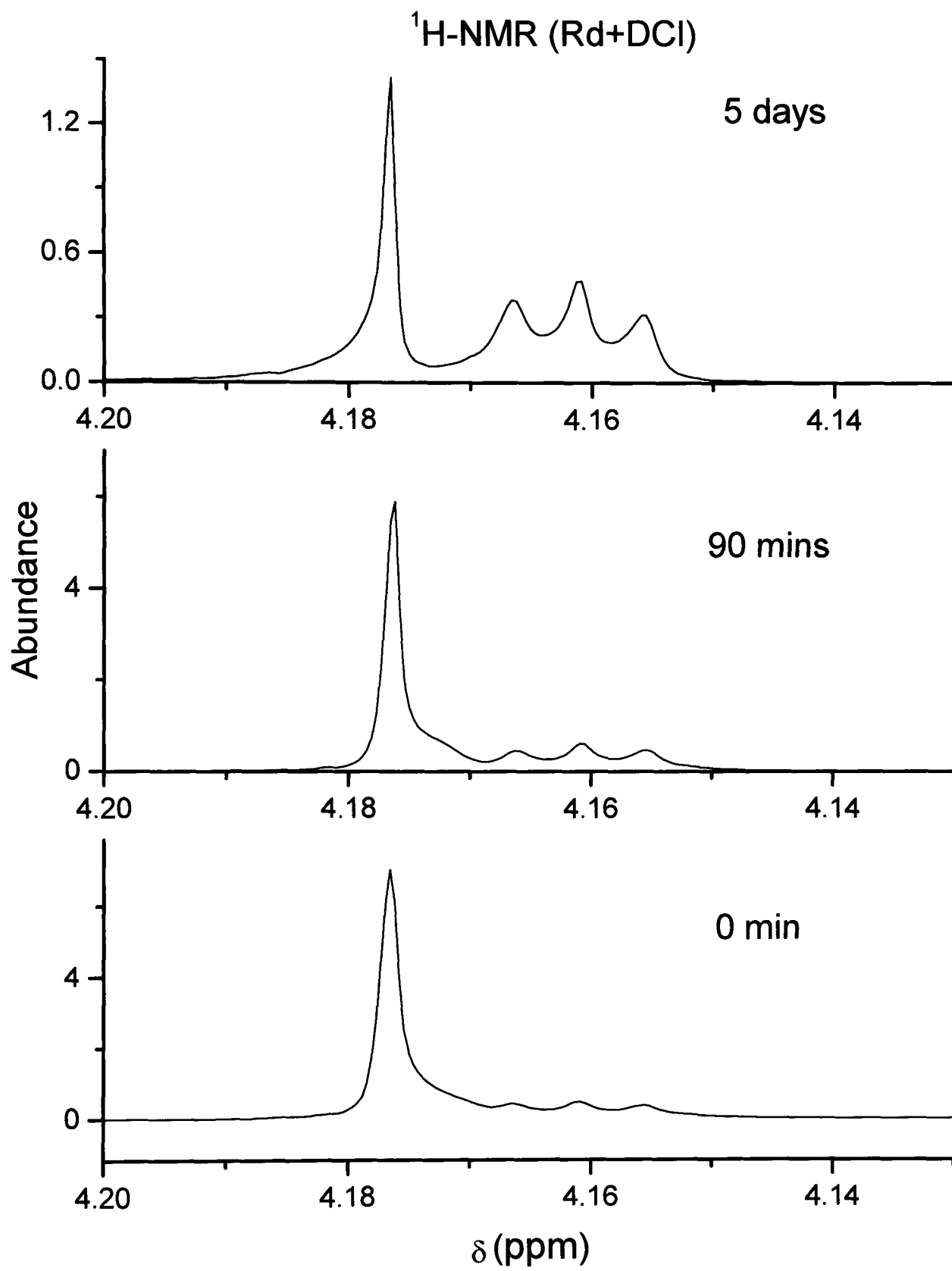


Figure 1.4. $^1\text{H-NMR}$ spectra of Rd in the solution state, in the presence of DCI.

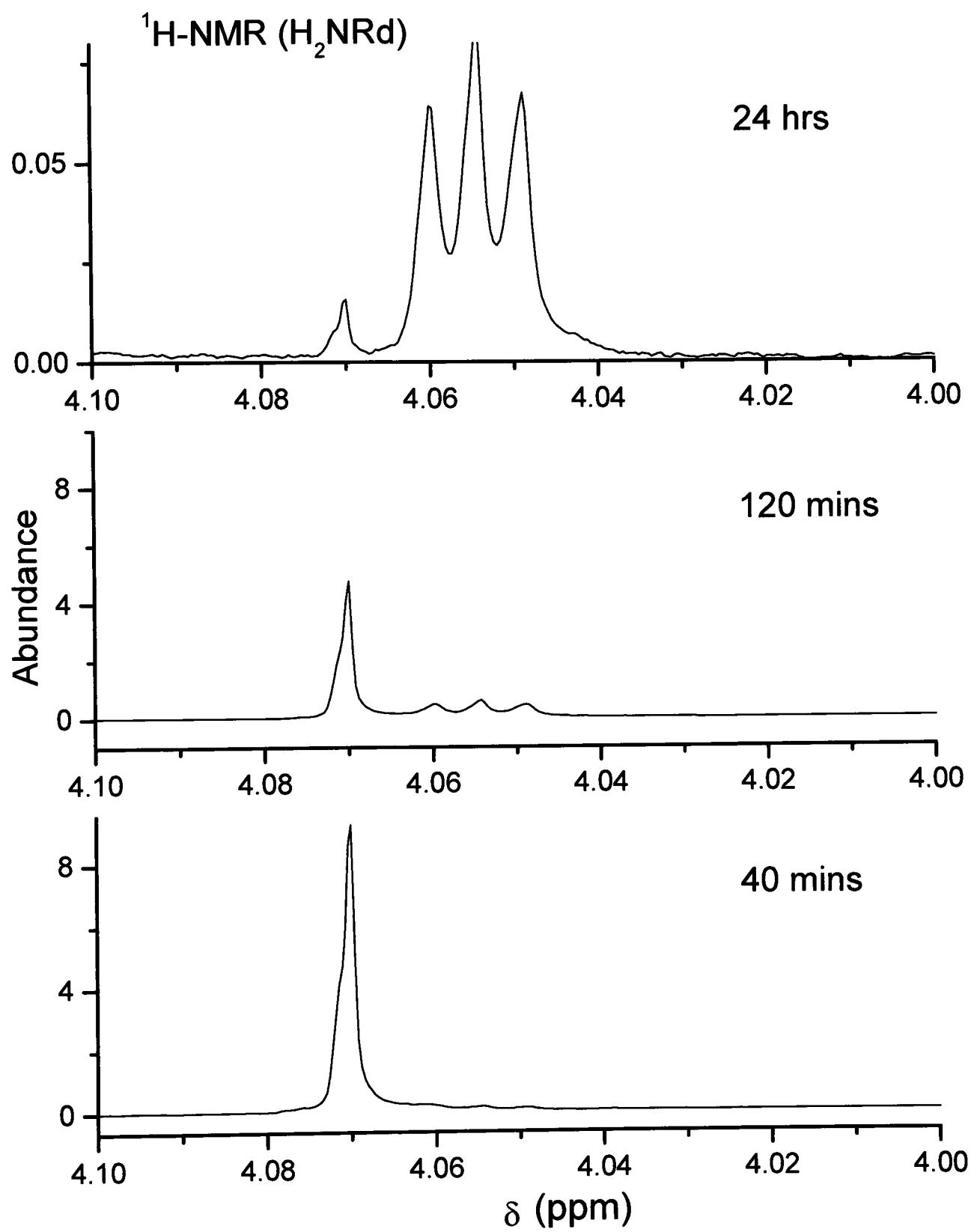


Figure 1.5. ¹H-NMR spectra of H₂NRd in the solution state.

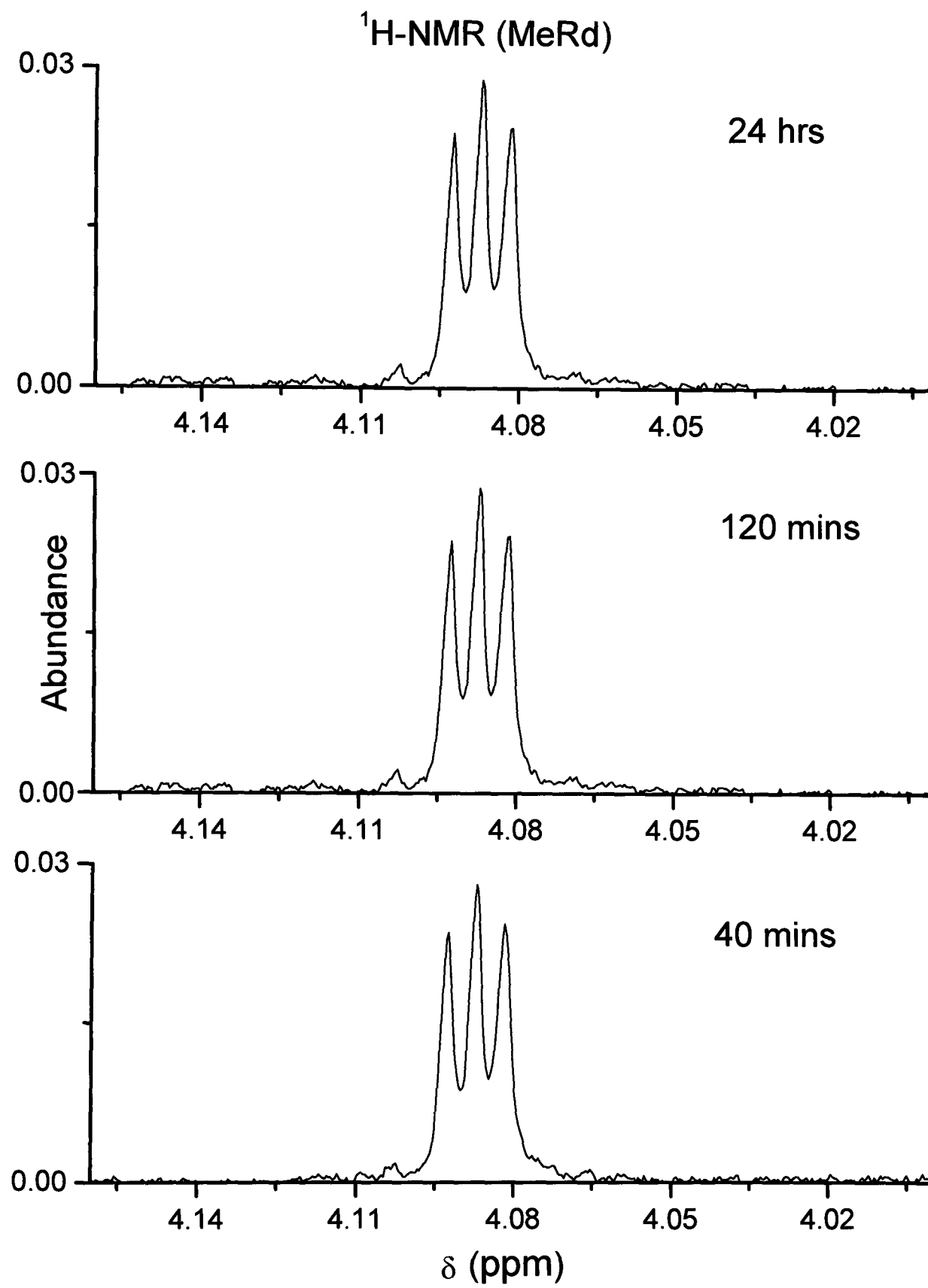


Figure 1.6. ¹H-NMR spectra of MeRd in the solution state (CD₃OD).

1.3. Mass Spectra of Rd and its Derivatives

The mass spectra of these molecules (Figs. 1.9-1.11) have also been investigated. Mass spectral data for the three molecules were recorded on a BioQ Tandem mass spectrometer using loop injection into a flow of methanol. MS-MS were acquired with a collision energy of 25 volts using argon as the collision gas.

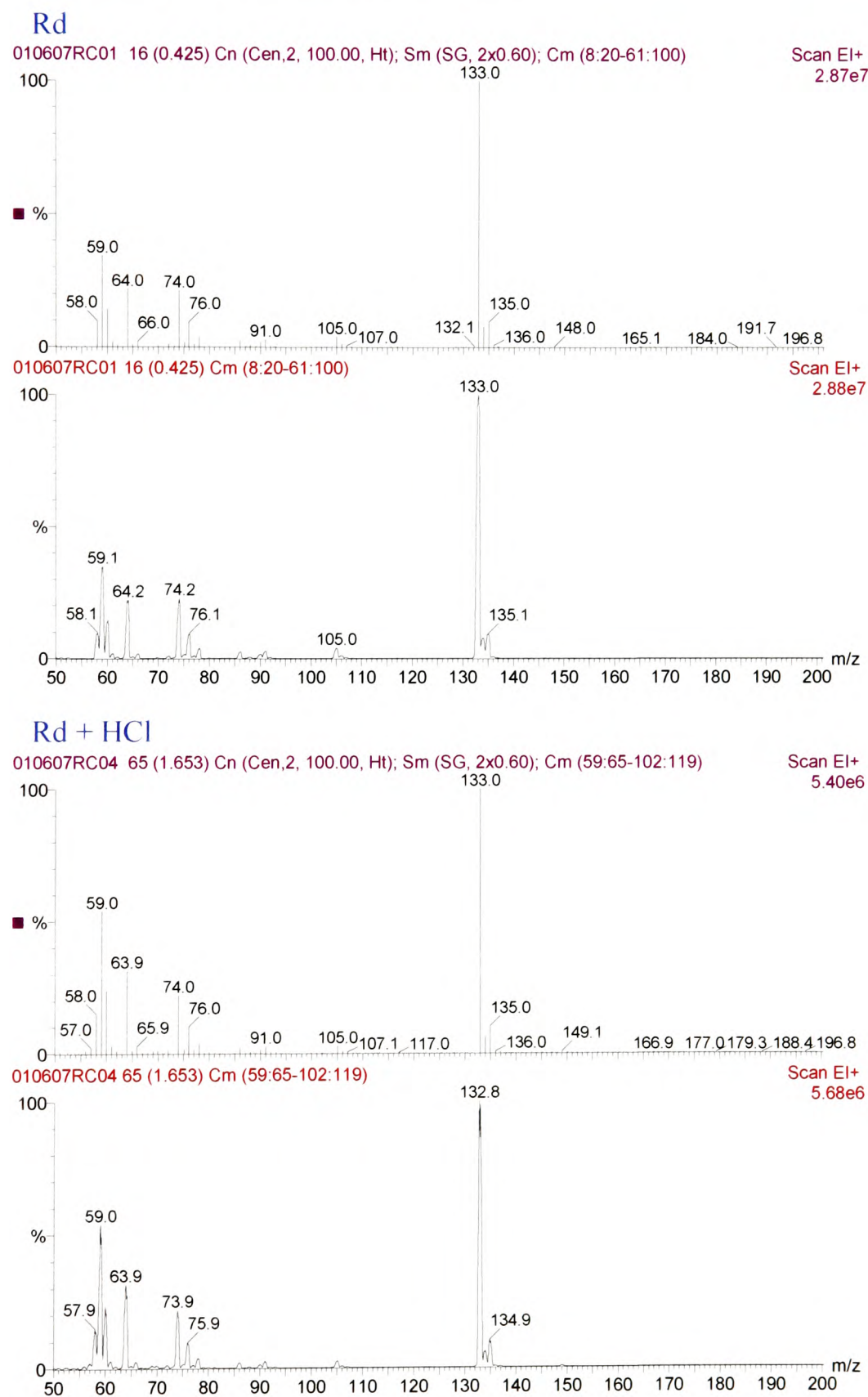


Figure 1.9. Mass spectra of Rd alone and Rd in HCl.

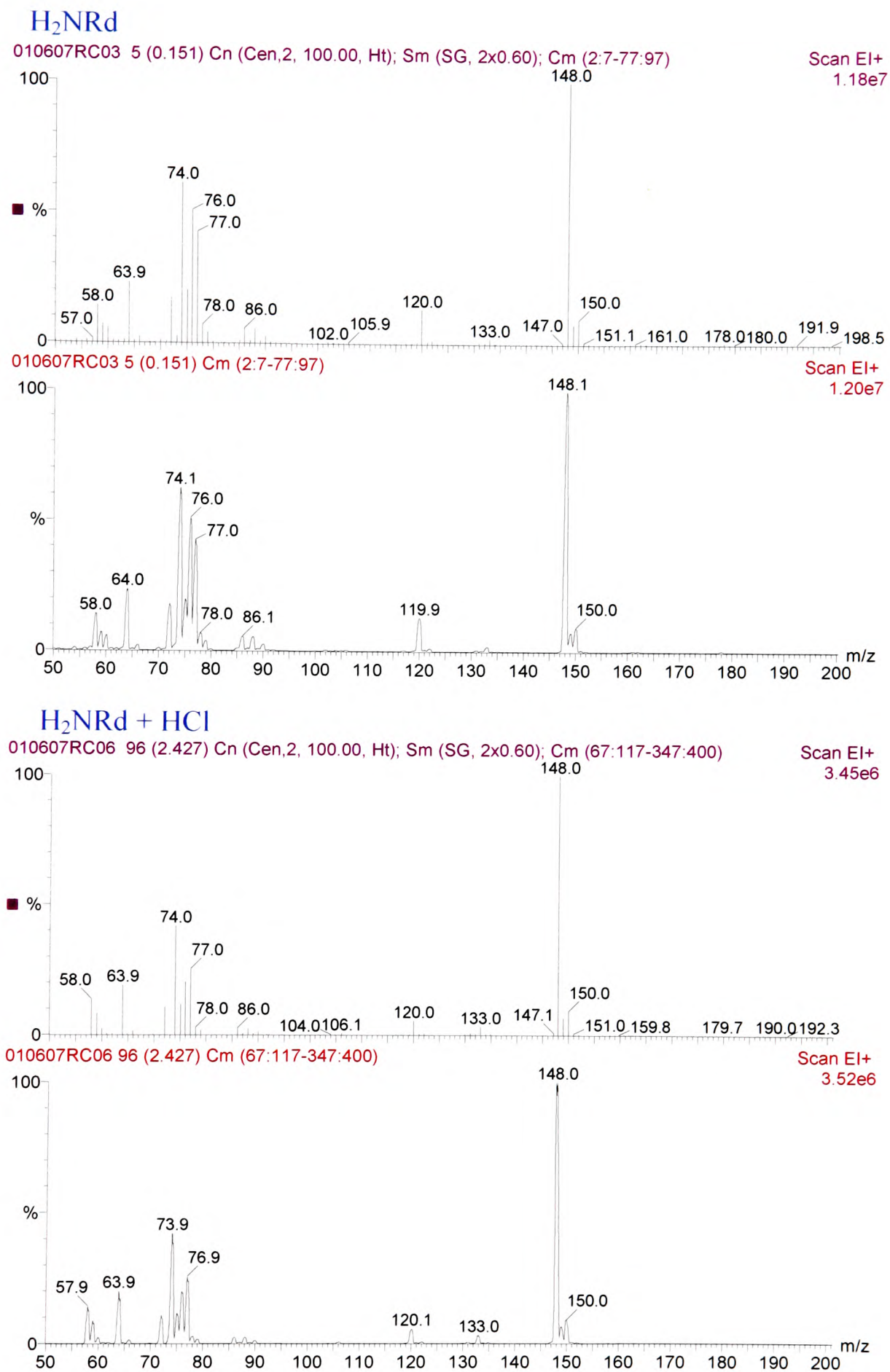


Figure 1.10. Mass spectra of H₂NRd alone and H₂NRd in HCl.

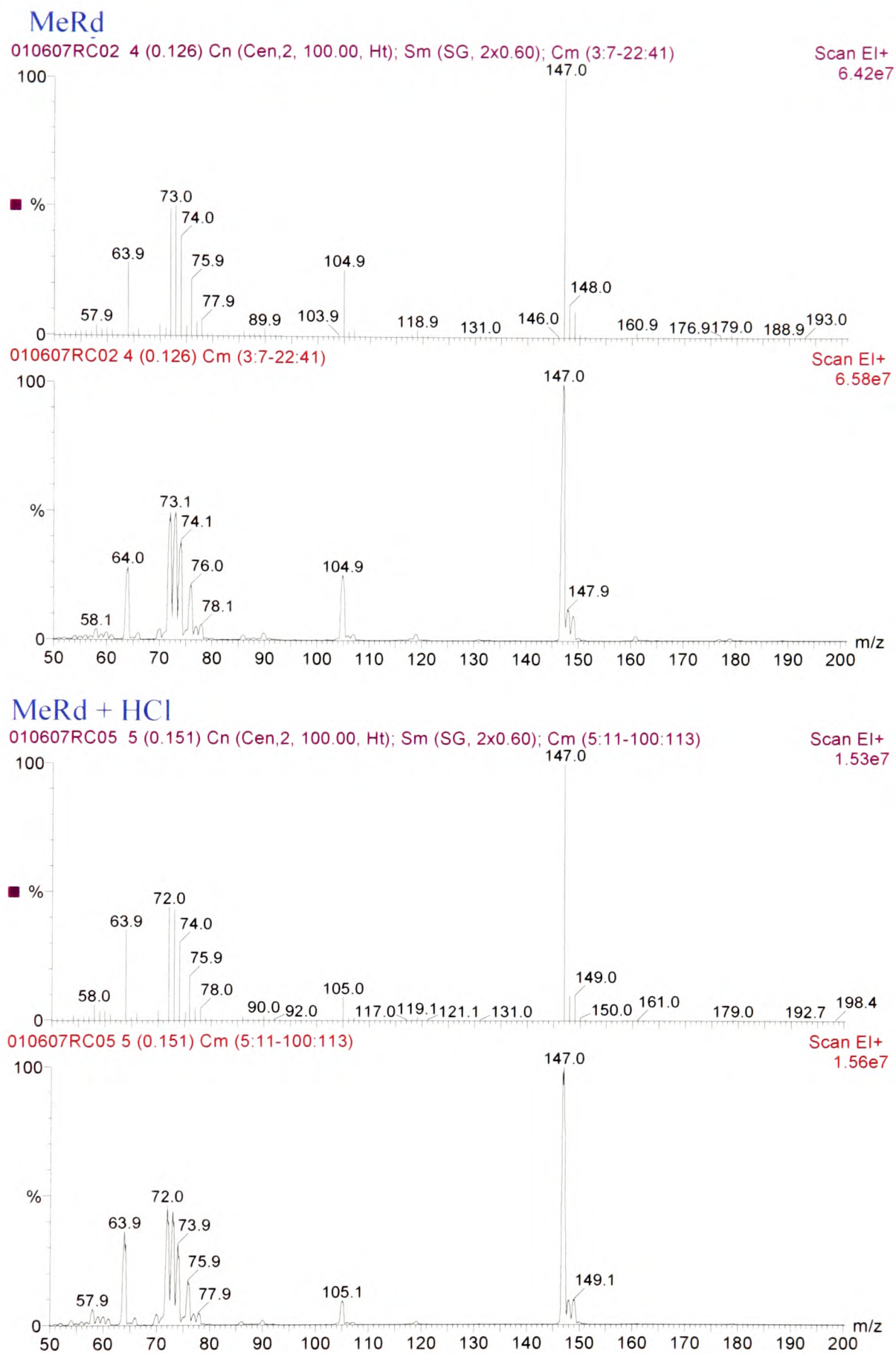


Figure 1.11. Mass spectra of MeRd alone and MeRd in HCl.

The mass spectroscopy results show that the molecules are pure and there is no change in the mass spectra after the addition of HCl.

1.4. Resonance Structures of Rd

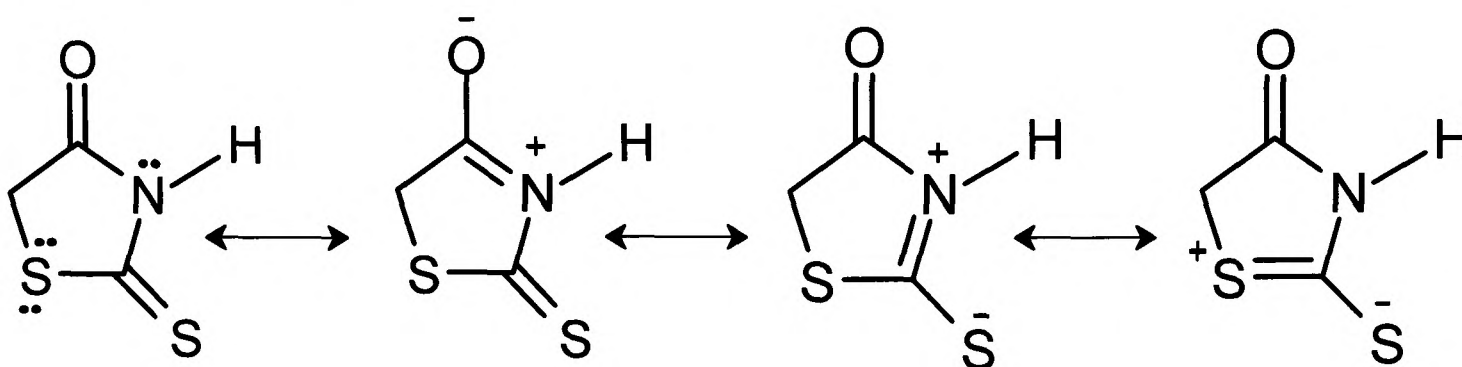


Figure 1.12. Schematic representation of the possible resonance structures of rhodanine.

1.5. X-ray Crystallographic Structure of Rd

The following data for the X-ray crystallographic structure of Rd was retrieved from the Cambridge structural data base³.

Lengths		Angles	
a	10.02	alpha	90
b	7.67	beta	102.63
c	7.28	gamma	90

System: Monoclinic

Space group: P21/n

Space group number: 14

R-factor = 0.14

Z = 4

Calculated cell volume = 545.954

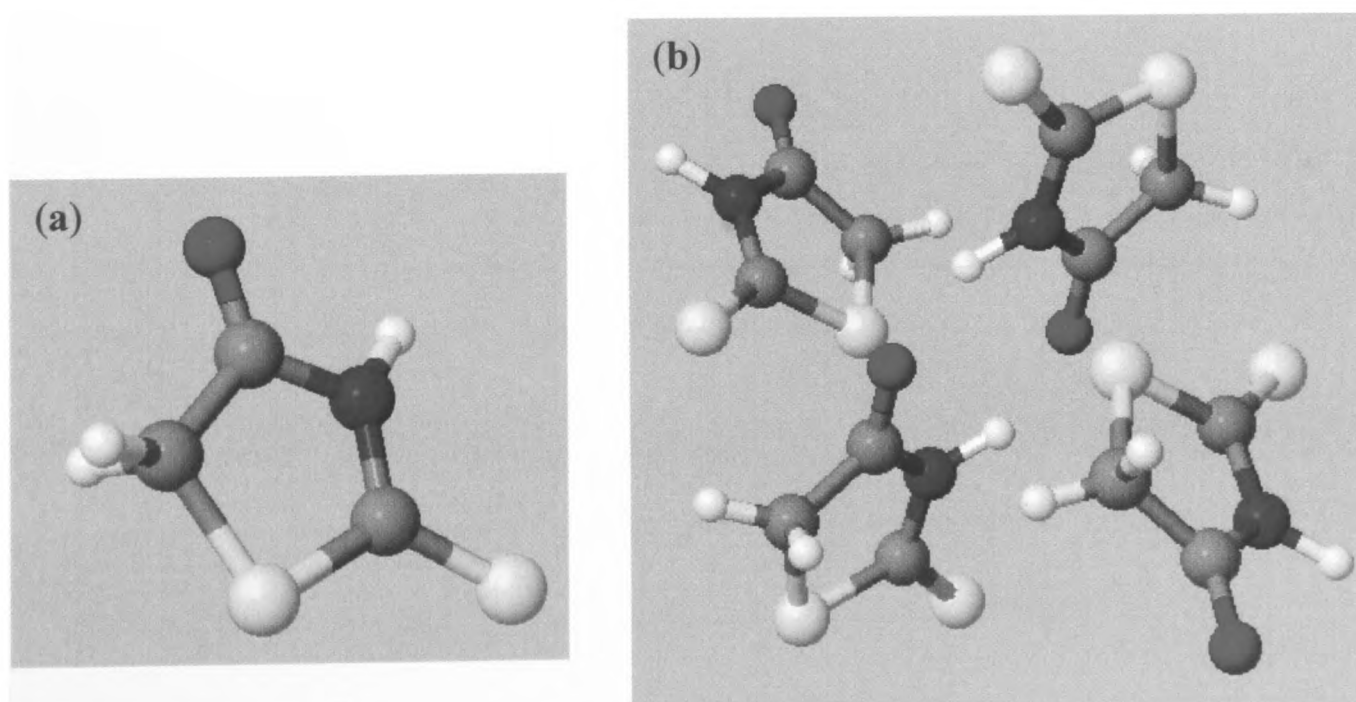


Figure 1.13. X-ray crystallographic structure of Rd showing (a) an isolated molecule and (b) crystal packing.

References

- [1] O. Navratil and J. Kotas, *Coll. Czech. Chem. Comm.*, **30**, (1965), 2736.
- [2] N. Mofaddel, N. Bar, D. Villemin and P. L. Desbene, *Anal. Bioanal. Chem.*, **380**, (2004), 664.
- [3] D. van der Helm, A. E. Lessor and L. L. Merritt, *Acta Cryst.*, **15**, (1962), 1227.

Addendum

Publications in Preparation

- 1. S. Jabeen**, T. J. Dines, R. Withnall and B. Z. Chowdhry
Fenamates: Vibrational Spectroscopy and DFT Calculations of Polymorphic Forms
(*J. Phys. Chem.*)
- 2. S. Jabeen**, T. J. Dines, R. Withnall and B. Z. Chowdhry
Sulphonamides: Studies of Polymorphic Forms by Raman/FT-IR and Density
Functional Theory Calculations (*J. Pharm. Sci.*)
- 3. S. Jabeen**, T. J. Dines, Rex Palmer and B. Z. Chowdhry
High resolution Crystal Structures of 3-Aminorhodanine and 3-Methylrhodanine
(*J. Biomol. & Org. Chem.*)
- 4. S. Jabeen**, T. J. Dines, R. Withnall and B. Z. Chowdhry
Vibrational Spectroscopy and DFT Calculations of Polymorphs of Metformin
(*J. Pharm. Sci.*)
- 5. S. Jabeen**, T. J. Dines, and R. Withnall, and B. Z. Chowdhry
SERS and DFT calculations of rhodanine and its derivatives adsorbed on Ag and Au
substrates (*Surf. Sci.*)
- 6. S. Jabeen**, T. J. Dines, R. Withnall and B. Z. Chowdhry
Influence of Aggregating Agents on Ag and Au Nanoparticles (NPs) aggregation
(*Langmuir*)
- 7. S. Jabeen**, T. J. Dines, R. Withnall, B. Z. Chowdhry
Experimental and theoretical (DFT) Vibrational Spectroscopic Investigations of
Rhodanine and its Derivatives in the Solid State (*J. Phys. Chem.*)
- 8. S. Jabeen**, B. Z. Chowdhry, R. Withnall, and T. J. Dines
DFT calculations of the Raman spectra of zwitterionic α -amino acids (*J. Phys.
Chem.*)
- 9. S. Jabeen**, I.T. Shadi, R. Withnall, S. A. Leharne and B.Z. Chowdhry
FT-Raman and SERRS analysis of two structurally related triarylmethane dyes:
Victoria blue B and Victoria blue BO
(*Anal. Chim. Acta.*)

.....

Workshops/Conferences Attended

Workshops

- **Gaussian Workshop (Applications)**
5th -6th September (2006)
- **Gaussian Workshop for Beginners**
27th -28th September (2005)
Imperial College London and NSCCS, London, UK

.....

Conferences

- **Faraday Discussion 132: SER(R)S**
19th - 21st September (2005)
Imperial College, London, UK
- **20th International Conference on Raman Spectroscopy (ICORS)**
20-25th August (2006)
(Yokohama, Japan)

- **Proceedings of the 20th International Conference on Raman Spectroscopy**
Ed: H. Hamaguchi (2006)



	Page N^o
1 Resonance Raman Spectroscopy of Flower Petals Babur Z. Chowdhry, Robert Withnall, Saima Jabeen , and Stephen A. Leharne	359
2 Sulphonamides: Studies of Polymorphic Forms by Raman & FT-IR Babur Z. Chowdhry, Saima Jabeen , Trevor J. Dines, Stephen A. Leharne, and Robert Withnall	360
3 Theoretical and Experimental Investigations of the Vibrational Spectra of Sultams Babur Z. Chowdhry, Saima Jabeen , Trevor J. Dines, Robert Withnall, Summia Naz, Laura J. Waters, and Karl Hemming	361
4 Experimental and Computational Studies of β-Cyano-L-alanine Andrew P. Mendham, Trevor J. Dines, Saima Jabeen , Robert Withnall, and Babur Z. Chowdhry	364
5 Raman Studies of Selenomethionine and Selenocystine Andrew P. Mendham, Saima Jabeen , Trevor J. Dines, Robert Withnall, and	365

-
- Babur Z. Chowdhry
- 6 Tea-tree Oil: Raman and NMR spectroscopic and Calorimetric Investigations**
Saima Jabeen, Trevor J. Dines, Andrew P. Mendham, Robert Withnall, and Babur Z. Chowdhry 367
- 7 Photocorrelation Spectroscopy and Zeta-Potential Measurements of a SERS Substrate**
Robert Withnall, Saima Jabeen, Trevor J. Dines, and Babur Z. Chowdhry 393
- 8 DFT calculations of the Raman spectra of zwitterionic α -amino acids**
Trevor J. Dines, Babur Z. Chowdhry, Saima Jabeen, and Robert Withnall 410
- 9 Vibrational Spectroscopic Investigations of Rhodanine and Structural Derivatives in the Solid State**
Robert Withnall, Saima Jabeen, Trevor J. Dines, Steven Leharne, and Babur Z. Chowdhry 425
- 10 Experimental and Theoretical Studies of 3-Aminoquinuclidine**
Robert Withnall, Saima Jabeen, Trevor J. Dines, Steven A. Leharne, and Babur Z. Chowdhry 445
- 11 Experimental & Theoretical Vibrational Spectroscopic Studies of Amino Acids**
Saima Jabeen, Trevor J. Dines, Stephen A. Leharne, Robert Withnall, and Babur Z. Chowdhry 471
- 12 Computational and Experimental Vibrational Spectroscopic Studies of Fenamates**
Saima Jabeen, Trevor J. Dines, Stephen A. Leharne, Robert Withnall, and Babur Z. Chowdhry 472
- 13 Raman & *Ab Initio* Studies of Phosphorylated Amino Acids**
Saima Jabeen, Trevor J. Dines, Stephen A. Leharne, Robert Withnall, and Babur Z. Chowdhry 473

(Note: all the experimental and theoretical work for all the above titled posters, presented at ICORS, is complete)